Dissertation

Submitted to the

Combined Faculty of Natural Sciences and Mathematics

Heidelberg University, Germany

for the degree of

Doctor of Natural Sciences (Dr. rer. nat.)

Presented by

M. Eng. Wansheng Zong

Oral examination: July 26th, 2023

Synthesis and Characterization of Large Azaacenes and Stable Azaacene Radical Anions

Gutachter: Prof. Dr. Uwe H. F. Bunz

Prof. Dr. Milan Kivala

Acknowledgement

Studying in Heidelberg University is a dreamlike experience for me. In 2017, when I was still an undergraduate student, my teacher Prof. Dr. Xu shared his living and studying abroad experience to me. I was looking forward to it, but never thought I would stay in Germany someday at that moment. Thanks to my supervisor, Prof. Dr. Uwe H. F. Bunz, gave me an opportunity to do PhD research in AK Bunz. Now I am so lucky to have been studying here, pursuing my doctor degree.

At first, I would like to show my deepest gratitude to my respectful supervisor, Prof. Dr. Uwe H. F. Bunz. During these years, Prof. Bunz has offered me with the valuable guidance in every stage of the working and writing. Without his patient instruction, insightful criticism, and expert guidance, the completion of this thesis would not have been possible. It's my great honor to be his student. I also want to express my sincere appreciation to Dr. Jan Freudenberg for his permanent guidance and kind help during the time of my research. His professional and valuable advice contributes a lot to my works. He showed great tolerance for my lack of experimental and writing experiences.

I would like to take this opportunity to thank Nikolai Hippchen and Nico Zeitter for their kind supports and cooperations on the project of heptacenes. Besides, I would also thank Prof. Dr. Andreas Dreuw and his Ph.D. student Marco Bauer, for the quantum chemical calculations on the project of tetraazahexacenes.

I would like to express a special gratitude to Dr. Hao Zhang, Saskia Braun and Daniel Ehjeij, my kind colleagues, who kindly took care of me for my first year in Heidelberg University. Their patient guidance and fruitful discussion made me adapt to laboratory and residential environment quickly.

I would like to thank Mrs. Kerstin Brödner, Olena Tverskoy, Kerstin Windisch, and Mr. Holger Lambert for their selfless dedication and effective organization to provide us an easeful working circumstance. I would also like to thank all staffs in Organisch-Chemisches Institut for their

kind help in chemicals and measurements, including Chemikalienausgabe, X-ray crystal structure analysis, MS analysis, NMR measurement, and elemental analysis.

I am also very grateful to my intelligent colleagues, Dr. Kai Seehafer, Dr. Frank Rominger, Dr. Gaozhan Xie, Dr. Michael Ganschow, Dr. Thomas Wiesner, Dr. Lukas Ahrens, Dr. Victor Brosius, Dr. Steffen Maier, Svenja Weigold, Benedikt Dittmar, Kathleen Fuchs, Maximilian Elter, Philipp Ludwig, Marcus Dodds, Daniel Sleeman, Pascal Merten, Fabian Jester et al. for their kind advice and valuable discussion during my research. I'm so lucky to have these very great persons as my colleagues.

I deeply appreciate my good friends, Ke Tian, Dr. Weiwei Zuo, Dr. Ke Wang and Xiaohui Wang who are always there to support and encourage me. With their company, I have never felt lonely.

Finally, I would like to thank my beloved family. My parents are so unselfish, lovely, and open-minded. Their constant support, care, and love make me brave when I face difficulties in my study and life.

I am very grateful to the CSC (Chinese Scholarship Council) for their financial support of my Ph.D. research.

Abstract

The objective of this thesis was the synthesis and characterization of larger (aza)acenes (> pentacenes) and their radical anions. The thesis focuses on the stabilization of azaacenes by positioning the silylethynyl groups adjacent to the central pyrazine / pyrazinopyrazine rings, which renders azaacenes immune to Diels-Alder reactions, butterfly dimerization and endoperoxide formation (Figure 1).

Six (aza)heptacenes containing 0, 2, 4 or 6 nitrogen atoms and four triisopropylsilyl (TIPS) ethynyl substituents were synthesized. The position of the four TIPS ethynyl substituents determines the (aza)heptacenes' stability. The symmetric 7,16-diaza-6,8,15,17-tetrakis (triisopropylsilylethynyl)heptacene (**DAH1**), in which the two nitrogen atoms occupy the central ring and the four TIPS-ethynyl substituents fill the four positions in the two directly adjacent rings, is much more stable than any hitherto reported (aza)heptacenes and survives several weeks in solution on the benchtop according to UV-Vis studies. Thin film transistors with μ_e = 0.042 cm^2V^{-1} s^{-1} were produced for **DAH1**. The tetraazaheptacene (**TAH**) is also reasonably stable ($\tau_{1/2}$ > 7 d), but hexaazaheptacene (**HAH**) is such a strong oxidant that undergoes spontaneous reduction ($\tau_{1/2}$ ≈ 5 d) according to UV-Vis studies.

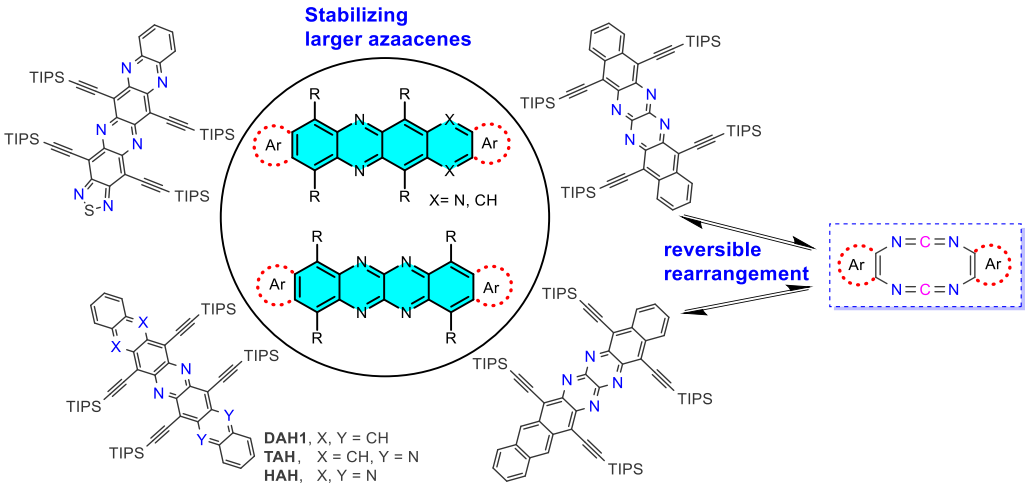

Figure 1. Schematic structure (stabilizing azaacenes core) along with exemplary target molecules from this work (periphery).

A series of 5,8,13,16-tetraethynyl-6,7,14,15-tetraazahexacenes were synthesized – all were persistent in solution. Upon crystallization, the derivatives with TIPS ethynyl substituents equilibrate into their didehydrotetrazecines (cyclic biscarbodiimide) isomers in the solid state. This solid-state ring opening is enforced by the bulk of the substituents, crystal packing energy and aromaticity given in terms of Clar sextets – with increasing steric bulk the crystal lattice itself enforces ring opening. This process is fully reversible, upon dissolution, the steric force disappears and the bis-carbodiimides revert into the azaacene form. The reversible rearrangement process was also observed in the pentacene and heptacene congeners.

Zusammenfassung

Das Ziel dieser Arbeit war die Synthese und Charakterisierung größerer (Aza)Acene (> pentacen) und ihrer Radikalanionen. Das Hauptaugenmerk lag auf den Stabilisierungsstrategien durch Positionierung der Silylethinyl- Gruppen benachbart zu den zentralen Pyrazin-/Pyrazinopyrazin-Ringen, die Acene gegen Diels-Alder-Reaktionen, Butterfly-Dimerisierung und Endoperoxidbildung immun machen (Abbildung 1).

Sechs (Aza)heptacene mit 0, 2, 4, 6 Stickstoffatomen und Variation der Platzierung der vier Triisopropyl (TIPS) Ethinylsubstituenten wurden synthetisiert, um die dramatische Wirkung des Stickstoffgehalts und des Substitutionsmusters auf die Stabilität der Heptacene zu unterstreichen. Das symmetrische 7,16-Diaza-6,8,15,17-tetrakis(triisopropylsilylethinyl) heptacen (**DAH1**), bei dem die beiden Stickstoffatome den zentralen Ring besetzen und die vier TIPS-Ethinylsubstituenten die vier Positionen in den beiden direkt benachbarten Ringen einnehmen. UV-Vis-Studien zufolge ist die Bildung von Ringen viel stabiler als alle bisher beschriebenen (Aza)heptacene. Für **DAH1** wurde eine Einkristallstruktur erhalten und Dünnschichttransistoren mit μ_e = 0.042 cm^2V^{-1} s^{-1} hergestellt. Die Position der TIPS-Ethinylgruppen bestimmt die Stabilität des Azaheptacens. Das Tetraazaheptacen (**TAH**) ist ebenfalls einigermaßen stabil ($\tau_{1/2}$ > 7 d), aber Hexaazaheptacen (**HAH**) ist ein so starkes Oxidationsmittel, dass laut UV-Vis-Studien spontan reduziert wird ($\tau_{1/2}$ ≈ 5 d).

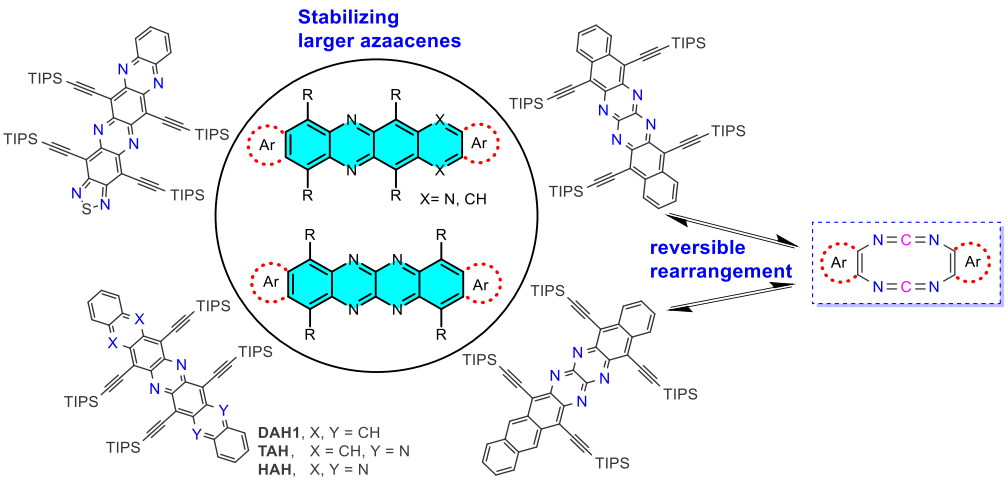

Abbildung 1. Schematische Struktur (stabilisierender Azaacenkern) zusammen mit beispielhaften Zielmolekülen aus dieser Arbeit (Peripherie).

Eine Reihe von 5,8,13,16-Tetraethinyl-6,7,14,15-tetraazahexazenderivaten wurde synthetisiert – alle waren in Lösung persistent. Bei der Kristallisation äquilibrieren die Derivate mit TIPS-Ethinylsubstituenten zu ihren Didehydrotetrazecin-Isomeren (zyklisches Biscarbodiimid). Diese Ringöffnung im Festkörper wird durch die Sterik der Substituenten, die Kristallpackungsenergie und die Aromatizität, die in Form von Clar-Sextetten gegeben ist, erzwungen – mit zunehmendem sterischen Anspruch erzwingt das Kristallgitter selbst die Ringöffnung. Dieser Prozess ist vollständig reversibel. Beim Auflösen verschwindet die Kristallpackungsenergie und die Biscarbodiimide reagieren in die Azaacenform zurück. Der reversible Umlagerungsprozess wurde auch bei den Pentacen- und Heptacen-Kongeneren beobachtet.

Abbreviations

OFET	organic field-effect transistors
OPV	organic photovoltaics
OLED	organic light-emitting diode
NLO	non-linear optical materials
NDI	naphthalenetetracarboxylic diimide
TTF	tetrathiafulvalene
BTBT	[1]benzothieno[3,2-b]benzothiophene
P3HT	poly(3-hexylthiophene-2,5-diyl)
PPV	poly(p-phenylene vinylene)
TNCQ	tetracyanoquinodimethane
PDIF-CN_2	*N,N′*-1H,1H-perfluorobutyldicyanoperylene-carboxydi-imide
PCBM	phenyl-C61-butyric acid methyl ester
p(NDI2OD-T2)	poly[N,N’-bis(2-octyldodecyl)-naphthalene-1,4,5,8-bis(dicarboximide)-2,6-diyl]-alt-5,5’-(2,2’-bithiophene)
TIPS-Pen	6,13-Bis(triisopropylsilylethynyl)pentacene
TIPS-TAP	6,13-bis(triisopropylsilylethinyl)-5,7,12,14-tetraazapentacene
TIPS-DAP	6,13-bis(triisopropylsilylethinyl)-5,7, -diazapentacene
DAH	diazaheptacene
TAH	tetraazaheptacene
HAH	hexaazaheptacene
TAHex	tetraazahexacene
DAHex	diazahexacene
TIPS	tri-*iso*-propylsilyl
TES	triethylsilyl
TMS	trimethylsilyl
TBDMS	*tert*-butyldimethylsilyl
*t*Bu	*tert*-butyl
*s*Bu	*sec*-butyl
*i*Pr	*iso*-propyl

CVD	chemical vapor deposition
FMO	frontier molecular orbitals
EA	electron affinity
IP	ionization potential
HOMO	highest occupied molecular orbital
LUMO	lowest occupied molecular orbital
Calcd.	calculated
Compd.	compound
DCM	dichloromethane
EE	ethyl acetate
PE	petroleum ether
Tol	toluene
THF	tetrahydrofuran
Et_2O	diethyl ether
$CDCl_3$	deuterated chloroform
CD_2Cl_2	deuterated dichloromethane
SiO_2	silicon dioxide
DFT	density-functional theory
NMR	nuclear magnetic resonance
TLC	thin layer chromatography
UV-Vis	ultraviolet-visible spectrophotometry
CV	cyclic voltammetry
IR	infrared spectroscopy
HRMS	high resolution mass spectrometry
GCMS	gas chromatography–mass spectrometry
EI	electron ionization
ESI	electrospray ionization
ppm	parts per million
quant.	quantitative
M.p.	melting point
EPR	electron paramagnetic resonance

MALDI	matrix-assisted laser desorption/ionization
GP	general procedure
et al.	and others (lat. et alia)
DI	demineralization
MnO_2	manganese(IV) oxide
PbO_2	lead(IV) oxide
NaH_2PO_2	sodium hypophosphite
$Cu(OAc)_2$	copper(II) acetate
NICS	nucleus-independent chemical shift
Pd_2dba_3	tris(dibenzylideneacetone)dipalladium(0)
RuPhos	2-dicyclohexylphosphino-2',6'-diisopropoxybiphenyl
RuPhos Pd G1	(RuPhos) palladium(II) phenethylamine chloride (1:1 MTBE solvate), chloro-(2-dicyclohexylphosphino-2',6'-diisopropoxy-1,1'-biphenyl)[2-(2-aminoethyl)phenyl]palladium(II) - methyl-t-butyl ether adduct
$SnCl_2$	stannous chloride
n-BuLi	*n*-butyllithium
KI	potassium iodide
Cs_2CO_3	caesium carbonate
$LiAlH_4$	lithium aluminium hydride
NBS	*N*-bromosuccinimide
NCS	*N*-chlorsuccinimid
NIS	*N*-chlorsuccinimid
BBr_3	boron tribromide
LDA	lithium diisopropylamide
Fc	ferrocene
Bu_4NPF_6	tetrabutylammonium hexafluorophosphate
KC_8	potassium graphite
r.t.	room temperature
δ	chemical shift
μ	mobility
$\tau_{1/2}$	half-life
h	hour

min	minutes
d	days
λ	wavelength
Å	angstrom
Z	the number of molecules in the unit cell

Table of Content

Chapter 1. Introduction

1.1 Organic Semiconductors and Field-Effect Transistors

In 1977, Shirakawa, MacDiarmid and Heeger reported the conductivity of halogen-doped polyacetylene, which is regarded to be the birth of organic electronics.[1-3] This research area is mainly concerned with the development and application of organic materials with semiconducting properties.

Due to the structural variability of organic materials, organic semiconductors are widely researched as active components in field-effect transistors[4-5] (organic field-effect transistors, OFETs), organic solar cells[6-7] (organic photovoltaics, OPVs) and as organic light-emitting diodes (OLEDs). There are already some commercially available applications of organic electronics, such as mobile electronic displays[8-9] and bioelectronic devices (Figure 2).[10-11] However, most of the developed technologies are not yet ready for the market — only in the start-up phase. In particular, the still expandable efficiency and the limited service life are the hurdles to broadening market conquest.[12] A key to addressing this issue lies in organic synthesis, which should make it possible to prepare new materials with high stability and broad modifiability.

Figure 2. LG R30, flexible OLED panel at CES 2016 (left, copyright Street Co'); flexible, transparent organic solar cells (middle, copyright ELE Times Bureau) and liquid-processed OFET on flexible substrate (right, copyright IP Tech).[13-15]

Organic semiconductors are categorized into small molecules (e.g. rubrene,[16] pentacene,[17-19] oligothiophenes,[20] naphthalenetetracarboxylic diimide (NDI),[21-24] and their derivatives), and conjugated polymers (e.g. polythiophenes,[25-27] polyphenylene,[28] poly(triarylamine)[29] and

their derivatives). In polymeric semiconductors, additional charge transport can take place along the polymer backbone. This is not possible with small semiconductor molecules, so that a regular arrangement of the molecules in the solid state with sufficient electronic coupling is necessary for the charge transport. Small conjugated molecules have far less synthetic batch-to-batch variance, which provides adequate assurance of a stable device performance, thus having higher potential for commercial applications.

Alternatively, semiconductors can also be categorized by their transporting channel into hole (p-type) conductors and electron (n-type) conductors as shown in Figure 3. The charge transport in a semiconductor can take place through the translation of a negative charge or a positive charge. To make this possible, there must be a sufficient overlap of the wave functions of neighboring semiconductor molecules.[30] Fewer n-type organic semiconductors, required to fabricate complementary metal-oxide-like logic circuits together with p-channel OFETs,[31] have been exploited, and their mobility values are on average still lower in comparison to p-type organic semiconductors.[32-35]

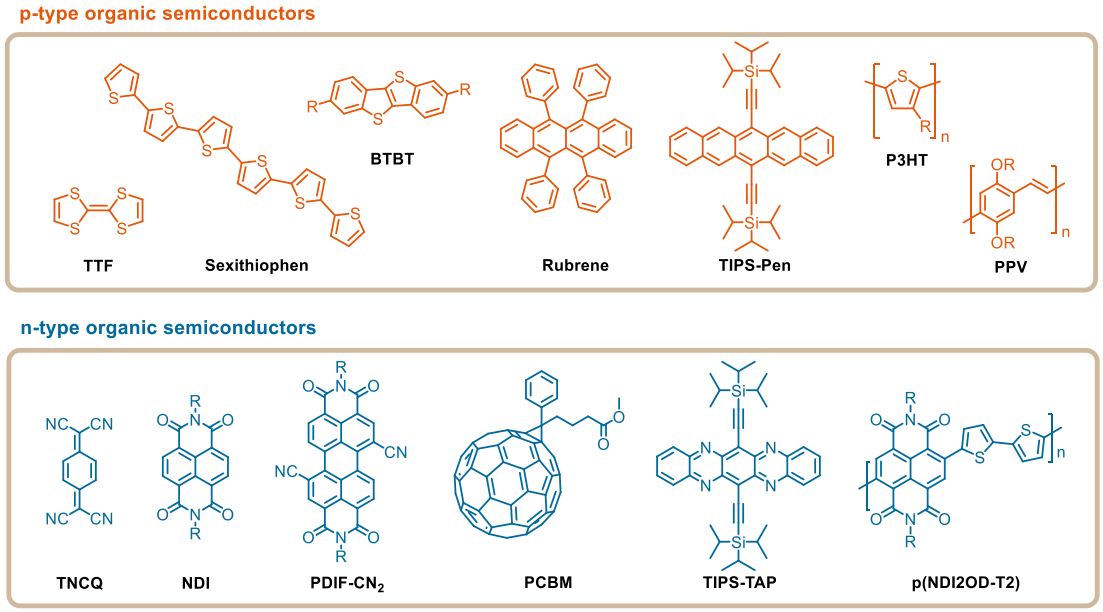

Figure 3. Representative p- and n-type organic semiconductors (TTF,[36] sexithiophene,[37] BTBT,[38] rubrene,[16] TIPS-Pen,[39] P3HT,[40] PPV,[41] TNCQ,[42] NDI,[21-24] PDIF-CN_2,[43-45] PCBM,[46-48] TIPS-TAP,[49] p(NDI2OD-T2)[50]).

Field-effect transistors are an indispensable component in every electronic circuit in the digital age. An example should show the extent to which transistors are used in everyday life: The

latest single-chip systems for mobile phones have several billion transistors on areas of less than 100 mm^2. For large-area applications on flexible substrates or paper where peak performance is not required, silicon is not an option for technical or economic reasons, and organic semiconductors represent attractive alternatives. Furthermore, OFETs are of low cost, low weight, and easy to prepare in comparison with inorganic transistors.[51]

A typical OFET is made up of a source electrode, a drain electrode, a semiconductor layer, a dielectric layer, and a gate electrode. The modulation of the source-drain current in transistors is realized by tuning the density of charge carriers in the thin organic semiconductor layer, generated by an electric field applied between the semiconductor and the gate electrode. Due to the variable processing of the components, four different vertical component architectures can be distinguished (Figure 4). Each architecture has its advantages and disadvantages. In this work, we use bottom-gate/top-contact and top-gate/bottom-contact transistors. Experiments and calculations showed that the contact resistance at the interface between the semiconductor and the source and drain electrodes has a smaller influence on the device performance in these architectures than in the others.[52-54]

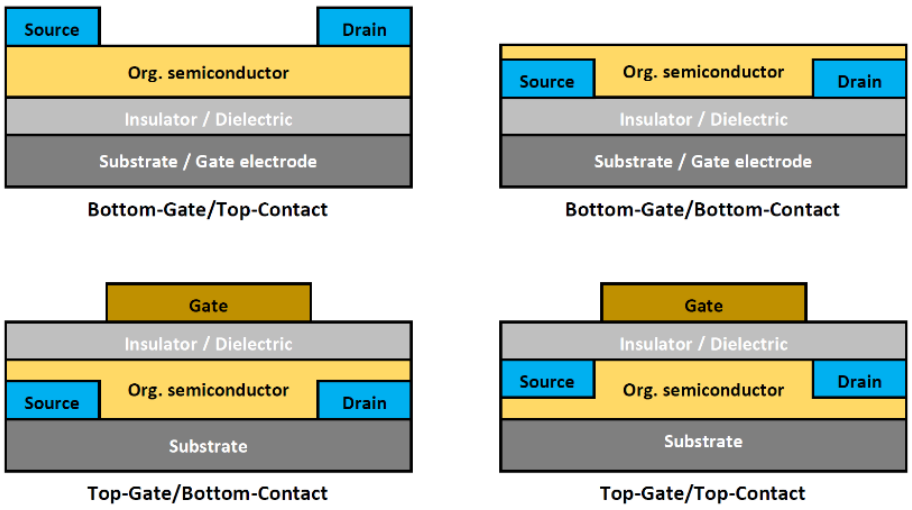

Figure 4. Schematic representation of different transistor architectures.

The charge carrier mobility (μ, cm^2V^{-1} s^{-1}) of OFETs is the most important device parameter for many of their target applications, and higher carrier mobilities allow switching transistors between on and off states at higher frequencies. So far, impressive improvements have been

achieved for OFET performances with the charge carrier mobilities over 10 cm^2V^{-1} s^{-1}, which are far better than that of amorphous silicon (0.1-1 cm^2V^{-1} s^{-1}) and have entered the mobility regime of multi-crystalline silicon.[31, 55-56]

1.2 Acenes and Azaacenes

1.2.1 Acenes

A large transfer integral and a low reorganization energy of the semiconductor materials are decisive for an optimal electron transfer rate in the electrical component. Both are addressed by extended aromatic and rigid systems in highly ordered crystal packings (acenes as typical representatives).

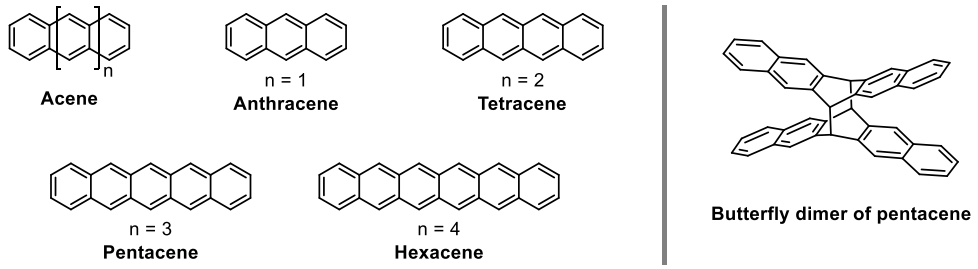

Figure 5. Acene homologues (left) and typical dimerization products of pentacene (right).[57]

The nomenclature of acenes was suggested by Clar[58] in 1939 based on the parent compound anthracene and was intended to distinguish this class from its nonlinear representative, phenanthrene. The distinction should not only be seen as a simplification, it also underlines their chemical difference. In contrast to nonlinear fused ring systems, acenes exhibit only one Clar electron sextet.[59] As the number of fused benzene rings increases, the energy levels of the frontier orbitals move energetically closer together, resulting in a smaller optical gap. The corresponding decrease in the gap hints that the semiconducting character of the higher acenes. However, due to the reduced energetic spacing of the frontier orbitals, the acenes become more unstable with increasing size. Pentacene is easily oxidized into endoperoxides under ambient conditions,[57] or dimerized to its "butterfly dimers"[60-61] in the absence of oxygen (Figure 5). Despite its semiconducting properties, the processing of pentacene is limited to techniques such

as chemical vapor deposition (CVD) due to its low solubility.[19] Unsubstituted hexacene can only be obtained by vacuum sublimation in the dark under inert conditions.[62]

Anthony et al.[63] introduced silyacetylene residues, typically tri-isopropylsilylethynyls (TIPS) to pentacene to stabilize the critical 6,13-positions (Scheme 1). As a result, the tendency for dimerization is reduced and the solubility is increased by the sterically demanding silylacetylene residues. With this concept, the stability and processibility of acenes with an increasing number of fused benzene rings were improved and even hexacene and heptacence[64] were stabilized.

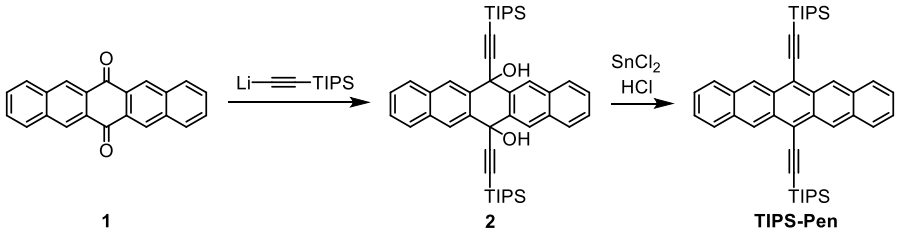

Scheme 1. Synthesis of **TIPS-Pen** reported by Anthony et al.[63]

The bulky side groups alter the crystal packing of pentacene (Figure 6).[39] Parent pentacene packs in a herringbone motif. The TIPS ethynyl substituents suppress the face-to-edge orientation of the molecules, so **TIPS-Pen** crystallizes in a brick wall motif. With measured carrier mobilities in solution-processed thin films on the order of 1 cm^2V^{-1} s^{-1}, **TIPS-Pen** has become a reference substance for p-channel semiconductors.[65-67]

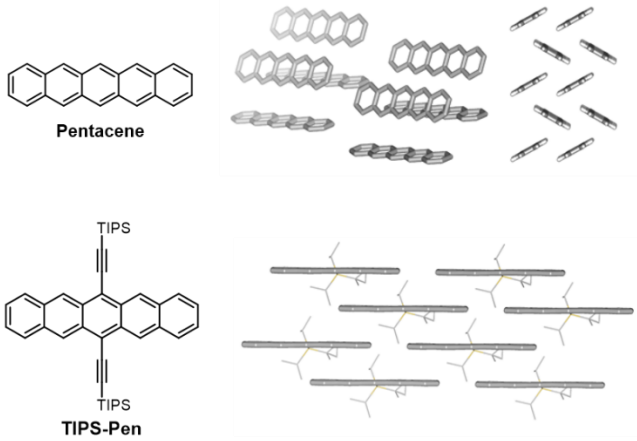

Figure 6. Crystal structure of pentacene in herringbone motif (top) and **TIPS-Pen** in brick wall motif (bottom).[39] Hydrogen atoms were omitted for clarity.

Halogenation of (aza)acenes allows to engineer molecular packing and fine-tune their frontier molecular orbitals (FMOs) and electron affinity (EA) to align better with common work-function electrodes. For example, FMO energy levels of perfluoropentacene[68] or perfluororubrene[69] are lowered with respect to that of their parent molecules, resulting in HOMO/LUMO levels that facilitate electron transport. Anthony et al.[70] and Bao et al.[71] functionalized **TIPS-Pen** to various substitutions resulting in ambipolar to even n-channel materials (Figure 7).

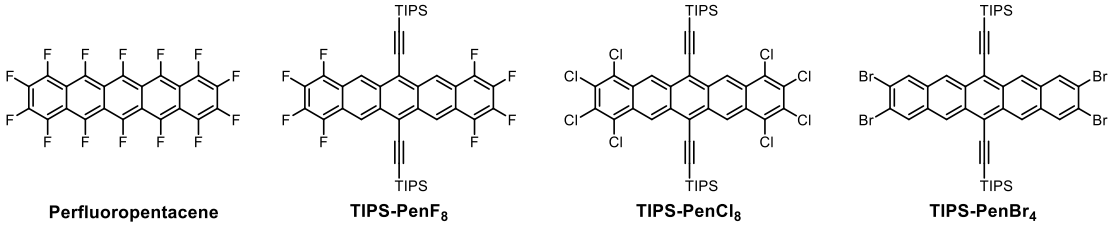

Figure 7. Halogenated pentacene and **TIPS-Pen** derivatives reported by Tokito et al., Anthony et al. and Bao et al. [68, 70-71]

1.2.2 Azaacenes

As early as around 1900, Fischer[72] and Hinsberg et al.[73] reported the synthesis of *N*-heteroacenes by melt condensation of aromatic *o*-diamines with *o*-diols or *o*-chlorides. Subsequent oxidation of **3** attempted by Badger and Pettit[74] did not furnish the azaacene, but the tetraazapentacenequinone **4** (Scheme 2). The synthesis of the di- or tetraazapentacenes **5**, **6** and **7** succeeded in 1966 and 1967 by Zimmermann, Kummer, and Leete et. al,[75-76] who oxidized the *N,N'*-dihydro compounds **5-H$_2$**, **6-H$_2$** and **7-H$_2$** with *p*-chloranil, PbO_2 or $Cu(OAc)_2$, respectively.

However, the use of *N*-heteroacenes as semiconductor materials was realized 100 years later. The first OFET of *N*-heteroacenes was published by Nuckolls et al.[77] using the dihydro species **5-H$_2$** and **6-H$_2$** as hole transport materials with mobilities up to 6×10^{-3} and 2×10^{-5} $cm^2 V^{-1}s^{-1}$, respectively. In 2009, Miao et al.[78] vapor-deposited **5-H$_2$** on a SAM (self-assembled monolayer) coated SiO_2 surface, which achieved hole mobility up to 0.45 $cm^2V^{-1} s^{-1}$. Miao et al.[79] also prepared the OFETs of *p*-quinone **4** by thermal evaporation, realizing an electron mobility up to 9×10^{-2} $cm^2 V^{-1} s^{-1}$.

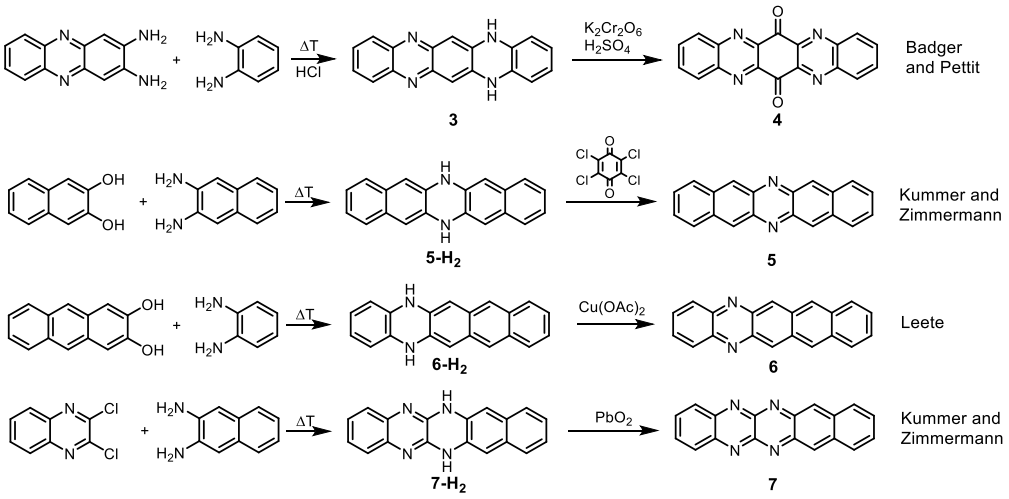

Scheme 2. Synthesis of the historic first tetraazapentacenquinone **4**,[74] diazapentacenes **5**[72] and **6**,[73] and tetraazapentacene **7**.[72]

Using Anthony's ethynylation method, Bunz et al.[49] and Miao et al.[80] succeeded in synthesizing the symmetrical **TIPS-TAP** and **TIPS-DAP** (Scheme 3). It was found that the ethynylated derivatives of this class of compounds can be very gently converted from the dihydro to the oxidized derivatives using manganese dioxide. Absorption and emission red shift upon oxidation.

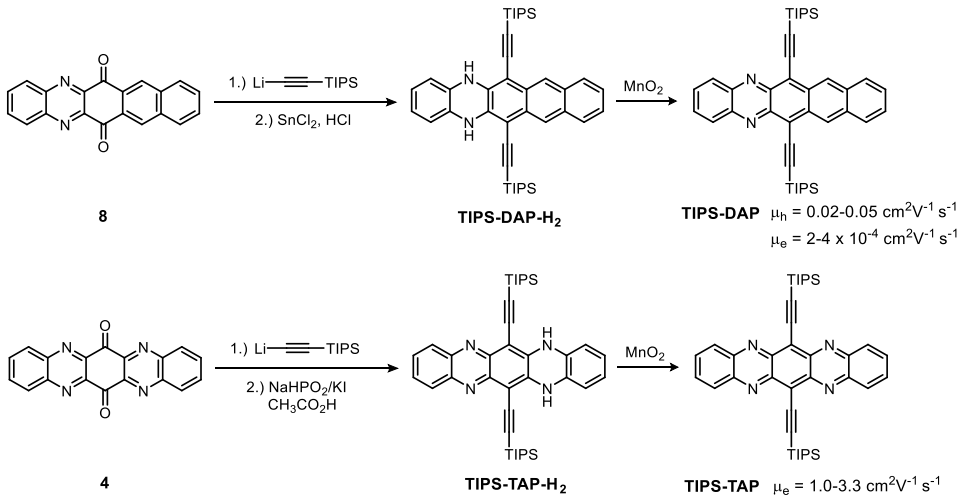

Scheme 3. Synthetic routes to **TIPA-DAP** and **TIPS-TAP** reported by Miao et al.[80] and Bunz et al.[49]

Sequentially replacing a benzene ring with a pyrazine ring in a pentacene backbone (from **TIPS-Pen** to **TIPS-DAP** to **TIPS-TAP**) lowers both the HOMO and LUMO energy levels (Figure 8). These are a consequence of the electron-withdrawing nature of unsaturated N atoms.

In the solid state, a regular brick wall motif formed, which facilitates the charge transport to achieve ambipolar properties for **TIPS-DAP** and a electron mobility of up to 3.30 cm^2V^{-1} s^{-1} for **TIPS-TAP**.[80-82]

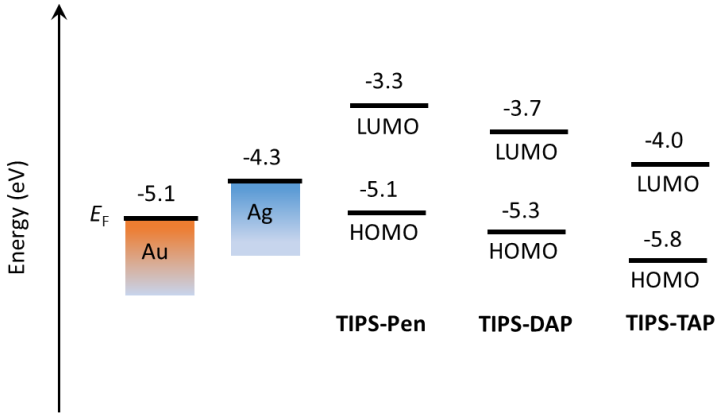

Figure 8. Schematic representation of work function of the metal electrodes (E_F) and semiconductors.[80, 83-84]

Figure 9 displays a series of azapentacenes with a different number of N atoms. Diazapentacene **9**,[85] which exhibits the energetically highest LUMO (-3.35 eV) among the azapentacenes, showed only hole mobility with gold as electrode. In contrast, tetraazapentacene **10**[85] showed ambipolar charge transport, its structural isomer (**TIPS-TAP**) only showed electron charge transport. Bunz et al.[49] proved the energetically low-lying LUMO (-3.81 eV) of **TIPS-TAP** and its compact molecular packing in the two dimensional brick wall structure. **10** with higher LUMO (-3.68 eV) and limited π-interactions in the crystal in comparison of **TIPS-TAP**, showed comparatively low charge mobility. Therefore, the performance is strongly dependent on the position of the pyrazine units in the acene skeleton.

In 2012, Miao et al.[86] published structurally isomeric hexaazapentacenes **11a**, **b** that carry the pyrazine units in the middle of the acene skeleton (Figure 9). The hexaazapentacenes' strong electron affinity (LUMO = -4.32 eV) allow them to oxidize dihydroanthracene to anthracene. Efforts to incorporate the oxidized compounds into OFETs failed due to their thermal instability and high oxidation potential. Hill et al.[87] reported decaazapentacene **12** with the energetically lowest LUMO levels of all azapentacenes known to date (-4.38 eV), which is only persistent to allow the measurement of a solution UV-Vis spectrum but gradually returns to its parent

reduced state on standing. To construct stable *N*-heteroacenes, the adjustment of acene size, substituents, and the number of electron-deficient heteroaromatics is mandatory.

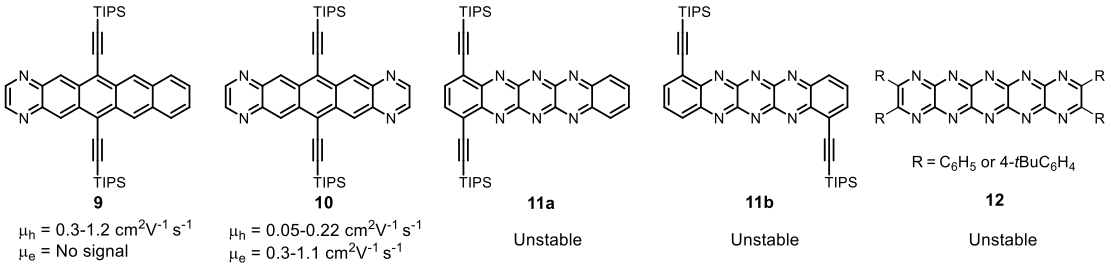

Figure 9. Diazapentacene **9**, tetraazapentacene **10** and hexaazapentacenes **11a, b** reported by Miao et al.[85-86] and decaazapentacene **12** reported by Hill et al.[87]

To further modify the electrochemical properties, the acenes were substituted with halogen atoms (Cl, Br, I) leading to a further strengthening of the electron affinities and thus to a concomitant reduction in the LUMO. **TAP-Cl$_4$** is prepared analogously to **TIPS-TAP** from a tetrachlorotetraazapentacenequinone with subsequent introduction of the silyacetylene residues (Scheme 4).[88] **TAP-Br$_4$** and **TAP-I$_4$** were reported by a different approach: the TIPS ethynyl-functionalized benzothiadiazole is condensed with the catechol and then reductively opened with SmI_2 to the *ortho*-diamine. A subsequent condensation gives **TAP-Br$_4$**[89] and **TAP-I$_4$**.[90] Electron mobilities of 27.8 $cm^2V^{-1}s^{-1}$ for **TAP-Cl$_4$,**[88] 0.56 $cm^2V^{-1}s^{-1}$ for **TAP-Br$_4$**[89] and 1.35 $cm^2V^{-1}s^{-1}$ for **TAP-I$_4$**[90] could be achieved as n-channel semiconductors in organic field-effect transistors.

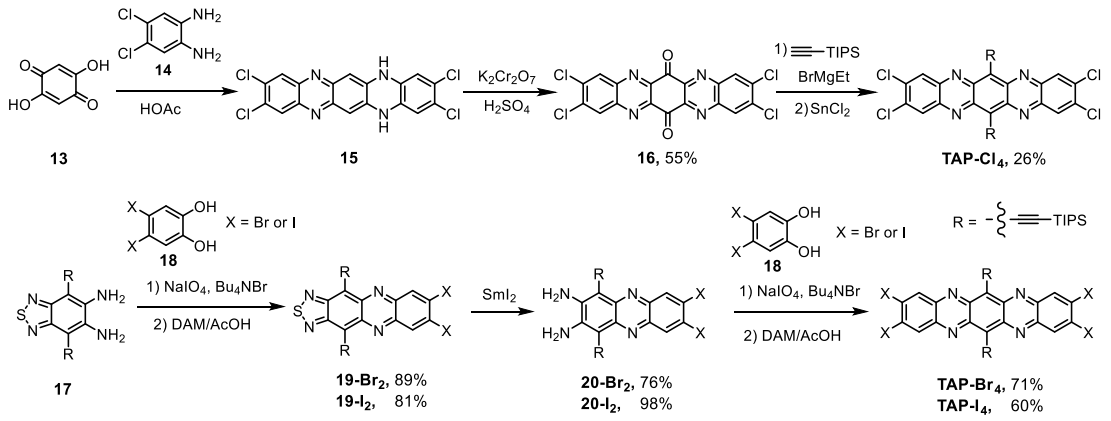

Scheme 4. Synthesis routes to halogenated **TAP-Cl$_4$**, **TAP-Br$_4$** and **TAP-I$_4$** reported by Bunz et al. [89-90] and Miao et al.[88]

1.2.3 Stabilization of Extended Linear Acenes

The approach of expanding conjugated aromatic π-system to achieve improved semiconductor materials is widely investigated. An improved intermolecular overlap is made possible by increasingly space-consuming π systems, which leads to the expectation of a larger transfer integral and thus more efficient charge transport.[91] Additionally, the gap is reduced by raising the energy of the HOMO and lowering of the LUMO frontier orbital, which reduces the transistor voltage required for charge carrier injection.[92-93]

To extend the (aza)acenes, an essential challenge is their high propensity towards oxidation and dimerization.[94] Bunz et al.[95-97] reported a series of stable azahexacenes by Buchwald-Hartwig cross-coupling reactions (Scheme 5). Diazahexacene **24**[97] is persistent for short periods of time in the solid state and even in solution. In contrast, dimerization product **22** was observed for hydrocarbon analogue **21** in the single crystal.[94] The incorporation of additional pyrazine moieties (**26**) into azaacenes suppress both oxidation and dimerization.[95-96]

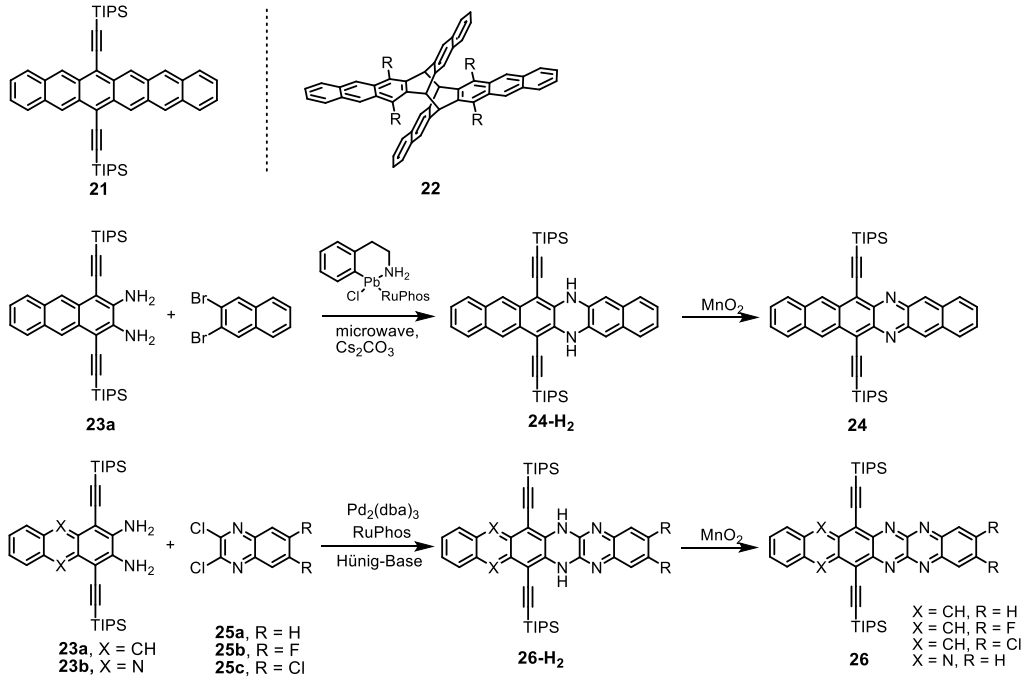

Scheme 5. TIPS functionalized hexacene **21** and its dimerization product **22** (top) reported by Anthony et al.[94] and synthesis routes to TIPS functionalized di-, tetra- and hexaazahexacenes **24**, **26** reported by Bunz et al.[95-97]

Synthesis of heptacenes is challenging (Figure 10). Anthony et al.[64] reported the heptacenes **27** with a pair of silylethynyl groups bearing different alkyl substituents. The size of substituents correlated with the stability of the heptacenes. Wudl et al.[98] stabilized heptacenes by symmetrically attaching phenyl substituents combined with TIPS groups on the central ring (**28**). Addition of trifluoromethyl group to the phenyl substituents further stabilizes the heptacenes. Bunz et al.[99] improved the stability of heptacenes **29** by placing six silylethynyl substituents on every other benzene ring. These sterically more shielded heptacenes are inert to endoperoxide formation and dimerization.

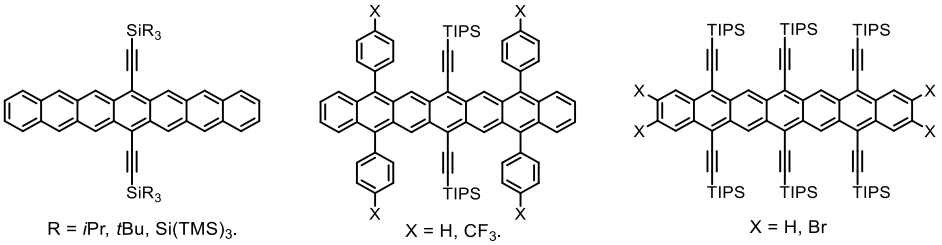

Figure 10. Stabilized heptacenes **27, 28, 29** reported by Anthony et al.,[64] Wudl et al.[98] and Bunz et al.[99]

Azaheptacenes are rarely reported. Oxidation of **30-H₂** with one single pair of bulky silylethynyl substituents led to the isolation of butterfly-dimer **31** as the sole product (Scheme 6). A diazaheptacene **32** with four (tri-*sec*-butylsilyl)ethynyl substituents was moderately persistent in solution but spontaneously dimerized into its [4+4]-cycloadducts, hindering the evaluation of their solid-state structure.[100]

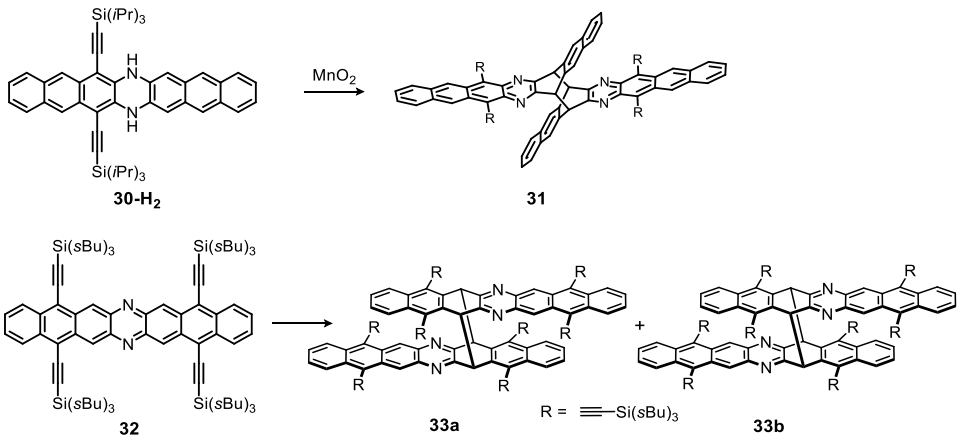

Scheme 6. *N,N'*-dihydrodiazaheptacene **30-H₂** and diazaheptacene **32** reported by Bunz et al.[100]

Azaheptacenes (non-benzannulated species without e.g. pyrene[101-102] or coronene[103] substructures) with more than two N atoms are unknown. Bunz et al.[104] used the condensation of *para*-dihydroxyquinone to prepare the first *N,N'*-dihydrotetraazaheptacene **35** (Scheme 7). However, the preparation of the oxidized tetraazaheptacene was failed.

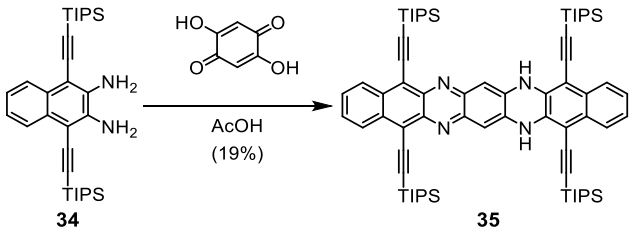

Scheme 7. Synthesis route to the *N,N'*-dihydrotetraazaheptacene **35** reported by Bunz et al.[104]

1.2.4 Acenes End-Capped with 1,2,5-Thiadiazoles

Tailoring molecular packing is crucial and affects charge transport properties.[105-106] Thiadiazoles are attractive rigid and planar electron accepting moieties, which have been employed as organic semiconductors and as acceptors in OPV.[107-108] End-capping of thiadiazoles (Figure 11) is an attractive method to prepare heteroacenes with electron transporting capabilities. In contrast to acenes and azaacenes, S-N short contacts dominate the packing of chalcogenadiazoles – phenazinothiadiazoles (or its derivatives) exhibit brick wall packing of head-to-head dimers supported by S-N-interactions in the solid state.[109] The fluorinated phenazinethiadiazole **39-F$_4$** show electron mobilities up to 0.07 cm^2V^{-1} s^{-1}.[110] Bis(thiadiazolo)benzene **40**, a synthetically useful intermediate, has been employed as precursor to aromatic *ortho*-tetramine.[111]

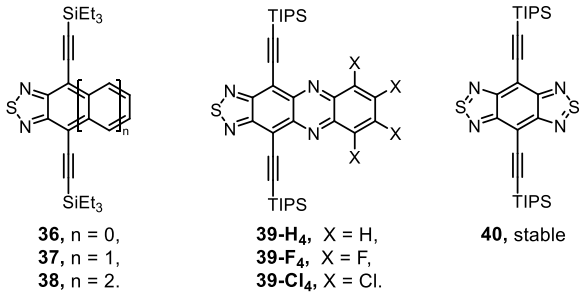

Figure 11. Alkynylated acenothiadiazoles **36**, **37** and **38**, phenazinothiadiazoles **39** and benzobisthiadiazole **40** reported by Bunz et al.[109-111]

An attractive but fundamentally more difficult question is that of the larger linear acenes end-capped with thiadiazoles (Figure 12). Müllen's attempts to produce compound **41** and **42** was met without success as it spontaneously reacted into its butterfly-type dimer.[112] Lindner et al.[110] prepared **43** incorporated more electronegative moieties, but it was not stable enough for device application, as **43** decomposes to the dihydro-compound during purification. Müller et al.[113] reported the preparation of tetrakis(thiadiazolo)-annulated tetraazaacenes **44**. These compounds display up to seven benzene/pyrazine rings, but do not show enhanced electron affinities, as the two or four attached benzothiadiazole units are resonance-separated from the acene body, maximizing the number of Clar sextets.

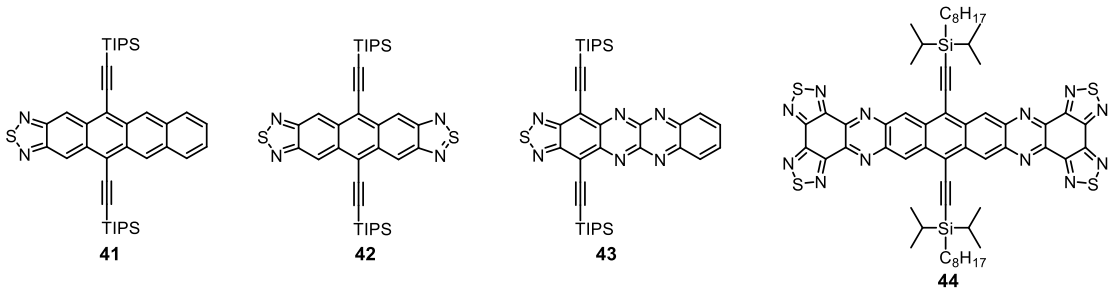

Figure 12. Larger linear acenes end-capped with thiadiazoles moieties reported by Müllen et al.[112] and Bunz et al.[110, 113]

1.3 Azaacene Radical Anions

For an n-channel material such as **TIPS-TAP**, electrons need to be injected into the LUMO of the semiconductor at the electrode interface in the OFET.[114] The radical anions formed in the process are species that appear briefly in the component, the structure and properties of which provide insight into the charge transport.

Investigation of the unpaired spin density of **TIPS-TAP**$^{\bullet-}$ contribute to the understanding of the charge transport mechanism for n-type transporting materials. In 2016, Marder et al.[115] reported the preparation of anionic radical **TIPS-TAP**$^{\bullet-}$ and dianion **TIPS-TAP**$^{2-}$ (Scheme 8) by reducing **TIPS-TAP** with one and two equivalent potassium anthracenide respectively. **TIPS-TAP** displayed an absorption spectrum with a λ_{max} at 675 nm. Upon reduction into its radical anion, a redshift to 1400 nm was observed (Figure 13). The dianions on the other hand

displayed a blue-shifted absorption with a λ_{max} at 592 nm. In addition, **TIPS-TAP**$^{\bullet-}$ is stable with respect to disproportionation into **TIPS-TAP** and **TIPS-TAP**$^{2-}$.[116]

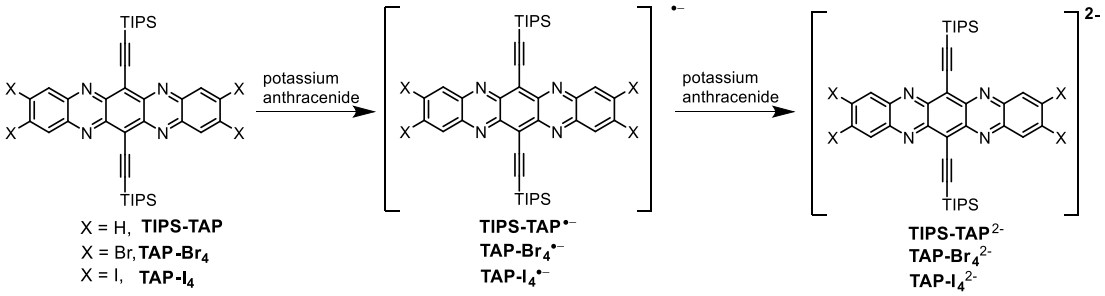

Scheme 8. Reduction of **TIPS-TAP**, **TAP-Br$_4$** and **TAP-I$_4$** into their radical anions and dianions using potassium anthracenide reported by Marder et al.[115] and Bunz et al.[89-90]

A few years later, Bunz et al. reported improved synthetic approach for **TIPS-Br$_4$**[89] and **TAP-I$_4$**,[90] excellent n-transporting materials. The authors reduced the neutral compounds into their radical anions and dianions by potassium anthracenide. The mono- and dianionic behaviors of **TAP-Br$_4$** and **TAP-I$_4$** (Figure 13) are similar to that of **TIPS-TAP**. Taking **TAP-Br$_4$** as an example, the spectrum of the radical monoanion is the most red-shifted while the spectrum of the dianion is opposite, that is, the most blue-shifted. Notably, **TAP-Br$_4$**$^{\bullet-}$ is stable in dry diethyl ether under air for several weeks. The radical anion shows only small changes in bond lengths when compared to the neutral species, resulting in low reorganization energies.[90]

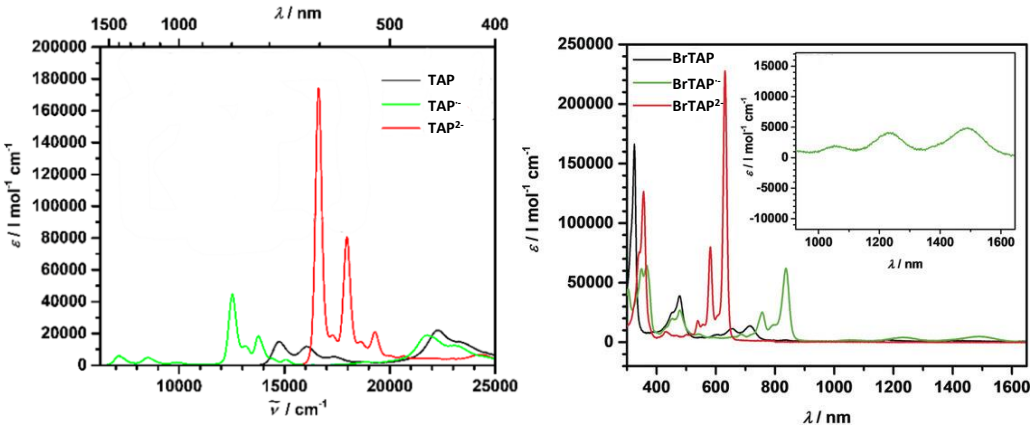

Figure 13. UV-Vis spectra of the neutral (black), singly negatively charged (green), and doubly negatively charged (red) of **TAP** (left) and **TAP-Br$_4$** (right).[89, 116] Left panel adapted with permission of ref. 71 © 2017, American Chemical Society, and right panel adapted with permission of ref. 72 © 2018, Wiley-VCH.

1.4 Objective

Acenes and heteroacenes are the most important organic semiconductors. Substituted acenes have been applied as p-type semiconductors in OFETs, solar cells and in light-emitting devices. Electron transporting materials with the same level of performance are also highly desirable – N-heteroacenes, especially azapentacenes, exhibit good electron transport mobilities. Up to now, the larger N-heteroacenes (> hexacene) are only marginally stable, so their full potential is not reached, arousing great research interest. The larger azaacenes' electronic properties suggest them as non-traditional NLO materials and singlet fission materials. However, their high reactivity (dimerization, oxidation/reduction etc.) has to be faced – soluble and processible derivatives are challenging to prepare.

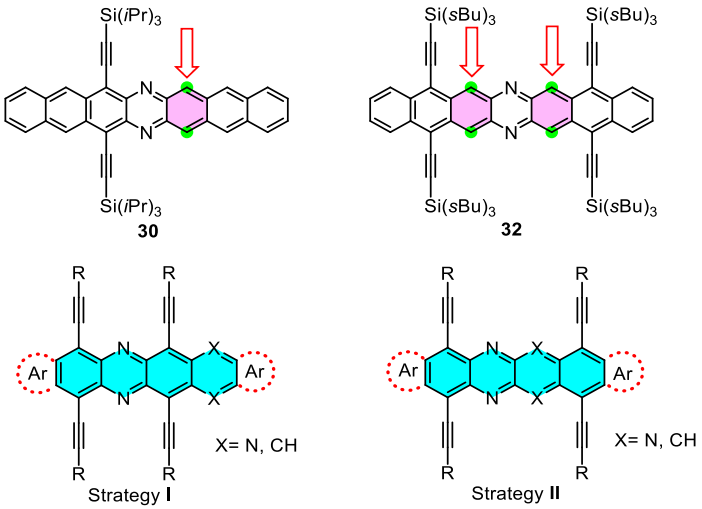

Figure 14. Known diazaheptacenes **30** and **32**[100] (top), and stabilizing strategies proposed in this work (bottom). Centers in need for stabilization are highlighted with red arrows.

Up to now, true azaheptacenes (non-benzannulated species without e.g. pyrene or coronene substructures) are reactive and terra incognita. In our previous attempt, oxidation of **30-H₂** with only one single pair of bulky silylethynyl substituents led to the isolation of a butterfly-dimer as the sole product. **32** with four (tri-*sec*-butylsilyl)ethynyl substituents (Figure 14) was moderately persistent in solution but spontaneously dimerized into its [4+4]-cycloadducts.

In **32**, the two benzene rings adjacent to the central pyrazine (6,8,15,17 positions, highlighted with red arrows) are highly reactive. Structural strategies **I** and **II** (Figure 14) with a variation

of the silylethynyl substituents and the pyrazine patterns in the acene backbone are proposed to stabilize the larger azaacenes. Positioning the silylethynyl groups adjacent to the central pyrazine (or pyrazinopyrazine) ring should protect the center of the azaacenes more effectively than with more arene rings in between – these strategies should suppress dimerization via [4+4] cycloaddition and Diels-Alder pathways; the middle pyrazine ring renders these species stable to oxidation. Fourfold TIPS-ethynyl substituents makes azaheptacenes soluble and processible, a prerequisite for their applications in organic electronics.

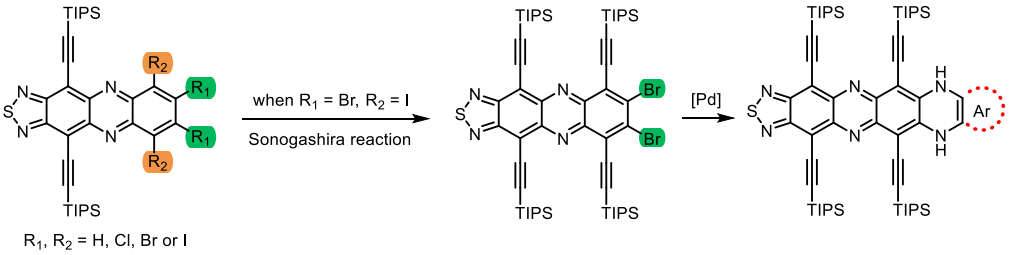

Scheme 9. Halogenated phenanzinothiadiazoles and the synthesis route of larger heteroacenes end-capped with 1,2,5-thiadiazoles in this work.

1,2,5-Thiadiazoles offer the possibility to fine-tune packing and in-plane transfer integrals. When halogenated N-heteroacenes were merged with thiadiazoles, the generated halogenated phenanzinothiadiazoles should be n-type organic semiconductors (Scheme 9). It should also render the charge carrying species, their radical anions, persistent under ambient conditions and allow their investigation. Phenanzinothiadiazoles substituted with bromine in the ortho positions and iodine on the para positions, could serve as a building block for larger heteroacenes by a combination of a regioselective Sonogashira reaction and Buchwald-Hartwig coupling reaction.

Chapter 2. Synthesis, Characterization and Application of Halogenated Phenanzinothiadiazoles

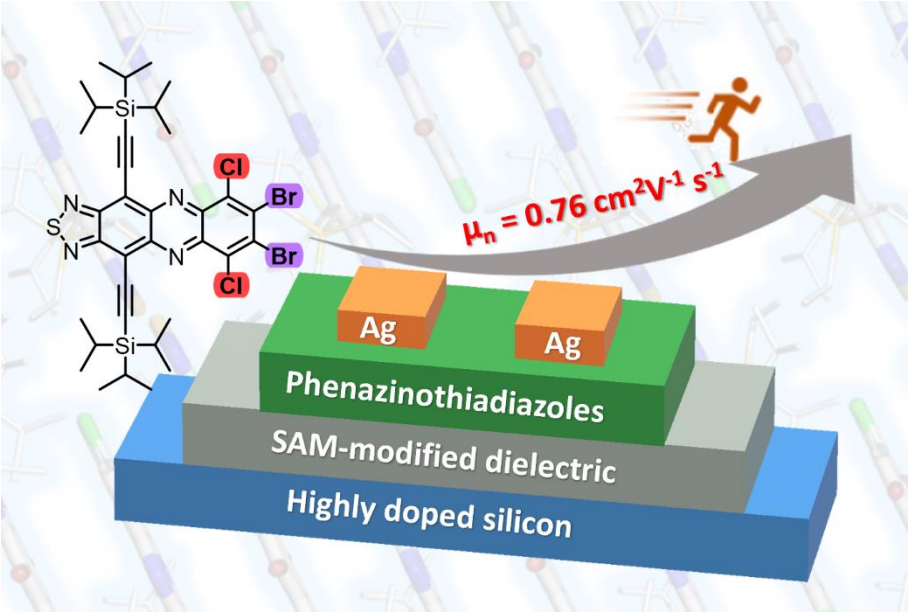

2.1 Introduction and Research Purpose

Chalcogenadiazole end-capping[113, 117-118] is a method for "crystal engineering" of heteroacenes with electron transporting capability. In contrast to acenes and azaacenes, S-N short contacts dominate the packing of chalcogenadiazoles,[119] leading to closely packed head-to-head-dimers with a slight lateral offset. Halogenation of (aza)acenes impacts molecular packing and electron affinity (EA) to align better with common work-function electrodes. The FMO energy levels of perfluoropentacene[68] or perfluororubrene[69] are lowered with respect to that of their parent molecules, facilitating electron transport. Miao and Bunz et al. modified **TAP**[120] with four halogen substituents, to obtain **TAP-Cl$_4$**,[88] **TAP-Br$_4$**[89] and **TAP-I$_4$**,[90] with significantly improved electron mobilities (the average mobility of **TAP-Cl$_4$** up to 14.9 cm^2V^{-1} s^{-1}). Regarding acenothiadiazoles, we reported fluorinated or chlorinated derivatives with average electron mobilities of 0.07 cm^2 V^{-1} s^{-1} for **39-F$_4$** and 0.04 cm^2 V^{-1} s^{-1} for **39-Cl$_4$** (Figure 15).[110]

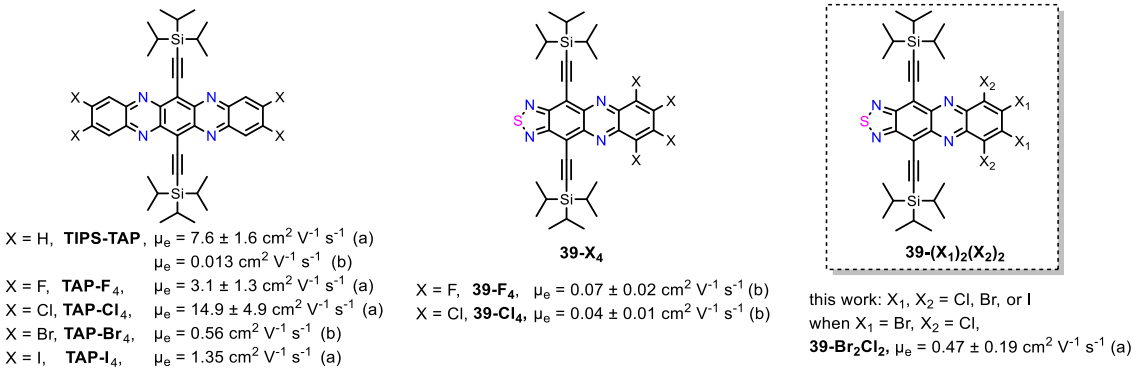

Figure 15. Molecular structures and transistor performance of previously reported halogenated phenazinothiadiazoles[110] and **TIPS-TAP** derivatives[88-90] as well as scope of this work. Device architectures: (a) bg/tc (bottom gate/top contact) OFET with SAM modified dielectric, (b) bg/tc OFET with parylene C as dielectric.

In this chapter, we merge halogenated N-heteroacenes with 1,2,5-thiadiazoles. This electron-deficient heteroarene building block serves two benefits: (i) In combination with tetrahalogenation, it renders the charge carrying species of the phenazinothiadiazoles, their radical anions, persistent under ambient conditions and allows their investigation. (ii) It introduces short contacts between linearly arranged molecules in the solid-state, increasing transfer integrals.

2.2 Synthesis of Halogenated Phenanzinothiadiazoles

To synthesize tetrahalogenated phenazinothiadiazoles, tetrahalogenated *ortho*-quinones **49** (Scheme 10) are critical starting materials. **46-Cl$_2$** and **46-Br$_2$** were synthesized after a procedure similar with that reported in the literature.[121] Halo-desilylation[122] using NBS, NCS or NIS gave the tetrahalogenated veratroles **47** with moderate to good yields (45% to 89%). These veratroles were demethylated by BBr_3 to give dihydroxybenzenes **48** with good yields ranging from 73% to 90%. Oxidation of **48** with periodate furnished *ortho*-quinones **49** in quantitative yields.

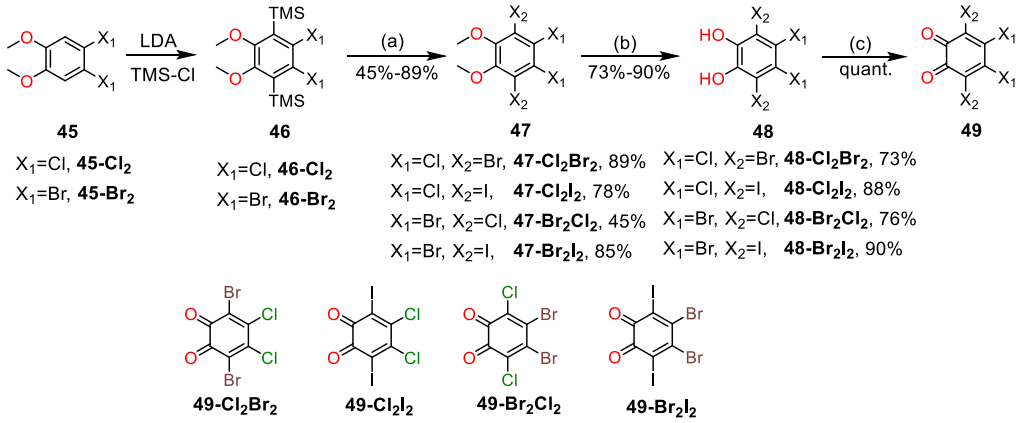

Scheme 10. Synthesis of tetrahalogenated *o*-quinones **49**. Conditions: (a) NCS/NBS/NIS, CH_3CN, 90 °C; (b) BBr_3, DCM, 0 °C → rt; (c) $NaIO_4$, $Bu_4N^+I^-$, DCM/H_2O, rt.

Tetrahaloorthoquinones **49** were condensed with diaminobenzothiadiazole **17**[111] in a mixture of DCM/AcOH at 40 °C to yield the targeted tetrahalogenated phenazinothiadiazoles **39** as blue solids in yields ranging from 30%-62% (Scheme 11).

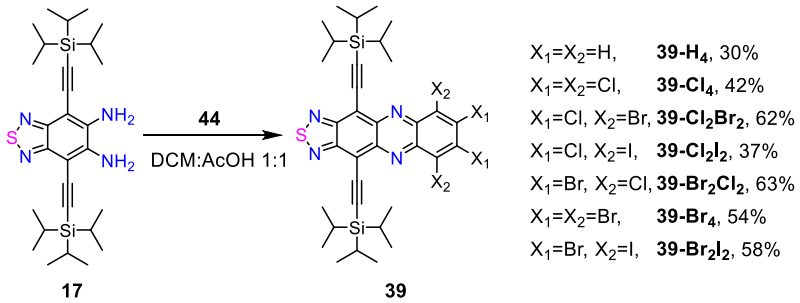

Scheme 11. Synthesis of tetrahalogenated phenazinothiadiazoles **39** and reference compound **39-H$_4$**.

The charge carrying species were prepared by reduction of **39** with KC_8-(18-crown-6) in THF (Scheme 12). Treatment of **39** with one equivalent KC_8 furnished dark yellow solutions of monoanions **39**$^{\bullet-}$. Upon further reduction, two equivalent KC_8 furnished dark red solutions of dianions **39**$^{2-}$.

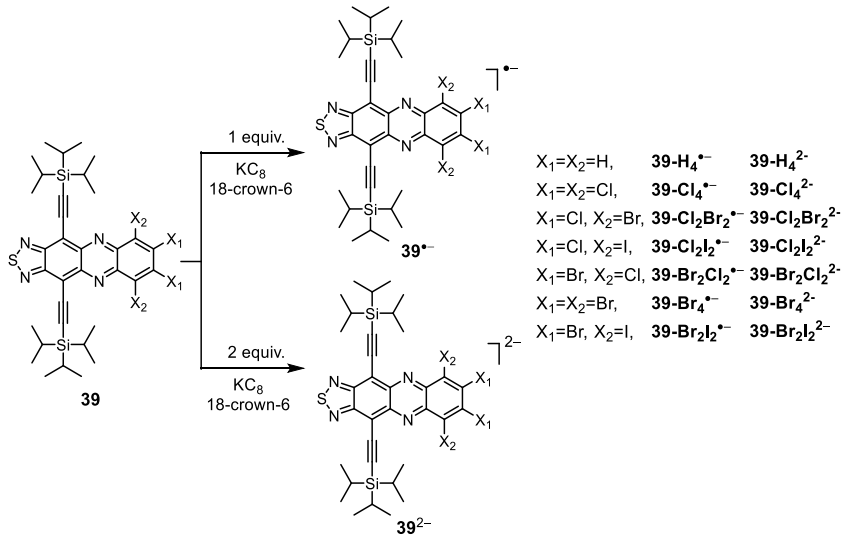

Scheme 12. Preparation of the anions and dianions of **39**.

Tetrakis((triisopropylsilyl)ethynyl) dibromo phenazinothiadiazole **50** was synthesized by introducing an additional pair of TIPS ethynyl group to the backbone via a selective Sonogashira reaction[123] of **39-Br$_2$I$_2$**. Tetraazapentaceno thiadiazole **51** was prepared by Buchwald-Hartwig coupling[124] with phenylenediamine and subsequent oxidation of the *N,N'*-dihydro compounds (Scheme 13). **51** was isolated through column chromatography for characterization and cultivation of single crystals.

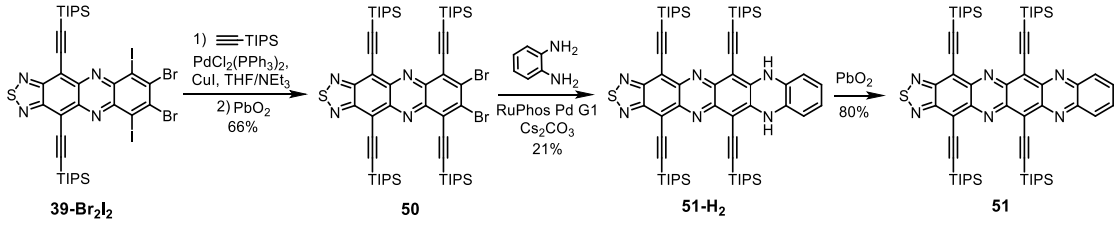

Scheme 13. Synthesis of tetraazapentaceno thiadiazole **51**.

Buchwald-Hartwig coupling[124] of **50** with diamino naphthalene **34** furnished sixfold *N,N'*-dihydro tetraazahexaceno thiadiazoles **52** with low yield (~5%). But the oxidation of the *N,N'*-dihydro compound led to the elimination of naphthalene and disruption of the benzene rings, resulting in an indole moiety attached to the backbone (**53**, ~60%, Scheme 14). The failure of

the oxidation reaction may attribute to the combined effect of high steric pressure as well as large and electron-deficient conjugated backbone.

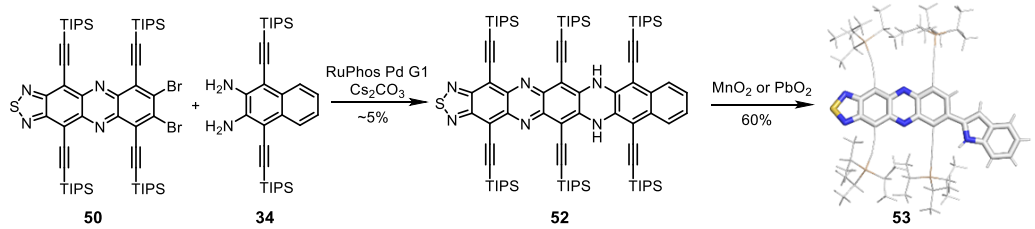

Scheme 14. Synthesis of *N,N'*-dihydro tetraazahexaceno thiadiazole **52** and its degradation specie **53**.

2.3 Results and Discussion

The UV-Vis spectra of **39** measured in DCM (Figure 16a) showed similar absorption profiles: the onset of the lowest energy absorption maxima of **39-H$_4$** in solution was 664 nm, and halogenated **39** showed red-shifted onset between 701-706 nm.

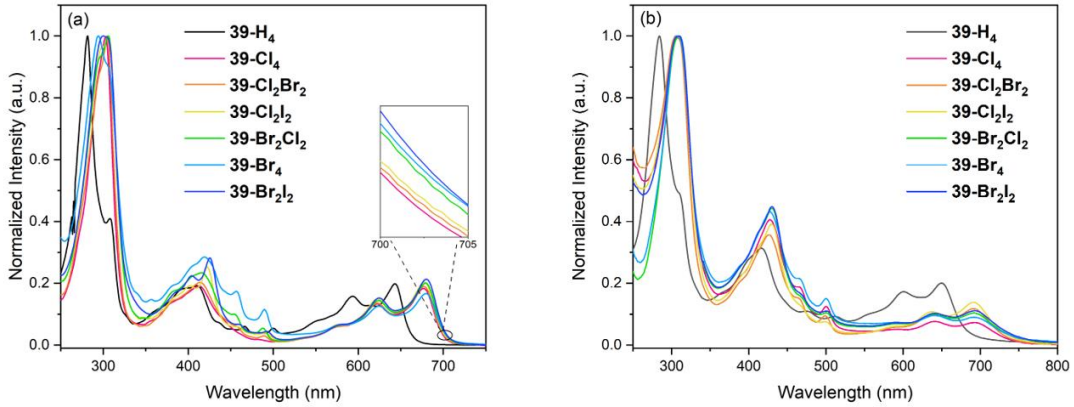

Figure 16. Normalized UV-Vis absorption spectra of **39** (a) in DCM (10^{-5} mol L^{-1}) with magnification of the onset absorption and (b) in thin films.

From **39-Cl$_4$** to **39-Br$_2$I$_2$** (Table 1), the longest wavelength absorption was gradually redshifted by ca. 1-2 nm with increasing halide atom size. Additionally, the absorption maxima of **39-Br$_2$Cl$_2$** was red-shifted by 3 nm in comparison to that of **39-Cl$_2$Br$_2$**, indicating that the less electronegative pair of halogen atoms on the eastern position contributes more to absorption than in the south/north position. Thin-films for UV-Vis spectroscopy were prepared by spin-coating chloroform solution of **39** (10 mg/mL). As shown in Figure 16b and summarized in Table 1, the absorption in films were similar to those in solution, but only slight red-shifted.

Table 1. Optoelectronic properties of phenazinothiadiazoles **39**.

Compd.	$\lambda_{on\ sol.}$ [a] [nm]	$\lambda_{on\ film}$ [b] [nm]	LUMO [c] [eV]	HOMO [c] [eV]	$E_{red,0/-1}$ [d] [V]	$E_{red,-1/-2}$ [e] [V]	EA [f] [eV]	IP [g] [eV]
39-H$_4$	664	698	-3.85	-5.77	-0.92	-1.48	-3.88	-5.75
39-Cl$_4$	701	741	-4.08	-6.00	-0.77	-1.33	-4.03	-5.80
39-Cl$_2$Br$_2$	702	743	-4.09	-6.00	-0.73	-1.32	-4.07	-5.84
39-Cl$_2$I$_2$	703	743	-4.08	-6.00	-0.69	-1.29	-4.11	-5.87
39-Br$_2$Cl$_2$	705	754	-4.09	-6.00	-0.71	-1.24	-4.09	-5.85
39-Br$_4$	706	754	-4.10	-6.00	-0.70	-1.26	-4.10	-5.86
39-Br$_2$I$_2$	706	761	-4.09	-6.00	-0.65	-1.19	-4.15	-5.91

[a] Onset of the lowest energy absorption maxima in solution; [b] onset of the lowest energy absorption maxima in thin film; [c] frontier molecular orbital energies calculated by DFT calculation[125] (Gaussian16 B3LYP, def2TZVP); [d] the first reduction potential measured CV; [e] the second reduction potential measured via CV; [f] electron affinities (EA) estimated from first reduction potentials of CV curves, EA = − 4.80 eV − $E_{red,0/1}$;[126] [g] ionization potentials (IP) calculated by IP = EA - $E_{optical\ gap}$; $E_{optical\ gap}$ calculated from $\lambda_{on\ sol.}$.

Reduction potentials were determined by cyclic voltammetry (CV) in DCM internally referenced against Fc/Fc^+ using a Pt working electrode and Bu_4NPF_6 as electrolyte. These compounds showed similar CV curves. Taking **39-Br$_2$Cl$_2$** as an example, two reduction waves were observed at -0.71 V and -1.24 V (Figure 17a), respectively, and the electron affinities (EA) are estimated to -4.09 eV.

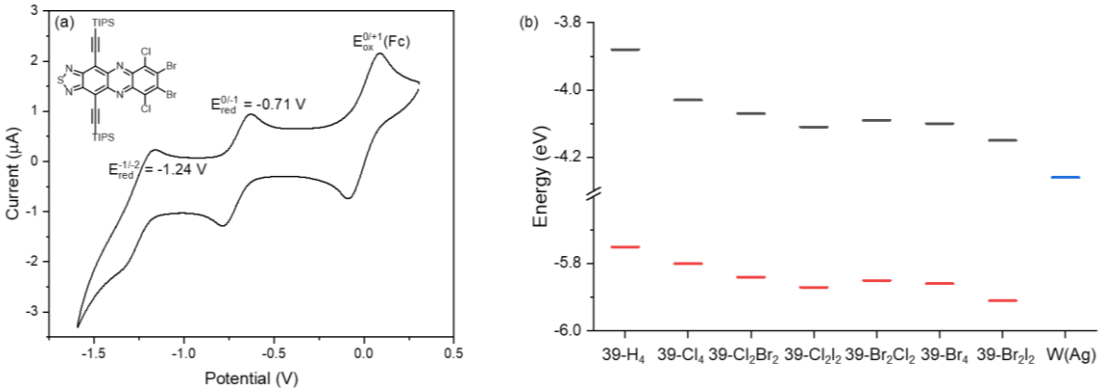

Figure 17. (a) Cyclic voltammograms of **39-Br$_2$Cl$_2$** in DCM (internally referenced against Fc/Fc^+ using a Pt working electrode and Bu_4NPF_6 as electrolyte) and (b) comparison of EAs (black) and IPs (red) of **39** and the work function W of silver (blue).

In comparison with the EA values of **39** estimated from CV (Table 1), from Cl to Br to I, the heavier halogens are more effective in lowering the EA although Cl is more electronegative (Figure 17b). This trend also holds for the second reduction event of the series. Independent of the nature of halide substitution, density functional theory (DFT) calculations (B3LYP, def2TZVP, gas phase) predicted all of the HOMO and LUMO energies to be around -6.00 eV and ca. -4.09 eV, respectively (Figure 18).

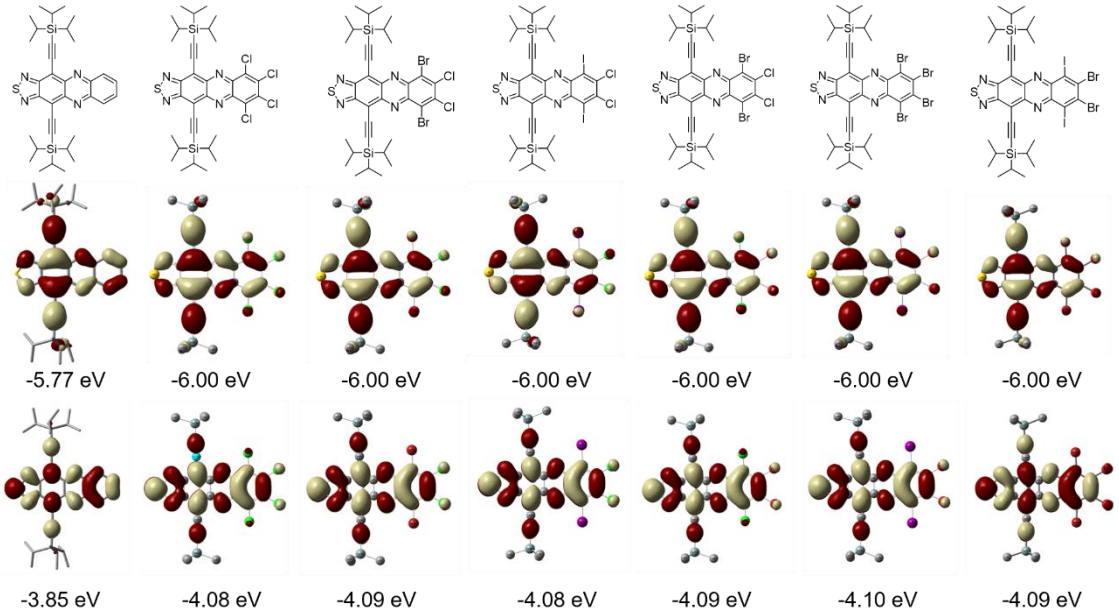

Figure 18. Frontier molecular orbital distribution of **39**.

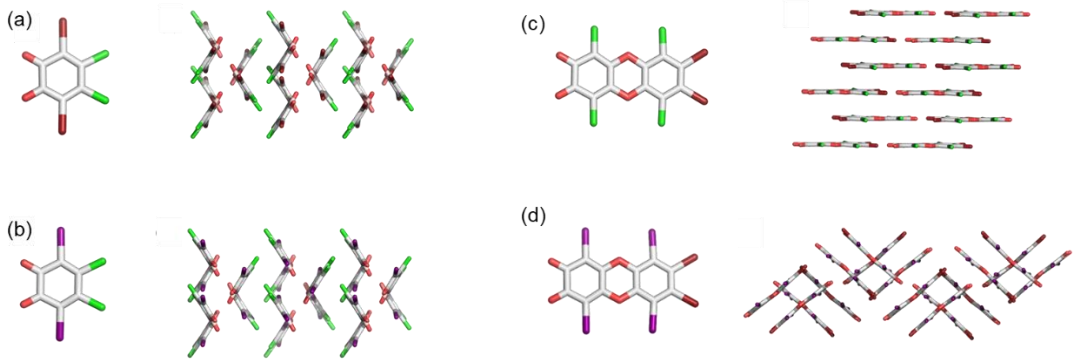

Figure 19. Chemical structure, crystal structure and packing motif obtained for (a) **49-Cl$_2$Br$_2$**, (b) **49-Cl$_2$I$_2$**, (c) dimer of **49-Br$_2$Cl$_2$** and (d) dimer of **49-Br$_2$I$_2$**.

Specimen of tetrahaloorthoquinones **49** for X-ray crystallography were grown by slow diffusion of *n*-hexane into a DCM solution. Interestingly, **49-Br$_2$Cl$_2$** and **49-Br$_2$I$_2$** showed the

propensity to self-condensed into their dimers (Figure 19), which was probably formed by condensation reaction of *ortho*-quinones with unoxidized dihydroxybenzenes. Therefore, **49-Br_2Cl_2** and **49-Br_2I_2** have to be prepared in-situ for undergoing reactions, while **49-Cl_2Br_2** and **49-Cl_2I_2** are stable and could be stored at ambient conditions.

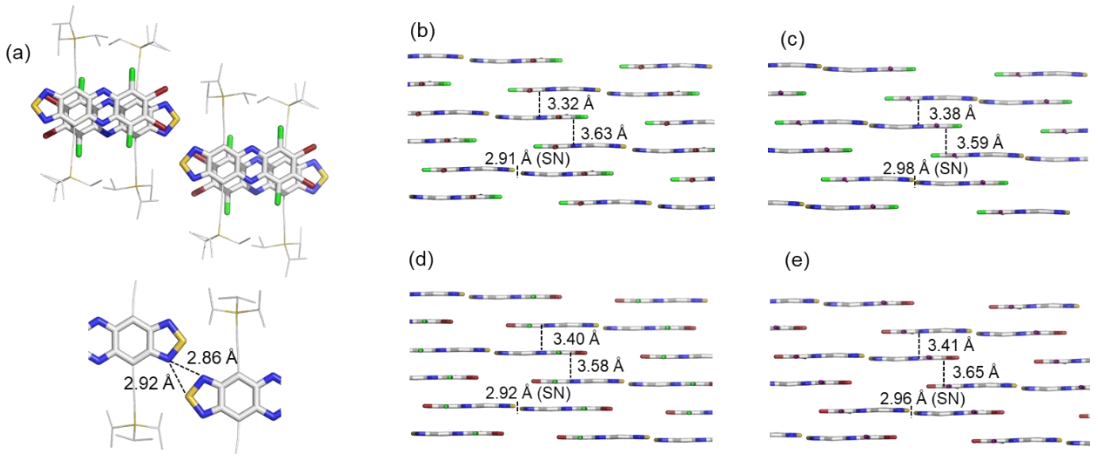

Figure 20. Crystal structures: (a) left: top view of **39-Br_2Cl_2**; right: S-N short contacts. Packing motif of (b) **39-Cl_2Br_2**, (c) **39-Cl_2I_2**, (d) **39-Br_2Cl_2** and (e) **39-Br_2I_2** illustrating the intermolecular distances in the structure. For clarity hydrogens and side chains in the packing motifs are omitted.

Table 2. Crystal parameters of compounds **39**.

Compd.	a [Å]	b [Å]	c [Å]	S-N distance [Å]	π-π distance [Å]	d_{001}-spacing [Å]
39-Cl_4	7.38	14.28	17.16	2.90	3.32, 3.55	16.66
39-Cl_2Br_2	7.94	14.26	17.20	2.91	3.32, 3.63	17.00
39-Cl_2I_2	9.20	14.14	17.98	2.92	3.38, 3.59	16.98
39-Br_2Cl_2	7.85	14.33	17.27	2.92	3.40, 3.58	16.78
39-Br_4	8.08	14.34	17.48	3.06	3.43, 3.57	16.91
39-Br_2I_2	9.22	14.16	18.14	2.98	3.39, 3.64	17.00

Specimen of tetrahalogenated phenazinothiadiazoles **39** for X-ray crystallography were grown by slow evaporation of their chloroform solutions. These molecules exhibit similar crystal structure, so **39-Br_2Cl_2** was taking as an example shown in Figure 20. The π-π planes overlap almost over the whole backbone, and the thiadiazole moieties display dominant short S-N short contacts (chalcogen bonding, square motif), which are not outcompeted by potential halogen bonding. All targets show brick wall packing of their head-to-head dimers, and the space

between π-stacks is occupied by the TIPS groups. By comparing the π-stacking and S-N distances (Table 2), the thiadiazoles bearing the halogen atoms with a larger volume (from Cl to Br to I) π-stack less closely due to the increased size.

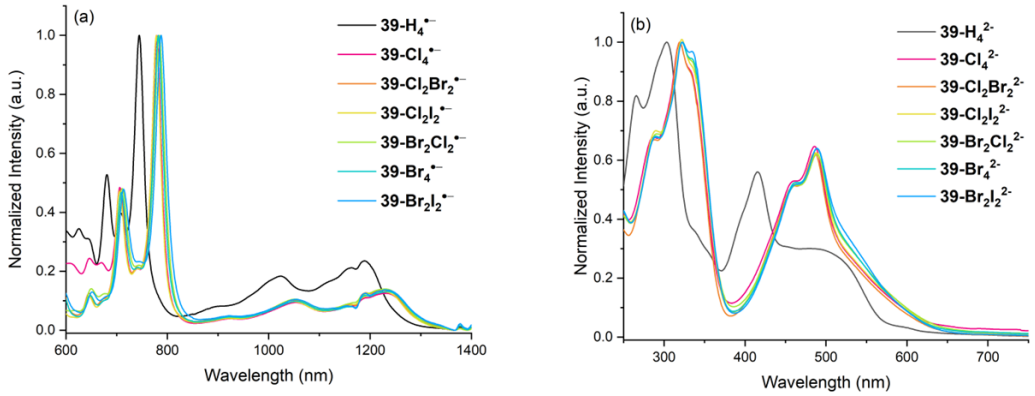

Figure 21. Normalized UV-Vis absorption spectra of (a) **39**$^{\bullet-}$ and (b) **39**$^{2-}$ in THF (10^{-5} mol L^{-1}) solution.

Absorption of **39**$^{\bullet-}$ in THF red-shifted to around 1250 nm (Figure 21a) with a similar sequence of absorption onsets as their neutral species. Upon further reduction, a blue-shifted absorption wave around 500 nm was observed for dianions **39**$^{2-}$ (Figure 21b). Through an investigation of the evolution of UV-Vis absorption spectra of **39**$^{\bullet-}$ at ambient conditions (Figure 22a), halogenation significantly improves the stability of radical anions in comparison with **39-H$_4$**$^{\bullet-}$. Besides, from Cl to Br to I, the heavier halogens are more effective in stabilizing the radical anions with respect to oxygen, which is consistent with the EA values estimated by cyclic voltammetry.

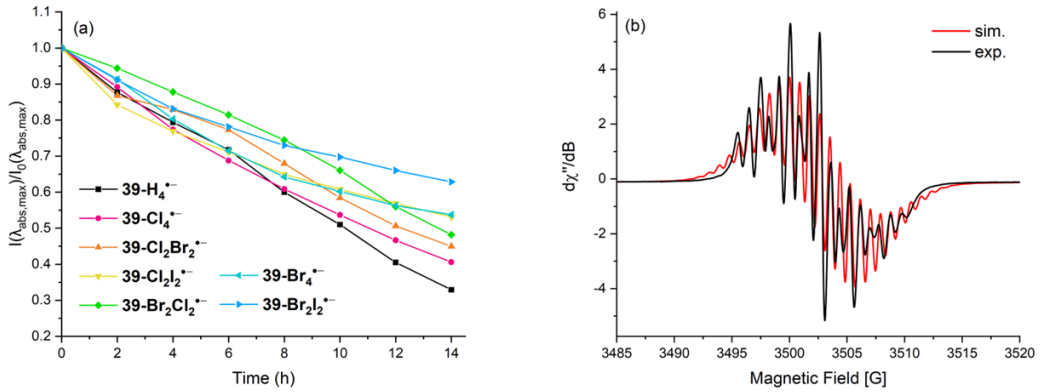

Figure 22. (a) Time-dependent evolution of UV-Vis absorption intensities at $\lambda_{abs,\,max}$ for **39**$^{\bullet-}$ in THF (10^{-5} mol L^{-1}) at room temperature exposed to the air in the dark. (b) Experimental and simulated EPR spectra of **39-Br$_2$I$_2$**$^{\bullet-}$ in a toluene/THF mixture at room temperature.

The radical anions **39**$^{\bullet-}$ display complex electron paramagnetic resonance (EPR) spectra, depending on the substitution pattern. The spectrum of **39-Br$_2$I$_2$**$^{\bullet-}$ was shown in Figure 22b, and the spectra of other derivatives are shown in Figure 173 (see chapter 7). The simulated spectrum of **39-Br$_2$I$_2$**$^{\bullet-}$ gives g_{iso} = 2.006, a hyperfine coupling to two pairs of nitrogen atoms ($\alpha(^{14}N)$ = 5.10; 4.91 MHz), one pair of iodine atoms ($\alpha(^{127}I)$ = 2.34 MHz) and one pair of bromine atoms ($\alpha(^{79, 81}Br)$ = 2.27 MHz). The g_{iso} values increase with the molecular mass of the radical anions (g_{iso} (**39-H$_4$**$^{\bullet-}$) = 2.0042, g_{iso} (**39-Cl$_4$**$^{\bullet-}$) = 2.0046, g_{iso} (**39-Cl$_2$Br$_2$**$^{\bullet-}$) = 2.0051, g_{iso} (**39-Cl$_2$I$_2$**$^{\bullet-}$) = 2.0057, g_{iso} (**39-Br$_2$Cl$_2$**$^{\bullet-}$) = 2.0052, g_{iso} (**39-Br$_4$**$^{\bullet-}$) = 2.0058, g_{iso} (**39-Br$_2$I$_2$**$^{\bullet-}$) =2.0062). The larger outer orbitals result in higher orbital angular momentum influencing the g factor of the molecule.[127] As the steric hindrance grows with the halogen size, the g factor deviates increasingly from the electron g factor g_e.

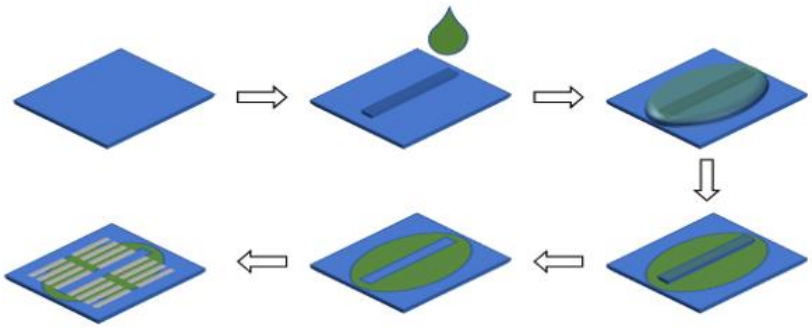

Figure 23. Processing procedure (ambient conditions): A silicon strip was placed in the middle of the SAM-modified substrate. After drop-casting, the solvent was evaporated while being protected from atmospheric drafts. The strip was removed and silver electrodes were evaporated onto the film.

To study electron transport of halogenated phenazinothiadiazoles, my colleague Nikolai Hippchen fabricated bottom gate/top contact thin film OTFTs with silver contacts. Its work function is close to the EA values of the halophenazinothiadiazoles (Figure 17). We used a drop-cast technique[128-129] in combination with a CDPA[130-131] coated dielectric. A silicon pinner was placed on the substrate, an ethyl acetate solution of **39** (0.5-0.75 mg/mL) was drop cast onto the strip and the substrates were protected from undesired turbulences. After evaporation of the solvent at 295 K, the pinner, guiding the direction of crystal growth, was removed to result in crystalline films (Figures 23).

Table 3. Device characteristics of **39.**

Compd.	$\mu_{e\ max}$ [$cm^2\ V^{-1}\ s^{-1}$]	$\mu_{e\ ave}$ [a] [$cm^2\ V^{-1}\ s^{-1}$]	Threshold voltage V_{th} [V]	On/off ratio
39-Cl$_4$	0.25	0.16 ± 0.09	35	10^4-10^5
39-Cl$_2$Br$_2$	0.62	0.38 ± 0.17	9	10^5-10^6
39-Cl$_2$I$_2$	0.15	0.09 ± 0.05	10	10^4-10^5
39-Br$_2$Cl$_2$	0.76	0.47 ± 0.19	25	10^5-10^6
39-Br$_4$	0.14	0.08 ± 0.03	22	10^4-10^5
39-Br$_2$I$_2$	0.51	0.39 ± 0.09	28	10^5-10^6

[a] Averaged mobility calculated from five different channels on at least two different substrates.

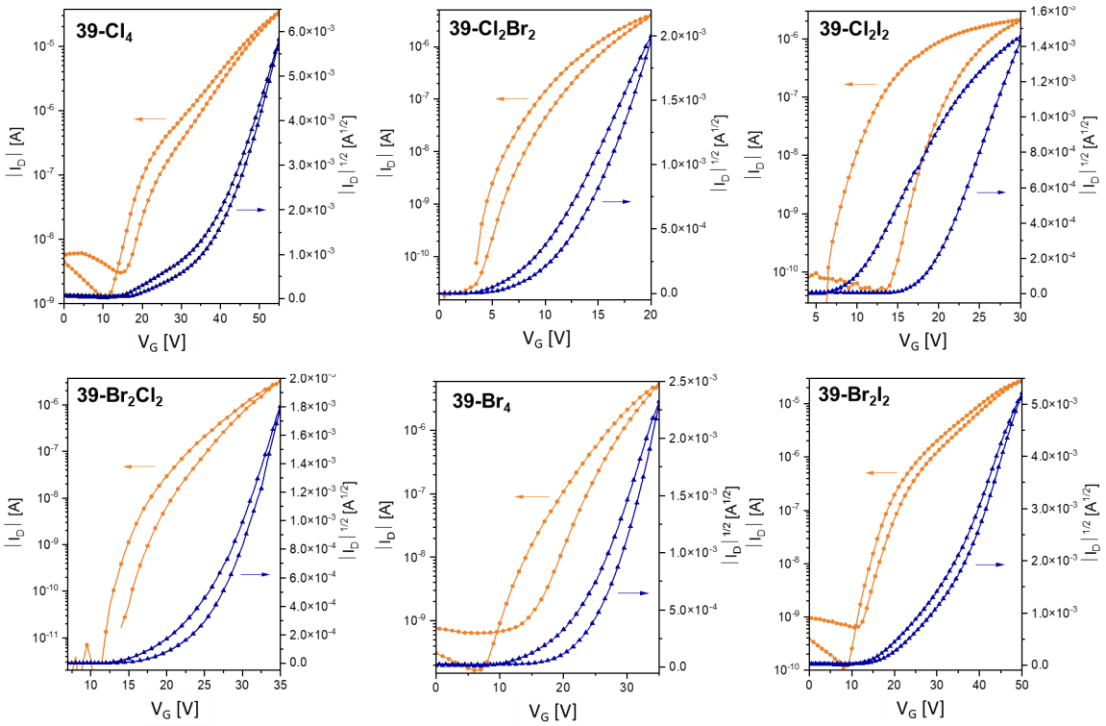

Figure 24. Transfer characteristics of **39**.

The device characteristics are showed in Figures 24 and 25, and parameters are summarized in Table 3, average values were obtained from a total of five transistors each from at least two different substrates. For literature known **39-Cl$_4$**,[110] the average mobility was quadrupled from 0.04 to 0.16 $cm^2V^{-1}\ s^{-1}$, a consequence of substrate modification with a SAM and guided crystal growth. **39-Br$_2$Cl$_2$** exhibited the highest mobility (μ_{max} = 0.76 $cm^2V^{-1}\ s^{-1}$). All compounds show good on/off ratios around 10^5. Compounds with mixed halide substituents, especially bromine/chlorine derivatives, gave the best mobilities (μ_{ave}(**39-Br$_2$Cl$_2$**) = 0.47 $cm^2V^{-1}\ s^{-1}$,

(μ_{ave}(**39-Cl$_2$Br$_2$**) = 0.38 cm^{2}V^{-1} s^{-1}). The lowest mobility was determined for for **39-Br$_4$** with μ_{ave} = 0.08 cm^{2}V^{-1} s^{-1}, followed by **39-Cl$_2$I$_2$** (0.09 cm^{2}V^{-1} s^{-1}).

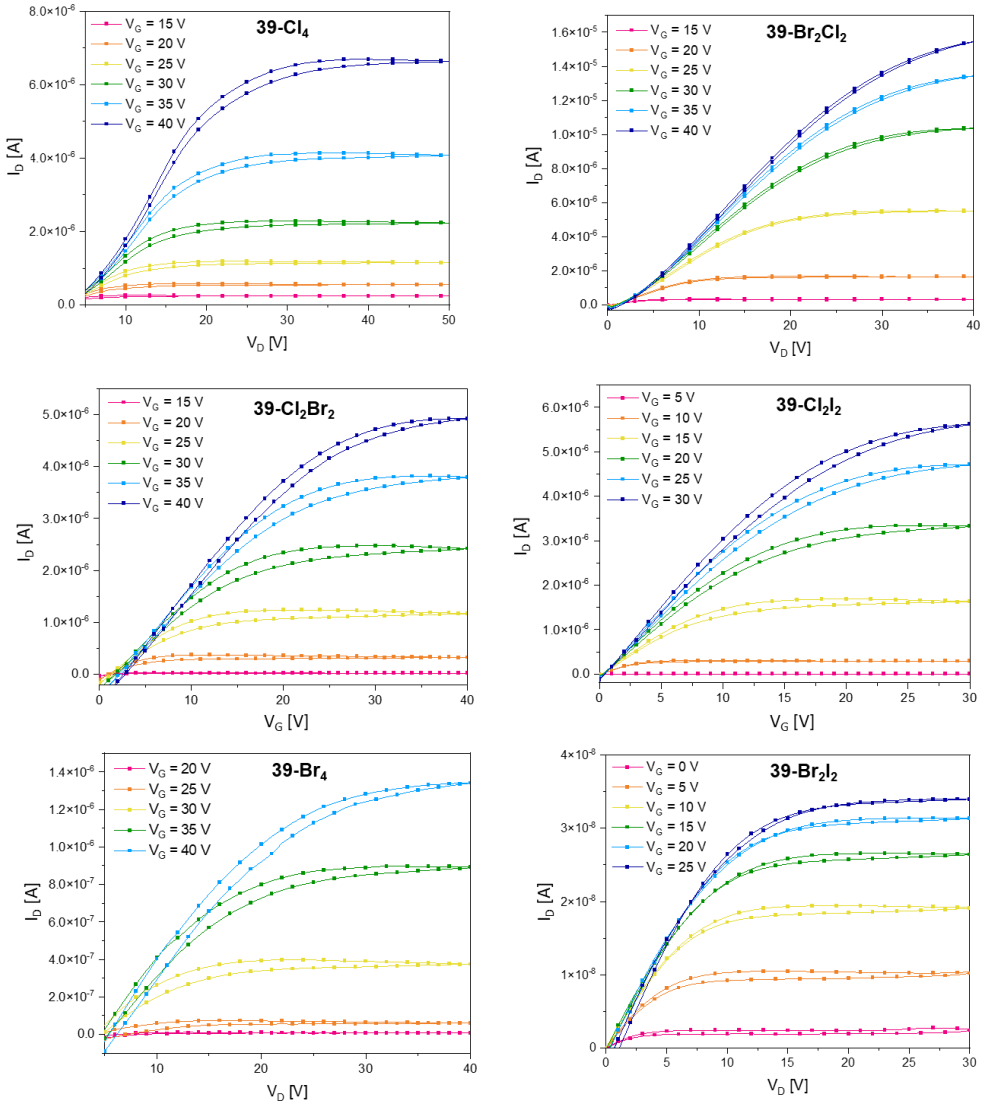

Figure 25. Output characteristics of **39**.

It is reasonable to assume that the quality of the semiconductor films dominates the resulting mobilities: Films of **39-Br$_2$Cl$_2$** consist of quasi uniform crystalline rods bridging the two electrodes, but **39-Cl$_2$I$_2$** exhibits feather-like crystal growth rendering complete orthogonal alignment between electrodes impossible. Furthermore, there is an increased number of grain boundaries (Figure 26). The film quality correlates with the solubility of the materials - it decreases with higher atomic weight of the halides and increases for mixed substitution patterns. The poor film quality of **39-Cl$_2$I$_2$** is also reflected in the transfer characteristics (Figure 24) through increased hysteresis.

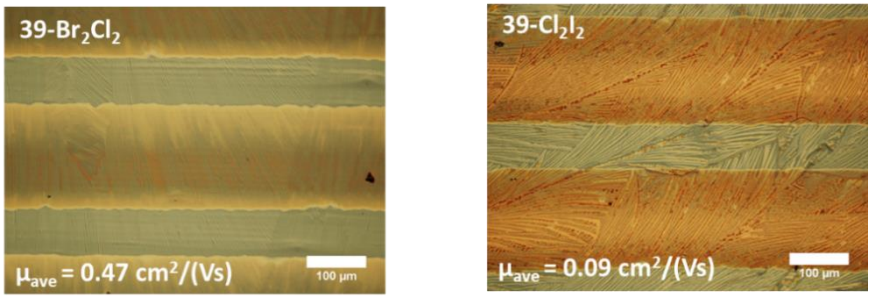

Figure 26. Exemplary films of **39-Br$_2$Cl$_2$** and **39-Cl$_2$I$_2$** with silver electrodes.

The calculated transfer integrals with the ADF software package[132] and reorganization energies with Gaussian 16 software package[24] and estimated electron mobilities[88] are shown in Table 4. Dimer pair π-π A yields the highest transfer integrals (except for **39-Cl$_4$**), particularly for the heavier halogen derivatives ($V_{\pi\text{-}\pi,A}$ (**39-Br$_2$I$_2$**) = 72.2 meV). For π-π dimers B containing iodine on the acene zig-zag edge, $V_{\pi\text{-}\pi B}$ values are lower ($V_{\pi\text{-}\pi B}$ (**39-Br$_2$I$_2$**) = 5.6 meV) due to a lateral shift and thus less overlap along the acene backbone. The S-N short contacts (Table 2) lead to increased transfer integrals between the as-formed dimers (Table 4). The mobilities calculated from these values all range between 0.28 to 0.82 cm^2V^{-1} s^{-1} and are close to the mobilities obtained experimentally. The trend of the calculated values, however, does not match that of the experimental results; this is most likely due to differences in film morphologies as described above.

Table 4. Transfer integrals V, reorganization energies λ, and calculated mobilities for electron transfer of **39.**

Compd.	V [meV] π-π A	V [meV] S-N contact	V [meV] π-π B	λ [meV]	Calculated mobility [cm^2V^{-1} s^{-1}]
39-Cl$_4$	37.3	39.3	37.8	221.07	0.275
39-Cl$_2$Br$_2$	48.7	36.1	24.9	217.01	0.303
39-Cl$_2$I$_2$	67.1	30.8	7.1	215.30	0.643
39-Br$_2$Cl$_2$	48.5	34.7	36.4	217.01	0.327
39-Br$_4$	56.8	19.5	38.8	209.45	0.416
39-Br$_2$I$_2$	72.2	31.0	5.6	208.47	0.819

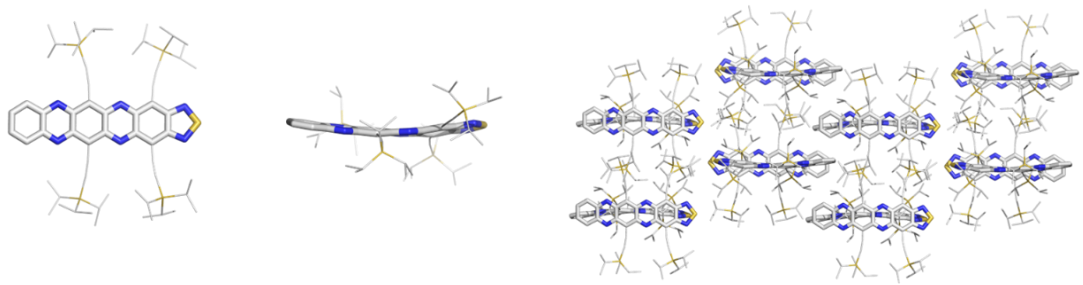

Figure 27. Solid state structure and packing motif obtained for **51**. Hydrogen atoms were omitted for clarity.

Specimen of **51** cultivated for X-ray crystallography was grown by slow diffusion of methanol into its chloroform solution. The acene unit is twisted and the TIPS-ethynyl groups are significantly bent due to the steric pressure (Figure 27). The crystal structure of **51** displays edge to face packing without appreciable π-π interactions or S-N short contacts.

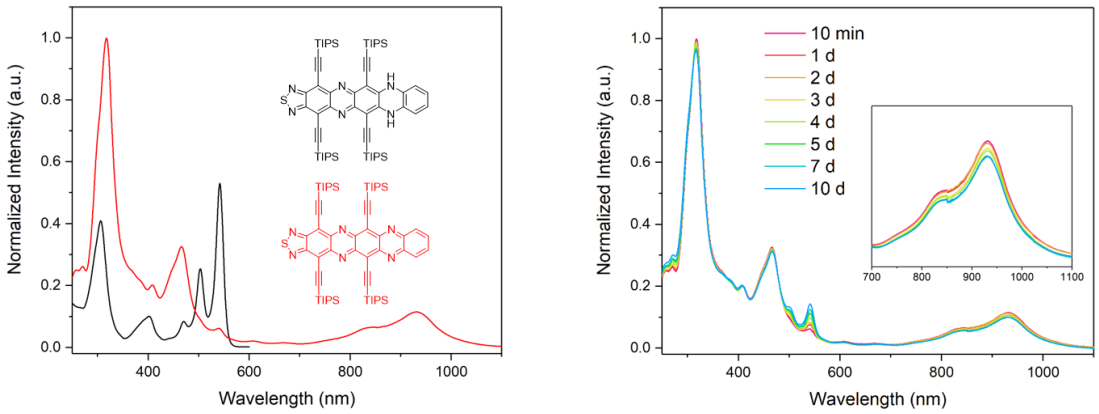

Figure 28. (a) UV-Vis absorption spectra of *N,N'*-dihydro- **51-H₂** and oxidized **51**; (b) time-dependent absorption evolution of **51** in dry DCM (10^{-5} mol L^{-1}) in ambient conditions.

51-H₂ shows an absorption onset at around 570 nm. Upon oxidation to **51**, the absorption onset red-shifted to 1050 nm (Figure 28a), supporting the presence of the oxidized tetraazapentaceno thiadiazole. The stability of **51** was evaluated by UV-Vis spectroscopy in dilute DCM solution (10^{-5} mol L^{-1}) under ambient conditions (Figure 28b). Surprisingly, **51** remains stable in dilute solution for up to 10 days. It is only slightly reduced to its *N,N'*-dihydro- precursor ($I_{10\ d}/I_0$ ≈ 90% at λ_{max}), i.e., is completely stable.

2.4 Conclusion

In conclusion we have demonstrated a synthetic route to a total of 7 phenazinothiadiazoles – 6 being substituted with different patterns of halogen atoms. The brick wall packing motif of dimers is ideal for application in organic field-effect transistors and the electron affinities are suitable for electron transport. Electron mobilities (μ_e) up to 0.76 $cm^2 V^{-1} s^{-1}$ for **39-Br_2Cl_2** were obtained. Calculated charge carrier mobilities were in the same order of magnitude. Compared to literature known compounds **39-Cl_4** and **39-F_4**,[110] three of the four newly synthesized derivatives display increased mobilities. The charge carrying species of the compounds, viz the radical anions were synthesized and analyzed through EPR and UV-Vis. Preorganization in the crystal lattice due to the thiadiazole head-to-head interactions may be beneficial to obtain higher in-plane transfer integrals and thus overall mobilities but this strategy has to be extended to both ends of the acene core. Attempts by Müllen et al.[112] failed due to the sensitivity of these acene-endcapped thiadiazoles towards [4+4] dimerization, while the sterically more shielded tetraazapentaceno thiadiazole **51** reasonably inhibits the dimerization and is isolable and stable.

Chapter 3. Synthesis, Characterization and Application of Stable Azaheptacenes

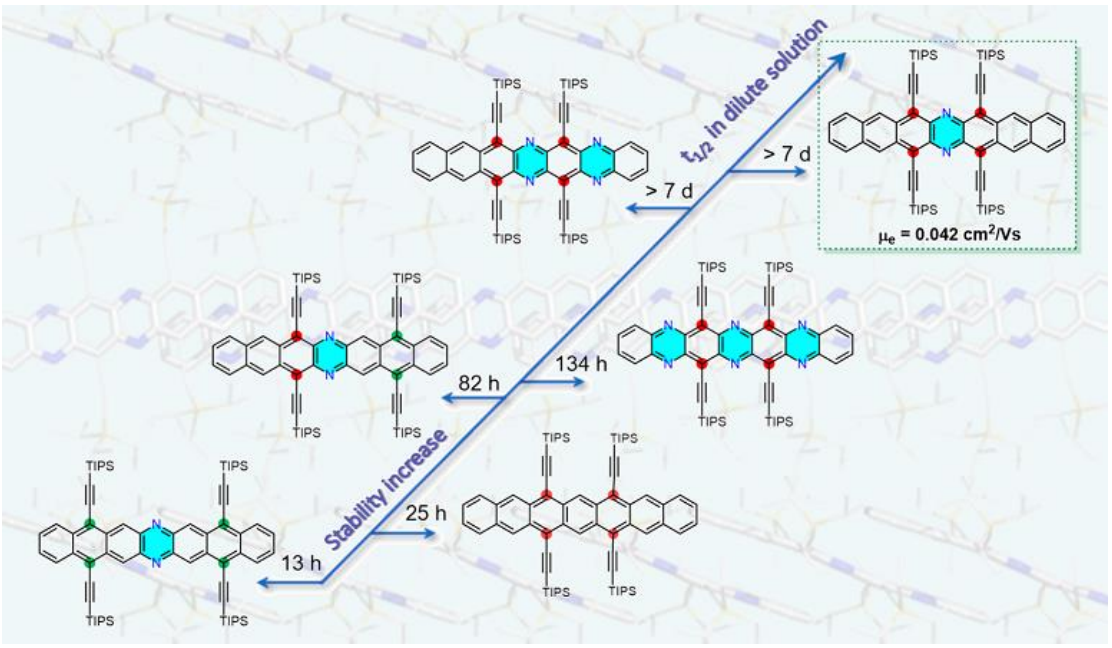

3.1 Introduction and Research Purpose

Acenes and azaacenes enjoy a renaissance in interest as particularly the larger representatives are predicted to display unusual and attractive properties spanning from partial diradical character to vanishing HOMO-LUMO gaps and electric and electronic properties that makes them useful in a whole slate of different applications including OFETs, OPVs as well as nontraditional NLO materials. However, their high reactivity (dimerization, oxidation/reduction etc.) makes the preparation of soluble and processible derivatives challenging.

The addition of two TIPS-ethynyl groups to the central ring makes pentacene solution processible[65, 67, 133] and adds significant stability.[134] If the steric bulk is increased by larger silyl groups (Si(SiMe$_3$)), reasonably stable hexacene[94] and, marginally stable but isolable heptacene **54**[64] (Figure 29) results. In contrast to their hydrocarbon analogues,[98-99, 135] isolable azaheptacenes are unknown, despite Dutt's claim in 1926.[74, 136] True azaheptacenes (non-benzannulated species without e.g. pyrene or ovalene substructures) are rarely reported due to their instability arising from the presence of only one Clar sextet. **DAH3** with four (tri-*sec*-butylsilyl)ethynyl substituents was moderately persistent in solution but dimerized into its [4+4]-cycloadducts upon crystallization, hindering the evaluation of its solid-state structure.[100]

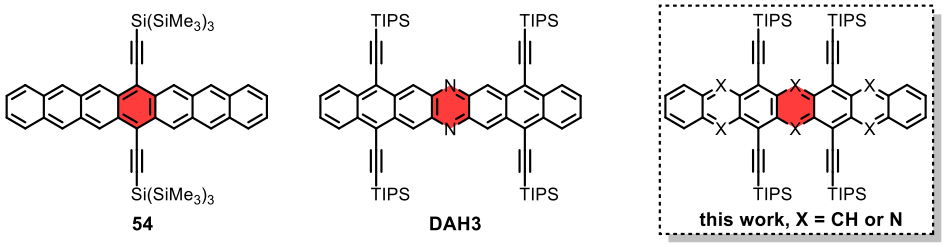

Figure 29. Known heptacene **54**,[64] diazaheptacene **DAH3** and the (aza)heptacenes in this work.[100]

In this chapter, we present the stability of a series of (aza)heptacenes with various nitrogen content (0, 2, 4, 6) in the backbone and transposition of the TIPS-ethynyl substituents – soluble, isolable and processible di- and tetraazaheptacenes and a marginally stable hexaazaheptacene resulted.

3.2 Synthesis of (Aza)heptacenes

To construct **DAH1** and **DAH2**, diaminoanthracene **23a**[95] and dibromoanthracene **55**[100] or **56** are the critical building blocks. Anthraquinone derivatives were alkynylated and aromatized using $SnCl_2$ to furnish **51**. Pd-catalyzed coupling of **23a** with **55** or **56** furnished dihydro-precursor **DAH2-H₂** (85%) and **DAH1-H₂** (63%) in surprising yields (Scheme 15) despite the steric hindrance posed by the four TIPS-ethynyl groups. Oxidation of **DAH1-H₂** with MnO_2 gave **DAH1** (72%) as the main product, and also lead to **57** (10%) as a by-product, an isomer of **DAH1-H₂**. **DAH2** was accessed in 85% yield starting from **DAH2-H₂**.

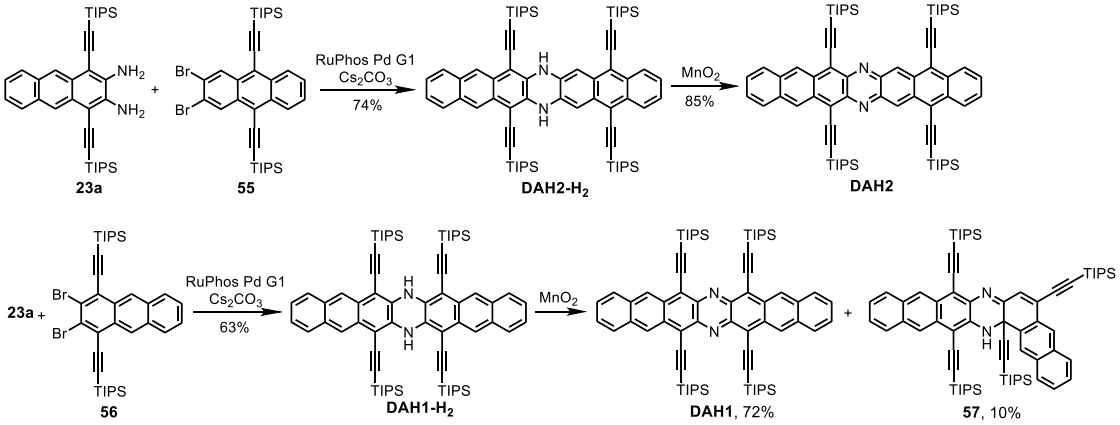

Scheme 15. Synthesis of **DAH1** and **DAH2**.

The synthesis of **TAH-H₂** and **HAH-H₂** exploits *ortho*-quinone **49-Br₂I₂**, obtained from dibromodiiodoveratrole by demethylation and oxidation (see chapter 2). **49-Br₂I₂** was freshly prepared and condensed with diaminoanthracene **23a** or diaminophenazine **23b**[137] to yield tetrahaloazapentacenes **58a**,**b**. **58a** was reacted with 5 equivalents of TIPS-acetylene under Sonogashira[123] conditions (50 °C) into tri- to hexa-ethynylated *N,N'*-dihydro- intermediates, which underwent oxidation with PbO_2. Column chromatography afforded tetraethynylated dibromo-pentacene **59a** in 39% yield (Scheme 16). Excellent regioselectivity was achieved transforming **58b** to **59b** with 10 equivalents of TIPS acetylene at room temperature under Sonogashira conditions (75% yield). **59a**,**b** were Buchwald-Hartwig coupled to *ortho*-phenylenediamine to give *N,N'*-dihydro-precursors (**TAH-H₂** and **HAH-H₂**).

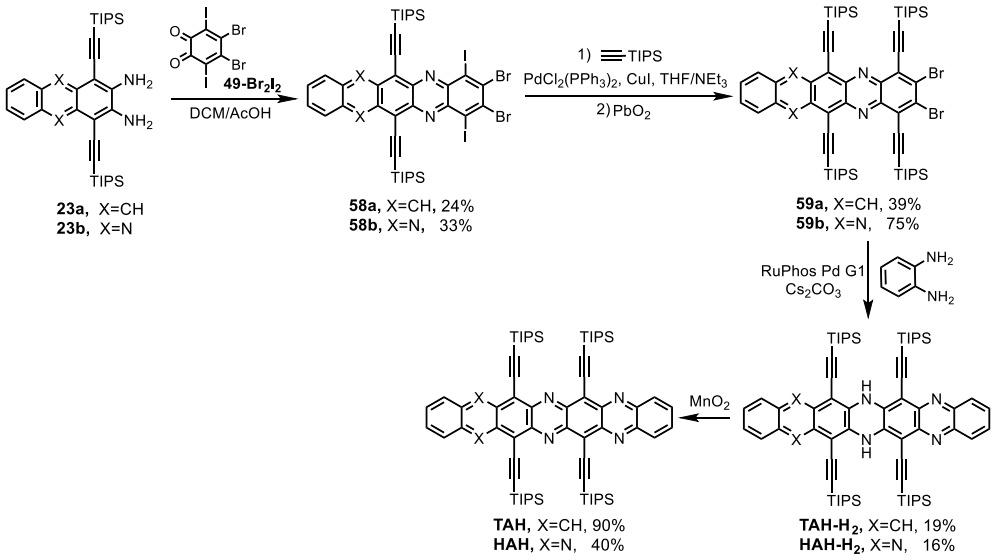

Scheme 16. Synthesis of **TAH** and **HAH**.

DAH-H$_2$ and **TAH-H$_2$** reacted with MnO_2 (100 equiv.) in 10 min to furnish **DAH** and **TAH**. **HAH-H$_2$** was only partially oxidized into **HAH** even after 5 h. All of the three heptacenes were isolated through column chromatography. Afterwards, a small amount of methanol was added to the fractions as anti-solvent to precipitate the products. The solvent was evaporated quickly in a schlenk line under nitrogen atmosphere to furnish **DAH**, **TAH** and **HAH** as microcrystalline solids for characterization (NMR, UV-Vis, CV, IR and cultivation of single crystals) and preparation of their radical anions.

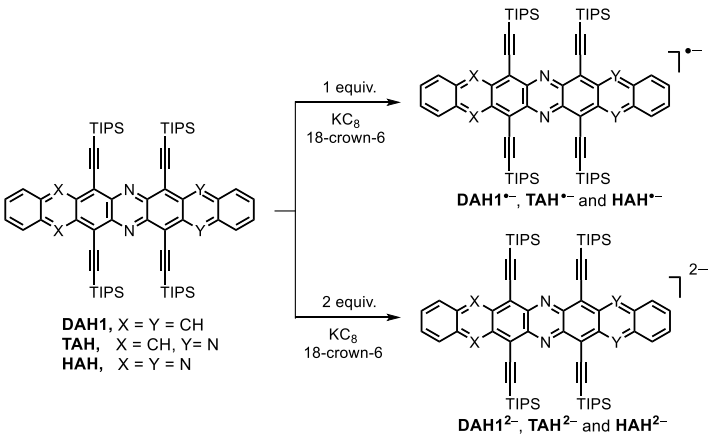

Scheme 17. Preparation of the anions and dianions of **DAH1**, **TAH** and **HAH**.

The mono- and dianions of the azaheptacenes were prepared by reduction with KC_8-(18-crown-6) in THF (Scheme 17). Treatment with one equivalent reductant furnished the dark yellow

solution of monoanions **DAH1**$^{\bullet-}$, **TAH**$^{\bullet-}$ and **HAH**$^{\bullet-}$. Upon further reduction, two equivalent reductant furnished red solutions of the dianions **DAH1**$^{2-}$, **TAH**$^{2-}$ and **HAH**$^{2-}$.

The hydrocarbon analogue **Hep** containing no N atoms was synthesized by my colleague Nico Zeitter to compare with azaheptacenes substituted with the same TIPS placement.

3.3 Results and Discussion

Six target (aza)heptacenes are depicted in this chapter. In **Hep**, **DAH1**, **TAH** and **HAH** we increase the nitrogen content in heptacenes without changing the TIPS-ethynylation pattern (6,8,15,17 positions); while **DAH1**, **DAH2** and **DAH3** unveil the importance of the substitution pattern on the diazaheptacenes' stability.

Figure 30 displays the UV-Vis absorption spectra of *N,N'*-dihydro compounds and respective oxidized heptacenes. Upon oxidation the optical properties change. The absorption onsets for **DAH1**, **DAH2**, **TAH** and **HAH** are red-shifted to 1074, 1064, 1152 and 1045 nm, supporting the presence of the azaheptacenes. **TAH**'s most red-shifted absorption is a consequence of its donor-acceptor character.[96] Hydrocarbon **Hep** is the most blue-shifted congener (absorption onset: 950 nm). The heptacene p-bands are broadened and/or display shoulders at the longest wavelengths, attributed to their arising diradical character,[138] although all NMR spectra are well-resolved.

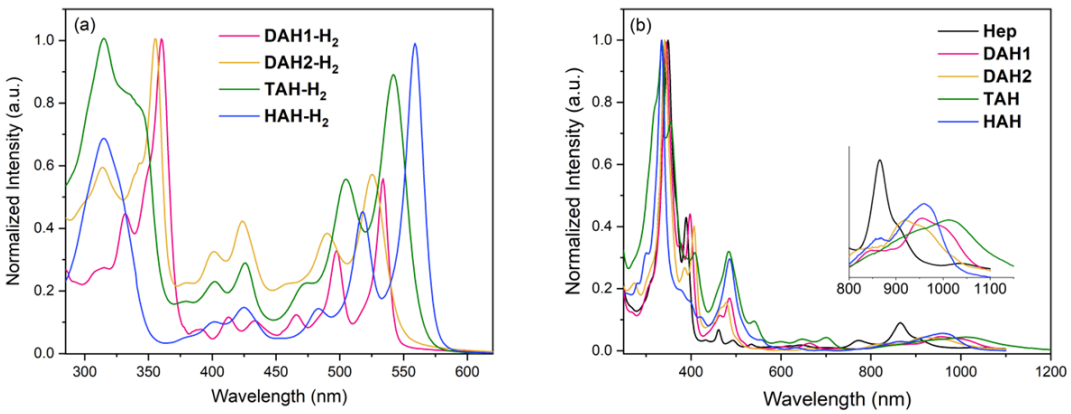

Figure 30. Normalized UV-Vis absorption spectra of (a) *N,N'*-dihydro compounds and (b) oxidized azaheptacenes in DCM.

Figure 31 shows a comparison of IR spectra of the *N,N'*-dihydro compounds and the respective oxidized azaheptacenes. The lack of the N-H vibration mode around 3350 cm^{-1} for **DAH1**, **DAH2**, **TAH** and **HAH** indicates the existence of the oxidized species, which is also proof of azaheptacene formation.

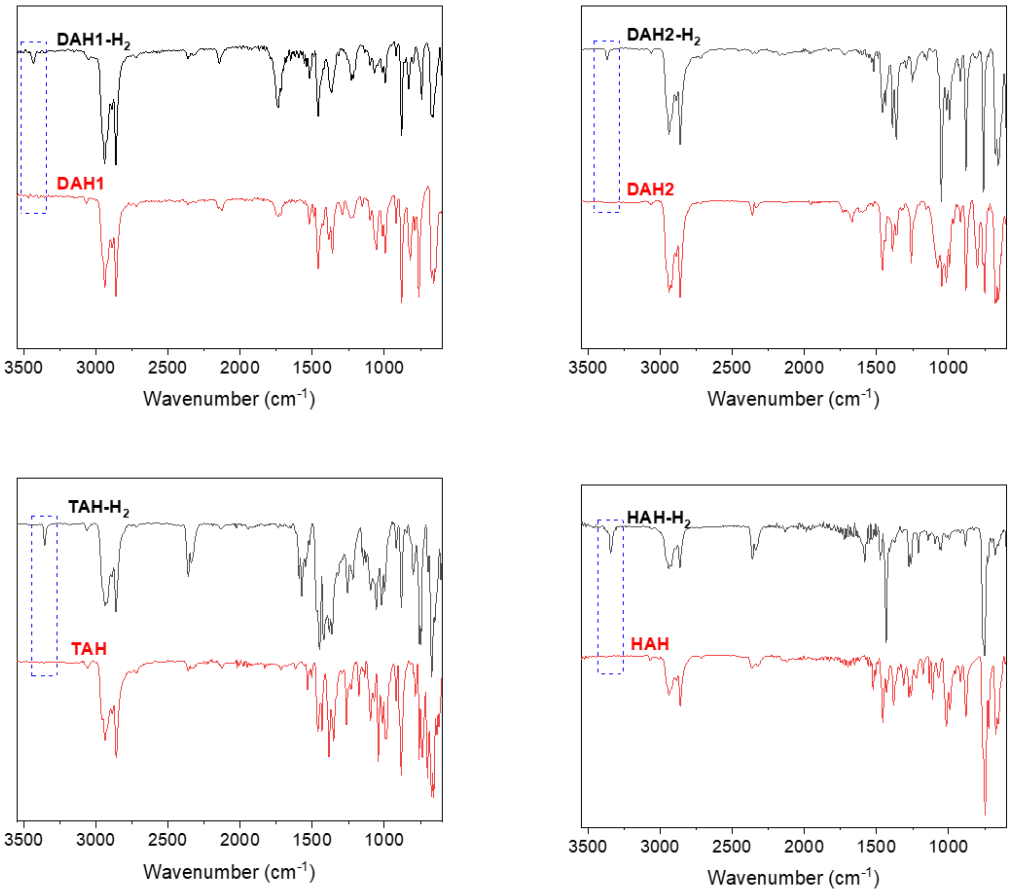

Figure 31. FT-IR spectra of dihydro compounds (black) and azaheptacenes (red).

The stability of three isomers (**DAH1**, **DAH2** and **DAH3**) were compared by time-dependent evolution of the ^{1}H NMR spectra to evaluate substituents pattern matters (Figure 32). The NMR of **DAH3** exhibited growing resonances attributed to butterfly dimers (~85% consumption after 6 h) and could not be captured without any sign of butterfly adduct.[100] Under the same conditions, **DAH1** and **DAH2**, with more centralized substituents were neither prone to Diels Alder reaction nor to butterfly dimerization for at least 6 h without any changes in the spectra, which highlights the effect of the substituent pattern of diazaheptacenes with a central pyrazine unit.

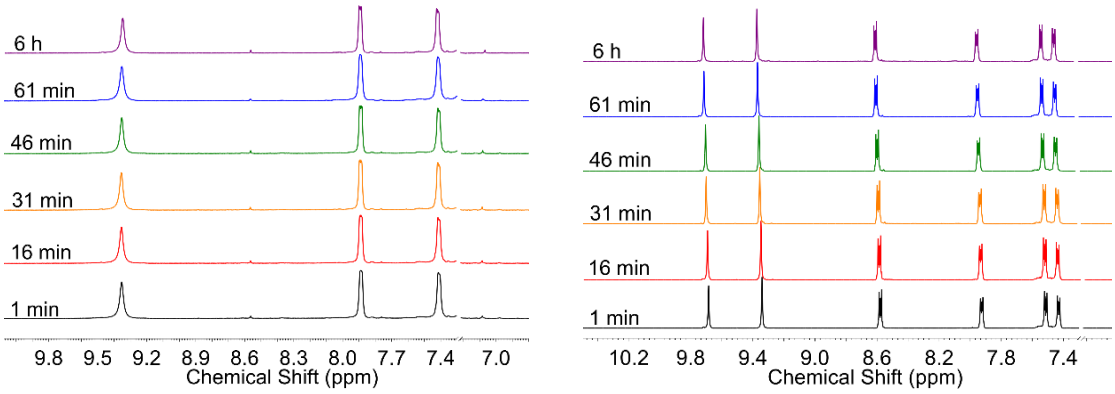

Figure 32. Time-dependent ^{1}H NMR spectra of **DAH1** (left) and **DAH2** (right) in $CDCl_3$ under ambient conditions magnifying all signals in the aromatic region. Chloroform peak was omitted for clarity.

Time-dependent evolution of UV-Vis absorption spectra (Figure 33) experiments were conducted to investigate the long-term stability. The half-life ($\tau_{1/2}$) of **DAH2** and **DAH3** (DCM solution, 10^{-5} mol L^{-1}) are 4 d and 6 h, respectively. Solutions of **DAH1** were unchanged after 7 d under ambient light and atmosphere (Figure 33b) and it seems to be completely stable. Similar to heptacenes,[64, 98-99] the position of the TIPS-ethynyl groups determine their stability – silylethynyl groups adjacent to the central ring protect the center of the azaacene more effectively than those with more arene rings in between.

Next we studied the effect of N atom loading on stability. Adding another pyrazine moiety, **TAH** started to decompose after 7 d (I_{7d}/I_0 = 82% at λ_{max}, Figure 33e). **HAH** displayed a $\tau_{1/2}$ of 5 d – it was spontaneously reduced to its *N,N'*-dihydro species (Figure 33f). In contrast to the decay channels of alkynylated acenes, this process is reversible – reoxidation proceeded quantitatively to **HAH**. Removing the central pyrazine unit dramatically decreases the stability and forms endoperoxide as degradation product ($\tau_{1/2\ Hep}$ = 25 h, Figure 33a), although this is still reasonably stable for a hydrocarbon heptacene as it is only protected by four substituents compared to the most stable congener with six.[99]

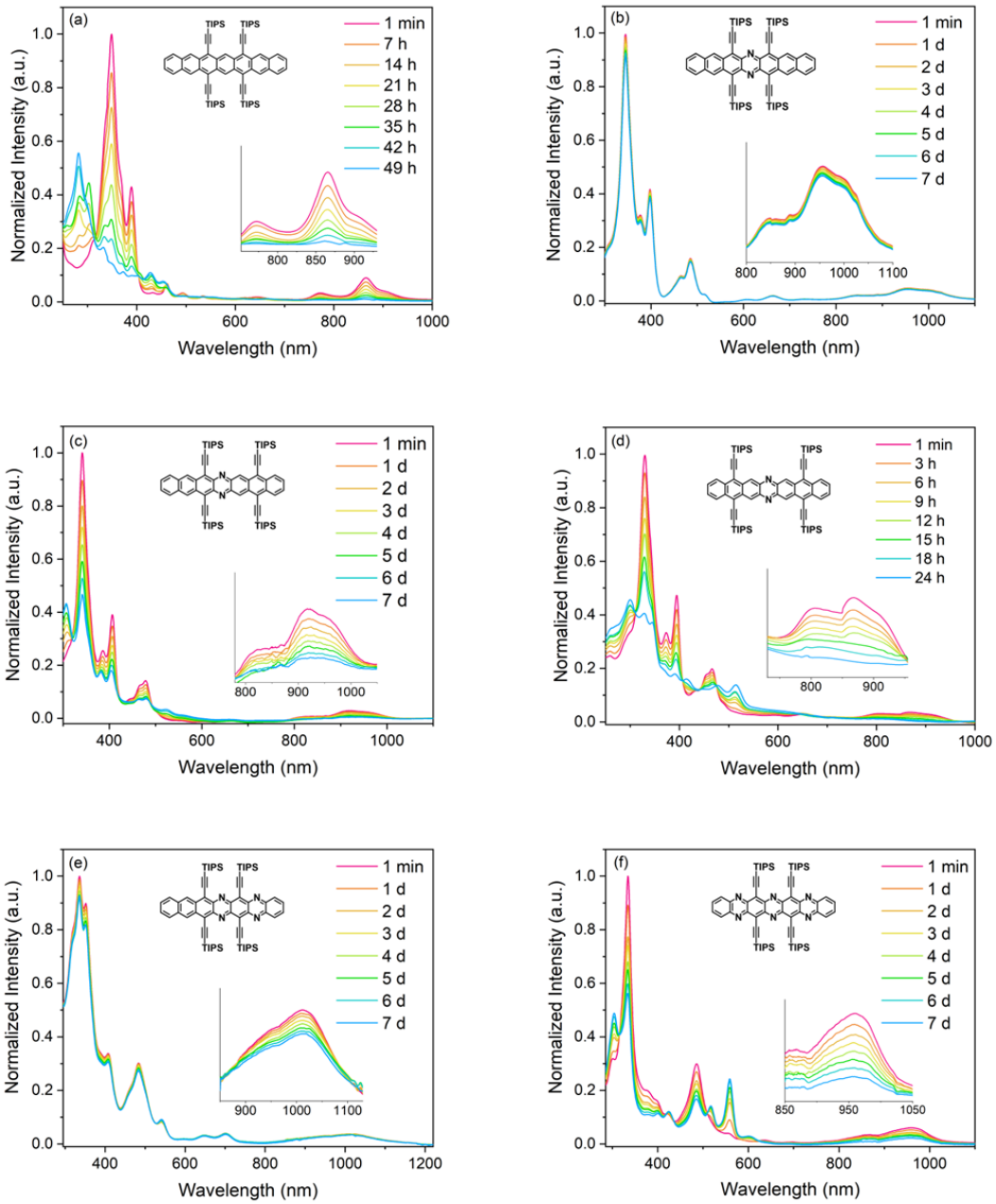

Figure 33. Time-dependent evolution of UV-Vis spectra of (a) **Hep** (b) **DAH1**, (c) **DAH2**, (d) **DAH3,** (e) **TAH** and (f) **HAH** in DCM (10^{-5} mol L^{-1}) under ambient light and atmosphere. The inset shows magnification of the time-dependent evolution of the p-bands.

The rank order of stability is **DAH1**>**TAH**>**HAH**≈**DAH2**>**Hep**>**DAH3** (Figure 34). Stability therefore depends upon the number of nitrogen atoms and the placement of the four TIPS-ethynyl substituents.

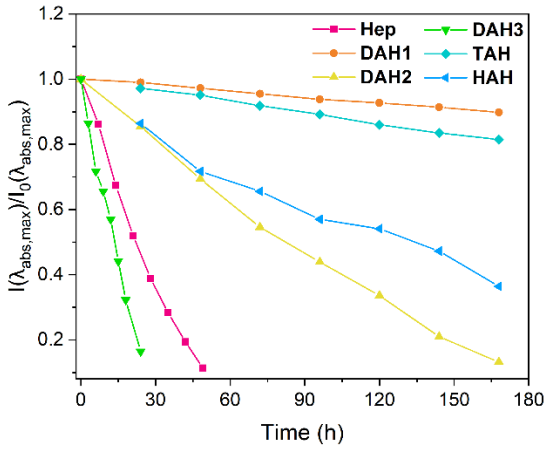

Figure 34. Stability comparison of (aza)heptacenes via time-dependent evolution of UV-Vis spectra.

The LUMOs of **Hep**, **DAH**, **TAH** and **HAH** are evenly distributed over the molecular skeleton; while the HOMO of **TAH** has small coefficients at the pyrazine rings (Figure 35),[139] resulting in a decreased gap in comparison with **DAH** and **HAH**, consistent with its red-shifted UV-Vis absorption (Figure 30).

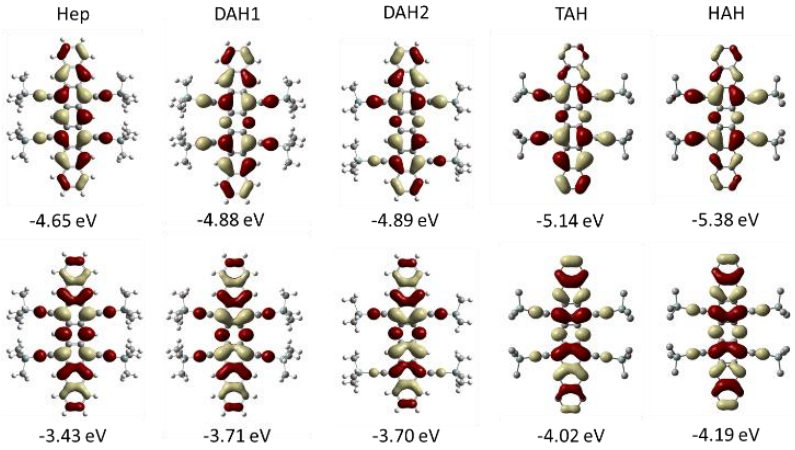

Figure 35. FMO distribution of *N,N'*-dihydro compounds and oxidized (aza)heptacenes.

Cyclic voltammetry spectra (Figure 36) display two oxidation waves and two reduction waves for **Hep** and **DAH1** (**DAH2** displays a similar CV behavior to **DAH1**, see Figure 172, chapter 7). In contrast, **TAH** and **HAH** display two and three reduction waves, respectively, leading to strong electron affinities (< -4.10 eV), suggesting that their radical anions might be stable in air (*vide infra*).

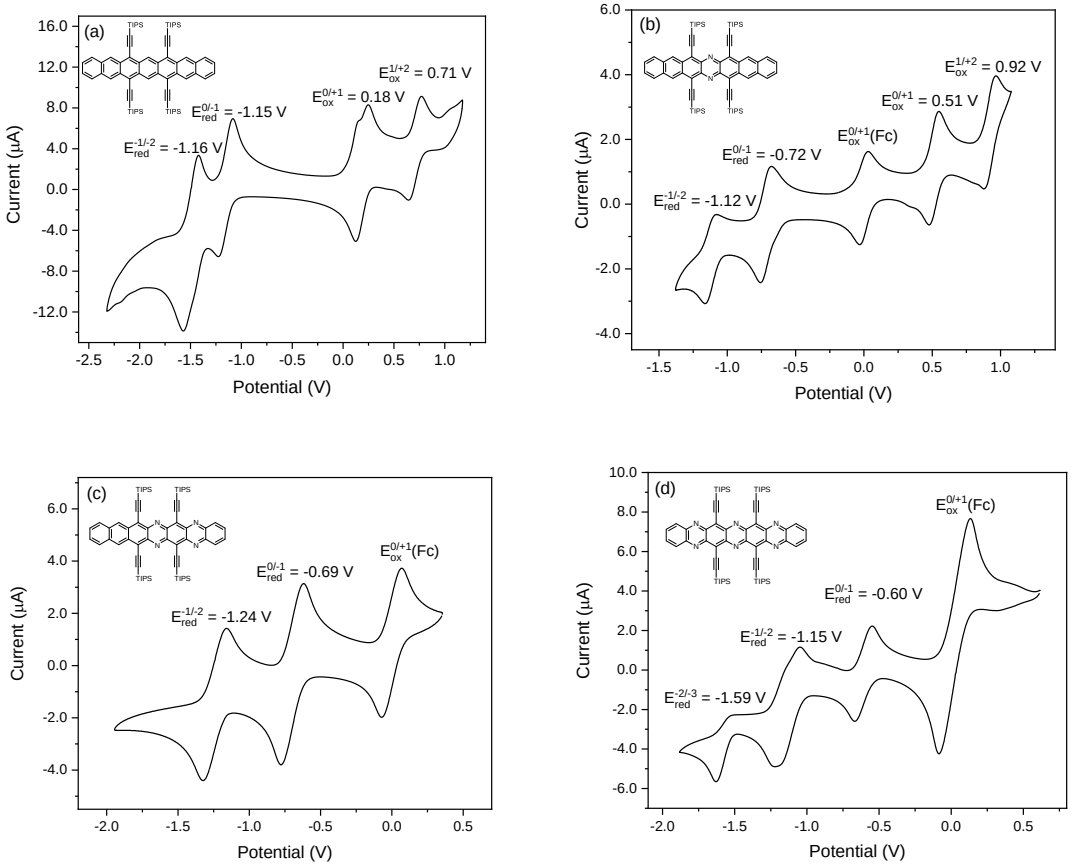

Figure 36. Cyclic voltammograms of (a) **Hep**, (b) **DAH1**, (c) **TAH** and (d) **HAH** in DCM (Fc/Fc^+ as reference, Pt as working electrode and Bu_4NPF_6 as electrolyte).

Table 5. Photophysical and calculated properties of (aza)heptacenes.

Compd.	$\lambda_{abs\ on}$ [a] [nm]	$\lambda_{abs\ max}$ [b] [nm]	$E_{g\ meas}$ [c]/ $E_{g\ cal}$ [d] [eV]	$E_{1/2}^{red1}$ [e] [V]	EA[f]/E_{LUMO} [g] [eV]	IP[h]/ E_{HOMO} [g] [eV]
Hep	950	865	1.30/1.22	-1.15	-3.65/-3.43	-4.95/-4.65
DAH1	1074	957	1.15/1.17	-0.72	-4.08/-3.71	-5.23/-4.88
DAH2	1064	917	1.17/1.19	-0.77	-4.03/-3.70	-5.20/-4.89
TAH	1152	1011	1.08/1.12	-0.69	-4.11/-4.02	-5.19/-5.14
HAH	1045	961	1.19/1.19	-0.60	-4.20/-4.19	-5.39/-5.38

[a] Onset of the lowest energy absorption maxima; [b] most intense absorption of the p-band; [c] optical gap calculated by λ_{onset}; [d] HOMO LUMO gap calculated by DFT calculation;[125] [e] first reduction potentials measured by cyclic voltammetry in DCM against Fc/Fc^+ as the internal standard (−4.80 eV) using a Pt working electrode and Bu_4NPF_6 as electrolyte; [f] electron affinities (EA) estimated from first reduction potentials EA = − 4.80 eV − E_{red};[126] [g] FMO values calculated by DFT calculation[125] (Gaussian16 B3LYP, def2TZVP; TMS groups were used instead of TIPS); [h] ionization potential (IP) =EA− $E_{g\ meas}$.

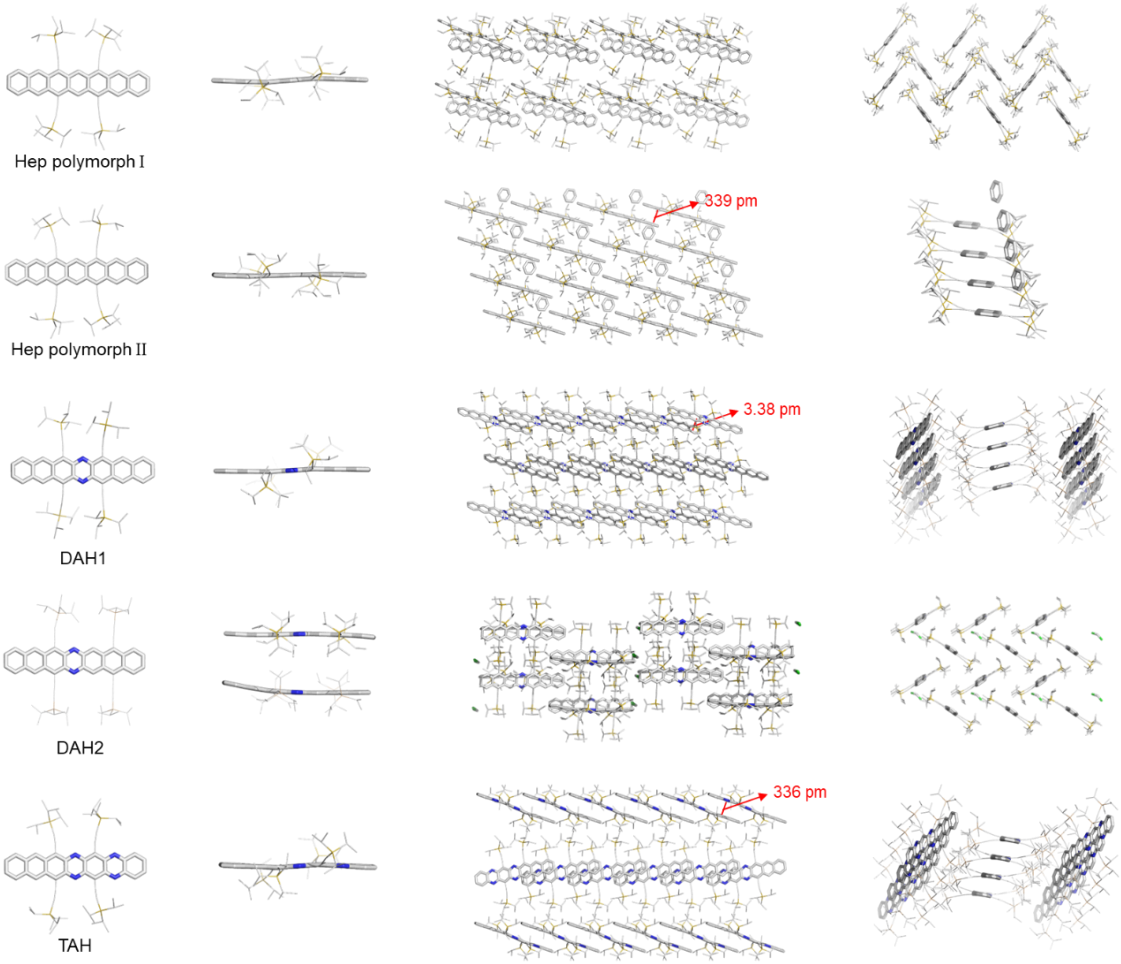

Figure 37. Solid state structure and packing motif obtained for (aza)heptacenes. Hydrogen atoms were omitted for clarity. **TAH** resides on an inversion center without inversion symmetry, so the outer nitrogen atoms superimpose with the carbon atoms of the other side and all possibly different distances and angles of both halves of the molecule are averaged.

Crystalline specimen of (aza)heptacenes were grown by slow diffusion of methanol into their chloroform (**Hep** polymorph I, **DAH1**, and **TAH**) or dichloromethane solutions (**DAH2**), or via cooling their concentrated solutions in benzene (**Hep** polymorph II). **Hep** (polymorph II) and **DAH2** crystallize as solvates with benzene and dichloromethane, respectively.

As shown in Figure 37, the backbones of all acenes slightly deviates from planarity – most are S-shaped. **DAH2** contains two independent molecules per unit cell, one of the two is strongly bent. The backbone of **Hep** (polymorph II) is almost planar, exhibiting one dimensional stacks along one direction with a mean π-π distances of 339 pm between the overlapping, but slightly offset two terminal rings. **DAH1** and **TAH** exhibit an overlap of ~3.5 and 3 rings along the

backbone and columnar stacking with π-π distances between of 338 and 336 pm, respectively. The non-central pyrazine ring in **TAH** is statistically disordered throughout the crystal lattice. **Hep** (polymorph I) and **DAH2** lack obvious π-π interactions, demonstrating an edge-to-face arrangement. Using the same method of crystal growth for **DAH1** did not lead to the inclusion of benzene into the crystal lattice.

Table 6. Crystal parameters for (aza)heptacenes.

Compd.	space group	Z	a [Å]	b [Å]	c [Å]	α (deg.)	β (deg.)	γ (deg.)	cell volume [Å^3×10^3]	solvate
Hep (polymorph I)	$P2_1/c$	2	15.99	15.39	15.04	90.0	113.1	90.0	3.40	–
Hep (polymorph II)	$P\bar{1}$	1	9.79	13.69	15.80	67.7	86.6	78.1	19.2	C_6H_6
DAH1	$P2_1/n$	2	9.14	17.96	20.63	90.0	95.6	90.0	3.37	–
DAH2	$P\bar{1}$	4	15.03	15.17	32.47	79.3	79.2	89.7	7.09	DCM
TAH	$P2_1/c$	2	9.49	20.15	17.14	90.0	91.3	90.0	3.28	–

Crystalline specimen of **HAH** were grown by slow diffusion of methanol into its DCM solution. Single crystal analysis of **HAH** demonstrates a similar herringbone packing as **TAH**, but found that hydrogen atoms at the central pyrazine rings occupied about 50% of the molecules (Figure 38), providing further evidence for its spontaneous reduction. From a historical perspective, Dutt's first claim of a hexaazaheptacene in 1926 has now been realized ca. 100 years later testimony to the difficulties in isolating the larger azaacenes.[136]

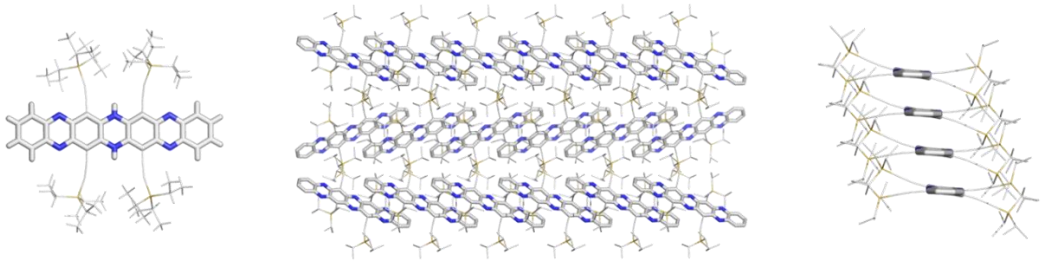

Figure 38. Solid state structure and packing motif obtained for **HAH**. Hydrogen atoms were omitted for the packing motif.

To explore of the formation of the by-product **57**, crystalline specimen of the precursor of **DAH1** and **57** was cultivated by diffusion of methanol into its chloroform solution. As a result, the solid-state structure of **DAH1-H$_2$** (Figure 39) was found as the only structure in the sample – no possible precursors (-H_2) for by-product **57** was found in the crystal.

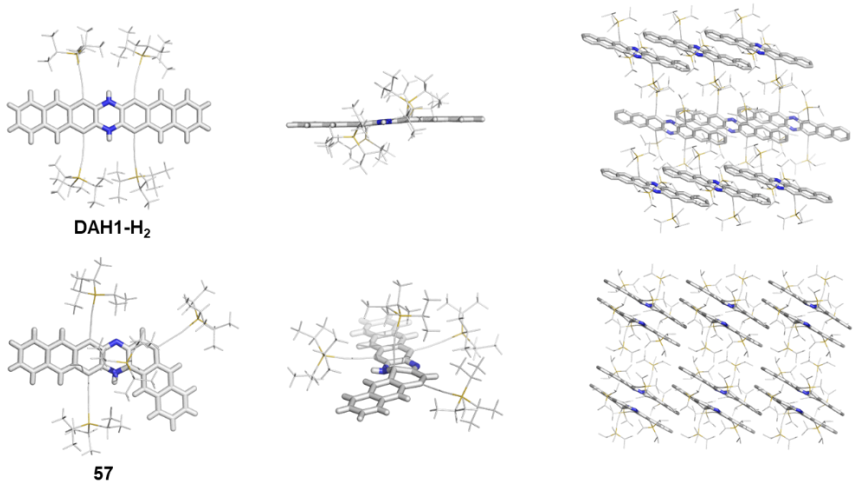

Figure 39. Solid state structure and packing motif obtained for **DAH1-H$_2$** and **57**.

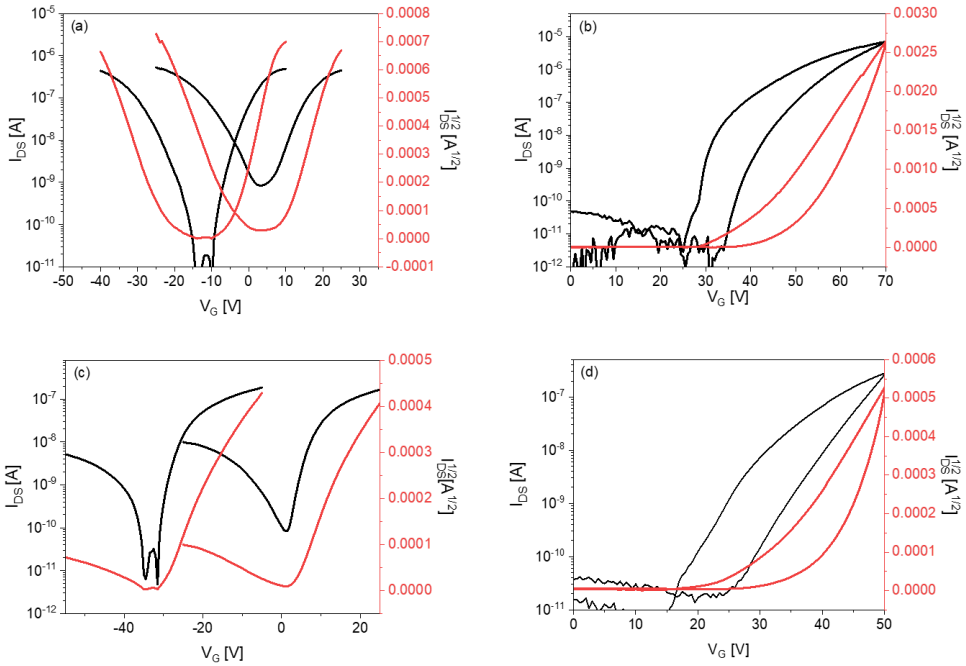

Figure 40. Transfer characteristics of (a) **Hep** (b) **DAH1**, (c) **DAH2** and (d) **TAH**.

Table 7. Charge carrier mobilities of drop-casting transistors of **Hep**, **DAH1**, **DAH2** and **TAH**.

Compd.	$\mu_{e\text{-}max}$ [$cm^2V^{-1}\ s^{-1}$]	$\mu_{e\text{-}ave}$ [$cm^2V^{-1}\ s^{-1}$]	$\mu_{p\text{-}max}$ [$cm^2V^{-1}\ s^{-1}$]	$\mu_{p\text{-}ave}$ [$cm^2V^{-1}\ s^{-1}$]
Hep	2.3×10^{-2}	1.2×10^{-2}	3.8×10^{-2}	2.3×10^{-2}
DAH1	4.2×10^{-2}	1.7×10^{-2}	—	—
DAH2	4.9×10^{-3}	2.7×10^{-3}	1.7×10^{-3}	5.7×10^{-4}
TAH	3.1×10^{-3}	1.5×10^{-3}	—	—
Hexaethynyl-heptacene[99]	1.4×10^{-3}	7.7×10^{-4}	1.7×10^{-3}	1.1×10^{-3}
TIPS-Pen[65]	—	—	1.8	0.65
TIPS-TAP[140]	11.0	7.6	—	—

The transistors of (aza)heptaccenes were fabricated by my colleague Nikolai Hippchen, the results are summarized in Table 7. **DAH1** and **TAH** exhibit electron transport in bottom gate/top contact field-effect transistors (Figure 40) with best electron mobilities at 0.042 cm^2V^{-1} s^{-1} and 0.0031 cm^2V^{-1} s^{-1}, respectively. **Hep** and **DAH2** exhibit ambipolar transport with $\mu_{e\text{-}max}$ = 0.023 cm^2V^{-1} s^{-1} and $\mu_{p\text{-}max}$ = 0.038 cm^2V^{-1} s^{-1} for **Hep** (**DAH2**: $\mu_{e\text{-}max}$ = 0.005 cm^2V^{-1} s^{-1} and $\mu_{p\text{-}max}$ = 0.0017 cm^2V^{-1} s^{-1}). The discrepancies between the calculated and experimental values are, in addition to the limitations of the calculation methodology, probably due to the quality of the thin films. In comparison with hexaethynyl-heptacene,[99] the mobility of **Hep** improved to be 30 times higher for the n-channel transport and 22 times higher for the p-channel transport, respectively. The transporting performance of **Hep**, **DAH1** and **TAH** is expected to be further improved through device optimization.

Table 8. Calculated transfer integrals (only highest shown), reorganization energies and mobilities for electron and hole transport.

Entry	Transfer integral [meV]		Reorganization energy [meV]		μ_{theo} [cm^2V^{-1} s^{-1}]	
	electron	hole	electron	hole	electron	hole
Hep (polymorph I)	2.9	1.2	133.0	104.3	1.4×10^{-2}	3.9×10^{-3}
Hep (polymorph II)	24.9	10.8	133.0	104.3	9.2×10^{-1}	2.5×10^{-1}
DAH1	77.2	49.7	145.2	102.3	3.5	2.6
DAH2	4.2	4.8	142.0	101.6	2.0×10^{-2}	2.4×10^{-2}
TAH	90.1	11.9	133.0	-	4.6	-
Hexaethynyl-heptacene[99]	7.7	0.7	135.2	111.2	1.6×10^{-1}	7.2×10^{-3}
TIPS-Pen[65]	129.8	23.5	187.5	132.8	3.5	2.6×10^{-1}
TIPS-TAP[140]	102.5	1.3	203.0	207.4	1.8	4.3×10^{-4}

The transfer integrals of all possible pairs of neighbouring molecules were calculated by my colleague Philipp Ludwig through the ADF software package.[132] Reorganization energies were computed by the four-point method using Gaussian16.[35] We obtained the electron and hole transport mobilities μ (Table 8) from the transfer integral and the reorganization energies. Only the highest transfer integral of each compound is shown in Table 8.

In comparison with the calculated mobilities of hexaethynylheptacene,[99] **Hep** showed higher transporting potential, indicating a smaller number of centrally placed TIPS-ethynyl substituents facilitates charge transport. **DAH1** is a promising ambipolar transporting material

with theoretical hole mobility up to 2.6 cm^2V^{-1} s^{-1} and electron mobility up to 3.5 cm^2V^{-1} s^{-1}, comparable to that of **TIPS-Pen**.[65] **TAH** might be a promising n-type transporting material with theoretical electron mobilities up to 4.6 cm^2V^{-1} s^{-1}, even higher than that of **TIPS-TAP**.[140] When comparing these calculated mobilities, one must keep in mind that they are based on a diffusion model, which is only valid for crystal structures with a single molecule per unit cell of perfect translational symmetry and is thus expected to provide an estimation of the upper limit of the packing analyzed.[141]

The mono- and dianions of the azaheptacenes were investigated by UV-Vis absorption spectra. In comparison of the neutral species, the absorption of **DAH1**$^{\bullet-}$, **TAH**$^{\bullet-}$ and **HAH**$^{\bullet-}$ in THF red-shifted upon reduction to 1615, 1734 and 1811 nm, respectively (Figure 41). As expected, a blue-shifted absorption was observed for the dianions **DAH1**$^{2-}$, **TAH**$^{2-}$ and **HAH**$^{2-}$ at λ_{max} = 713, 755 and 792 nm, respectively.

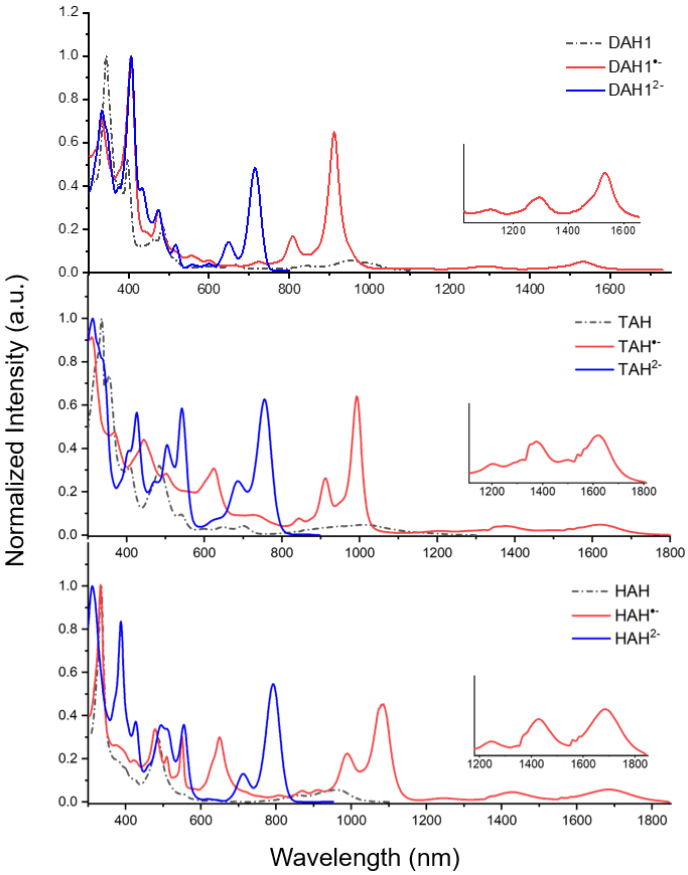

Figure 41. Absorption spectra of **DAH1, TAH and HAH** in their neutral (black dotted), mono- (red solid) and dianionic forms (blue solid) in THF solutions.

Gradually degradation for the dilute solutions of **DAH1**$^{\bullet-}$ and **TAH**$^{\bullet-}$ was observed under ambient conditions in 48 h, while **HAH**$^{\bullet-}$ was more persistent because of its high electron affinity (Figure 42). When moisture was excluded, the degradation process was significantly slowed down in dry air (persistent for one week), similar to the case of tetrabrominated tetraazapentacene.[89]

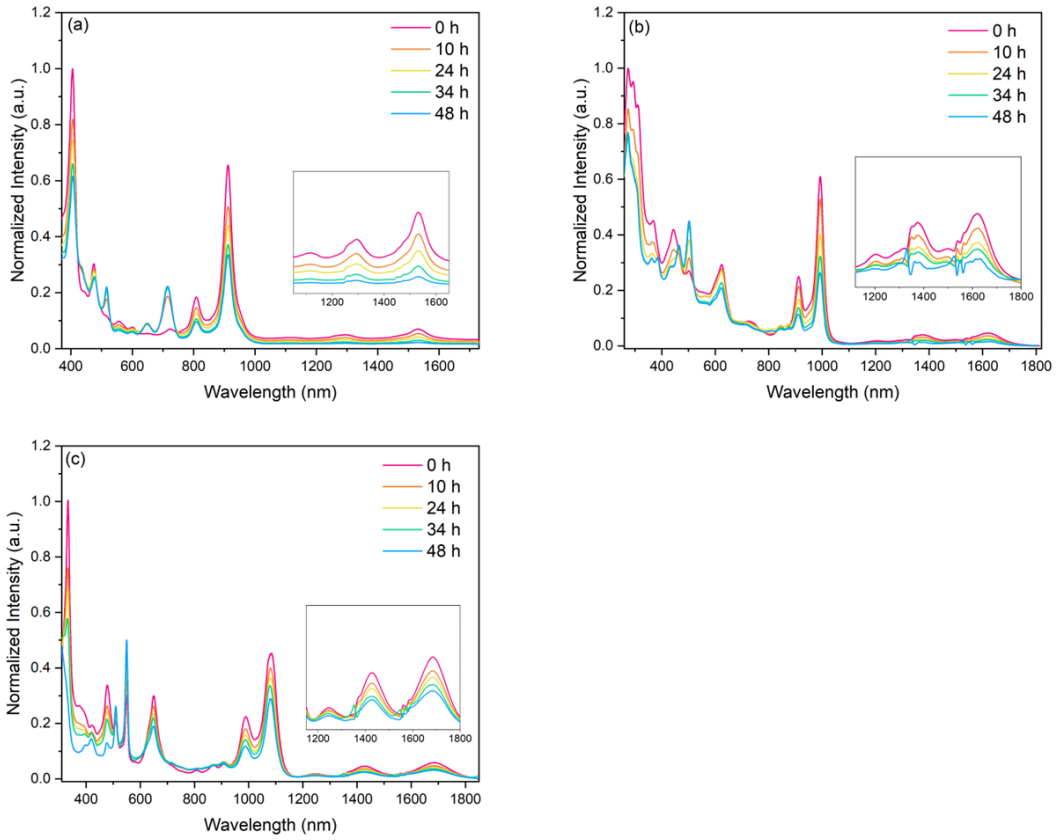

Figure 42. Time-dependent evolution of UV-Vis spectra of (a) **DAH1**$^{\bullet-}$, (b) **TAH**$^{\bullet-}$ and (c) **HAH**$^{\bullet-}$ in THF under ambient conditions (exposed to the air).

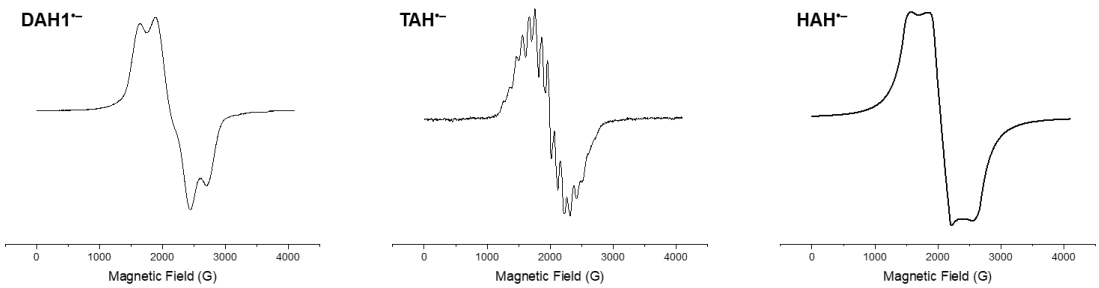

Figure 43. Electron paramagnetic resonance (EPR) spectra of **DAH1**$^{\bullet-}$, **TAH**$^{\bullet-}$and **HAH**$^{\bullet-}$ in a toluene/THF mixture at room temperature.

The radical anions were also evident from EPR spectra (Figure 43). **DAH1**$^{\bullet-}$, **TAH**$^{\bullet-}$ and **HAH**$^{\bullet-}$ display similar g values at 2.003. **TAH**$^{\bullet-}$ demonstrates more splitting peaks due to its asymmetric structure. We succeeded in growing single crystals of the monoanions **TAH**$^{\bullet-}$ and **HAH**$^{\bullet-}$ – the molecular structures are depicted in Figure 44. The monoanions are well separated from the potassium counterions complexed by two additional THF molecules and one 18-crown-6 molecule, suggesting charge delocalization over the whole azaacene backbone.

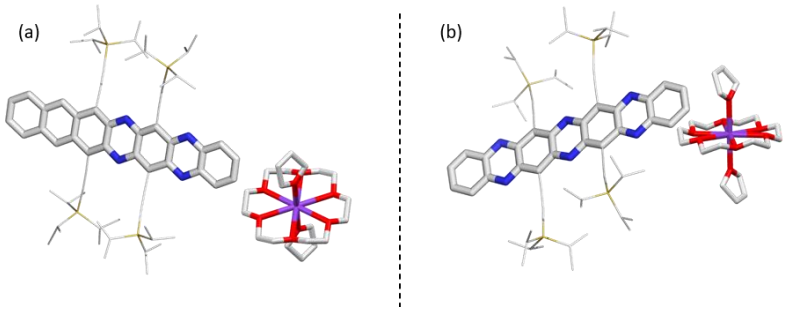

Figure 44. Crystal structure for (a) **TAH**$^{\bullet-}$ and (b) **HAH**$^{\bullet-}$. Hydrogen atoms were omitted and TIPS-ethynyl substituents were reduced in size for clarity. **TAH** resides on an inversion center without inversion symmetry, so the outer nitrogen atoms superimpose with the carbon atoms of the other side and all possibly different distances and angles of both halves of the molecule are averaged.

3.4 Conclusion

In conclusion, we have prepared stable azaheptacenes, claimed ~100 years ago.[136] The substitution pattern in **DAH1** renders it immune to Diels Alder reactions, butterfly dimerization and endoperoxide formation; the correct placement of the silylethynyl substituents is critical for the azaheptacenes' stability. In solution, an increasing number of pyrazine units destabilize azaheptacenes: We observe spontaneous reduction as the main degradation pathway of these electron-poor systems. **DAH1** and **TAH**, more stable than any hitherto reported azaheptacene, are promising n-type semiconductors, according to the calculated mobilities – we will further explore their application in thin-film transistors in the future. The dibromides **53a,b** are precursors to azaoctacenes and azanonacenes if they are coupled to diamino-naphthalenes and -anthracenes. With our report, we also hope to spur applications of azaheptacenes in organic electronics, as stability issues should not be a limiting factor.

Chapter 4. Synthesis, Characterization and Crystallization-Induced Ring-Opening Effect of Tetraazahexacenes

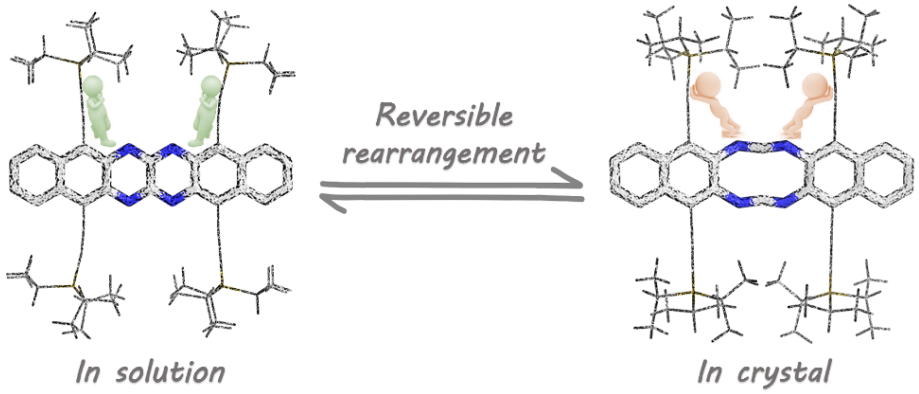

4.1 Introduction and Research Purpose

In this chapter, a series of 5,8,13,16-tetraethynyl-6,7,14,15-tetraazahexacenes were prepared varying their alkynyl substituents in size. All of the tetraazahexacenes are persistent in solution. Upon crystallization, the derivatives with triisopropyl (TIPS), dimethyl-*tert*-butylsilyl (TBDMS) and triethylsilyl (TES) substituents rearrange into tetraazacyclodecahexaenes - cyclic biscarbodiimides to different extents (Scheme 18), depending on the size of the substituents. The ring opening to these didehydrotetrazecines is promoted by the increased steric demand of the substituents and the gain of two Clar sextets in the products – for the TIPS-ethynylated tetraazahexacene, only the cyclic biscarbodiimide is detected in single crystals.

The heat of fusion of benzene is 2.3 kcal/mol and it linearly increase with the acenes rings' increases (naphthalene 4.2 kcal/mol, anthracene 6.9 kcal/mol).[142, 143] Therefore, in larger acenes one can expect significant effects of the crystal packing – the crystal lattice itself enforces ring opening. In solution or in amorphous thin films, the force disappears and the bis-carbodiimides revert into the azaacene form.

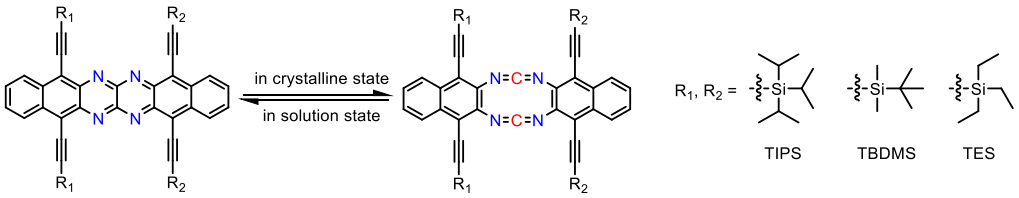

Scheme 18. Reversible transition for tetraethynylated tetraazahexacene to their dinaphtho-didehydrotetrazecine between solution sate and crystalline state.

4.2 Synthesis of Tetraazahexacenes

The synthesis of diamino- and dichloro- starting materials is depicted in Scheme 19. **60** were treated with suitable alkynyllithium reagents, and the corresponding diols **61** were reduced by sodium hypophosphite and potassium iodide in acetic acid to furnish naphtho thiadiazole **62**. After reduction with lithium aluminum hydride the diamino naphthalenes **34** were isolated. Dichloro- benzoquinoxalines **63** were synthesized by condensation reaction with diethyloxalate and underwent chlorination with moderate yields.

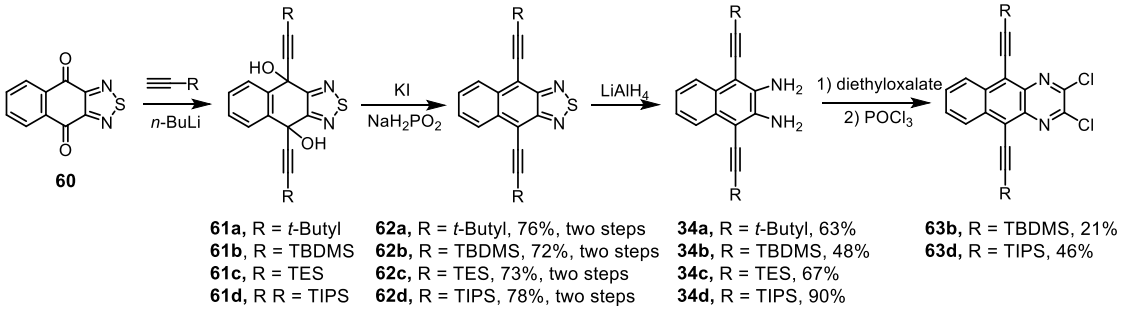

Scheme 19. Synthesis of the diamino naphthalene **34** and dichloro- benzoquinoxaline **63**.

The target molecules were obtained by Buchwald-Hartwig Pd-catalyzed coupling[124] of diamino **34a-d**[109, 144] and dichloro **63b** and **63d**[145] according to established protocols gave the *N,N'*-dihydro-precursors **TAHex-H₂** (yields between 28%~46%, Scheme 20). Their oxidation with PbO_2 furnished tetraazahexacenes **TAHex1-5** in quantitative yield. Diazahexacene **DAHex** was synthesized by Pd-catalyzed coupling of **34d** and **55**[100] followed by oxidation with PbO_2 in satisfactory yield (Scheme 20).

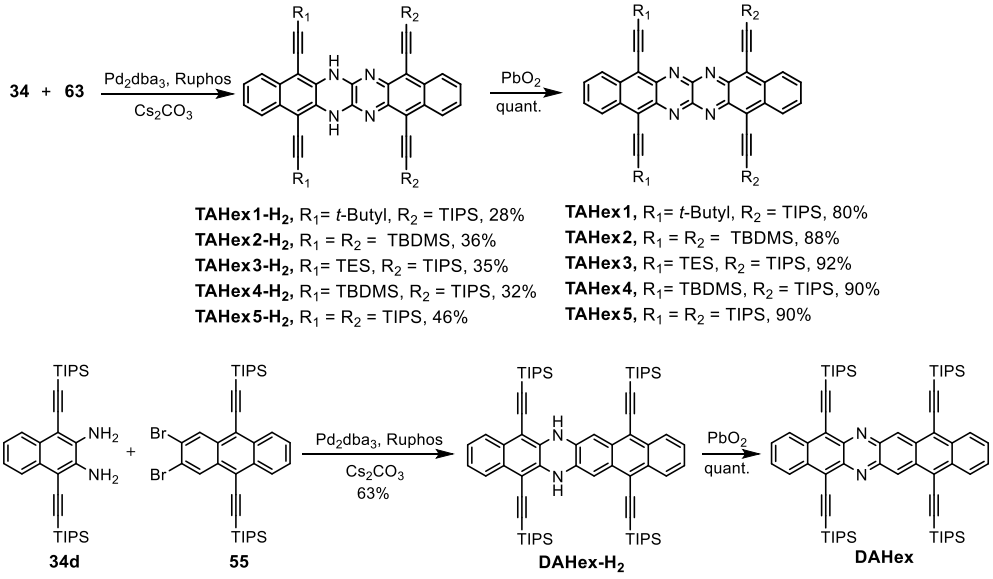

Scheme 20. Synthesis of the tetraazahexacenes **TAHex 1-5** and diazahexacenes **DAHex**.

Tetraazapentacene **65** and tetraazaheptacene **66** were synthesized via a similar procedure from **TAHex** (Scheme 21). Buchwald-Hartwig Pd-catalyzed coupling of dichloro **63d** and diamino-benzene **64**[146] or diamino- anthracene **23a**[95] furnished *N,N'*-dihydro-precursors **65-H₂** and **66-H₂**, which were oxidized with PbO_2 into **65** and **66** in satisfactory yields (90% for **65** and 76% for **66**).

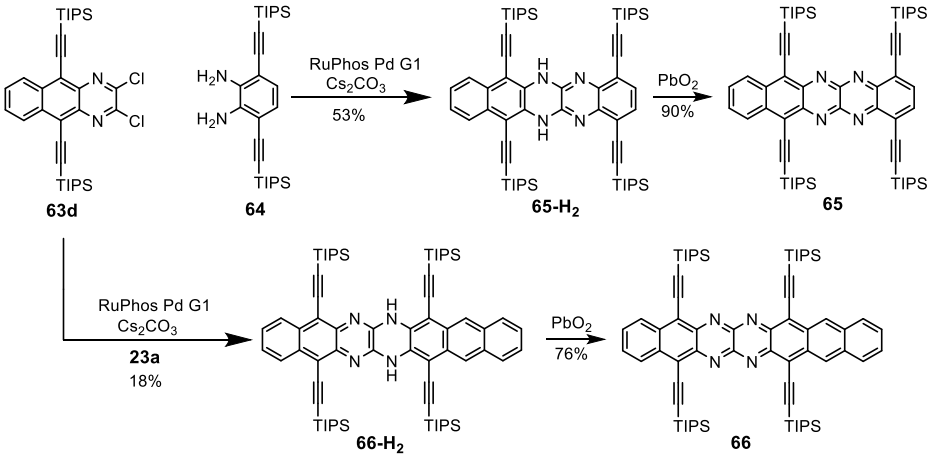

Scheme 21. Synthesis of the tetraazapentacene **65** and tetraazaheptacene **66**.

The mono- and dianion of **TAHex5** were synthesized by reduction with KC_8-(18-crown-6) in THF (Scheme 22). Treatment with one equivalent reductant furnished a dark yellow solution of monoanion **TAHex5**$^{\bullet-}$. Upon further reduction, a dark red solution was obtained for the dianion **TAHex5**$^{2-}$. Crystals of **TAHex5**$^{\bullet-}$ were grown by slow diffusion of pentane into a THF solution of **TAHex5**$^{\bullet-}$ in a nitrogen-filled glovebox at 5°C.

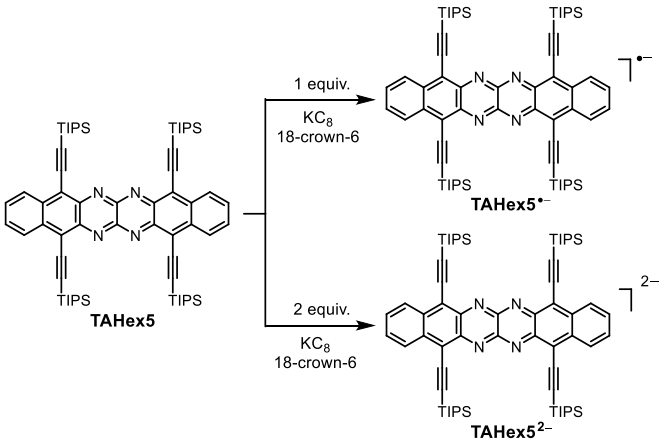

Scheme 22. Preparation of the radical anion and dianion of **TAHex5**.

4.3 Results and Discussion

Solvate-free, single crystalline specimen of **TAHex1**, **2**, **5** were grown by slow diffusion of methanol into their chloroform solutions (Figure 45). Surprisingly, the constitution of **TAHex1**, **2**, **5** obtained from X-ray crystallographic analysis depended on the alkynyl substituents as well as temperature during analysis and the space groups of the polymorphs. **TAHex1** (brick wall, 200 K, space group $P\bar{1}$) displays the expected acene backbone, similar to our previously reported bis-TIPS-ethynylated tetraazahexacenes.[147] The bis-TIPS-ethynylated derivative **TAHex5** packs in a modified edge-to-face motif and crystallizes as a cyclodecatetraene biscarbodiimid (**BCD**) backbone (200 K, acene:carbobisimide 98%:2%, C2/c). At 293 K, the crystal of **TAHex5** exhibited a ratio of acene:carbobisimide of 12%:88%. In the crystal structure of the TBDMS substituted congener (C2/c) acene and carbodiimide structures are superimposed at 200 K – in two crystalline specimen, the ratio was estimated as 36%:64% or 65%:35% (averaged as 50%:50%, **TAHex2** : **BCD2**). The latter single crystal contained only the tetraazahexacene isomer at 293 K. When crystals of **TAHex2** were grown from DCM/MeOH rather than $CHCl_3$/MeOH, two different polymorphs were obtained with either DCM (space group $P\bar{1}$) or MeOH (space group $P2_1/c$) as solvates containing solely **TAHex2**. The crystal structure of **TAHex3** also showed a mixture of acene/carbobisimide with an approx. 1:2 ratio, but a crystal model could not be established due to the disorder of the different silyl groups.

To conclude, the isomerization reaction occurs for tetraazahexacenes (**TAHex**), if they pack in the C2/c space group. Larger alkynyl substituents shift the ratio to a higher content of the open tetraazacyclodecahexaene while increasing the temperature favors the azaacene form. In contrast, X-ray crystallography of **DAHex** revealed an azaacene packing in a C2/c space group (Figure 45) with disordered silylethynyl substituents due to the symmetry of the crystal, but the ten-membered didehydrodiazecine form is absent, which proves isomerization behavior is unique to tetraazahexacenes (*vide infra*).

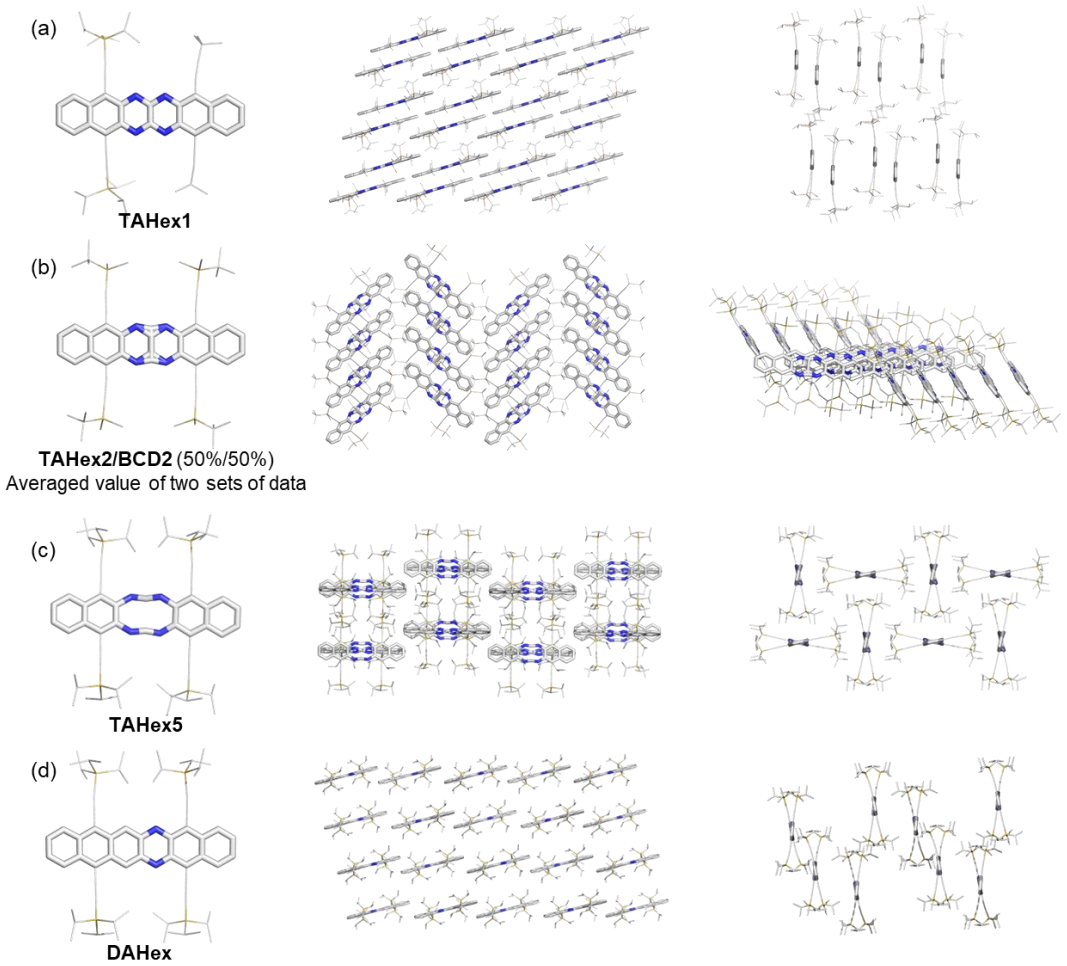

Figure 45. X-ray crystallographic structures obtained for tetraazahexacenes/biscyclodiimides **TAHex1, 2**, **5** and diazahexacene **DAHex** measured at 200 K. Hydrogen atoms were omitted and TIPS-ethynyl substituents were reduced in size for clarity.

Table 9. Crystal parameters measured at 200 K and at room temperature for tetraazahexacenes/ biscyclodiimides **TAHex1, 2, 5** and diazahexacene **DAHex**.

Group	compd.	temp. (K)	Z	space group	ratio of acene/ carbobisimide	crystallization method	solvate
1	**TAHex1**	200	2	$P\bar{1}$	100% / 0	$CHCl_3$/MeOH	–
2	**TAHex2**	200	4	C2/c	36% / 64%	$CHCl_3$/MeOH	–
	TAHex2	200	4	C2/c	65% / 35%	$CHCl_3$/MeOH	–
	TAHex2	293	4	C2/c	100% / 0	$CHCl_3$/MeOH	–
3	**TAHex2**	200	1	$P\bar{1}$	100% / 0	DCM/MeOH	DCM
	TAHex2	299	1	$P\bar{1}$	100% / 0	DCM/MeOH	DCM
	TAHex2	200	4	$P2_1/c$	100% / 0	DCM/MeOH	MeOH
4	**TAHex5**	200	8	C2/c	2% / 98%	$CHCl_3$/MeOH	–
	TAHex5	293	8	C2/c	12% / 88%	$CHCl_3$/MeOH	–
5	**DAHex**	200	8	C2/c	100% / 0	$CHCl_3$/MeOH	–

Figure 46 shows a comparison of the ^{1}H NMR spectra of tetraazahexacenes **TAHex2** and **TAHex5** in CD_2Cl_2 measured at 295 K and 205 K. The aromatic chemical shifts of two compounds, at both 295K and 200K, are almost identical, indicating that only one component, i.e., only acene is present in solution.

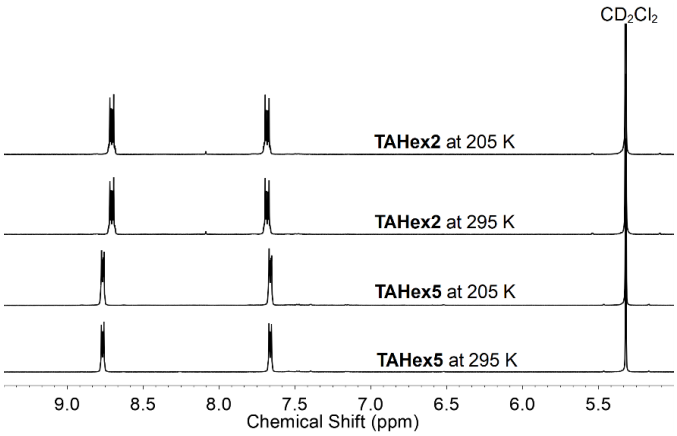

Figure 46. A comparison of ^{1}H NMR spectra of **TAHex2** and **TAHex5** in CD_2Cl_2 measured at 205 K and 295 K magnifying all signals in the aromatic region.

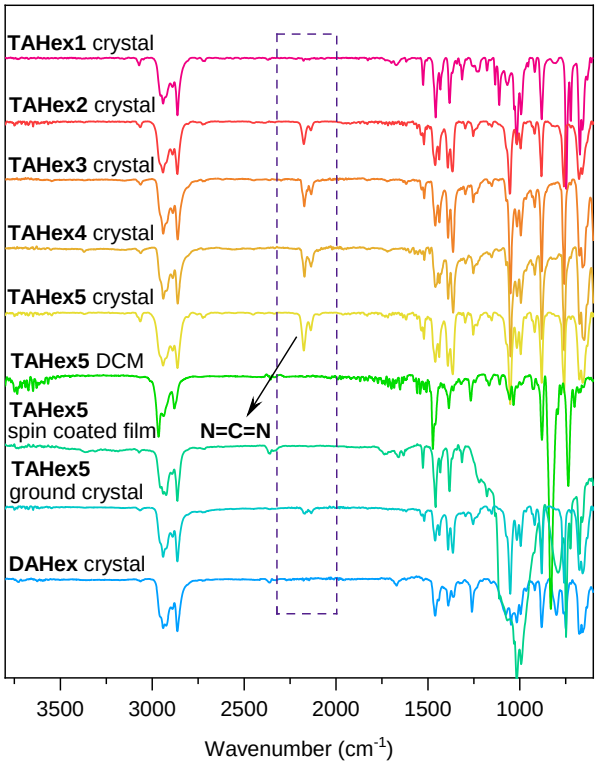

Figure 47. IR spectra of **TAHex1-5** and **DAHex** in the solvate-free, crystalline state and **TAHex5** in different states: in DCM (20 mg mL^{-1}); in spin-coated film (spin-coating the 20 mg mL^{-1} chloroform solution of **TAHex5** onto quartz slide at 600 r/min); and in the ground crystals (grinding the single crystal of **TAHex5** in a mortar for 1 min).

In the crystalline state, the IR of **TAHex5** shows a sharp N=C=N stretching peak around 2174 cm^{-1} in the IR, confirming the existence of a cyclic double carbodiimide. This peak, albeit in weaker intensity, was observed in the IR spectra (Figure 47) of solvate-free single crystals of **TAHex2-4**, as **TAHex2-4** and **BCD2-4** coexist. **TAHex1** does not display any absorption in this area, consistent with the X-ray crystallographic results. Contrasting the IR spectra of crystalline **TAHex5**, the IR spectra in solution and in spin-coated films (amorphous state) reveal the absence of the N=C=N stretching vibration, direct evidence for the transition from acene-form in solution to the carbodiimide in the crystalline state. After grinding crystals of **TAHex5**, the intensity of the N=C=N peak decreased, due to tribological destruction of the crystalline order (Figure 47). As expected, IR spectrum of **DAHex**'s crystal display the absence of N=C=N peaks, consistent with the X-ray crystallographic result.

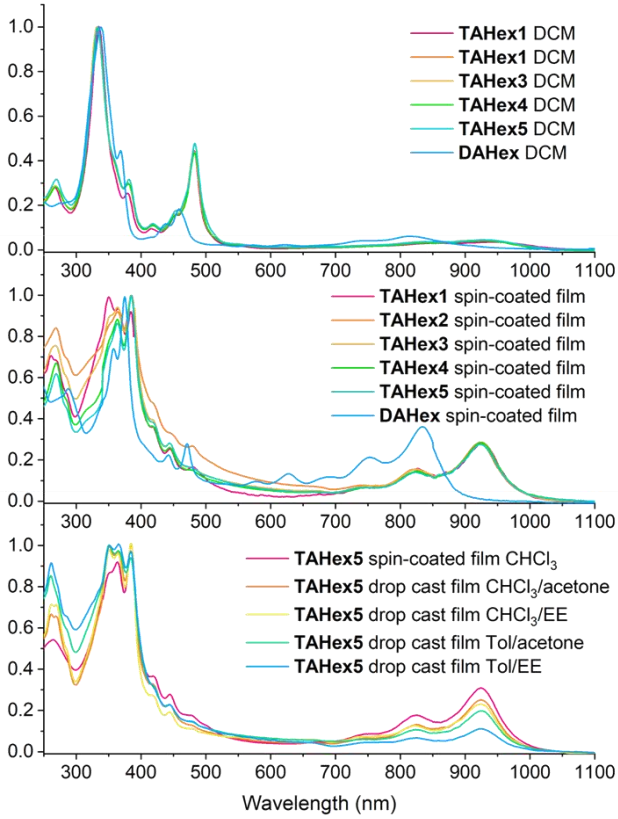

Figure 48. UV-Vis absorption spectra of **TAHex1-5** and **DAHex** in DCM (10^{-5} mol L^{-1}) (top) and in spin-coated films (middle) and **TAHex5** in drop cast films fabricated from different process (bottom). Sample preparation: spin-coated films were prepared by spin-coating the solution of **TAHex5** in chloroform (20 mg/mL) onto quartz at 600 r/min; drop cast films were prepared by drop casting **TAHex5** in different combinations of good solvents and anti-solvents (0.6 mg mL^{-1}, solvent/anti-solvent = 1:1) onto quartz.

The UV-Vis absorption spectra of **TAHex1-5** in dilute DCM solution and in spin-coated films are similar (Figure 48) – the p-bands at around 925 nm indicate that the acene structure is prevalent in solution and in the amorphous state. In comparison with the absorption in dilute solution, spin-coated films show an increased p-band intensity, obscuring absorption bands (if any) of the carbodiimide structure (**TAHex5**). **DAHex** displays blue-shifted p-bands at around 830 nm in DCM, and also an increased p-bands in spin-coated film.

A series of drop-cast films of **TAHex5** were prepared from different solvent combinations. They are inhomogeneous with crystalline and amorphous regions. Although the p-band at 925 nm does not disappear entirely, an optimized drop-casting procedure (from toluene/ethyl acetate) leads to a crystalline film, in which the p-band intensity (normalized) is 1/3 of that observed in spin-coated films (Figure 48).

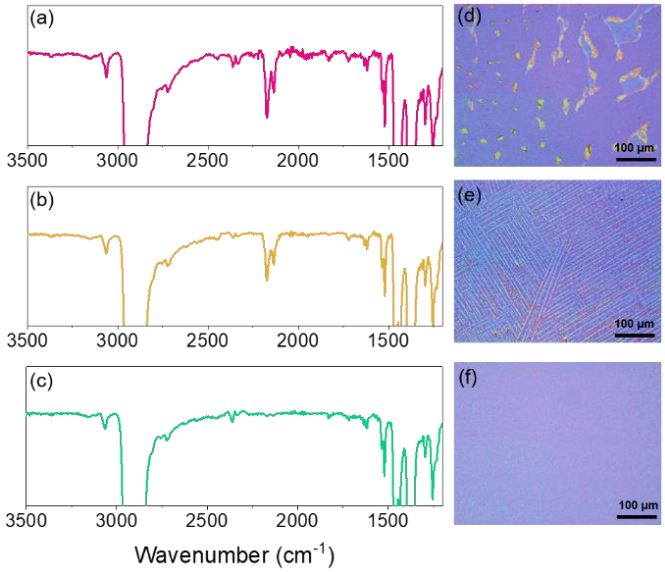

Figure 49. Left: IR spectra of **TAHex5** measured in different regions from a drop-cast film: (a) in inhomogeneous region, (b) in a crystalline region and (c) in an amorphous region. Right: micrographs under polarized light for different regions in the drop-cast film of **TAHex5**. (d) Inhomogeneous region, (e) crystalline region and (f) amorphous region.

As shown in Figure 49 d-f, micrographs of drop cast films of **THAex5** display different states (inhomogeneous, crystalline and amorphous regions). IR spectra were measured at different regions of these films (Figure 49a-c). Inhomogeneous and crystalline regions include or are composed of the carbodiimide isomer **BCD**; the amorphous regions consist of pure **TAHex5**.

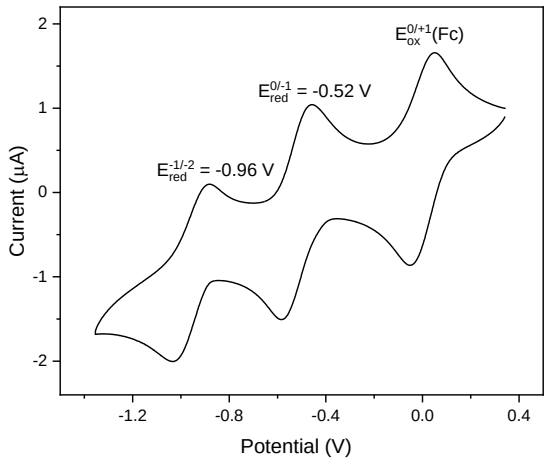

Figure 50. Cyclic voltammograms of **TAHex5** in DCM (Fc/Fc^+ as reference, Pt as working electrode and Bu_4NPF_6 as electrolyte).

Cyclic voltammetry (Figure 50) displays two oxidation waves and two reduction waves for **TAHex5** (EA = -4.28 eV), suggesting that their radical anions might be stable in air (*vide infra*). The LUMO of **TAHex5** are evenly distributed over the molecular skeleton, while its HOMO has small coefficients at the N atoms (Figure 51). The comparison of the experimental/theoretical optical gap as well as electron affinity (EA)/LUMO energy (Table 10) of the pair **TAHex5** / **BCD** is further proof that the azaacene re-forms upon dissolution.

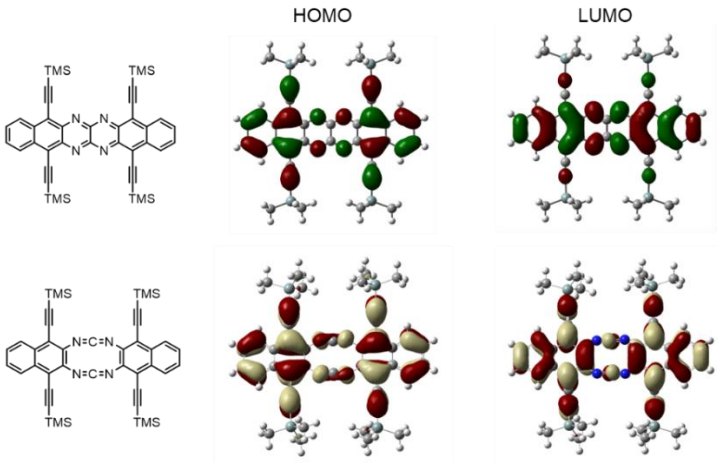

Figure 51. FMO distribution of **TAHex5'** and **BCD**. TMS groups were used instead of TIPS groups to simplify calculations.

Table 10. Photophysical and calculated properties of **TAHex5**, **TAHex5'** and **BCD'**.

Compd.	λ_{on} [c] [nm]	E_{gap} [d] [eV]	EA [e] [eV]	E_{LUMO} [f] [eV]
TAHex5 exp. [a]	1050	1.18	-4.28	—
TAHex5' cal. [b]	1200	1.03	—	-4.05
BCD' cal. [b]	420	3.33	—	-2.37

[a] UV-Vis and CV spectra measured in DCM; [b] TMS was used for calculation instead of TIPS; [c] onset of the lowest energy absorption maxima in DCM; [d] optical gap calculated by λ_{on} for **TAHex5**, or HOMO LUMO gap calculated by DFT calculation[125] for **TAHex5'** and **BCD'**; [e] electron affinity estimated from first reduction potentials of CV curve, EA = − 4.80 eV − E_{red};[126] [f] LUMO values calculated by DFT calculation (Gaussian16 B3LYP, def2TZVP).

To understand the selective ring opening for the three compounds, Marco Bauer from AK Dreuw helped us investigated the easiest and most straightforward computational ansatz for the ring opening mechanism, which is the bond dissociation of the central C atoms. The results are shown in Figure 52. Focusing on compound **TAHex5**, we found two minima on the potential energy surface (PES) in DCM as well as in the crystal environment. The thermodynamic minimum in DCM is compound **TAHex5**, while in the crystal environment we observe the minimum for biscarbodiimide **BCD5**. To obtain quantitative data without further refining the grid, a cubic spline fit was chosen here, due to the unknown functional behavior. Since the cubic spline minimizes the curvature, we can obtain a loose upper bound for the barriers, which is important to assess kinetic stabilities.

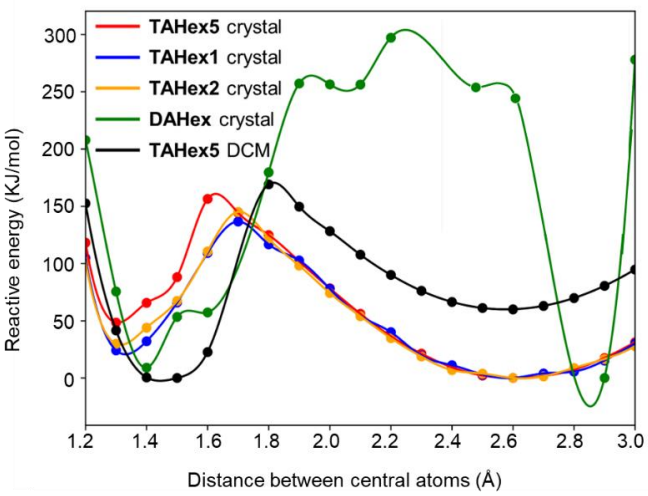

Figure 52. Relative energies of **TAHex1**, **2**, **5** and **DAHex** in solution and crystal environments are shown against the distance between the central carbon atoms. A cubic spline for each scan is shown as well. For clarification the data point providing the lowest energy has been set to 0 in each scan.

The spline computes the energy difference between compounds **TAHex5** and **BCD5** to 62 kJ/mol in DCM in favor of **TAHex5** and 48 kJ/mol in the crystal environment in favor of **BCD5**. The reaction barriers from **TAHex5** to **BCD5** in DCM and the crystal environment are 173 kJ/mol and 112 kJ/mol, while for the inverse reaction we obtain barriers of 111 kJ/mol and 161 kJ/mol, respectively. These barriers can be put in perspective using activated complex theory, which results in a half life time of roughly a day for a barrier of 105 kJ/mol at room temperature. Note that we approximate the proportionality factor with one and the standard free Gibbs energy with the relative energy, due to the similar structures of reactant and product. Considering that the cubic spline fit yields a loose upper bound to the barriers as well as methodological approximations, e.g. how the crystal environment was modeled, which are also likely to yield relative errors on the scale of a few kJ/mol, **TAHex5** is kinetically unstable in the crystal environment and thermodynamically stable in DCM. Comparing compound **TAHex1** to **TAHex5** in the crystal environment, we obtain a slightly higher barrier for compound **TAHex1** of 116 kJ/mol. Applying activated complex theory with the previously introduced approximations yields an increase of almost an order of magnitude to the half-life time (from a couple of days for compound **TAHex5** to months for compound **TAHex1**), emphasizing the impact of a minor increase of the barrier on the kinetic stability of the “closed” acenes. Taking the previously mentioned error bar for this value into account, the theoretical result for compound **TAHex1** suggests a kinetically stable crystal. Compound **DAHex** also shows a minimum for the ten-membered ring structure, which is actually energetically favorable over closo- **DAHex**, but the barrier is around 300 kJ/mol. Hence, compound **DAHex** is kinetically stable in the crystal environment up to very high temperatures. Comparing compound **TAHex2** to compound **TAHex1**, we obtain almost the same characteristics, namely an energy difference of 29 kJ/mol in favor of the open structure and a barrier of 116 kJ/mol. This however does not reproduce the experimental results of a mixed system. In order to reproduce this via a Boltzmann distribution at room temperature an energy difference of roughly 2 kJ/mol in favor of the open structure is required, which is almost 30 kJ/mol off from the calculated energy difference.

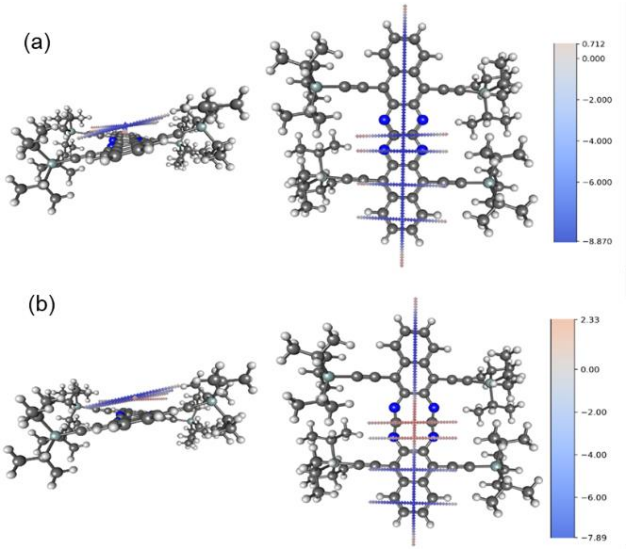

Figure 53. NICS(1.7)$_{zz}$-xy scans for (a) **TAHex5** and (d) **BCD5** in the crystal environment.

Two factors contribute in addition to the lowering of the reaction barrier within the crystal field to drive the formal electrocyclic ring opening: (i) Upon cleavage of the central bond, two Clar sextets are generated in the naphthalene termini at the expense of the intact acene backbone. This is reminiscent of the diradical forms of the larger acenes with the two spins residing on the central rings, generating two subsets of smaller acene fragments, each with their own Clar sextet. In **BCD5**, the central ten-membered ring with NICS (1.7) values of 2.33 ppm is non aromatic, but the aromatic naphtylene substituents display NICS values up to −7.89 ppm. In contrast, **TAHex5** the central pyrazines are aromatic with NICS values up to -8.87 ppm (Figure 53). (ii) The close proximity of the silyl substituents plus the crystal packing energy accommodates the ten-membered rings in the crystal lattice.

To investigate whether the acene or the didehydrotetrazecine structure prevails in the reduced state, the mono- and dianion of **TAHex5** were synthesized by reduction with KC_8-(18-crown-6) in THF. As expected, absorption in THF red-shifted upon reduction to 1600 nm (Figure 54a). Solutions of **TAHex5**$^{\bullet-}$ are persistent over 48 h in the dark while exposed to air (Figure 54b). Upon further reduction, a blue-shifted absorption was observed for the dianion **TAHex5**$^{2-}$ at λ_{max} = 685 nm. Absorption spectra support the presence of the intact acene backbone in solution in either case.

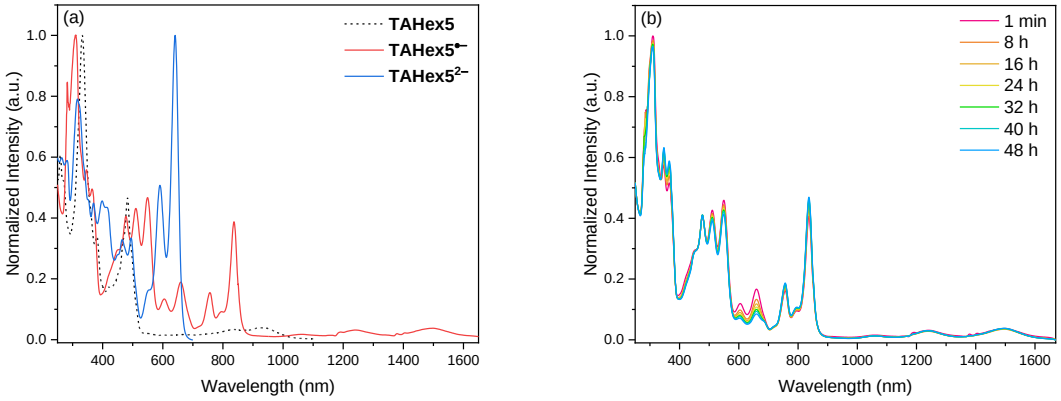

Figure 54. (a) UV-Vis absorption spectra of **TAHex5** in its neutral (black dotted), mono- (red solid) and dianionic form (blue solid) in THF solutions and (b) time-dependent evolution of UV-Vis spectra of **TAHex5**$^{\bullet-}$ (10^{-5} mol L^{-1} in dry THF) under ambient light and atmosphere.

Crystals of **TAHex5**$^{\bullet-}$ were grown by slow diffusion of pentane into a THF solution of **TAHex5**$^{\bullet-}$ in a nitrogen-filled glovebox at 5°C. As a result, only the acene form was found in a 2D packing arrays (Figure 55) of the radical anions. It may be due to the electronic structure of the radical anion or an effect of co-crystallized 18-crown-6.

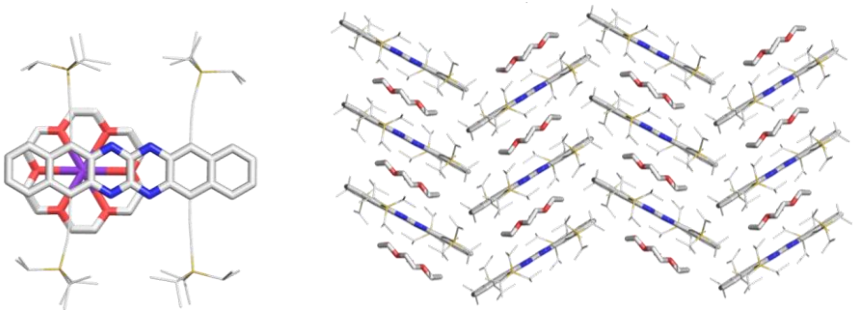

Figure 55. Crystal structure (left) and packing motif (right) of **TAHex5**$^{\bullet-}$. Hydrogen atoms were omitted and TIPS-ethynyl substituents were reduced in size for clarity.

The kinetics of this rearrangement were investigated by monitoring the dissolution of a single crystal of **TAHex5** in dichloromethane at room temperature via UV-Vis spectroscopy. As shown Figure 56, during the dissolution process, only bands of tetraazahexacenes were observable without a trace of signals of biscarbodiimide, which means the kinetics of this rearrangement are fast.

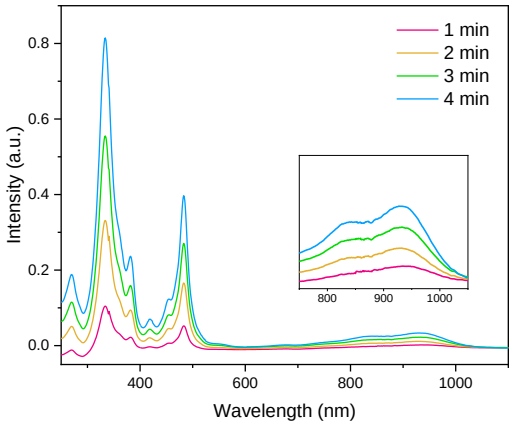

Figure 56. Time-dependent UV-Vis absorption spectra by monitoring the dissolution of a single crystal of **TAHex5** in dichloromethane at room temperature.

Single crystalline specimen of **65** and **66** were grown by slow diffusion of methanol into their chloroform solutions (Figure 57). Both of **65** and **66** showed similar crystallization behavior as their hexacene congener **TAHex5** – pack in a modified edge-to-face motif without π-π interactions. Tetraazapentacene **65** and tetraazaheptacene **66** also have the ring opening tendency from pyrazinopyrazine to biscarbodiimide cycloisomer, but with a different equilibrium constant.

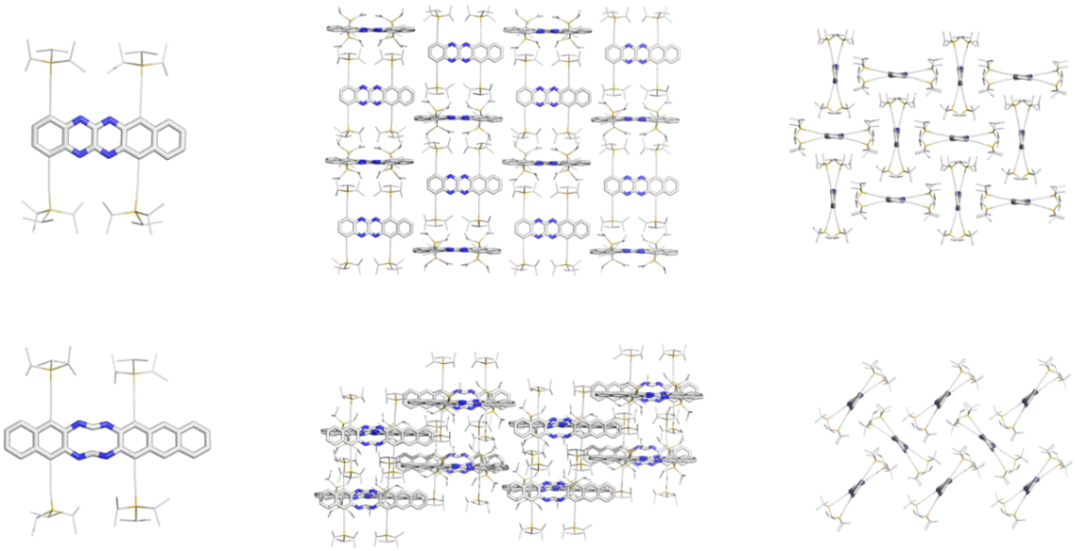

Figure 57. X-ray crystallographic structures obtained for **65** (top) and **66** (bottom) in the solid state. Hydrogen atoms were omitted and TIPS-ethynyl substituents were reduced in size for clarity.

As shown in Scheme 23, **65** displays acene structure in the single crystal as the main form (>80%), while crystal of **66** displays biscarbodiimide as the main form (≈65%). Measuring the single crystals of **65** at a low temperature (180 K) instead of room temperature (295 K) did not allow any robust conclusion about the change in ratio of the pentacene vs. the biscarbodiimide form (85%/15% at 180 K vs. 89%/11% at 295 K), as the margin of error is about 5%.

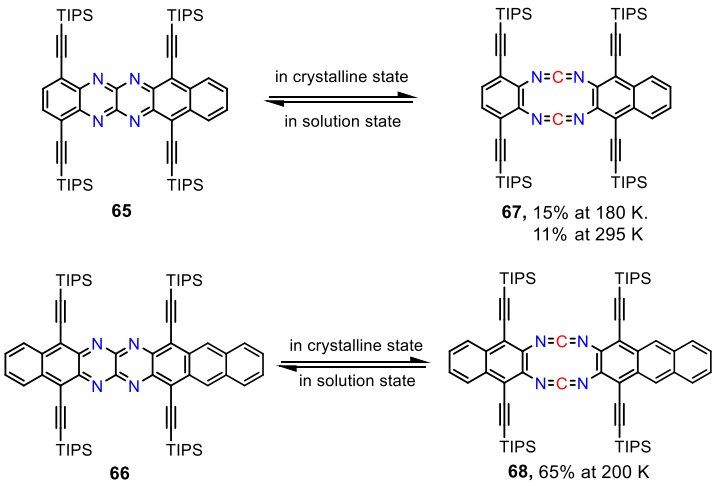

Scheme 23. Reversible transition for pyrazinopyrazine / biscarbodiimide structures for **65** and **66** between solution sate and crystalline state.

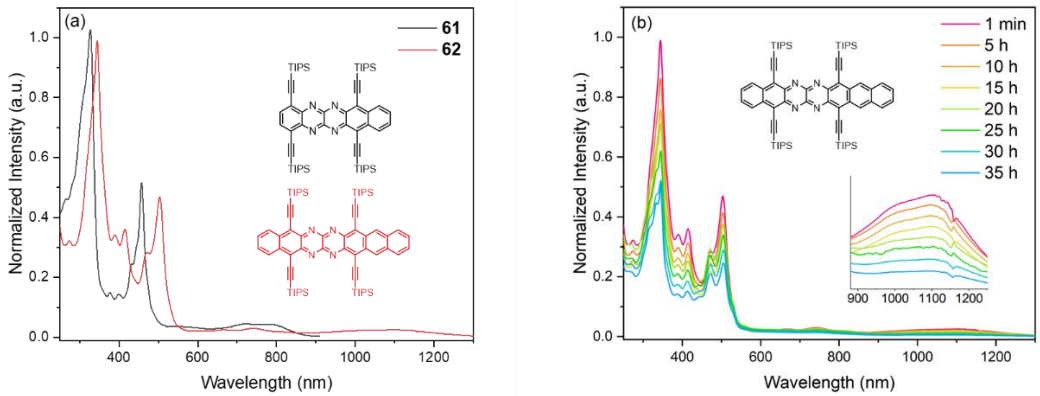

Figure 58. (a) Normalized UV-Vis absorption spectra of **65** and **66**; and (b) time-dependent evolution of UV-Vis spectra of **66** in DCM (10^{-5} mol L^{-1}) under ambient light and atmosphere. The inset shows magnification of the time-dependent evolution of the p-bands.

As expected, the UV-Vis spectra prove that both **65** and **66** are acenes in solution (Figure 58a), i.e., consistent with **TAHex5**. The stability of tetraazaheptacene **66**, an isomer of **TAH** (see chapter 3), was evaluated by UV-Vis using the same procedure as **TAH** depicted in chapter 3.

As shown in Figure 58b, the stability of **66** is dramatically decreased but it is still reasonably persistent with a $\tau_{1/2}$ = 20 h. The spontaneous reduction to its *N,N'*-dihydro precursor **66-H₂** is the main degradation pathway. The position of the TIPS-ethynyl groups and N atoms determine their stability – silylethynyl groups adjacent to the central pyrazine ring (**TAH**, chapter 3) protect the azacenes core more effectively.

4.4 Conlusion

In this chapter, we describe the spontaneous, reversible rearrangement by crystallization/ dissolution, which is to our knowledge unprecedented for the larger (aza)acenes. By a combination of spectroscopic methods and quantum-chemical calculations, we show that isomerization from tetraazahexacenes (**TAHex**), found in solution and in amorphous films, to the 10-membered biscarbodiimide cycloisomer (**BCD**) in the crystalline state, is dependent upon steric bulk alkyl substituents by lowering the barrier for the formal electrocyclic ring opening within the crystal lattice. This solid-state ring opening is therefore enforced by the bulk of the substituents, crystal packing energy and aromaticity given in terms of Clar sextets – with increasing steric bulk the crystal lattice itself enforces ring opening. This process is fully reversible, as upon dissolution the acene re-forms. This behavior also contrasts that of the previously reported photoisomerization of tetracyanotetraazanaphthalene, which reversibly forms it tetrazecine form upon UV irradiation in argon or xenon matrices.[148] If this isomerism could be exploited, it could be a route to access the larger (aza)acenes: In the solid state, the 10-membered ring isomers could serve as a reservoir to store these sensitive compounds – upon dissolution the acene backbones are regenerated allowing to study the properties of the larger, hitherto inaccessible (aza)acenes. Additionally, this method should also allow the synthesis of cyclic biscarbodiimide, which could be simply obtained by rearrangement of acenes.

Chapter 5. Summary and Outlook

In chapter 2 we have demonstrated a synthetic route to six phenazinothiadiazoles substituted with different patterns of halogen atoms (Figure 59). Compared to literature known compounds **39-H$_4$**, **39-Cl$_4$** and **39-F$_4$**,[110] three of the four derivatives with mixed halides gave the best carrier mobilities (μ_{ave}(**39-Br$_2$Cl$_2$**) = 0.47 cm^{2}V^{-1} s^{-1}, μ_{ave}(**39-Cl$_2$Br$_2$**) = 0.38 cm^{2}V^{-1} s^{-1}, μ_{ave}(**39-Br$_2$I$_2$**) = 0.39 cm^{2}V^{-1} s^{-1}). The lowest carrier mobility was determined for **39-Br$_4$** with μ_{ave} = 0.08 cm^{2}V^{-1} s^{-1}. The quality of the semiconductor films dominates the resulting mobilities – the film quality correlates with the solubility of the materials which decreases with higher atomic weight of the halides and increases for mixed substitution patterns.

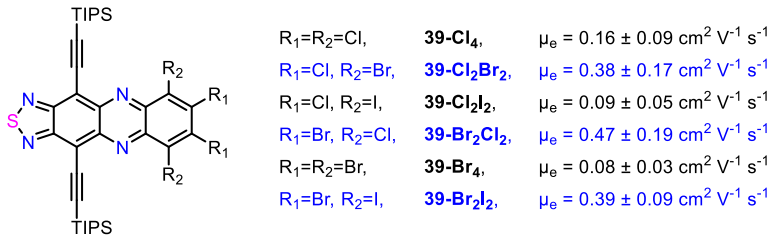

Figure 59. Chemical structures and transistor mobilities of tetrahalogenated phenazinothiadiazoles **39**.

6,13-Bis((triisopropylsilyl)ethynyl) tetraazapentacene **TIPS-TAP**[49] and diazapentacene **TIPS-DAP**[80] are promising benchmark n-channel semiconductors. The symmetric tetrahalogenated derivatives of **TIPS-TAP, TAP-Cl$_4$**,[88] **TAP-Br$_4$**[89] and **TAP-I$_4$**[90] exhibit significantly improved electron mobilities (average mobility of **TAP-Cl$_4$** up to 14.9 cm^{2}V^{-1} s^{-1}), but the octahalogenated- and the asymmetric tetrahalogenated- derivatives are currently unknown. Regarding the effect of different halogenation patterns on the performance of phenazinothiadiazoles, it is of interest to explore the halogenation effect on the **TIPS-TAP** and **TIPS-DAP** derivatives, especially with mixed halide substituents. The synthesis of tetrahalo-*ortho*-quinones **49** (chapter 2, Scheme 10) and dibromodiiodo- **TIPS-TAP** and -**TIPS-DAP** derivatives (chapter 3, Scheme 16) are described above, so **69** should be should be synthetically achievable (Scheme 24). The synthesis of octahalogenated- tetraazapentacene **71** exploits **39** as starting materials. Reduction with SmI_2 should give the diamino- **70**, followed by condensation reaction with *o*-quinones **49** to furnish **71**.

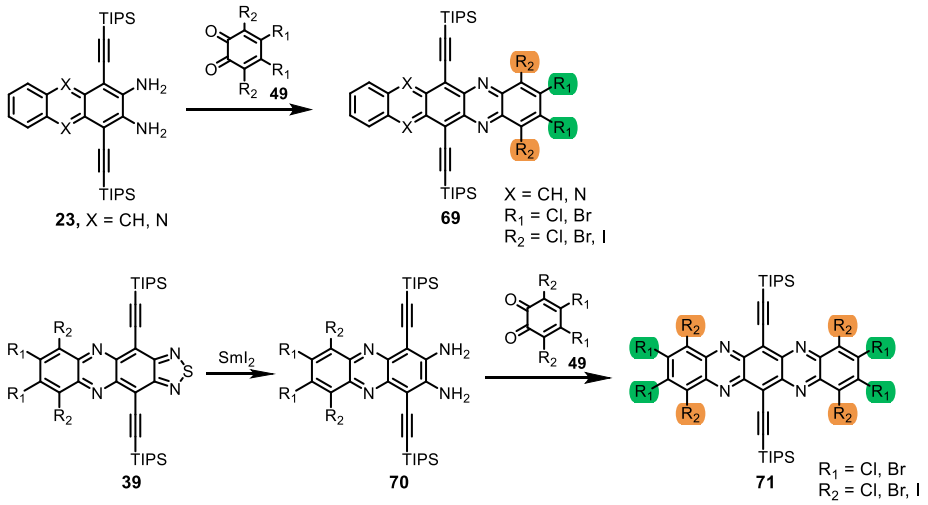

Scheme 24. Proposed synthetic route to target tetrahalogenated azapentacenes **69** and octahalogenated azapentacenes **71**.

In chapter 3, we investigated the stability of several (aza)heptacenes containing 0, 2, 4, 6 nitrogen atoms and varied the placement of the four TIPS-ethynyl substituents - soluble and processible di- and tetraazaheptacenes and a marginally stable hexaazaheptacene resulted (Figure 60). The diazaheptacene **DAH1**, in which the two nitrogen atoms occupy the central ring and the four TIPS-ethynyl substituents fill the four positions on the two directly adjacent rings is by all definitions stable as solid and in solution, and that much more than any hitherto reported (aza)heptacene. It survives several weeks in dilute solution on the benchtop according to UV-Vis studies. The position of the TIPS-ethynyl groups determines the azaheptacene's stability. A tetraazaheptacene **TAH** is also reasonably stable. We also prepared a hexaazaheptacene **HAH** which is such a strong oxidant that it undergoes spontaneous reduction. Two to four nitrogen atoms in azaheptacenes strike a proper balance between oxidative stabilization and resistance towards reduction. Removing the two nitrogen atoms from **DAH1** results in **Hep**, which is still relatively stable but decomposes in a matter of days in solution; this dramatic difference in stability demonstrates the importance of the two nitrogen atoms to stabilize the heptacene backbone. **DAH1** and **TAH** are promising n-type semiconductors (the best mobility of **DAH1** amounted up to 0.042 cm^2V^{-1} s^{-1}) according to the calculated mobilities – we will further explore their application in thin-film transistors in the future.

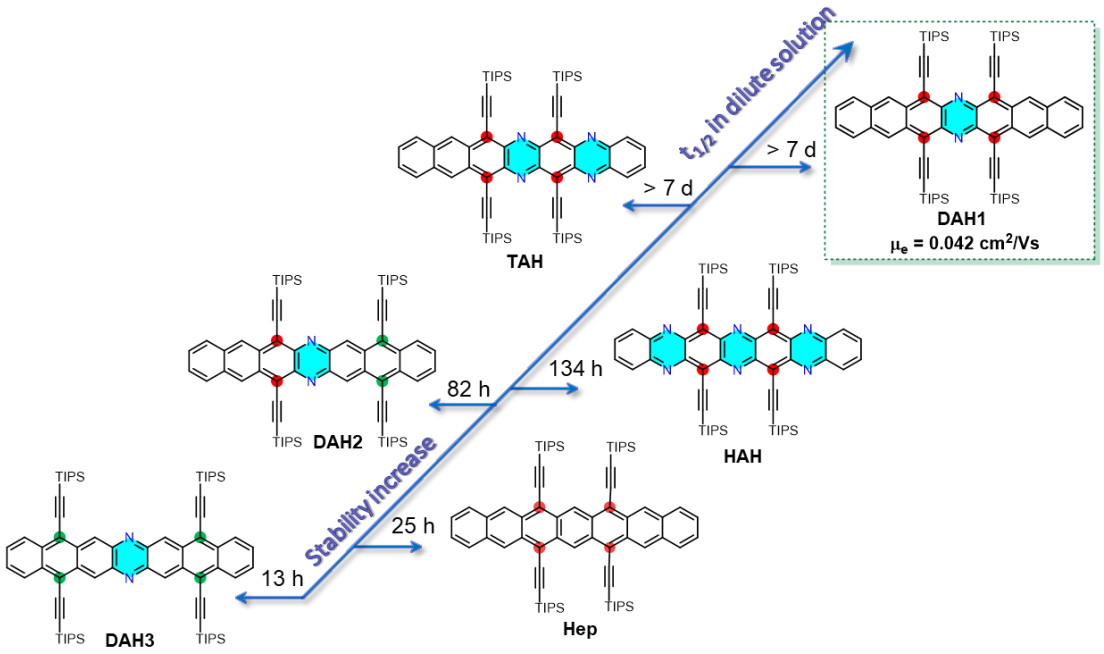

Figure 60. Stability ranking of the (aza)heptacenes described in chapter 3.

In chapter 3, we also developed a regioselective Pd-catalyzed functionalization of tetrahalo-azapentacenes as intermediates to azaheptacenes. However, it did not escape our attention that this route should grant access to azaoctacenes and azanonacenes and beyond. It is a modular synthetic tool set, we expect azaacenes to reach and exceed the size of the largest acene derivatives reported today.

The dibromides **59** are ideal precursors to azaoctacenes and azanonacenes, if they are coupled to diamino-naphthalenes **34** and -anthracenes **23** (Scheme 25). An alternative route is to transform dibromides **59** to diamines **74** by Müllen's[112] method – **59** should couple with benzophenone imine using $Pb_2(dba)_3$ as catalyst and *rac*-BINAP as ligand to give diphenylmethaneiminesubstituted intermediates, diamino-substituted **74** should be obtained after hydrolysis. **74** could also serve as a useful coupling partner for azaoctacenes **72** and azanonacenes **73** via Buchwald-Hartwig Pd-catalyzed coupling followed by oxidation. Hexaaza- and octaazaacenes should be strong oxidants, which will be difficult to oxidize but retain great interest with respect to their radical anions.

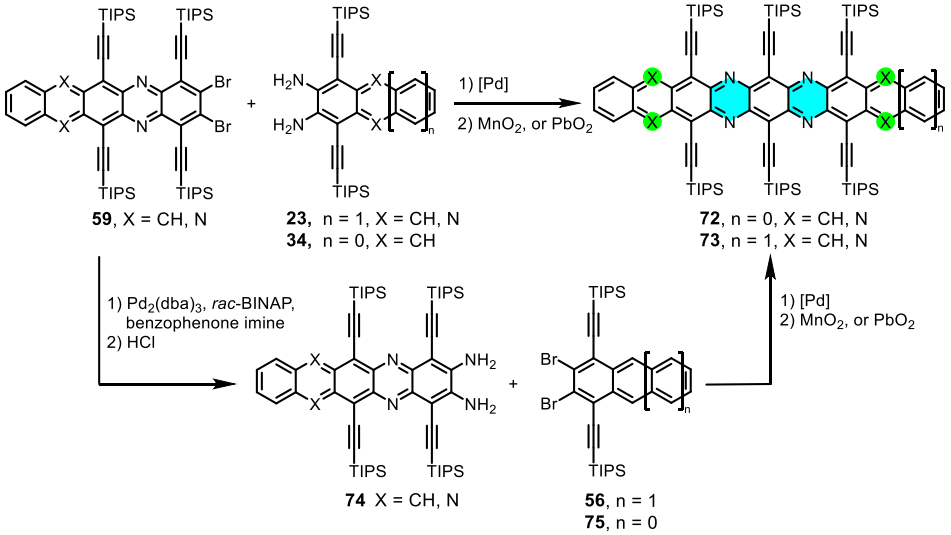

Scheme 25. Proposed synthetic route to target azaoctacenes **72** and azanonacenes **73**.

In chapte 4, we explored a new type of crystallization-induced reaction of substituted tetraaza-pentacenes, hexacenes and heptacenes. **65**, **TAHex2-5** and **66** (Scheme 26) equilibrate with their didehydrotetrazecine isomers (10-membered biscarbodiimde form) in the solid state, but remain acenes in solution and also in the amorphous solid state. This solid-state ring opening is enforced by aromaticity given in terms of Clar sextets and depends on the bulk of the substituents. With increasing steric bulk, the crystal packing energy enforces ring opening. This process is fully reversible, as upon dissolution, the acenes re-forms (Scheme 26). A spontaneous, reversible rearrangement by crystallization / dissolution was investigated, and may be utilized as a reservoir for the storage of long and sensitive pyrazinopyrazine-based acenes in the solid-state.

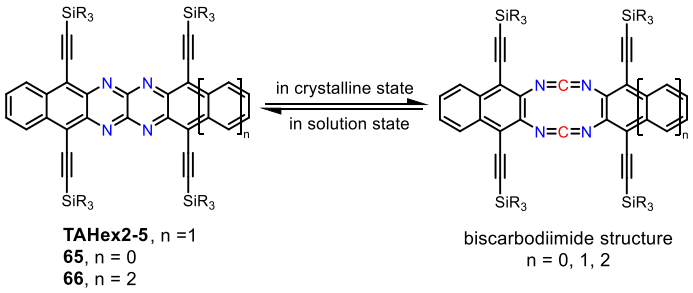

Scheme 26. Reversible transition between tetraazacenes and their biscarbodiimide isomers between solution sate and crystalline state.

This modular route may be utilized as a reservoir for the storage of long and sensitive pyrazinopyrazine-based acenes in the solid-state – dissolution allows the study of acenes' properties, which should grant access to hitherto inaccessible large (aza)acenes.

The synthesis of the didehydrotetrazecine isomer (**82**) of an octafluorotetraazaoctacene is depicted in Scheme 27, which might remain the 10-membered biscarbodiimde form in solid state and also in solution according to calculations. First, **76** combines with **77** in a Cava reaction into **78**, which is treated with suitable alkynyllithium reagents, and the corresponding diol intermediate is directly reduced by $SnCl_2$ to furnish anthraceno thiadiazole **79**. After reduction with lithium aluminum hydride the coupling partner **80** is obtained. Dichloro coupling partner **81** is synthesized by condensation reaction with diethyloxalate and underwent chlorination. Buchwald-Hartwig Pd-catalyzed coupling followed by oxidation should give dioctafluoroanthraceno didehydrotetrazecine **82**.

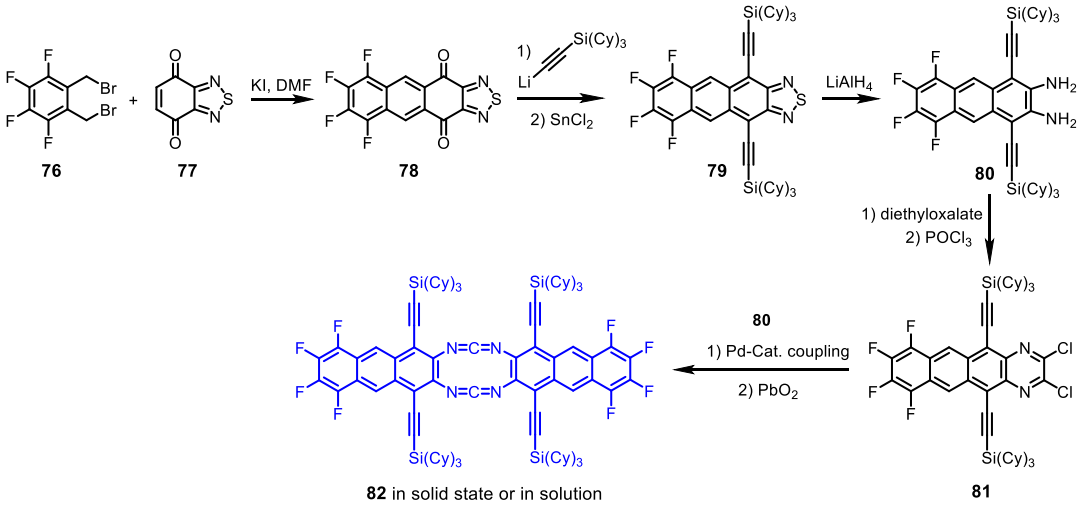

Scheme 27. Proposed synthetic route to dioctafluoroanthraceno didehydrotetrazecine **82**.

Chapter 6. Experimental Section

6.1 General Remarks

Chemicals were either purchased from the chemical store at the Organisch-Chemisches Institute of the University of Heidelberg or from commercial laboratory suppliers. Chemicals were purchased from Sigma-Aldrich, Abcr, TCI or Acros. Reagents were used without further purification unless otherwise noted.

Solvents were purchased from the store of the Theoretikum or chemical store at the Organisch-Chemisches Institute of the University of Heidelberg and distilled prior use if necessary. All of the other absolute solvents were dried by an MB SPS-800 using drying columns.

Flash column chromatography was carried out using neutral silica gel S (0.032 mm-0.062 mm), purchased from Sigma Aldrich. Basic aluminum oxide, ranging 70-290 mesh (50-200 μm), was purchased from Sigma Aldrich and applied to separate the target molecules when necessary. As noted, Celite 545 (Fluka) was used for filtration.

Thin layer chromatography (TLC) was performed on Macherey & Nagel Polygram® SIL G/UV254 pre-coated plastic sheets. Components were visualized by observation under UV light (254 nm or 365 nm).

Nuclear magnetic resonance (NMR) spectra were recorded at r.t. on the following spectrometers: Bruker Avance III 300 (300 MHz), Bruker Avance III 400 (400 MHz), Bruker Avance III 500 (500 MHz) or Bruker Avance III 600 (600 MHz). Chemical shifts (δ) are given in parts per million (ppm) relative to internal solvent signals.[149] Multiplicities are denoted at the centre of the signal as s (singlet), d (doublet), dd (doublet doublet), t (triplet), or m (multiplet).

High resolution mass spectra (HRMS) were obtained from electron impact (EI), electrospray ionization (ESI) or matrix-assisted laser desorption/ionization (MALDI) on a Bruker ApexQe hybrid 9.4 TFT-ICR-MS at the Organisch-Chemisches Institute of the University of Heidelberg.

Gas chromatography-mass spectrometry (**GCMS**) chromatograms were recorded using a HP 5890 Series II Plus model, coupled with a HP 5972 Mass Selective Detector. As the capillary column, a HP 1 Crosslinked Methyl Silicone (25 m x 0.2 mm x 0.33 μm) was employed, with helium as carrier gas. The acquired data were analyzed using ACD/Labs Spectrus Processor 2012.

Infrared spectroscopy (IR) were recorded from powder samples (chapters 2 and 3) on a JASCO FT/IR-4100 with the software JASCO Spectra Manage II, or recorded from crystals or neat films on a FT-IR spectrometer (Bruker LUMOS) with a Germanium ATR-crystal and from concentrated solutions on FT-IR spectrometer Bruker Vector 22 (chapters 4). For the most significant bands the wave numbers are given.

Melting points (m.p.) were determined in open glass capillaries with a melting point apparatus MELTEMP (Electrothermal, Rochford, UK).

UV-Vis absorption spectra were recorded on a JASCO UV-VIS V-660 or JASCO UV-VIS V-670 and processed with the software JASCO Spectra Manage II. ASCII-files were exported and visualized by Origin.

Cylic voltammetry (CV) measurements were performed on a VersaSTAT 3 potentiostat by Princeton Applied Research. Experiments were carried out using a gold or glass carbon working electrode, a platinum/titanium wire auxiliary electrode, a silver wire reference electrode, a 0.1 M NBu_4PF_6 solution in degassed DCM, and ferrocene/ferrocenium as the reference redox system and internal standard (−4.8 eV).[126]

Crystal structure analysis was performed on Bruker Smart CCD or Bruker APEX diffractometers with Mo Kα radiation source (0.71073 Å), under direction of Dr. F. Rominger. Intensities were corrected for Lorentz and polarization effects; an empirical absorption correction was applied using SADABS based on the Laue symmetry of the reciprocal space. All structures were solved by direct methods and refined against F^2 with a Full-matrix least-squares algorithm using the SHELXTL (Version 2008/4) software package.

Device fabrication substrate modification: A sliced, highly p-doped silicon wafer ($R < 0.005$

Ω) with 100 nm thick thermally grown SiO_2 was successively cleaned via ultra-sonication in acetone, isopropanol and ethanol, each for 10 min. It was washed with water and dried under a stream of nitrogen. The wafer was placed in freshly produced Caro´s acid and heated to 100 °C for 20 min. After cleaning with water and drying, a 150 mM solution of $Al(NO_3)_3 \times 9\ H_2O$ in ethanol was spin-coated (5000 rpm; 40 s) onto the substrate. Right after that the wafer was heated to 300 °C for 30 min. For the formation of the self-assembled monolayer, the substrate was placed in a 15.0 mM solution of 12-cyclohexyldodecylphosphonic acid (CDPA)[8] in isopropanol for 16 h. Then the substrate was cleaned by ultra-sonication in isopropanol for 10 min, rinsed with water and dried in a stream of nitrogen. The capacitance of the dielectric layer is 26.5 nF cm^{-2}.

Thin film fabrication: Drop-cast films were prepared by dropping the prepared solution onto the substrate with the pinner and covering the wafer against unwanted wind flows. To form the electrodes, a 40 nm thick layer of silver was deposited through a shadow mask onto the organic layer in a vacuum evaporator at a pressure below 2 x 10^{-6} bar. Transistor characteristics were measured with a semiconductor characterization system (Keithley 4200-SCS) in a nitrogen filled glove box. The field-effect mobilities were determined in the saturated regime using the equation $\mu = \left(\frac{\partial\,(I_{DS})^{1/2}}{\partial\,V_G}\right)^2 \frac{2L}{W\,C_i}$, where I_{DS} is the source-drain current, W is the channel width, L the channel length, C_i is the capacitance per unit area of the gate dielectric layer, μ is the field-effect mobility.

Field-effect measurements: OFET measurements were performed by using a Keithley 2634B source meter. Transfer characteristics were measured under a nitrogen atmosphere in the range of V_{GS} from 0 V to 80 V. The same range of changes was used for V_{DS} during output characteristics measurements. The charge carrier mobility was derived from transfer characteristics ($|V_{DS} = 80V|$) in the saturation regime.

General procedure (GP):

GP1: Halodesilylation

Bis(trimethylsilyl) veratroles (1.00 equiv.) and NIS/NBS/NCS (4.00 equiv.) were dissolved in

acetonitrile under nitrogen. The reaction mixture was stirred at 95 ºC for 7 days. After cooling to room temperature, the mixture was poured into aqueous Na_2SO_3 solution and extracted with DCM. The combined organic phase was washed repeatedly with deionized (DI) water and dried over $MgSO_4$. After removing the organic solvents, the crude product was purified by column chromatography (PE/ethyl acetate, 10:1) to obtain tetrahalogenated veratroles as white solids.

GP2: Demethylation of veratroles

Under an inert atmosphere, boron tribromide (3.00 equiv.) was added dropwise to a solution of tetrahalogenated veratroles (1.00 equiv.) in DCM while cooling in an ice bath. The mixture was allowed to warm to room temperature and stirred overnight. DI water was added slowly to the reaction mixture under nitrogen to decompose excess boron tribromide while cooled in ice bath. The cold solution was filtered and the precipitate was washed with water and cold DCM to obtain tetrahalogenated catechols as a grey solid.

GP3: Oxidation of catechols

Tetrahalogenated catechols (1.00 equiv.) was dissolved in 10 mL of DCM. After addition of sodium periodate (2.00 equiv.) and $Bu_4N^+I^-$ (0.05 equiv.), dissolved in 10 mL of DI water, the reaction mixture was stirred at room temperature for 30 min. The mixture was diluted with DCM and washed repeatedly with Na_2SO_3 solution and DI water. The organic phase was dried over $MgSO_4$, concentrated as a dark red solid and can be used for the next step without further purification. Characterization of *ortho*-quinones were performed after purified by column chromatography (PE/DCM, 8:1).

GP4: Cyclocondensation reaction

The freshly prepared *ortho*-quinones (1.20 equiv.) and the *ortho*-diamine (1.00 equiv.) were dissolved in DCM/acetic acid (1:1) and stirred at room temperature for 24 h. After evaporation of the solvent, the crude product was purified by column chromatography (PE/DCM, 10:1) to furnish the tetrahaloazaacenes.

GP5: Sonogashira reaction

Under inert conditions a mixture of dibromodiiodoazaacenes (1.00 equiv.), CuI (0.5 equiv.),

$(PPh_3)_2PdCl_2$ (0.20 equiv.) and TIPS acetylene (5.00 equiv.) were dissolved in degassed THF/triethylamine (1:1). The reaction mixture was stirred at room temperature (or 50 °C) for 36 h. After cooling to room temperature, the mixture was purified by column chromatography (PE→PE/DCM, 30:1). The resulting mixture of dihydro compounds were dissolved in DCM and oxidized with PbO_2 (20 equiv.) for 1 h. After filtering through Celite and solvent removal under vacuum, the crude product was purified by column chromatography (PE→PE/DCM, 10:1) to furnish tetraethynylated dibromoazaacenes.

GP6: Buchwald-Hartwig coupling using RuPhos Pd G1

The dibromides (1.00 equiv.), diamines (1.50 equiv.), RuPhos Pd G1 (ethyl *t*-butyl ether adduct) (0.50 equiv.) P(*t*-Bu)$_3$HBF$_4$ (0.50 equiv.) and Cs_2CO_3 (4.00 equiv.) were dissolved in dry, degassed toluene in a heatgun-dried flask under nitrogen. The mixture was heated to 100 °C for 6 h. After cooling to room temperature, the mixture was filtrated over silica, the solvent was removed and the residue was purified by column chromatography (PE/DCM, 5:1) to furnish the *N,N'*-dihydro- azaacenes.

GP7: Buchwald-Hartwig coupling using $Pd_2(dba)_3$

The dichloride (1.00 equiv.), diamine (1.50 equiv.), $Pd_2(dba)_3$ (0.50 equiv.) RuPhos (1.00 equiv.) and Cs_2CO_3 (10.0 equiv.) were dissolved in dry, degassed toluene in a heatgun-dried flask under nitrogen. The mixture was heated to 100 °C for 6 h. After cooling to room temperature, the mixture was filtrated over silica, the solvent was removed and the residue was purified by column chromatography (PE/DCM, 5:1) to furnish the *N,N'*-dihydro- azaacenes.

GP8: Oxidation of *N,N'*-dihydro- azaacenes

An excess of MnO_2 (100 equiv.) or PbO_2 (100 equiv.) was added to solutions of *N,N'*-dihydro-azaacenes (1.00 equiv.) in DCM (10 mL) and stirred at room temperature for 30 min. The solvent was removed and the residue was purified by column chromatography (PE/DCM, 5:1→1:1). To avoid decomposition, a small amount of methanol was added to the fractions to precipitate the products after separation. Afterwards, the solvent was evaporated as fast as possible in a schlenk line under nitrogen to furnish microcrystalline target azaacenes.

6.2 Synthesis Details and Analytical Data

6.2.1 Synthesis of Phenanzinothiadiazoles (Chapter 2)

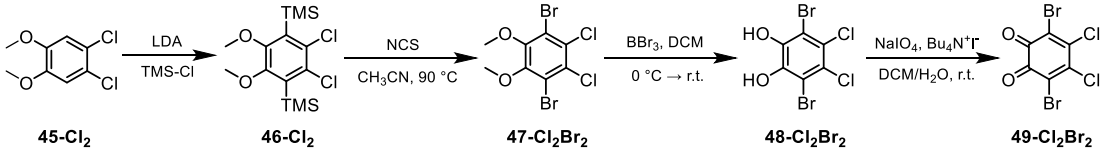

1,2-Dichloro-4,5-dimethoxy-3,6-bis(trimethylsilyl)benzene (46-Cl_2): 1,2-Dichloro-4,5-dimethoxybenzene (5.00 g, 24.2 mmol, 1.0 equiv.) and trimethylsilyl chloride (15.3 mL, 120.7 mmol, 5.0 equiv.) were dissolved in anhydrous THF (50 mL) in a flame-dried Schlenk flask and cooled to -30 °C. A solution of LDA (2 M, 36.2 mL, 76.5 mmol, 4.0 equiv.) was added over the course of 20 min. The resulting solution was stirred at -30 °C for an additional hour and subsequently allowed to warmed to room temperature overnight. The reaction was quenched with 1 M hydrochloric acid and extracted with DCM three times. The combined organic fractions were dried over $MgSO_4$, filtered and the organic volatiles evaporated under reduced pressure. The residue was dissolved in MeOH and stored in a refrigerator, leading to the precipitation of the **46-Cl_2** (8.06 g, 22.9 mmol, 95%) as colorless needles. m.p. = 129 °C. ^{1}H NMR (300 MHz, $CDCl_3$, r.t.) δ = 3.73 (s, 6H), 0.42. (s, 18H) ppm. ^{13}C NMR (75 MHz, $CDCl_3$, r.t.) δ = 157.0, 135.9, 133.9, 60.7, 2.3 ppm. IR: $\tilde{\nu}$ = 2963, 2899, 2831, 1341, 1248, 1209, 1159, 1020, 915, 830 cm^{-1}. GCMS (EI+): *m/z* $[M]^+$ calcd for $C_{14}H_{24}Cl_2O_2Si_2$ 350.069; found 350.071.

1,2-Dichloro-3,6-dibromo-4,5-dimethoxybenzene (47-Cl_2Br_2): **GP1** was applied to **46-Cl_2** (1.00 g, 2.85 mmol) and *N*-bromosuccinimide (2.03 g, 11.4 mmol) in 50 mL acetonitrile yielding **47-Cl_2Br_2** (0.92 g, 2.54 mmol, 89 %) as a white powderous solid. m.p. = 136 °C. ^{1}H NMR (300 MHz, $CDCl_3$, r.t.) δ = 3.90 (s, 6H) ppm. ^{13}C NMR (75 MHz, $CDCl_3$, r.t.) δ = 151.2, 130.1, 119.6, 61.4 ppm. IR: $\tilde{\nu}$ = 2941, 2857, 1448, 1386, 1361, 1218, 1011, 919, 780 cm^{-1}. GCMS (EI+): *m/z* $[M]^+$ calcd for $C_8H_6Br_2Cl_2O_2$ 365.806; found 365.800. R_f = 0.50 (SiO_2, PE / Et_2O 10:1, v/v).

1,2-Dichloro-3,6-dibromo-4,5-dihydroxybenzene (48-Cl_2Br_2): GP2 was applied to **47-Cl_2Br_2** (800 mg, 2.19 mmol) and boron tribromide (1.65 g, 6.58 mmol) in 20 mL DCM yielding

48-Cl_2Br_2 (539 mg, 1.60 mmol, 73%) as a grey powderous solid. m.p. = 164 °C. ^{1}H NMR (500 MHz, THF-d_8, r.t.) δ = 9.20 (s, 2H) ppm. ^{13}C NMR (126 MHz, THF-d_8, r.t.) δ = 145.1, 124.7, 111.7 ppm. IR: $\tilde{\nu}$ = 3409, 2361, 1448, 1385, 1275, 1160, 981, 921, 788, 705 cm^{-1}. HR-MS(ESI+): *m/z* $[M+H]^+$ calcd for $C_6H_3Br_2I_2O_2$ 338.7749; found 338.7749. R_f = 0.35 (SiO_2, PE / EE 5:1, v/v).

1,2-Dichloro-3,6-dibromo-3,5-cyclohexadiene-1,2-dione (49-Cl_2Br_2): GP3 was applied to **48-Cl_2Br_2** (500 mg, 1.48 mmol), sodium periodate (635 mg, 2.97 mmol) and $Bu_4N^+I^-$ (27.4 mg, 74.2 µmol) in 20 mL of DCM/DI water (1:1) yielding **49-Cl_2Br_2** (493 mg, 1.47 mmol, quant.) as a dark red solid. m.p. = 107 °C. ^{13}C NMR (101 MHz, $CDCl_3$, r.t.). δ = 169.4, 146.9, 125.7 ppm. IR: $\tilde{\nu}$ = 2926, 2365, 1507, 1436, 1217, 1133, 971, 831, 747 cm^{-1}. HR-MS (ESI+): *m/z* $[M+H]^+$ calcd for $C_6HBr_2Cl_2O_2$ 336.7592; found 336.7593. R_f = 0.35 (SiO_2, PE / DCM 10:1, v/v).

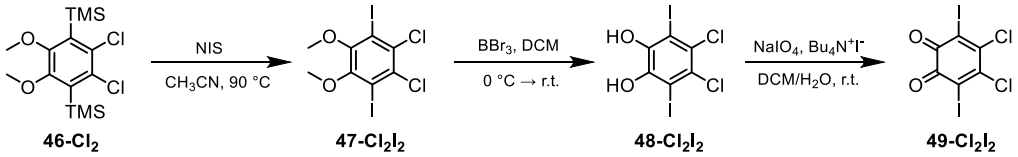

46-Cl_2 **47-Cl_2I_2** **48-Cl_2I_2** **49-Cl_2I_2**

1,2-Dichloro-3,6-diiodo-4,5-dimethoxybenzene (47-Cl_2I_2): **GP1** was applied to **46-Cl_2** (1.00 g, 2.85 mmol) and *N*-iodosuccinimide (2.56 g, 11.4 mmol) in 50 mL acetonitrile yielding **47-Cl_2I_2** (0.81 g, 2.22 mmol, 78 %) as a white powderous solid. m.p. = 145 °C. ^{1}H NMR (300 MHz, $CDCl_3$, r.t.) δ = 3.87 (s, 6H) ppm. ^{13}C NMR (75 MHz, $CDCl_3$, r.t.) δ = 152.7, 132.5, 99.4, 61.0 ppm. IR: $\tilde{\nu}$ = 2936, 2849, 1443, 1370, 1341, 1005, 914, 769, 704 cm^{-1}. GCMS (EI+): *m/z* $[M]^+$ calcd for $C_8H_6Cl_2I_2O_2$ 457.783; found 457.792. R_f = 0.50 (SiO_2, PE / Et_2O 10:1, v/v).

1,2-Dichloro-3,6-diiodo-4,5-dihydroxybenzene (48-Cl_2I_2): GP2 was applied to **47-Cl_2I_2** (800 mg, 1.74 mmol) and boron tribromide (1.31 g, 5.23 mmol) in 20 mL DCM yielding **48-Cl_2I_2** (660 mg, 1.53 mmol, 88%) as a grey powderous solid. m.p. = 169 °C. ^{1}H NMR (400 MHz, THF-d_8, r.t.) δ = 8.92 (s, 2H) ppm. ^{13}C NMR (101 MHz, THF-d_8, r.t.) δ = 146.9, 127.5, 91.4 ppm. IR: $\tilde{\nu}$ = 3403, 1540, 1438, 1379, 1313, 1275, 1145, 958, 888, 764 cm^{-1}. HR-MS(ESI+): *m/z* $[M+H]^+$ calcd for $C_6H_3Br_2I_2O_2$ 430.7521; found 430.7521. R_f = 0.35 (SiO_2, PE / EE 5:1, v/v).

1,2-Dichloro-3,6-diiodo-3,5-cyclohexadiene-1,2-dione (49-Cl_2I_2): GP3 was applied to **48-Cl_2I_2** (500 mg, 1.16 mmol), sodium periodate (497 mg, 2.32 mmol) and $Bu_4N^+I^-$ (21.4 mg, 58.0 µmol) in 20 mL of DCM/DI water (1:1) yielding **49-Cl_2I_2** (496 mg, 1.15 mmol, quant.) as a dark red solid. m.p. = 115 °C. ^{13}C NMR (101 MHz, $CDCl_3$, r.t.) δ = 170.6, 151.1, 108.5 ppm. IR: $\tilde{\nu}$ = 2920, 2361, 1682, 1488, 1233, 1208, 1112, 748, 722, 629, 542 cm^{-1}. HR-MS (ESI+): *m/z* $[M+H]^+$ calcd for $C_6HBr_2I_2O_2$ 428.7365; found 428.7365. R_f = 0.35 (SiO_2, PE / DCM 10:1, v/v).

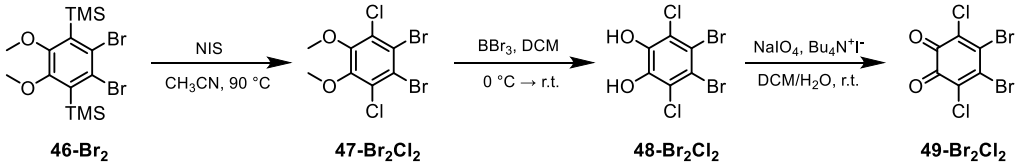

46-Br_2 **47-Br_2Cl_2** **48-Br_2Cl_2** **49-Br_2Cl_2**

1,2-Dibromo-3,6-dichloro-4,5-dimethoxybenzene (47-Br_2Cl_2): **GP1** was applied to **46-Br_2** (1.00 g, 2.27 mmol) and *N*-chlorosuccinimide (1.21 g, 9.08 mmol) in 50 mL acetonitrile yielding **47-Br_2Cl_2** (0.37 g, 1.02 mmol, 45 %) as a white powderous solid. m.p. = 139 °C. ^{1}H NMR (500 MHz, $CDCl_3$, r.t.) δ = 3.92 (s, 6H) ppm. ^{13}C NMR (126 MHz, $CDCl_3$, r.t.) δ = 150.6, 129.8, 122.0, 61.5 ppm. IR: $\tilde{\nu}$ = 2940, 2852, 1443, 1385, 1340, 1259, 1001, 902, 750 cm^{-1}. GCMS (EI+): *m/z* $[M]^+$ calcd for $C_8H_6Br_2Cl_2O_2$ 365.806; found 365.800. R_f = 0.56 (SiO_2, PE / Et_2O 10:1, v/v).

1,2-Dibromo-3,6-dichloro-4,5-dihydroxybenzene (48-Br_2Cl_2): GP2 was applied to **47-Br_2Cl_2** (800 mg, 2.19 mmol) and boron tribromide (1.65 g, 6.58 mmol) in 20 mL DCM yielding **48-Br_2Cl_2** (561 mg, 1.66 mmol, 76%) as a grey powderous solid. m.p. = 165 °C. ^{1}H NMR (400 MHz, THF-d_8, r.t.) δ = 9.26 (s, 2H) ppm. ^{13}C NMR (101 MHz, THF-d_8, r.t.) δ = 144.3, 122.0, 116.0 ppm. IR: $\tilde{\nu}$ = 3390, 1540, 1456, 1375, 1275, 1166, 952, 763 cm^{-1}. HR-MS(ESI+): *m/z* $[M+H]^+$ calcd for $C_6H_3Br_2I_2O_2$ 338.7749; found 338.7749. R_f = 0.35 (SiO_2, PE / EE 5:1, v/v).

1,2-Dibromo-3,6-dichloro-3,5-cyclohexadiene-1,2-dione (49-Br_2Cl_2): **GP3** was applied to **48-Br_2Cl_2** (500 mg, 1.48 mmol), sodium periodate (635 mg, 2.97 mmol) and $Bu_4N^+I^-$ (27.4 mg, 74.2 µmol) in 20 mL of DCM/DI water (1:1) yielding **49-Br_2Cl_2** (495 mg, 1.47 mmol, quant.) as a dark red solid. m.p. = 107 °C. ^{13}C NMR (101 MHz, $CDCl_3$, r.t.) δ = 169.0, 139.7, 134.9

ppm. IR: $\tilde{\nu}$ = 2925, 2351, 1675, 1540, 1442, 1234, 1136, 997, 748, 564 cm^{-1}. HR-MS (ESI+): *m/z* [M+H]$^+$ calcd for $C_6HBr_2Cl_2O_2$ 336.7592; found 336.7593. R_f = 0.35 (SiO_2, PE / DCM 10:1, v/v).

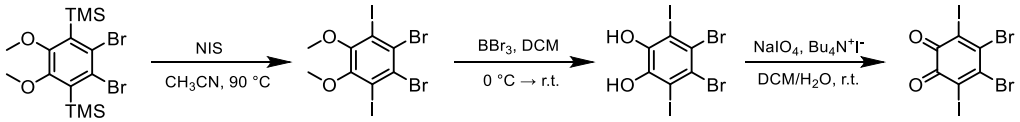

1,2-Dibromo-3,6-diiodo-4,5-dimethoxybenzene (47-Br_2I_2): **GP1** was applied to **46-Br_2** (1.00 g, 2.27 mmol) and *N*-iodosuccinimide (2.04 g, 9.08 mmol) in 50 mL acetonitrile yielding **47-Br_2I_2** (1.05 g, 1.93 mmol, 85%) as a white powderous solid. m.p. = 143 °C. ^{1}H NMR (500 MHz, $CDCl_3$, r.t.) δ = 3.85 (s, 6H) ppm. ^{13}C NMR (126 MHz, $CDCl_3$, r.t.) δ = 152.8, 126.6, 102.6, 60.7 ppm. IR: $\tilde{\nu}$ = 2933, 2848, 2306, 2322, 1455, 1371, 1003, 763, 690 cm^{-1}. GCMS (EI+): *m/z* [M]$^+$ calcd for $C_8H_6Br_2I_2O_2$ 547.680; found 547.800. R_f = 0.56 (SiO_2, PE / Et_2O 10:1, v/v).

1,2-Dibromo-3,6-diiodo-4,5-dihydroxybenzene (48-Br_2I_2): GP2 was applied to **47-Br_2I_2** (800 mg, 1.46 mmol) and boron tribromide (1.10 g, 4.38 mmol) in 20 mL DCM yielding **48-Br_2I_2** (683 mg, 1.31 mmol, 90%) as a grey powderous solid. m.p. = 167 °C. ^{1}H NMR (300 MHz, THF-d_8, r.t.) δ = 8.86 (s, 2H) ppm. ^{13}C NMR (76 MHz, THF-d_8, r.t.) δ = 147.1, 121.6, 94.5 ppm. IR: $\tilde{\nu}$ = 3381, 1540, 1428, 1361, 1269, 1140, 915, 713, 668 cm^{-1}. HR-MS(ESI+): *m/z* [M+H]$^+$ calcd for $C_6H_3Br_2I_2O_2$ 518.6424; found 518.6424. R_f = 0.35 (SiO_2, PE / EE 5:1, v/v).

1,2-Dibromo-3,6-diiodo-3,5-cyclohexadiene-1,2-dione (49-Br_2I_2): GP3 was applied to **48-Br_2I_2** (500 mg, 962 µmol), sodium periodate (412 mg, 1.92 mmol) and $Bu_4N^+I^-$ (17.8 mg, 48.1 µmol) in 20 mL of DCM/DI water (1:1) yielding **49-Br_2I_2** (487 mg, 943 µmol, quant.) as a dark red solid. m.p. = 109 °C. ^{13}C NMR (126 MHz, $CDCl_3$, r.t.) δ = 170.0, 147.0, 112.5 ppm. IR: $\tilde{\nu}$ = 2960, 2922, 2872, 2853, 2359, 2339, 1470, 1458, 843 cm^{-1}. HR-MS (ESI+): *m/z* [M+H]$^+$ calcd for $C_6HBr_2I_2O_2$ 516.6269; found 516.6273. R_f = 0.35 (SiO_2, PE / DCM 10:1, v/v).

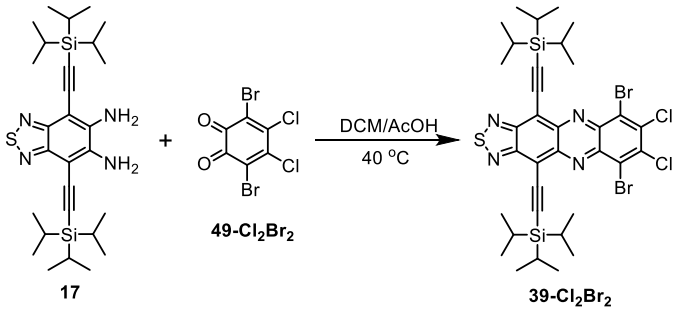

6,9-dibromo-7,8-dichloro-4,11-bis((triisopropylsilyl)ethynyl)-[1,2,5]thiadiazolo[3,4-b] phenazine (39-Cl_2Br_2): **GP4** was applied to **17** (200 mg, 380 µmol) and **49-Cl_2Br_2** (152 mg, 455 µmol) in 10 mL of DCM/AcOH (1:1) yielding **39-Cl_2Br_2** (194 mg, 235 µmol, 62%) as a blue solid. m.p. > 350 °C. ^{1}H NMR (500 MHz, $CDCl_3$, r.t.) δ = 1.24-1.38 (m, 42H) ppm. ^{13}C NMR (126 MHz, $CDCl_3$, r.t.) δ = 156.1, 142.3, 141.2, 138.5, 126.3, 115.3, 114.0, 101.8, 19.2, 11.9 ppm. IR: $\tilde{\nu}$ = 2940, 2862, 1559, 1463, 1387, 1267, 1015, 993, 881, 814, 750, 670 cm^{-1}. HR-MS (ESI+): *m/z* $[M]^+$ calcd for $C_{34}H_{42}Cl_2Br_2N_4SSi_2$ 826.0368; found 826.0369. Specimen for X-ray crystallography were grown by slow evaporation of concentrated chloroform solutions. R_f = 0.48 (SiO_2, PE / DCM 5:1, v/v).

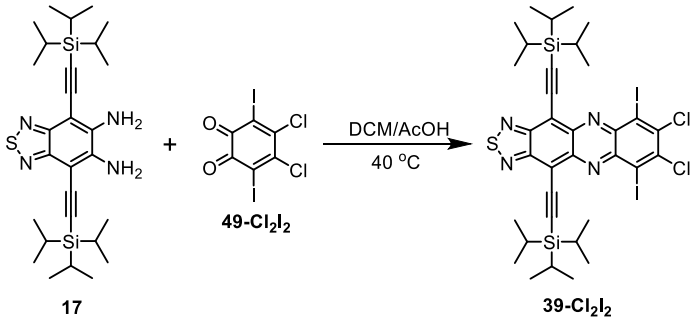

7,8-dichloro-6,9-diiodo-4,11-bis((triisopropylsilyl)ethynyl)-[1,2,5]thiadiazolo[3,4-b] phenazine (39-Cl_2I_2): **GP4** was applied to **17** (200 mg, 380 µmol) and **49-Cl_2I_2** (195 mg, 455 µmol) in 10 mL of DCM/AcOH (1:1) yielding **39-Cl_2I_2** (129 mg, 140 µmol, 37%) as a blue solid. m.p. > 350 °C. ^{1}H NMR (500 MHz, $CDCl_3$, r.t.) δ = 1.20-1.37 (m, 42H) ppm. ^{13}C NMR (126 MHz, $CDCl_3$, r.t.) δ = 154.3, 141.2, 140.4, 137.8, 115.5, 111.9, 108.1, 100.0, 19.2, 11.8 ppm. IR: $\tilde{\nu}$ = 2940, 2862, 1457, 1362, 1339, 1266, 1115, 1026, 881, 753, 669 cm^{-1}. HR-MS (ESI+): *m/z* $[M]^+$ calcd for $C_{34}H_{42}Cl_2I_2N_2SSi_2$ 918.0141; found 918.0140. Specimen for X-ray crystallography were grown by slow evaporation of concentrated chloroform solutions. R_f = 0.48 (SiO_2, PE / DCM 5:1, v/v).

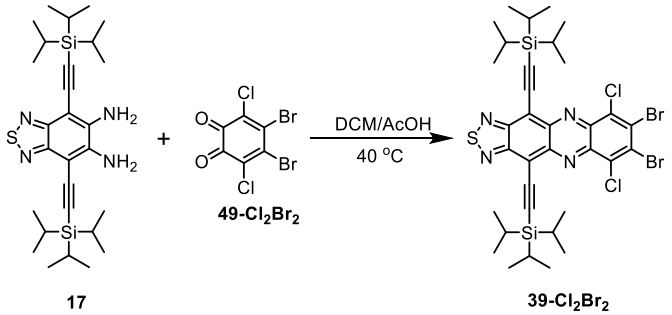

7,8-dibromo-6,9-dichloro-4,11-bis((triisopropylsilyl)ethynyl)-[1,2,5]thiadiazolo[3,4-b] phenazine (39-Br_2Cl_2): **GP4** was applied to **17** (200 mg, 380 µmol) and **49-Br_2Cl_2** (152 mg, 455 µmol) in 10 mL of DCM/AcOH (1:1) yielding **39-Br_2Cl_2** (197 mg, 238 µmol, 63%) as a blue solid. m.p. > 350 °C. ^{1}H NMR (300 MHz, $CDCl_3$, r.t.) δ = 1.19-1.37 (m, 42H) ppm. ^{13}C NMR (75 MHz, $CDCl_3$, r.t.) δ = 156.1, 142.1, 140.6, 134.9, 130.5, 115.5, 114.2, 101.7, 19.2, 11.9 ppm. IR: $\tilde{\nu}$ = 2939, 2862, 1444, 1362, 1026, 1255, 1150, 1026, 921, 881, 755, 672, 570 cm^{-1}. HR-MS (ESI+): *m/z* $[M]^+$ calcd for $C_{34}H_{42}Cl_2Br_2N_4SSi_2$ 826.0368; found 826.0369. Specimen for X-ray crystallography were grown by slow evaporation of concentrated chloroform solutions. R_f = 0.48 (SiO_2, PE / DCM 5:1, v/v).

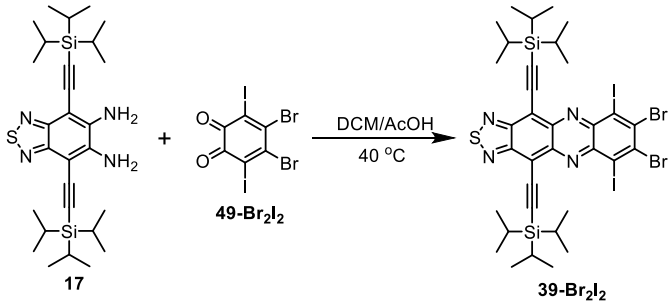

7,8-dibromo-6,9-diiodo-4,11-bis((triisopropylsilyl)ethynyl)-[1,2,5]thiadiazolo[3,4-b] phenazine (39-Br_2I_2): **GP4** was applied to **17** (200 mg, 380 µmol) and **49-Br_2I_2** (236mg, 455 µmol) in 10 mL of DCM/AcOH (1:1) yielding **39-Br_2I_2** (222 mg, 220 µmol, 62%) as a blue solid. m.p. > 350 °C. ^{1}H NMR (500 MHz, $CDCl_3$, r.t.) δ = 1.22-1.40 (m, 42H) ppm. ^{13}C NMR (126 MHz, $CDCl_3$, r.t.) δ = 156.3, 143.5, 143.0, 137.7, 114.8, 114.2, 113.9, 102.1, 19.3, 11.9 ppm. IR: $\tilde{\nu}$ = 2939, 2862, 1446, 1362, 1027, 920, 880, 828, 756, 669, 569 cm^{-1}. HR-MS (ESI+): *m/z* $[M+H]^+$ calcd for $C_{34}H_{43}Br_2I_2N_4SSi_2$ 1006.9198; found 1006.9179. Specimen for X-ray crystallography were grown by slow evaporation of concentrated chloroform solutions. R_f = 0.48 (SiO_2, PE / DCM 5:1, v/v).

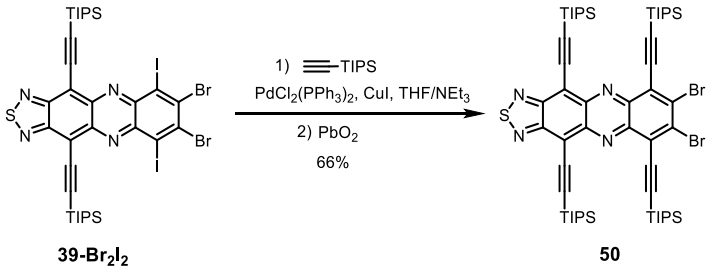

39-Br$_2$I$_2$ **50**

7,8-dibromo-4,6,9,11-tetrakis((triisopropylsilyl)ethynyl)-[1,2,5]thiadiazolo[3,4-b] phenazine (50): GP5 was applied to **39-Br$_2$I$_2$** (80.0 mg, 79.3 µmol), CuI (7.55 mg, 39.7 µmol), $(PPh_3)_2PdCl_2$ (11.1 mg, 15.9 µmol) and TIPS acetylene (396 mg, 72.3 mmol) in THF/triethylamine (15 mL, 1:1 v/v) yielding **50** (58.5 mg, 52.3 µmol, 66%) as a green powderous solid. m.p. > 350 °C. ^{1}H NMR (600 MHz, $CDCl_3$, r.t.) δ = 1.33-1.13 (m, 84H) ppm. ^{13}C NMR (151 MHz, $CDCl_3$, r.t.) δ = 156.6, 142.7, 140.8, 136.1, 126.5, 115.0, 114.4, 109.7, 103.4, 102.8, 58.6, 19.1, 19.0, 18.6, 12.0, 11.8 ppm. IR: $\tilde{\boldsymbol{\nu}}$ = 2939, 2862, 1444, 1362, 1026, 1255, 1150, 1026, 921, 881, 755, 672, 570 cm^{-1}. HR-MS (ESI+): *m/z* $[M]^+$ calcd for $C_{56}H_{84}Br_2N_4SSi_4$ 1117.5240; found 1117.5245. R_f = 0.58 (SiO_2, PE / DCM 7:1, v/v).

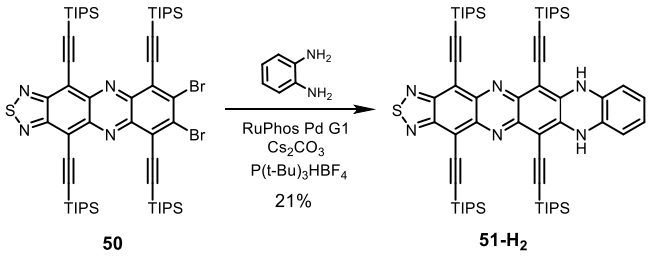

50 **51-H$_2$**

4,6,13,15-tetrakis((triisopropylsilyl)ethynyl)-7,12-dihydroquinoxalino[2,3-b][1,2,5] thiadiazolo [3,4-i]phenazine (51-H$_2$): GP6 was applied to **50** (50.0 mg, 44.7 µmol), *o*-phenylenediamine (7.26 mg, 67.1 µmol), RuPhos Pd G1 (18.3 mg, 22.4 µmol), P(*t*-Bu)$_3$HBF$_4$ (6.50 mg, 22.4 µmol) and Cs_2CO_3 (58.3 mg, 179 µmol) yielding red flaky crystalline **51-H$_2$** (9.98 mg, 9.39 µmol, 21%). m.p. > 350 °C. ^{1}H NMR (500 MHz, $CDCl_3$, r.t.) δ = 8.05-8.02 (m, 4H), 7.66 (dd, *J* = 6.7, 3.4 Hz, 2H), 1.34-1.15 (m, 84H) ppm. ^{13}C NMR (126 MHz, $CDCl_3$, r.t.) δ = 152.8, 143.2, 142.8, 134.2, 133.7, 129.4, 129.2, 108.8, 108.7, 101.4, 98.6, 97.7, 96.3, 19.1, 19.0, 12.1, 12.0 ppm. IR: $\tilde{\boldsymbol{\nu}}$ = 3356, 2940, 2862, 1559, 1463, 1387, 1267, 1015, 993, 881, 814, 750, 670 cm^{-1}. HR-MS (ESI+): *m/z* $[M]^+$ calcd for $C_{62}H_{90}N_6SSi_4$ 1063.8440; found 1063.8441. R_f = 0.29 (SiO_2, PE / DCM 5:1, v/v).

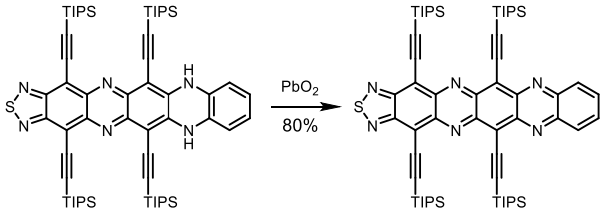

4,6,13,15-tetrakis((triisopropylsilyl)ethynyl)quinoxalino[2,3-b][1,2,5]thiadiazolo[3,4-i] phenazine (51): GP8 was applied to **51-H₂** (7.50 mg, 7.06 µmol) and MnO_2 (60.9 mg, 706 µmol) to furnish **51** (5.63 mg, 5.65 µmol, 80%) as a dark brown microcrystalline solid. m.p. > 350 °C. ^{1}H NMR (500 MHz, $CDCl_3$, r.t.) δ = 8.10 (dd, *J* = 7.0, 3.4 Hz, 2H), 7.76 (dd, *J* = 7.0, 3.3 Hz, 2H), 1.36-1.19 (m, 84H) ppm. ^{13}C NMR (126 MHz, $CDCl_3$, r.t.) δ = 157.3, 146.4, 145.5, 142.8, 142.1, 132.8, 130.6, 123.5, 116.9, 115.9, 115.0, 104.3, 103.7, 19.3, 19.1, 19.0, 12.1, 12.0 ppm. m.p. >350 °C (decomp.). IR: $\tilde{\nu}$ = 2941, 2864, 2360, 2340, 1444, 1275, 1080, 1016, 882, 842, 764, 671 cm^{-1}. HR-MS(MALDI+): *m/z* $[M+H]^+$ calcd for $C_{62}H_{89}Br_2N_4Si_4$ 1162.4732; found 1162.4760. R_f = 0.38 (SiO_2, petroleum ether/DCM 10:1, v/v). HR-MS (ESI+): *m/z* $[M+2H]^+$ calcd for $C_{62}H_{90}N_6SSi_4$ 1063.8440; found 1063.8443. R_f = 0.30 (SiO_2, PE / DCM 2:1, v/v).

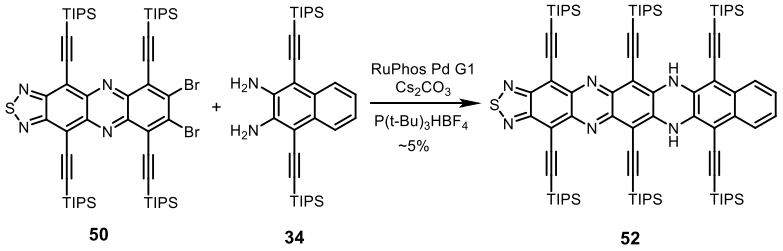

4,6,8,13,15,17-hexakis((triisopropylsilyl)ethynyl)-7,14-dihydrobenzo[6,7]quinoxalino[2,3-b][1,2,5]thiadiazolo[3,4-i]phenazine (52): GP6 was applied to **50** (20.0.0 mg, 17.9 µmol), **34** (13.9 mg, 26.8 µmol), RuPhos Pd G1 (7.31 mg, 8.95 µmol), P(*t*-Bu)$_3$HBF$_4$ (2.59 mg, 8.95 µmol) and Cs_2CO_3 (23.3 mg, 71.6 µmol) yielding red flaky crystalline **52** (1.30 mg, 5%). m.p. = 200 °C (decomp.). ^{1}H NMR (500 MHz, $CDCl_3$, r.t.) δ = 8.06 (s, 2H), 8.02 (dd, *J* = 4.3, 2.3 Hz, 2H), 7.84 (dd, *J* = 4.3, 2.2 Hz, 2H) 1.33-1.21 (m, 126H) ppm. ^{13}C NMR spectrum cannot be obtained due to the small amount of product. IR: $\tilde{\nu}$ = 3355, 2941, 2863, 1560, 1463, 1387, 1267, 1015, 994, 881, 814, 750, 669 cm^{-1}. HR-MS (ESI+): *m/z* $[M]^+$ calcd for $C_{88}H_{132}N_6SSi_6$ 1474.6360; found 1474.6365. R_f = 0.23 (SiO_2, PE / DCM 5:1, v/v).

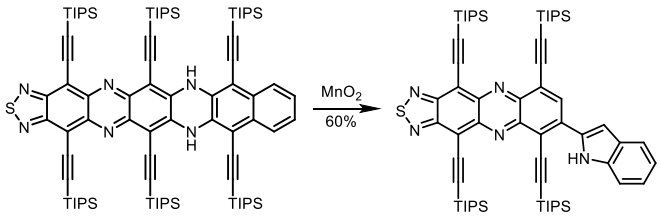

7-(1H-indol-2-yl)-4,6,9,11-tetrakis((triisopropylsilyl)ethynyl)-[1,2,5]thiadiazolo[3,4-b] phenazine (53): GP8 was applied to **52** (1.20 mg, 0.81 µmol) and MnO_2 (7.07 mg, 81.4 µmol) to furnish **53** (~0.50 mg, 60%) as a brown microcrystalline solid. Specimen of **53** for X-ray crystallography were grown by diffusion of methanol into their chloroform solutions. Other characterizations could not be performed because only traces of compound **53** were obtained as well as its instability. R_f = 0.25 (SiO_2, PE / DCM 2:1, v/v).

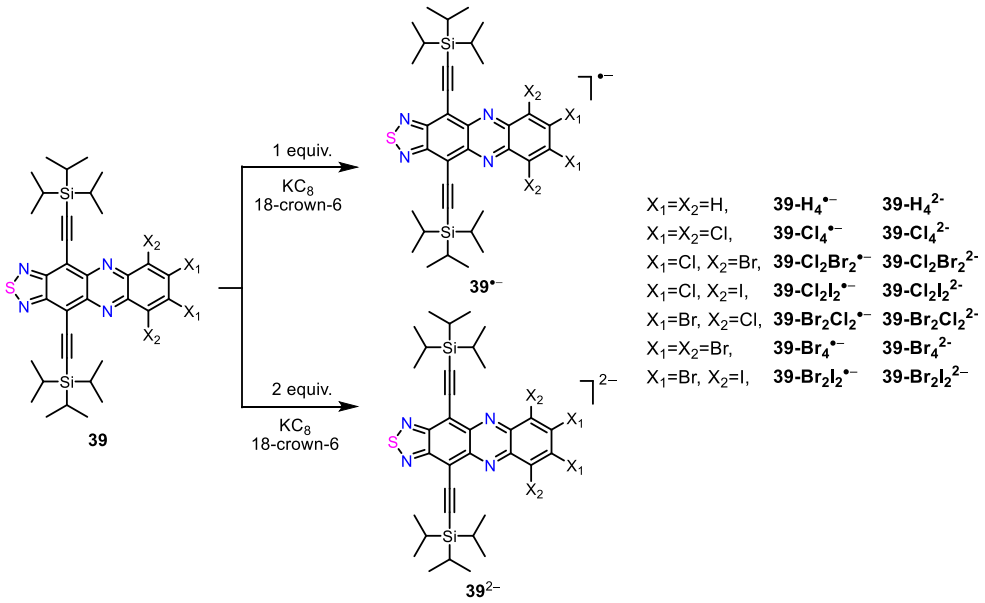

Preparation of the radical anions and dianions of 39

$39^{\bullet-}$: 39 (1.00 equiv.) and KC_8-(18-crown-6) (1.10 equiv.) were dissolved in dry THF (5 mL) in a 20 mL vial and stirred for 10 min in a nitrogen filled glove box to generate a dark yellow solution. After filtration, the solution was used for UV-Vis and EPR measurements. Attempts to obtain single crystalline specimen for single crystal analysis were not met with success.

39^{2-}: 39 (1.00 equiv.) and KC_8-(18-crown-6) (2.20 equiv.) were dissolved in dry THF (5 mL) in a 20 mL vial and stirred for 10 min in a nitrogen filled glove box to generate a red solution.

After filtration, the solution was used for UV-Vis and EPR measurements. Attempts to obtain single crystalline specimen for single crystal analysis were not met with success.

6.2.2 Synthesis of Azaheptacenes (Chapter 3)

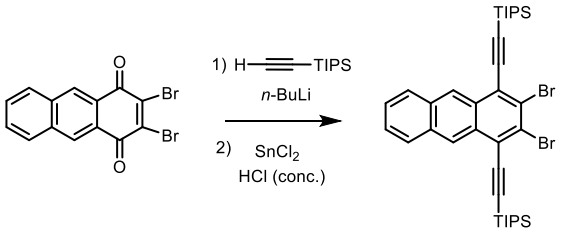

56

[(2,3-Dibromoanthracene-1,4-diyl)diethyne-2,1-diyl]bis(tripropan-2-ylsilane) (56): Under an inert atmosphere, tri-*iso*-propylsilyl acetylene (1.49 g, 8.20 mmol, 3.00 equiv.) was dissolved in dry THF (20 mL) at 0°C and treated with *n*-BuLi (3.28 mL, 2.50 M in hexane, 8.20 mmol, 3.00 equiv.). After stirring for 1.5 h at room temperature, the 2,3-dibromo-1,4-anthraquinone (1.00 g, 2.73 mmol, 1.00 equiv.) was added portionwise to form a light brown solution, which was stirred for 20 h. The reaction was quenched with aqueous ammonium chloride (50 mL), followed by extraction with diethyl ether (3 × 50 mL). The combined organic layer was washed with water and brine and dried over $MgSO_4$. Evaporation under reduced pressure gave the crude diol which was filtered through a plug of silica using petroleum ether and diethyl ether subsequently to separate it from excessive acetylene. After evaporation of the solvents, the intermediate diol was diluted in THF (20 mL) and a saturated solution of $SnCl_2$ in conc. hydrochloric acid (7 mL) was added to form a yellow reaction mixture, which was stirred for 2.5 h. At this point, the product was extracted with diethyl ether (3 × 50 mL) and the combined organic layer was washed with water (30 mL), 1 M aqueous sodium hydroxide (30 mL) and brine (30 mL). After drying over $MgSO_4$, the solvent was evaporated under reduced pressure. Flash column chromatography (PE/DCM, 10:1) yielding **56** as a blocky crystalline solid (670 mg, 0.96 mmol, 34 %). m.p. >350 °C (decomp.). ^{1}H NMR (500 MHz, $CDCl_3$, r.t.) δ = 8.99 (s, 2H), 8.04 (dd, *J* = 6.4, 3.3 Hz, 2H), 7.55 (dd, *J* = 6.4, 3.2 Hz, 2H), 1.31-1.26 (m, 42H) ppm. ^{13}C NMR (126 MHz, $CDCl_3$, r.t.) δ = 132.8, 130.2, 128.7, 127.0, 126.6, 126.3, 124.9, 105.5, 104.1,

19.0, 18.9, 11.6 ppm. IR: $\tilde{\nu}$ = 2939, 2862, 1518, 1459, 1359, 1289, 1063, 995, 881, 820, 765, 660 cm^{-1}. HR-MS(MALDI+): *m/z* [M]$^+$ calcd for $C_{36}H_{48}Br_2Si_2$ 694.1656; found 694.1642. R_f = 0.52 (SiO_2, PE / DCM 12:1, v/v).

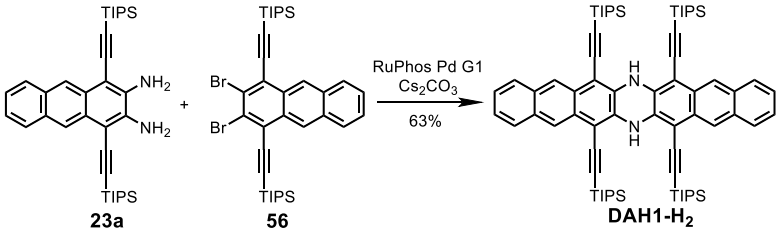

6,8,15,17-tetrakis((triisopropylsilyl)ethynyl)-7,16-dihydrodinaphtho[2,3-b:2',3'-i] phenazine (DAH1-H$_2$): **GP6** was applied to **23a** (61.2 mg, 107 µmol), **56** (50.0 mg, 71.8 µmol), RuPhos Pd G1 (29.3 mg, 35.9 µmol) and Cs_2CO_3 (93.5 mg, 287 µmol) yielding **DAH1-H$_2$** (49.9 mg, 45.2 µmol, 63%) as a yellow flaky crystalline solid. m.p. >350 °C (decomp.). ^{1}H NMR (600 MHz, $CDCl_3$, r.t.) δ = 8.56 (s, 4H), 7.82 (dd, *J* = 4.2, 2.2 Hz, 4H), 7.76 (s, 2H), 7.38 (dd, *J* = 4.3, 2.1 Hz, 4H), 1.30-1.16 (m, 84H) ppm. ^{13}C NMR (151 MHz, $CDCl_3$) δ = 131.9, 131.8, 129.2, 128.0, 125.5, 123.7, 106.6, 100.9, 99.4, 19.3, 12.4 ppm. IR: $\tilde{\nu}$ = 3434, 2941, 2864, 1740, 1460, 1371, 1223, 880, 831, 740, 669 cm^{-1}. HR-MS(MALDI+): *m/z* [M+H]$^+$ calcd for $C_{72}H_{99}N_2Si_4$ 1103.6880; found 1103.6843. R_f = 0.32 (SiO_2, PE / DCM 5:1, v/v).

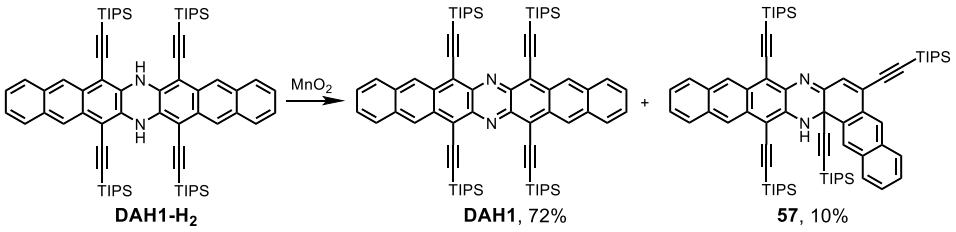

6,8,15,17-tetrakis((triisopropylsilyl)ethynyl)dinaphtho[2,3-b:2',3'-i]phenazine (DAH1): **GP8** was applied to **DAH1-H$_2$** (20.0 mg, 18.1 µmol) and MnO_2 (157 mg, 1.81 mmol) yielding **DAH1** (14.3 mg, 13.0 µmol, 72%) as a dark green microcrystalline solid. m.p. >350 °C (decomp.). ^{1}H NMR (600 MHz, $CDCl_3$, r.t.) δ = 9.35 (s, 4H), 7.89 (dd, *J* = 6.6, 3.2 Hz, 4H), 7.41 (dd, *J* = 5.9, 2.8 Hz, 4H), 1.49-0.80 (m, 84H). ^{13}C NMR (151 MHz, $CDCl_3$, r.t.) δ = 141.0, 134.6, 133.7, 128.9, 127.6, 127.2, 120.9, 111.9, 105.2, 19.3, 12.2 ppm. IR: $\tilde{\nu}$ = 2937, 2862, 1740, 1462, 1359, 1231, 1057, 994, 880, 821, 762, 661 cm^{-1}. HR-MS(MALDI+): *m/z* [M]$^+$ calcd for $C_{72}H_{96}N_2Si_4$ 1100.6645; found 1100.6637. R_f = 0.52 (SiO_2, PE / DCM 1:1, v/v).

6,9,16,17a-tetrakis((triisopropylsilyl)ethynyl)-17,17a-dihydrodinaphtho[2,3-a:2',3'-i] phenazine (57): 57 was obtained as a by-product of the oxidation reaction of **DAH1-H_2**: An excess of MnO_2 (100 equiv., 157 mg, 1.81 mmol) was added to a solution of **DAH1-H_2** (20.0 mg, 18.1 µmol) in DCM (5.00 mL) and stirred at room temperature for 10 min. The solvent was removed under vacuum and the residue was purified by column chromatography (PE/DCM, 5:1→1:1) yielding **57** (1.98 mg, 1.80 µmol, 10%) as a brown powderous solid. m.p. >350 °C (decomp.). ^{1}H NMR (600 MHz, $CDCl_3$, r.t.) δ = 9.01 (s, 1H), 8.67 (s, 1H), 8.46 (s, 1H), 8.08 (s, 1H), 7.98 (d, *J* = 8.2 Hz, 1H), 7.94 (d, *J* = 8.3 Hz, 1H), 7.90 (d, *J* = 7.2 Hz, 1H), 7.83 (d, *J* = 7.5 Hz, 1H), 7.64-7.53 (m, 2H), 7.50-7.46 (m, 1H), 7.46-7.40 (m, 1H), 7.08 (s, 1H) ppm. ^{13}C NMR (126 MHz, $CDCl_3$, r.t.) δ = 158.6, 138.8, 137.7, 134.3, 133.7, 133.2, 133.1, 131.8, 131.1, 131.0, 129.6, 129.0, 129.0, 128.7, 128.2, 128.1, 127.9, 127.7, 127.4, 127.3, 127.2, 126.4, 125.1, 124.8, 123.2, 120.0, 106.6, 104.2, 103.5, 102.8, 102.3, 102.2, 101.8, 86.9, 50.1, 19.3, 19.3, 19.1, 19.0, 18.4, 18.4, 11.8, 11.8, 11.6, 11.0 ppm. IR: $\tilde{\nu}$ = 2941, 2864, 2360, 2341, 1457, 1379, 1110, 1050, 881, 732, 669, 457 cm^{-1}. HR-MS(MALDI+): *m/z* $[M+H]^+$ calcd for $C_{72}H_{99}N_2Si_4$ 1103.6880; found 1103.6829. R_f = 0.45 (SiO_2, PE / DCM 1:1, v/v).

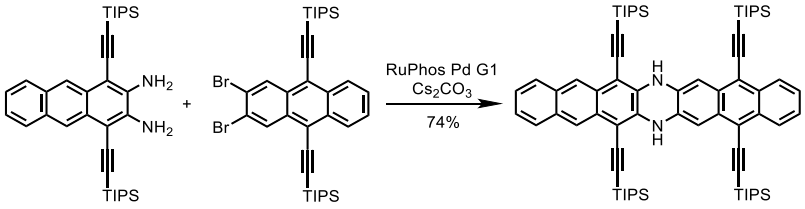

5,8,15,18-tetrakis((triisopropylsilyl)ethynyl)-7,16-dihydrodinaphtho[2,3-b:2',3'-i] phenazine (DAH2-H_2): **GP6** was applied to **23a** (49.0 mg, 86.1 µmol), **55** (40.0 mg, 57.4 µmol), RuPhos Pd G1 (23.4 mg, 28.7 µmol) and Cs_2CO_3 (74.8 mg, 229 µmol) yielding **DAH2-H_2** (46.9 mg, 42.5 µmol, 74%) as an orange flaky crystalline solid. m.p. >350 °C (decomp.). ^{1}H NMR (600 MHz, $CDCl_3$, r.t.) δ = 8.47 (m, 4H), 7.84 (dd, *J* = 3.8, 1.6 Hz, 2H), 7.48 (dd, *J* = 3.8, 1.7 Hz, 2H), 7.47 (s, 2H), 7.39 (dd, *J* = 3.7, 1.8 Hz), 7.29 (s, 2H), 1.42-1.14 (m, 84H) ppm. ^{13}C NMR (151 MHz, $CDCl_3$) δ = 133.3, 132.2, 131.8, 131.3, 131.2, 128.4, 127.9, 126.8, 126.2, 125.4, 123.1, 115.4, 105.8, 105.6, 104.3, 103.7, 100.2, 98.3, 18.8, 11.7, 11.6 ppm. IR: $\tilde{\nu}$ = 3369, 2943, 2865, 1462, 1436, 1394, 1361, 1056, 1013, 991, 876, 761, 661 cm^{-1}. HR-MS(MALDI+):

m/z $[M+H]^+$ calcd for $C_{72}H_{99}N_2Si_4$ 1103.6880; found 1103.6856. R_f = 0.33 (SiO_2, PE / DCM 5:1, v/v).

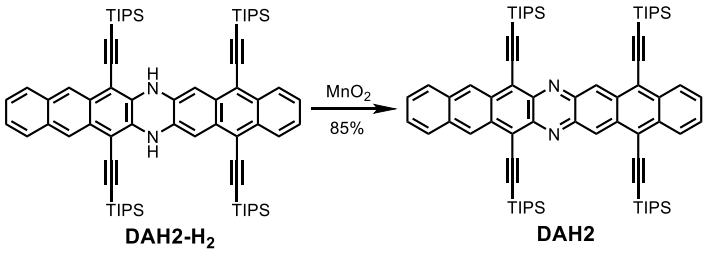

DAH2-H$_2$ **DAH2**

5,8,15,18-tetrakis((triisopropylsilyl)ethynyl)dinaphtho[2,3-b:2',3'-i]phenazine (DAH2): **GP8** was applied to **DAH2-H$_2$** (20.0 mg, 18.1 µmol) and MnO_2 (157 mg, 1.81 mmol) yielding **DAH2** (16.9 mg, 15.3 µmol, 85%) as a dark green microcrystalline solid. m.p. >350 °C (decomp.). ^{1}H NMR (600 MHz, $CDCl_3$, r.t.) δ = 9.69 (s, 2H), 9.34 (s, 2H), 8.58 (dd, *J* = 4.5, 2.1 Hz, 2H), 7.93 (dd, *J* = 4.3, 2.1 Hz, 2H), 7.51 (dd, *J* = 4.6, 2.0 Hz, 2H), 7.43 (dd, *J* = 4.5, 2.0 Hz, 2H), 1.46-1.16 (m, 84H) ppm. ^{13}C NMR (151 MHz, $CDCl_3$) δ = 142.4, 141.4, 134.4, 134.0, 133.5, 133.3, 129.1, 128.8, 127.8, 127.7, 127.3, 127.1, 120.9, 119.5, 110.9, 107.9, 104.5, 103.5, 19.1, 19.0, 11.7, 11.6 ppm. IR: $\tilde{\nu}$ = 2942, 2861, 1462, 1392, 1362, 1265, 1078, 1047, 1015, 878, 801, 747, 663 cm^{-1}. HR-MS(MALDI+): *m/z* $[M]^+$ calcd for $C_{72}H_{96}N_2Si_4$ 1100.6645; found 1100.6657. R_f = 0.56 (SiO_2, PE / DCM 1:1, v/v).

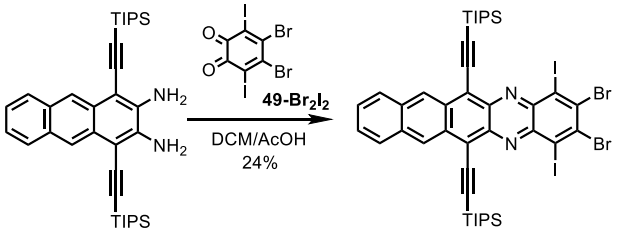

23a **58a**

2,3-dibromo-1,4-diiodo-6,13-bis((triisopropylsilyl)ethynyl)naphtho[2,3-b]phenazine (58a): GP4 was applied to **23a** (1.00 g, 1.76 mmol) and **49-Br$_2$I$_2$** (1.09 g, 2.11 mmol) in DCM/acetic acid (25 mL, 1:1) yielding **58a** (444 mg, 423 µmol, 24 %) as a blue powderous solid. m.p. >350 °C (decomp.). ^{1}H NMR (600 MHz, $CDCl_3$, r.t.) δ = 9.50 (s, 2H), 8.08-7.92 (m, 2H), 7.62-7.40 (m, 2H), 1.46-1.14 (m, 42H) ppm. ^{13}C NMR (151 MHz, $CDCl_3$, r.t.) δ = 142.2, 141.7, 136.2, 133.8, 133.6, 128.9, 127.6, 127.5, 120.9, 114.4, 111.2, 103.5, 19.3, 11.9 ppm. IR:

$\tilde{\nu}$ = 2938, 2861, 1459, 1371, 1337, 1105, 1016, 879, 760, 668 cm^{-1}. HR-MS(MALDI+): *m/z* [M+H]$^+$ calcd for $C_{42}H_{49}Br_2I_2N_2Si_2$ 1052.9792; found 1052.9791. R_f = 0.35 (SiO_2, PE / DCM 5:1, v/v).

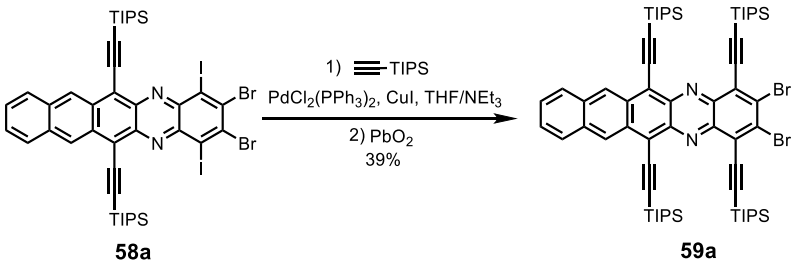

58a **59a**

2,3-dibromo-1,4,6,13-tetrakis((triisopropylsilyl)ethynyl)naphtho[2,3-b]phenazine (59a): GP5 was applied to **58a** (430 mg, 409 µmol), CuI (39.0 mg, 205 µmol), $(PPh_3)_2PdCl_2$ (57.4 mg, 81.8 µmol) and TIPS acetylene (373 mg, 2.05 mmol) in THF/triethylamine (12 mL, 1:1 v/v) yielding **59a** (186 mg, 159 µmol, 39%) as a green powderous solid. m.p. >350 °C (decomp.). ^{1}H NMR (500 MHz, $CDCl_3$, r.t.) δ = 9.49 (s, 2H), 7.99 (dd, *J* = 6.6, 3.2 Hz, 2H), 7.65-7.37 (m, 2H) 1.42-1.17 (m, 84H) ppm. ^{13}C NMR (126 MHz, $CDCl_3$, r.t.) δ = 142.0, 139.4, 134.9, 133.9, 133.4, 128.8, 127.4, 127.2, 126.5, 121.2, 111.3, 109.1, 104.4, 103.9, 19.2, 19.1, 12.1, 11.9 ppm. IR: $\tilde{\nu}$ = 2941, 2864, 2359, 2333, 1461, 1371, 1110, 1077, 1014, 882, 842, 765 cm^{-1}. HR-MS(MALDI+): *m/z* [M+H]$^+$ calcd for $C_{64}H_{91}Br_2N_2Si_4$ 1160.4727; found: 1160.4706. R_f = 0.40 (SiO_2, PE / DCM 10:1, v/v).

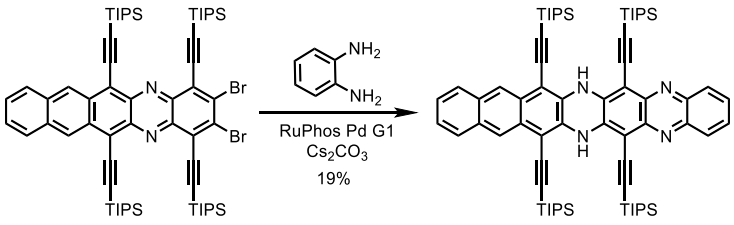

59a **TAH-H$_2$**

6,8,15,17-tetrakis((triisopropylsilyl)ethynyl)-7,16-dihydronaphtho[2,3-b]quinoxalino[2,3-i] phenazine (TAH-H$_2$) : **GP6** was applied to **59a** (180 mg, 155 µmol), *o*-phenylenediamine (25.1 mg, 233 µmol), RuPhos Pd G1 (63.4 mg, 77.6 µmol) P(*t*-Bu)$_3$HBF$_4$ (22.5 mg, 77.6 µmol) and Cs_2CO_3 (202 mg, 621 µmol) yielding **TAH-H$_2$** (32.6 mg, 29.5 µmol, 19%) as an orange-red flaky crystalline. m.p. >350 °C (decomp.). ^{1}H NMR (600 MHz, $CDCl_3$, r.t.) δ = 8.64 (s, 2H),

8.06 (s, 2H), 8.02 (dd, *J* = 4.3, 2.3 Hz, 2H), 7.84 (dd, *J* = 4.3, 2.2 Hz, 2H), 7.63 (dd, *J* = 4.4, 2.2 Hz, 2H), 7.42 (dd, *J* = 4.2, 2.0 Hz, 2H) 1.43-1.08 (m, 84H) ppm. ^{13}C NMR (151 MHz, $CDCl_3$, r.t.) δ = 143.5, 142.6, 135.3, 132.0, 130.5, 129.1, 129.1, 129.0, 128.0, 125.8, 124.1, 107.9, 107.6, 100.9, 100.2, 100.0, 99.3, 19.2, 19.1, 12.2 ppm. m.p. >250 °C (decomp.). IR: $\tilde{\nu}$ = 3356, 2938, 2862, 2359, 2134, 1573, 1449, 1363, 1255, 1056, 852, 757, 671 cm^{-1}. HR-MS(ESI+): *m/z* $[M]^+$ calcd for $C_{70}H_{96}N_4Si_4$ 1104.6707; found 1104.6709. R_f = 0.42 (SiO_2, PE / DCM 2:1, v/v).

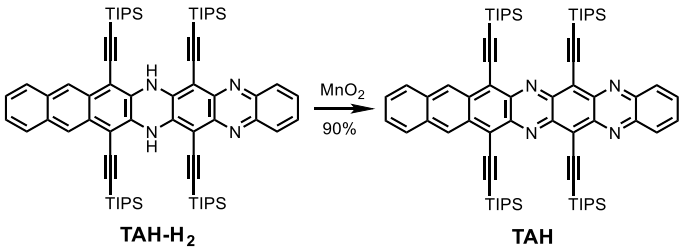

TAH-H$_2$ **TAH**

6,8,15,17-tetrakis((triisopropylsilyl)ethynyl)naphtho[2,3-b]quinoxalino[2,3-i]phenazine (TAH): **GP8** was applied to **TAH-H$_2$** (10.0 mg, 9.03 µmol) and MnO_2 (78.5 mg, 903 µmol) yielding **TAH** (8.95 mg, 8.12 µmol, 90%) as a dark brown microcrystalline solid. m.p. >350 °C (decomp.). ^{1}H NMR (600 MHz, $CDCl_3$, r.t.) δ = 9.37 (s, 2H), 8.13 (dd, *J* = 4.6, 2.2 Hz, 2H), 7.89 (dd, *J* = 4.6, 2.0 Hz, 2H), 7.76 (dd, *J* = 4.7, 2.1 Hz, 2H), 7.42 (dd, *J* = 4.6, 2.1 Hz, 2H) 1.43-1.05 (m, 84H) ppm. ^{13}C NMR (151 MHz, $CDCl_3$, r.t.) δ = 146.3, 145.3, 142.6, 141.5, 135.2, 134.3, 133.7, 133.0, 130.6, 129.0, 128.0, 123.3, 121.6, 116.3, 113.2, 105.0, 104.9, 30.1, 19.3, 12.5 ppm. m.p. >130 °C (decomposed into dark red solid with a red shine). IR: $\tilde{\nu}$ = 2938, 2860, 2127, 1533, 1462, 1384, 1264, 1043, 883, 785, 659 cm^{-1}. HR-MS(ESI+): *m/z* $[M]^+$ calcd for $C_{70}H_{94}N_4Si_4$ 1102.6552; found 1102.6550. R_f = 0.48 (SiO_2, PE / DCM 1:1, v/v).

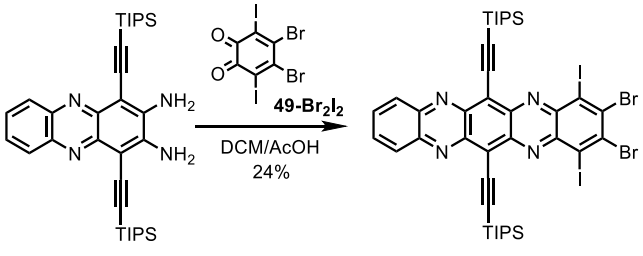

23b **58b**

2,3-dibromo-1,4-diiodo-6,13-bis((triisopropylsilyl)ethynyl)quinoxalino[2,3-b]phenazine (58b): GP4 was applied to **23b** (800 mg, 1.40 mmol) and **49-Br$_2$I$_2$** (870 mg, 1.68 mmol) in

DCM/acetic acid (20 mL, 1:1) yielding **58b** (485 mg, 462 µmol, 33%) as a green powderous solid. m.p. >350 °C (decomp.). ^{1}H NMR (500 MHz, $CDCl_3$, r.t.) δ = 8.20 (dd, *J* = 7.0, 3.4 Hz, 2H), 7.87 (dd, *J* = 7.0, 3.3 Hz, 2H), 1.44-1.22 (m, 42H) ppm. ^{13}C NMR (126 MHz, $CDCl_3$, r.t.) δ = 146.0, 144.2, 143.6, 142.8, 137.3, 132.9, 130.7, 123.1, 114.5, 114.3, 103.0, 19.3, 11.9 ppm. IR: $\tilde{\nu}$ = 2937, 2860, 1525, 1438, 1380, 1336, 1115, 1024, 881, 750, 672 cm^{-1}. HR-MS(MALDI+): *m/z* $[M+H]^+$ calcd for $C_{40}H_{47}Br_2I_2N_4Si_2$: 1054.9941; found: 1054.9941. R_f = 0.32 (SiO_2, PE / DCM 5:1, v/v).

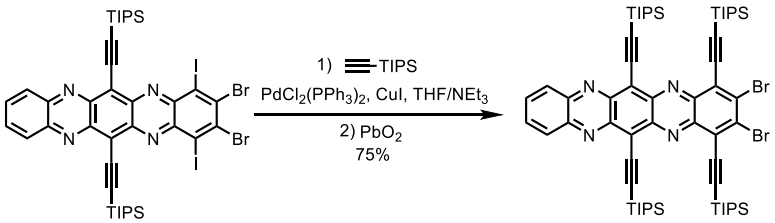

2,3-dibromo-1,4,6,13-tetrakis((triisopropylsilyl)ethynyl)quinoxalino[2,3-b]phenazine (59b): GP5 was applied to **58b** (460 mg, 437 µmol), CuI (41.5 mg, 218 µmol), $(PPh_3)_2PdCl_2$ (61.3 mg, 87.4 µmol) and TIPS acetylene (797 mg, 4.37 mmol) in THF/triethylamine (13 mL, 1:1) yielding **59b** (381 mg, 328 µmol, 75%) as a green powderous solid. m.p. >350 °C (decomp.). ^{1}H NMR (500 MHz, $CDCl_3$, r.t.) δ = 8.20 (dd, *J* = 6.9, 3.4 Hz, 2H), 7.83 (dd, *J* = 7.1, 3.4 Hz, 2H), 1.36-1.16 (m, 84H) ppm. ^{13}C NMR (126 MHz, $CDCl_3$, r.t.) δ = 145.7, 144.3, 142.6, 141.3, 136.0, 132.4, 130.5, 126.6, 123.4, 115.1, 109.7, 103.7, 103.6, 19.2, 19.1, 12.1, 11.9 ppm. IR: $\tilde{\nu}$ = 2941, 2864, 2360, 2340, 1444, 1275, 1080, 1016, 882, 842, 764, 671 cm^{-1}. HR-MS(MALDI+): *m/z* $[M+H]^+$ calcd for $C_{62}H_{89}Br_2N_4Si_4$ 1162.4732; found 1162.4760. R_f = 0.38 (SiO_2, PE / DCM 10:1, v/v).

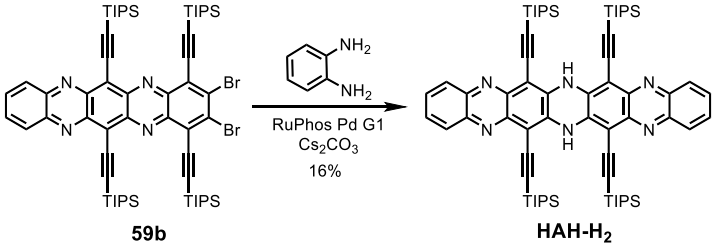

6,8,15,17-tetrakis((triisopropylsilyl)ethynyl)-7,16-dihydropyrazino[2,3-b:5,6b']diphenazine (HAH-H_2): **GP6** was applied to **59b** (355 mg, 305 µmol), *o*-phenylenediamine (49.6 mg, 457 mol), RuPhos Pd G1 (125 mg, 153 µmol) P(*t*-Bu)$_3$HBF$_4$ (44.3 mg, 153 µmol)

and Cs_2CO_3 (397 mg, 1.22 mmol) yielding **HAH-H₂** (54.1 mg, 48.9 µmol, 16%) as a red flaky crystalline. m.p. >350 °C (decomp.). ^{1}H NMR (500 MHz, $CDCl_3$, r.t.) δ = 8.30 (s, 2H), 8.05 (dd, *J* = 6.6, 3.4 Hz, 2H), 7.67 (dd, *J* = 6.7, 3.4 Hz, 2H), 1.35-1.21 (m, 84H) ppm. ^{13}C NMR (126 MHz, $CDCl_3$, r.t.) δ = 143.3, 142.9, 134.2, 129.6, 129.4, 109.2, 101.9, 98.7, 19.3, 12.3 ppm. IR: $\tilde{\nu}$ = 3345, 2941, 2864, 2360, 1582, 1476, 1433, 1275, 1210, 1061, 883, 750 cm^{-1}. HR-MS(ESI+): *m/z* $[M+H]^+$ calcd for $C_{68}H_{95}N_6Si_4$ 1107.6690; found 1107.6690. R_f = 0.45 (SiO_2, PE / DCM 2:1, v/v).

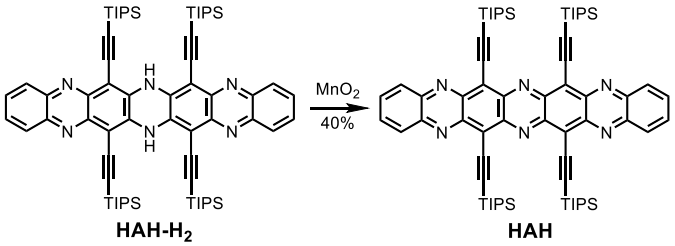

6,8,15,17-tetrakis((triisopropylsilyl)ethynyl)pyrazino[2,3-b:5,6-b']diphenazine (HAH): **GP8** was applied to **HAH-H₂** (10.0 mg, 9.03 µmol) and MnO_2 (78.5 mg, 903 µmol) yielding **HAH** (3.99 mg, 3.61 µmol, 40%) as a dark brown microcrystalline solid. m.p. >130 °C (decomposed into dark red solid with a red shine). ^{1}H NMR (600 MHz, $CDCl_3$, r.t.) δ = 8.13 (dd, *J* = 6.9, 3.3 Hz, 2H), 7.78 (dd, *J* = 7.0, 3.3 Hz, 2H), 1.37-1.21 (m, 84H) ppm. ^{13}C NMR (151 MHz, $CDCl_3$, r.t.) δ = 146.0, 145.1, 142.6, 132.5, 130.4, 123.4, 118.0, 104.3, 19.1, 12.0 ppm. IR: $\tilde{\nu}$ = 2940, 2861, 2369, 1524, 1456, 1381, 1275, 1111, 1015, 880, 747, 672 cm^{-1}. HR-MS(ESI+): *m/z* $[M+H]^+$ calcd for $C_{68}H_{93}N_6Si_4$ 1105.6535; found 1105.6533. R_f = 0.48 (SiO_2, PE / DCM 1:1, v/v).

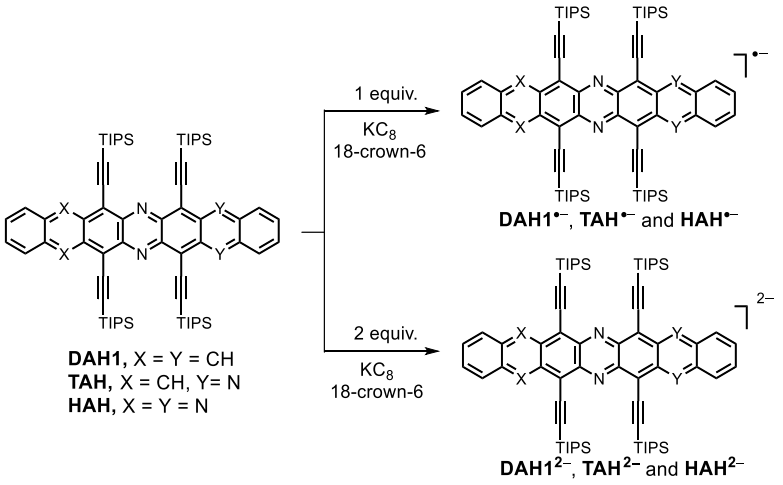

DAH1$^{\bullet-}$: **DAH1** (10.0 mg, 9.08 μmol) and KC_8-(18-crown-6) (4.0 mg, 9.98 μmol) were dissolved in dry THF (5 mL) in a 20 mL vial and stirred for 10 min in a nitrogen filled glove box to generate a dark red solution. After filtration, the solution was used for UV-Vis and EPR measurements. Attempts to obtain single crystalline specimen for single crystal analysis were not met with success.

DAH1^{2-}: **DAH1** (8.0 mg, 7.26 μmol) and KC_8-(18-crown-6) (6.4 mg, 15.97 μmol) were dissolved in dry THF (5 mL) in a 20 mL vial and stirred for 10 min in a nitrogen filled glove box to generate a dark yellow solution.

TAH$^{\bullet-}$: **TAH** (10.0 mg, 9.06 μmol) and KC_8-(18-crown-6) (4.0 mg, 9.96 μmol) were dissolved in dry THF (5 mL) in a 20 mL vial and stirred for 10 min in a nitrogen filled glove box to generate a dark red solution. After filtration, violet crystals formed on slow diffusion of dry pentane into the filtrate at 4 °C.

TAH^{2-}: **TAH** (8.0 mg, 7.25 μmol) and KC_8-(18-crown-6) (6.4 mg, 15.94 μmol) were dissolved in dry THF (5 mL) in a 20 mL vial and stirred for 10 min in a nitrogen filled glove box to generate a dark yellow solution.

HAH$^{\bullet-}$: **HAH** (10.0 mg, 9.04 μmol) and KC_8-(18-crown-6) (4.0 mg, 9.95 μmol) were dissolved in dry THF (5 mL) in a 20 mL vial and stirred for 10 min in a nitrogen filled glove box to generate a dark red solution. After filtration, violet crystals formed on slow diffusion of dry pentane into the filtrate at 4 °C.

HAH^{2-}: **HAH** (8.0 mg, 7.23 μmol) and KC_8-(18-crown-6) (6.4 mg, 15.92 μmol) were dissolved in dry THF (5 mL) in a 20 mL vial and stirred for 10 min in a nitrogen filled glove box to generate a dark yellow solution.

6.2.3 Synthesis of Tetraazahexacenes (Chapter 4)

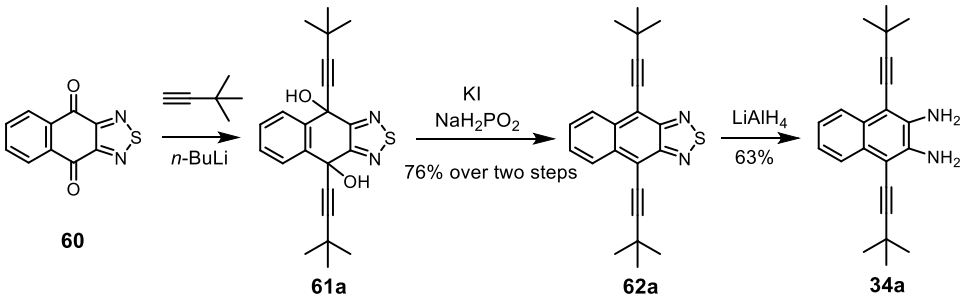

4,9-bis(3,3-dimethylbut-1-yn-1-yl)naphtho[2,3-c][1,2,5]thiadiazole (62a): To an heatgun-dried Schlenk flask was added *tert*-butylacetylene (1.20 mL, 9.71 mmol, 4.20 equiv.) and dry THF (10 mL), followed by 2.5 M n-butyllithium in hexane (3.70 mL, 9.25 mmol, 4.00 equiv.) at 0 °C. The solution was stirred at room temperature for 1 h, and then compound naphtho[2,3-c][1,2,5]thiadiazole-4,9-dione **60** (500 mg, 2.31 mmol, 1.00 equiv.) was added to the solution. The mixture was stirred at room temperature overnight and then quenched with wet diethyl ether. The residue was washed with water over three times and the solvent was evaporated to obtain the corresponding diol **61a** as viscous liquid. Without further characterization, the crude **61a** was suspended in acetic acid (20 mL) and potassium iodide (3.07 g, 18.5 mmol, 8.00 equiv.) and NaH_2PO_2 (1.63 g, 18.5 mmol, 8.00 equiv.) were added. The mixture was heated to reflux for 2 h. After cooling to room temperature, water (100 mL) was added to the mixture and the aqueous solution was extracted with dichloromethane (3 × 80 mL). The combined organic layers were dried in vacuum. The crude was further purified by chromatography on silica gel using a PE/DCM (v/v, 10:1) solvent mixture yielding **62a** (607 mg, 1.75 mmol, 76%, two steps) as a red crystalline solid. m.p. >350 °C (decomp.). ^{1}H NMR (500 MHz, $CDCl_3$, r.t.) δ = 8.45 (dd, *J* = 6.8, 3.2 Hz, 2H), 7.52 (dd, *J* = 6.9, 3.2 Hz, 2H), 1.54 (s, 18H) ppm. ^{13}C NMR (126 MHz, $CDCl_3$, r.t.) δ = 152.8, 134.9, 128.2, 126.9, 113.6, 112.7, 75.0, 31.8, 30.8 ppm. IR: $\tilde{\boldsymbol{\nu}}$ = 2964, 1455, 1397, 1360, 1251, 1202, 880, 855, 753, 521 cm^{-1}. HR-MS(ESI+): *m/z* $[M]^+$ calcd for $C_{22}H_{22}N_2S$ 346.1498; found 346.1499. R_f = 0.65 (SiO_2,PE / DCM 15:1, v/v).

1,4-bis(3,3-dimethylbut-1-yn-1-yl)naphthalene-2,3-diamine (34a): To a heatgun-dried Schlenk tube was added **62a** (450 mg, 1.30 mmol, 1.00 equiv.) and dry THF (5 mL). After

cooling to 0°C, $LiAlH_4$ (109 mg, 2.86 mmol, 2.20 equiv.) was added in small portions under N_2. After 2 h stirring at room temperature the mixture was quenched with a saturated NH_4Cl-solution. After adding water and dichloromethane, the aqueous phase was separated and washed three times with dichloromethane (3 × 50 mL). The combined organic layers were dried over $MgSO_4$ and the filtrate was evaporated. Purification by flash column chromatography using PE/EtOAc (v/v, 10:1) yielding **34a** (258 mg, 0.81 mmol, 63%) a dark yellow powderous solid. m.p. >350 °C (decomp.). ^{1}H NMR (400 MHz, $CDCl_3$, r.t.) δ = 8.03 (dd, J = 6.2, 3.3 Hz, 2H), 7.36 (dd, *J* = 6.3, 3.3 Hz, 2H), 4.33 (s, 4H), 1.54 (s, 18H) ppm. ^{13}C NMR (101 MHz, $CDCl_3$, r.t.) δ = 138.7, 128.5, 124.9, 124.6, 106.4, 103.5, 100.1, 1.2, 0.4 ppm. IR: $\tilde{\boldsymbol{\nu}}$ = 3398, 3319, 2962, 2862, 1613, 1508, 1437, 1360, 1259, 1027, 797, 752, 701, 625 cm^{-1}. HR-MS(ESI+): *m/z* $[M]^+$ calcd for $C_{22}H_{26}N_2$ 318.2091; found 318.2096. R_f = 0.35 (SiO_2, PE / EE 5:1, v/v).

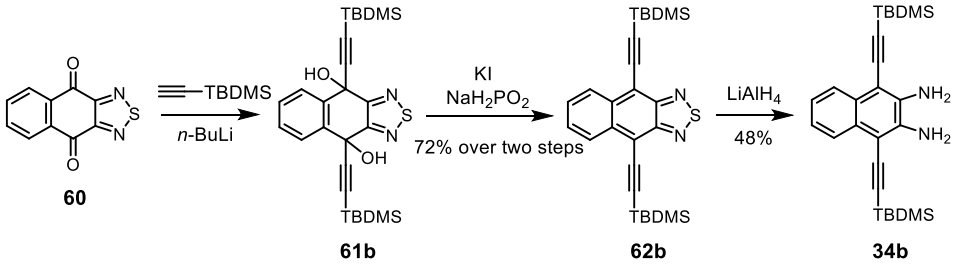

4,9-bis((tert-butyldimethylsilyl)ethynyl)naphtho[2,3-c][1,2,5]thiadiazole (62b): To an heatgun-dried Schlenk flask was added *tert*-butyldimethylsilylacetylene (3.63 mL, 19.4 mmol, 4.20 equiv.) and dry THF (20 mL), followed by 2.5 M n-butyllithium in hexane (7.40 mL, 18.5 mmol, 4.00 equiv.) at 0 °C. The solution was stirred at room temperature for 1 h, and then compound naphtho[2,3-c][1,2,5]thiadiazole-4,9-dione **60** (1.00 g, 4.63 mmol, 1.00 equiv.) was added to the solution. The mixture was stirred at room temperature overnight and then quenched with wet diethyl ether. The residue was washed with water over three times and the solvent was evaporated to obtain the corresponding diol **61b** as viscous liquid. Without further characterization, the crude **61b** was suspended in acetic acid (40 mL) and potassium iodide (6.15 g, 37.0 mmol, 8.00 equiv.) and NaH_2PO_2 (3.26 g, 37.0 mmol, 8.00 equiv.) were added. The mixture was heated to reflux for 2 h. After cooling to room temperature, water (200 mL) was added to the mixture and the aqueous solution was extracted with dichloromethane (3 ×

150 mL). The combined organic layers were dried in vacuum. The crude was further purified by chromatography on silica gel using a PE/DCM (v/v, 10:1) solvent mixture yielding **62b** (1.53 g, 3.31 mmol 72%, two steps) as a red crystalline solid. m.p. >350 °C (decomp.). ^{1}H NMR (400 MHz, $CDCl_3$, r.t.) δ = 8.53 (dd, *J* = 6.8, 3.2 Hz, 2H), 7.56 (dd, *J* = 6.9, 3.2 Hz, 2H), 1.13 (s, 18H), 0.36 (s, 12H) ppm. ^{13}C NMR (101 MHz, $CDCl_3$, r.t.) δ = 153.4, 135.6, 128.4, 128.0, 113.2, 109.6, 100.7, 26.8, 17.4, -4.0 ppm. IR: $\tilde{\nu}$ = 2926, 2855, 1460, 1386, 1361, 1246, 1040, 1005, 926, 808, 759, 676, 527 cm^{-1}. HR-MS(ESI+): *m/z* $[M]^+$ calcd for $C_{26}H_{34}N_2SSi_2$ 462.1976; found 462.1986. R_f = 0.55 (SiO_2, PE / DCM 1:15, v/v).

1,4-bis((tert-butyldimethylsilyl)ethynyl)naphthalene-2,3-diamine (34b): To a heatgun-dried Schlenk tube was added **62b** (850 mg, 1.84 mmol, 1.00 equiv.) and dry THF (20 mL). After cooling to 0°C, $LiAlH_4$ (153 mg, 4.04 mmol, 2.20 equiv.) was added in small portions under N_2. After 2 h stirring at room temperature the mixture was quenched with a saturated NH_4Cl-solution. After adding water and dichloromethane, the aqueous phase was separated and washed three times with dichloromethane (3 × 80 mL). The combined organic layers were dried over $MgSO_4$ and the filtrate was evaporated. Purification by flash column chromatography using PE/EtOAc (v/v, 10:1) yielding **34b** (385 mg, 0.89 mmol, 48%) a dark yellow powderous solid. m.p. >350 °C (decomp.). ^{1}H NMR (400 MHz, $CDCl_3$, r.t.) δ = 8.08 (dd, *J* = 5.0, 2.6 Hz, 2H), 7.36 (dd, *J* = 5.0, 2.6 Hz, 2H), 4.37 (s, 4H), 1.13 (s, 18H), 0.38 (s, 12H) ppm. ^{13}C NMR (101 MHz, $CDCl_3$, r.t.) δ = 138.8, 128.6, 124.9, 124.6, 103.9, 102.6, 102.0, 26.5, 17.2, -3.7 ppm. IR: $\tilde{\nu}$ = 3446, 3354, 2926.45, 2854, 2136, 1619, 1506, 1439, 1247, 1019, 831, 771, 687, 615 cm^{-1}. HR-MS(ESI+): *m/z* $[M]^+$ calcd for $C_{26}H_{38}N_2Si_2$ 434.7740; found 434.7732. R_f = 0.35 (SiO_2, PE / EE 5:1, v/v).

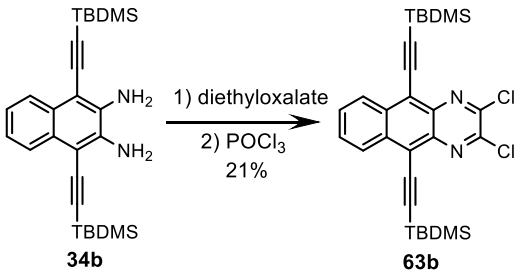

34b **63b**

5,10-bis((*tert*-butyldimethylsilyl)ethynyl)-2,3-dichlorobenzo quinoxaline (63b): A mixture of **34b** (350 mg, 805 µmol) and diethyloxalate (5.00 mL) was heated to reflux overnight. The mixture was evaporated and dried at 90°C under vacuum. The dark brown solid was dissolved in $POCl_3$ (5.00 mL) and heated to reflux for 20 h. After cooling down to room temperature, the reaction mixture was poured into water and neutralized with 1M NaOH solution. The residue was extracted three times with DCM, and the combined organic layers were dried over $MgSO_4$. The orange-black solution was evaporated and purified by flash column chromatography (PE/DCM, 5:1) to furnish **63b** (88.5 mg, 168 µmol, 21 %) as orange powderous solid. m.p. >350 °C (decomp.). ^{1}H NMR (400 MHz, $CDCl_3$, r.t.) δ = 8.65 (dd, *J* = 6.6, 3.3 Hz, 2H), 7.73 (dd, *J* = 6.6, 3.3 Hz, 2H), 1.14 (s, 18H), 0.34 (s, 12H) ppm. ^{13}C NMR (101 MHz, $CDCl_3$, r.t.) δ = 146.7, 139.1, 134.9, 129.2, 128.1, 120.5, 110.3, 100.0, 26.7, 17.5 ppm. IR: $\tilde{\boldsymbol{\nu}}$ = 2940, 2862, 1460, 1385, 1311, 1175, 1051, 1013, 880, 768, 723., 666, 583, 489 cm^{-1}. HR-MS(ESI+): *m/z* $[M]^+$ calcd for $C_{28}H_{34}Cl_2N_2Si_2$ 525.6640; found 525.6645. R_f = 0.46 (SiO_2, PE / DCM 10:1, v/v).

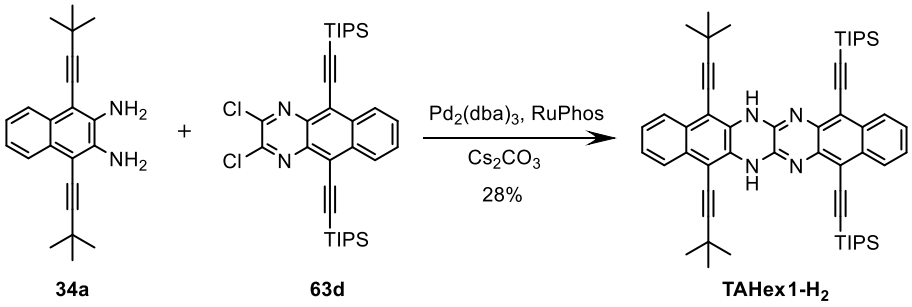

5,16-bis(3,3-dimethylbutyl)-8,13-bis((triisopropylsilyl)ethynyl)-6,15-dihydrobenzo-[6,7] quinoxalino [2,3] quinoxaline (TAHex1-H$_2$): **GP7** was applied to dichloro **63d** (50.0 mg, 82.0 µmol), diamino **34a** (39.2 mg, 123 µmol), $Pd_2(dba)_3$ (37.5 mg, 41.0 µmol), RuPhos (38.3 mg, 82.0 µmol) and Cs_2CO_3 (267 mg, 820 µmol) yielding **TAHex1-H$_2$** (19.6 mg, 22.9 µmol, 28 %) as a yellow powderous solid. m.p. >350 °C (decomp.). ^{1}H NMR (600 MHz, CD_2Cl_2, r.t.) δ = 8.32 (dd, *J* = 7.0, 3.4 Hz, 2H), 8.18-8.06 (m, 4H), 7.48 (dd, *J* = 7.0, 3.3 Hz, 2H), 7.43 (dd, *J* = 6.6, 3.4 Hz, 2H), 1.46 (s, 18H), 1.27-1.19 (m, 42H) ppm. ^{13}C NMR (151 MHz, CD_2Cl_2, r.t.) δ = 142.0, 135.9, 131.9, 131.3, 129.9, 126.8, 126.5, 126.1, 125.6, 124.6, 115.9, 112.6, 105.0, 101.7, 71.2, 31.4, 29.2, 19.1, 11.9 ppm. IR: $\tilde{\boldsymbol{\nu}}$ = 2924, 2863, 2360, 1453, 1362, 1261, 1079,

1016, 882, 801, 739, 676 cm^{-1}. HR-MS(ESI+): *m/z* $[M]^+$ calcd for $C_{56}H_{70}N_4Si_2$ 854.5134; found 854.5144. R_f = 0.58 (SiO_2, PE / Et_2O 20:1, v/v).

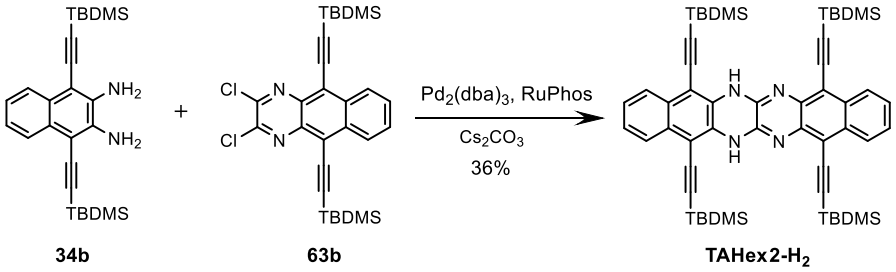

34b **63b** **TAHex2-H_2**

5,8,13,16-tetrakis((tert-butyldimethylsilyl)ethynyl)-6,15-dihydrobenzo-[6,7] quinoxalino [2,3]quinoxaline (TAHex2-H_2): GP7 was applied to dichloro **63b** (35.0 mg, 66.6 µmol), diamino **34b** (43.4 mg, 99.8 µmol), $Pd_2(dba)_3$ (30.5 mg, 33.3 µmol), RuPhos (31.1 mg, 66.6 µmol) and Cs_2CO_3 (217 mg, 666 µmol) yielding **TAHex2-H_2** (21.0 mg, 23.7 µmol, 36%) as a yellow powderous solid. m.p. >350 °C (decomp.). ^{1}H NMR (400 MHz, CD_2Cl_2, r.t.) δ = 8.19 (dd, *J* = 8.3, 4.4 Hz, 4H), 7.34 (dd, *J* = 8.4, 4.4 Hz, 4H), 4.41 (s, 2H), 1.13 (s, 36H), 0.35 (s, 24H) ppm. ^{13}C NMR (101 MHz, CD_2Cl_2, r.t.) δ = 139.3, 129.8, 128.6, 125.0, 124.8, 105.1, 103.3, 100.9, 26.5, 17.1 ppm. IR: $\tilde{\nu}$ = 2939, 2866, 1451, 1280, 1261, 1015, 882, 755, 670, 585 cm^{-1}. HR-MS(ESI+): *m/z* $[M]^+$ calcd for $C_{54}H_{70}N_4Si_4$ 886.4672; found 886.4680. R_f = 0.58 (SiO_2, PE / Et_2O 20:1, v/v).

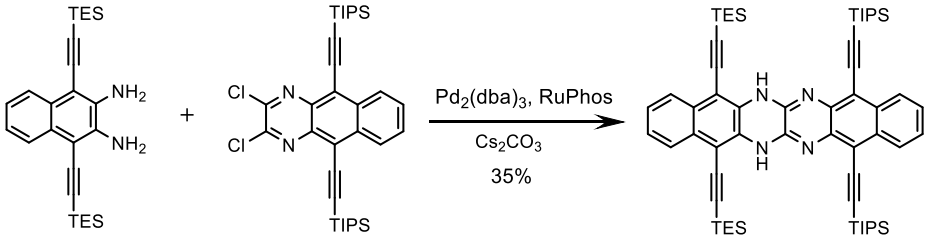

34c **63d** **TAHex3-H_2**

5,8,13,16-tetrakis((tert-butyldimethylsilyl)ethynyl)-6,15-dihydrobenzo-[6,7] quinoxalino [2,3]quinoxaline (TAHex3-H_2): GP7 was applied to dichloro **63d** (30.0 mg, 49.2 µmol), diamino **34c** (32.1 mg, 73.8 µmol), $Pd_2(dba)_3$ (22.5 mg, 24.6 µmol), RuPhos (23.0 mg, 49.2 µmol) and Cs_2CO_3 (160 mg, 492 µmol) yielding **TAHex3-H_2** (16.5 mg, 17.0 µmol, 35%) as a yellow powderous solid. m.p. >350 °C (decomp.). ^{1}H NMR (400 MHz, CD_2Cl_2, r.t.) δ = 8.43 (dd, *J* = 5.0, 2.6 Hz, 2H), 8.07 (dd, *J* = 5.2, 2.7 Hz, 2H), 8.04(s, 2H), 7.51 (dd, *J* = 5.2, 2.7 Hz,

2H), 7.46 (dd, *J* = 5.1, 2.6 Hz, 2H), 1.33-1.15 (m, 60H), 0.94-0.78 (m, 12H) ppm. ^{13}C NMR (101 MHz, CD_2Cl_2, r.t.) δ = 141.9, 140.0, 136.3, 133.2, 130.1, 127.0, 125.8, 116.1, 108.1, 106.9, 105.4, 104.5, 103.4, 99.1, 98.2, 19.1, 11.8, 7.9, 4.9 ppm. IR: $\tilde{\nu}$ = 2923, 2862, 1455, 1426, 1392, 1364, 1259, 1052, 1015, 880, 799, 761, 727, 668, 597 cm^{-1}. HR-MS(ESI+): *m/z* $[M]^+$ calcd for $C_{60}H_{82}N_4Si_4$ 970.5611; found 970.5602. R_f = 0.58 (SiO_2, PE / Et_2O 20:1, v/v).

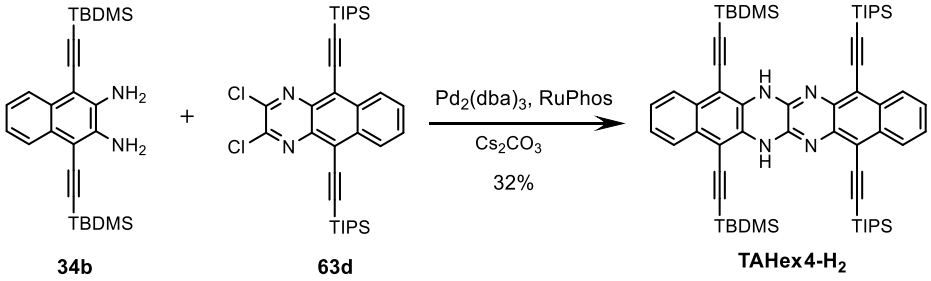

5,8,13,16-tetrakis((tert-butyldimethylsilyl)ethynyl)-6,15-dihydrobenzo-[6,7] quinoxalino [2,3]quinoxaline (TAHex4-H$_2$): GP7 was applied to dichloro **63d** (30.0 mg, 57.1 µmol), diamino **34b** (32.1 mg, 73.8 µmol), $Pd_2(dba)_3$ (22.5 mg, 24.6 µmol), RuPhos (23.0 mg, 49.2 µmol) and Cs_2CO_3 (168 mg, 492 µmol) yielding **TAHex4-H$_2$** (15.3 mg, 15.7 µmol, 32%) as a yellow powderous solid. m.p. >350 °C (decomp.). ^{1}H NMR (400 MHz, CD_2Cl_2, r.t.) δ = 8.41 (dd, *J* = 4.6, 2.2 Hz, 2H), 8.11 (dd, *J* = 4.6, 2.2 Hz, 2H), 8.06 (s, 2H), 7.49 (dd, *J* = 4.4, 2.3 Hz, 2H), 7.44 (dd, *J* = 4.4, 2.2 Hz, 2H), 1.35-1.27 (m, 36H), 1.19 (s, 26H), 0.48 (s, 10H) ppm. ^{13}C NMR (101 MHz, CD_2Cl_2, r.t.) δ = 142.0, 139.9, 136.4, 133.0, 130.2, 127.0, 125.8, 125.1, 116.3, 108.3, 106.2, 104.9, 103.1, 101.6, 98.9, 30.1, 26.5, 19.1, 17.1, 11.9 ppm IR: $\tilde{\nu}$ = 2940, 2863, 1455, 1426, 1275, 1260, 1015, 881, 751, 677, 586 cm^{-1}. HR-MS(ESI+): *m/z* $[M]^+$ calcd for $C_{60}H_{82}N_4Si_4$ 970.5611; found 970.5601. R_f = 0.58 (SiO_2, PE / Et_2O 20:1, v/v).

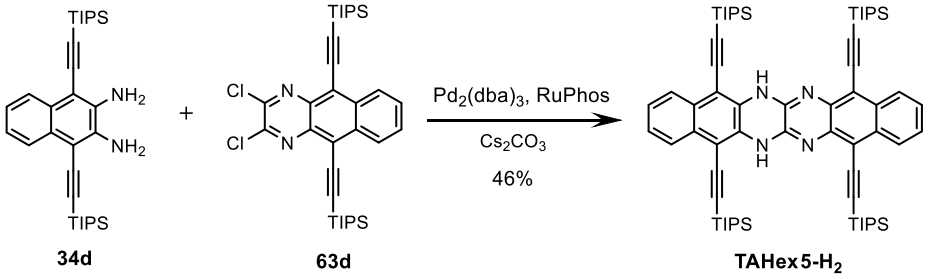

5,8,13,16-tetrakis((triisopropylsilyl)ethynyl)-6,15-dihydrobenzo-[6,7] quinoxalino [2,3] quinoxaline (TAHex5-H$_2$): GP7 was applied to dichloro **63d** (25.0 mg, 41.0 µmol), diamino

34d (31.9 mg, 61.5 µmol),$Pd_2(dba)_3$ (18.8 mg, 20.5 µmol), RuPhos (19.1 mg, 41.0 µmol) and Cs_2CO_3 (134 mg, 410 µmol) yielding **TAHex5-H₂** (19.9 mg, 18.9 µmol, 46%) as a yellow powderous solid. m.p. >350 °C (decomp.). ^{1}H NMR (600 MHz, CD_2Cl_2, r.t.) δ = 8.05 (dd, *J* = 6.2, 3.3 Hz, 4H), 7.34 (dd, *J* = 6.2, 3.3 Hz, 4H), 4.43 (s, 2H), 1.25-1.16 (m, 84H) ppm. ^{13}C NMR (151 MHz, CD_2Cl_2, r.t.) δ = 139.3, 128.7, 125.1, 124.7, 103.6, 103.1, 102.2, 19.0, 11.7 ppm. IR: $\tilde{\nu}$ = 2939, 2866, 1451, 1280, 1261, 1015, 882, 755, 670, 585 cm^{-1}. HR-MS(ESI+): *m/z* $[M+H]^+$ calcd for $C_{66}H_{95}N_4Si_4$ 1055.6628; found 1055.6638. R_f = 0.58 (SiO_2, PE / Et_2O 20:1, v/v).

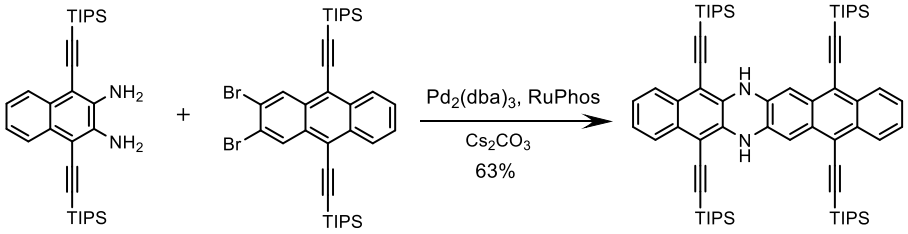

5,8,13,16-tetrakis((triisopropylsilyl)ethynyl)-6,15-dihydrobenzo[b]naphtho[2,3-i] phenazine (DAHex-H₂): **GP7** was applied to dibromo **55** (25.0 mg, 41.1 µmol), diamino **34d** (32.0 mg, 61.7 µmol), $Pd_2(dba)_3$ (18.8 mg, 20.6 µmol), RuPhos (19.2 mg, 41.1 µmol) and Cs_2CO_3 (134 mg, 411 µmol) yielding **DAHex-H₂** (27.3 mg, 25.9 µmol, 63%) as a yellow powderous solid. m.p. >350 °C (decomp.). ^{1}H NMR (500 MHz, CD_2Cl_2, r.t.) δ = 8.44 (dd, *J* = 3.8, 1.9 Hz, 2H), 7.93 (dd, *J* = 3.5, 1.9 Hz, 2H), 7.46 (dd, *J* = 3.8, 1.8 Hz, 2H), 7.32 (s, 2H), 7.29 (dd, *J* = 3.5, 1.8 Hz, 2H), 7.05(s, 2H), 1.39-0.71 (m, 84H) ppm. ^{13}C NMR (126 MHz, CD_2Cl_2, r.t.) δ = 133.1, 132.5, 132.3, 131.7, 131.2, 130.3, 130.2, 127.0, 126.4, 125.7, 125.1, 115.5, 105.5, 104.0, 101.7, 100.3, 30.1, 19.1, 12.0, 11.8, 1.2 ppm. IR: $\tilde{\nu}$ = 2942, 2861, 1462, 1436, 1388, 1362, 1049, 1015, 995, 882, 757 cm^{-1}. HR-MS(ESI+): *m/z* $[M]^+$ calcd for $C_{68}H_{96}N_2Si_4$ 1052.6645; found 1052.6639. R_f = 0.65 (SiO_2, PE / Et_2O 20:1, v/v).

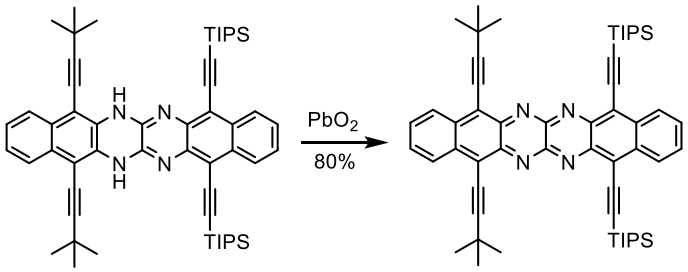

TAHex1-H$_2$ **TAHex1**

5,16-bis(3,3-dimethylbutyl)-8,13-bis((triisopropylsilyl)ethynyl)benzo-[6,7] quinoxalino [2,3] quinoxaline (TAHex1): GP8 was applied to dihydro **TAHex1-H$_2$** (15.0 mg, 17.5 µmol) and PbO_2 (420 mg, 1.75 mmol) yielding **TAHex1** (11.8 mg, 13.8 µmol, 80%) as a brown crystalline solid. m.p. >350 °C (decomp.). ^{1}H NMR (600 MHz, CD_2Cl_2, r.t.) δ = 8.75 (dd, *J* = 3.9, 1.8 Hz, 2H), 8.62 (dd, *J* = 3.9, 1.8 Hz, 2H), 7.64 (dd, *J* = 3.9, 1.8 Hz, 2H), 7.60 (dd, *J* = 3.9, 1.8 Hz, 2H), 1.66 (s, 18H), 1.38-1.22 (m, 42 H) ppm. ^{13}C NMR (151 MHz, CD_2Cl_2, r.t.) δ = 145.4, 145.3, 144.2, 138.2, 137.8, 129.6, 129.3, 128.5, 128.4, 122.1, 122.0, 116.8, 110.9, 103.0, 76.4, 31.5, 28.0, 19.4, 11.9 ppm. IR: $\tilde{\boldsymbol{\nu}}$ = 2940, 2863, 1458, 1382, 1111, 882, 774, 672 cm^{-1}. HR-MS(ESI+): *m/z* $[M+2H]^+$ calcd for $C_{56}H_{70}N_4Si_2$ 854.5134; found 854.5145. R_f = 0.43 (SiO_2, PE / DCM 5:1, v/v).

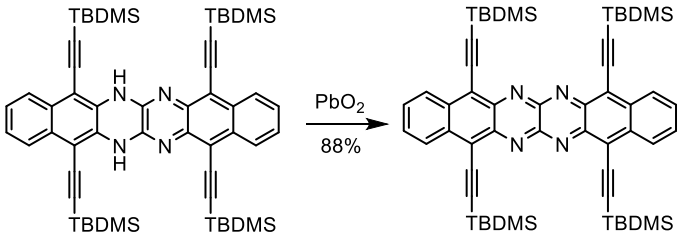

TAHex2-H$_2$ **TAHex2**

5,8,13,16-tetrakis((tert-butyldimethylsilyl)ethynyl)benzo-[6,7] quinoxalino [2,3] quinoxaline (TAHex2): GP8 was applied to dihydro **TAHex2-H$_2$** (18.0 mg, 20.3 µmol) and PbO_2 (485 mg, 2.03 mmol) yielding **TAHex2** (15.8 mg, 17.8 µmol, 88%) as a brown crystalline solid. m.p. >350 °C (decomp.). ^{1}H NMR (400 MHz, CD_2Cl_2, r.t.) δ = 8.71 (dd, *J* = 6.9, 3.2 Hz, 4H), 7.68 (dd, *J* = 6.9, 3.1 Hz, 4H), 1.21 (s, 36H), 0.47 (s, 24H) ppm. ^{13}C NMR (101 MHz, CD_2Cl_2, r.t.) δ = 145.5, 144.1, 138.5, 130.2, 128.4, 121.9, 112.7, 101.8, 26.7, 17.4 ppm. IR: $\tilde{\boldsymbol{\nu}}$ = 2940, 2863, 2174, 1462, 1439, 1392, 1365, 1053, 882, 761, 681 cm^{-1}. HR-MS(ESI+): *m/z* $[M+2H]^+$ calcd for $C_{54}H_{70}N_4Si_4$ 886.4672; found 886.4655. R_f = 0.45 (SiO_2, PE / DCM 5:1, v/v).

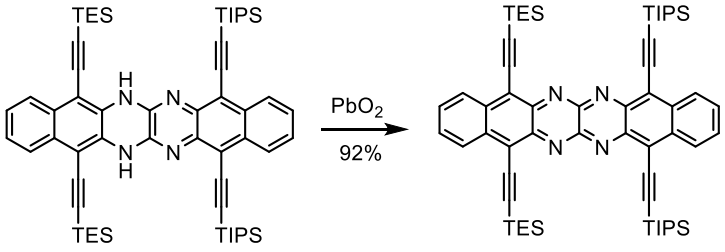

TAHex3-H$_2$ **TAHex3**

5,16-bis((triethylsilyl)ethynyl)-8,13-bis((triisopropylsilyl)ethynyl) benzo[g] benzo[6,7] quinoxalino [2,3-b]quinoxaline (TAHex3): GP8 was applied to dihydro **TAHex3-H$_2$** (15.0 mg, 15.4 µmol) and PbO_2 (369 mg, 1.54 mmol) yielding **TAHex3** (13.7 mg, 14.1 µmol, 92%) as a brown crystalline solid. m.p. >350 °C (decomp.). ^{1}H NMR (600 MHz, CD_2Cl_2, r.t.) δ = 8.75 (dd, *J* = 6.9, 3.2 Hz, 2H), 8.72 (dd, *J* = 6.8, 3.2 Hz, 2H), 7.67 (ddd, *J* = 6.9, 5.6, 3.1 Hz, 4H), 1.40-1.32 (m, 36H), 1.28-1.19 (m, 24H), 1.02-0.91 (m, 12H). ppm. ^{13}C NMR (151 MHz, CD_2Cl_2, r.t.) 145.7, 145.3, 144.2, 138.6, 138.4, 130.0, 129.9, 128.4, 122.0, 121.9, 111.9, 111.2, 103.1, 102.2, 19.2, 12.0, 7.9, 4.9 ppm. IR: $\tilde{\nu}$ = 2940, 2862, 2174, 1460, 1437, 1390, 1363, 1051, 880, 760, 656 cm^{-1}. HR-MS(ESI+): *m/z* $[M+H]^+$ calcd for $C_{60}H_{81}N_4Si_4$ 969.5533; found 969.5550. R_f = 0.48 (SiO_2, PE / DCM 5:1, v/v).

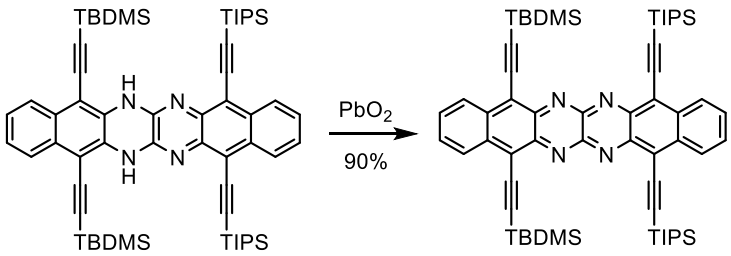

TAHex4-H$_2$ **TAHex4**

5,16-bis((tert-butyldimethylsilyl)ethynyl)-8,13-bis((triisopropylsilyl)ethynyl) benzo[g] benzo [6,7]quinoxalino[2,3-b]quinoxaline (TAHex4): GP8 was applied to dihydro **TAHex4-H$_2$** (12.0 mg, 12.3 µmol) and PbO_2 (295 mg, 1.23 mmol) yielding **TAHex4** (10.8 mg, 11.1 µmol, 90%) as a brown crystalline solid. m.p. >350 °C (decomp.). ^{1}H NMR (600 MHz, CD_2Cl_2, r.t.) δ = 8.75 (dd, *J* = 6.8, 3.1 Hz, 2H), 8.72 (dd, *J* = 6.8, 3.1 Hz, 2H), 7.68 (td, *J* = 6.7, 3.1 Hz, 4H), 1.45-1.30 (m, 36H), 1.19 (s, 26H), 0.46 (s, 10H) ppm. ^{13}C NMR (151 MHz, CD_2Cl_2, r.t.) δ = 145.7, 145.3, 144.1, 138.5, 138.5, 130.1, 130.0, 128.4, 128.3, 122.0, 121.9, 112.5, 111.2, 103.1, 101.8, 26.6, 19.2, 17.3, 12.0 ppm. IR: $\tilde{\nu}$ = 2940, 2862, 2172, 1460, 1436, 1388, 1361, 1054,

922, 880, 758, 650 cm^{-1}. HR-MS(ESI+): *m/z* $[M+2H]^+$ calcd for $C_{60}H_{82}N_4Si_4$ 970.5609; found 970.5601. R_f = 0.48 (SiO_2, PE / DCM 5:1, v/v).

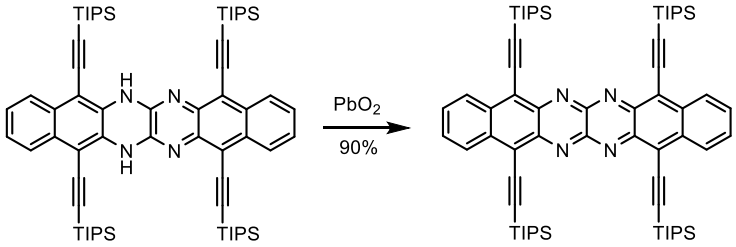

TAHex5-H$_2$ **TAHex5**

5,8,13,16-tetrakis((triisopropylsilyl)ethynyl)benzo-[6,7]quinoxalino[2,3]quinoxaline (TAHex5): GP8 was applied to dihydro **TAHex5-H$_2$** (22.0 mg, 20.8 µmol) and PbO_2 (498 mg, 2.08 mmol) yielding **TAHex5** (19.8 mg, 18.8 µmol, 90%) as a dark green crystalline solid. m.p. >350 °C (decomp.). ^{1}H NMR (600 MHz, CD_2Cl_2, r.t.) δ = 8.77 (dd, *J* = 6.9, 3.2 Hz, 4H), 7.66 (dd, *J* = 6.9, 3.1 Hz, 4H), 1.40-1.24 (m, 84 H) ppm. ^{13}C NMR (151 MHz, CD_2Cl_2, r.t.) δ = 145.5, 144.2, 138.6, 129.9, 128.5, 122.1, 111.2, 103.2, 19.2, 12.0 ppm. IR: $\tilde{\nu}$ = 2941, 2863, 2175, 1460, 1437, 1390, 1364, 1049, 993, 880, 759, 656 cm^{-1}. HR-MS(ESI+): *m/z* $[M+2H]^+$ calcd for $C_{66}H_{94}N_4Si_4$ 1054.6562; found 1054.6550. R_f = 0.45 (SiO_2, PE / DCM 5:1, v/v).

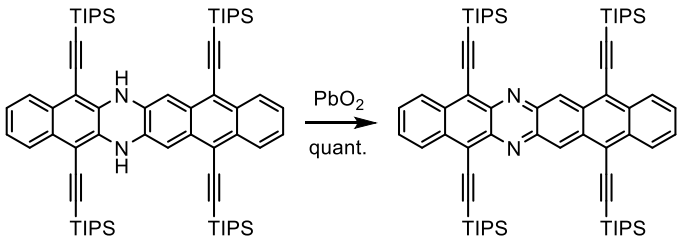

DAHex-H$_2$ **DAHex**

5,8,13,16-tetrakis((triisopropylsilyl)ethynyl)benzo[b]naphtho[2,3-i]phenazine (DAHex): **GP8** was applied to dihydro **DAHex-H$_2$** (20.0 mg, 19.0 µmol) and PbO_2 (454 mg, 1.90 mmol) yielding **DAHex** (19.9 mg, 18.9 quant.) as a brown crystalline solid. m.p. >350 °C (decomp.). ^{1}H NMR (600 MHz, CD_2Cl_2, r.t.) δ = 9.79 (s, 2H), 8.71 (dd, *J* = 4.5, 2.1 Hz, 2H), 8.64 (dd, *J* = 4.5, 2.1 Hz, 2H), 7.60 (dd, *J* = 4.6, 2.1 Hz, 2H), 7.56 (dd, *J* = 4.6, 2.1 Hz, 2H), 1.42-1.01 (m, 84H) ppm. ^{13}C NMR (151 MHz, CD_2Cl_2, r.t.) δ = 142.9, 141.8, 136.0, 134.7, 129.2, 128.9, 128.3, 128.2, 128.1, 121.4, 119.7, 118.1, 109.6, 108.6, 103.8, 103.6, 19.1, 12.0, 1.1 ppm. IR: $\tilde{\nu}$ = 2942, 2863, 1463 1390, 1362, 1260, 1048, 1016, 879, 799, 747 cm^{-1}. HR-MS(ESI+): *m/z* $[M+H]^+$ calcd for $C_{68}H_{95}N_2Si_4$ 1051.6567; found 1051.6549. R_f = 0.50 (SiO_2, PE / DCM 5:1, v/v).

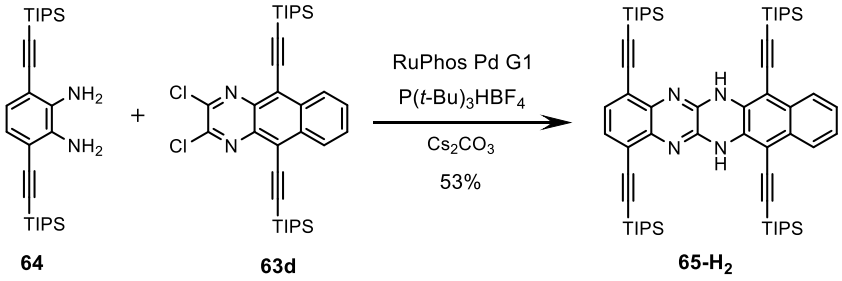

1,4,7,12-tetrakis((triisopropylsilyl)ethynyl)-6,13-dihydrobenzo[g]quinoxalino[2,3-b] quinoxaline (65-H₂): GP6 was applied to dichloro **63d** (20.0 mg, 32.8 µmol), diamino **64** (23.1 mg, 49.2 µmol), RuPhos Pd G1 (13.4 mg, 16.4 µmol), P(*t*-Bu)$_3$HBF$_4$ (4.76 mg, 16.4 µmol) and Cs_2CO_3 (42.7 mg, 132 µmol) yielding **65-H₂** (17.4 mg, 17.3 µmol, 53%) as a yellow powderous solid. m.p. >350 °C (decomp.). ^{1}H NMR (600 MHz, CD_2Cl_2, r.t.) δ = 8.02 (dd, *J* = 4.2, 2.2 Hz, 2H), 7.66 (s, 2H), 7.41 – 7.35 (m, (m, 4H)), 1.31-1.15 (m, 84H) ppm. ^{13}C NMR (151 MHz, CD_2Cl_2, r.t.) δ = 141.6, 140.5, 133.0, 131.6, 130.2, 126.7, 125.7, 125.3, 120.7, 106.6, 105.0, 102.9, 97.9, 30.1, 19.0, 14.3, 11.7, 1.1 ppm. IR: $\tilde{\nu}$ = 3350, 2939, 2866, 1451, 1280, 1261, 1015, 882, 755, 670, 585 cm^{-1}. HR-MS(ESI+): *m/z* $[M]^+$ calcd for $C_{62}H_{92}N_4Si_4$ 1005.7860; found 1005.7858. R_f = 0.65 (SiO_2, PE / DCM 5:1, v/v).

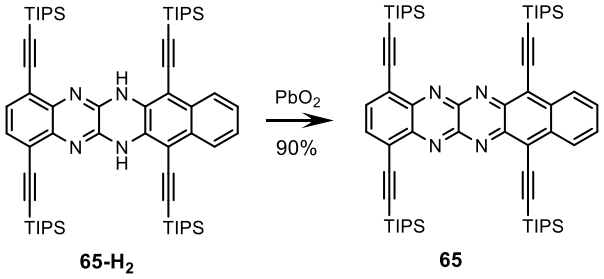

1,4,7,12-tetrakis((triisopropylsilyl)ethynyl)benzo[g]quinoxalino[2,3-b]quinoxaline (65): **GP8** was applied to dihydro **65-H₂** (5.00 mg, 4.97 µmol) and PbO_2 (119 mg, 497 µmol) yielding **65** (4.50 mg, 4.48 µmol, 90%) as a brown crystalline solid. m.p. >350 °C (decomp.). ^{1}H NMR (600 MHz, $CDCl_3$, r.t.) δ = 8.78 (dd, *J* = 6.8, 3.2 Hz, 1H), 8.05 (s, 1H), 7.65 (dd, *J* = 6.9, 3.1 Hz, 1H), 1.39-1.13 (m, 84H) ppm. ^{13}C NMR (151 MHz, $CDCl_3$, r.t.) δ = 148.0, 144.6, 144.0, 137.8, 129.3, 128.2, 125.5, 121.9, 110.7, 103.4, 102.8, 102.5, 19.0, 11.6 ppm. IR: $\tilde{\nu}$ = 2941, 2863, 2175, 1460, 1437, 1390, 1364, 1049, 993, 880, 759, 656 cm^{-1}. HR-MS(ESI+): *m/z* $[M]^+$ calcd for $C_{62}H_{90}N_4Si_4$ 1003.7700; found 1003.7704. R_f = 0.66 (SiO_2, PE / DCM 5:1, v/v).

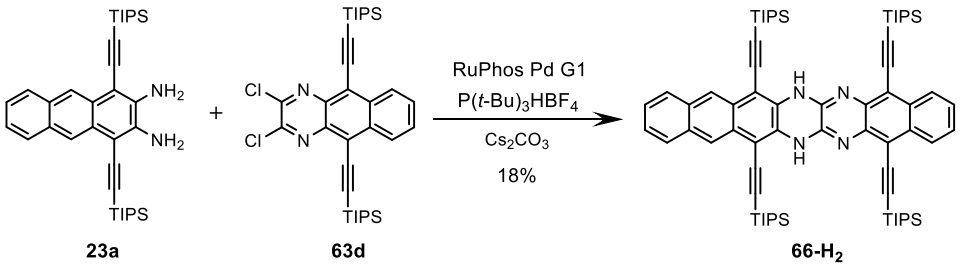

5,8,15,18-tetrakis((triisopropylsilyl)ethynyl)-7,16-dihydrobenzo[6,7]quinoxalino[2,3-b] naphtho[2,3-g]quinoxaline (66-H$_2$): **GP6** was applied to dichloro **63d** (20.0 mg, 32.8 µmol), diamino **23a** (28.0 mg, 49.2 µmol), RuPhos Pd G1 (13.4 mg, 16.4 µmol), P(*t*-Bu)$_3$HBF$_4$ (4.76 mg, 16.4 µmol) and Cs_2CO_3 (42.7 mg, 132 µmol) yielding **66-H$_2$** (6.50 mg, 5.88 µmol, 18%) as a red powderous solid. m.p. >350 °C (decomp.). ^{1}H NMR (600 MHz, $CDCl_3$, 253 K) δ = 8.64 (m, 2H), 8.46 (s, 2H), 8.26 (m, 2H), 7.89 (m, 2H), 7.54 (m, 2H), 7.46 (dd, *J* = 6.4, 3.2 Hz, 2H) 1.38-1.14 (m, 84H) ppm. ^{13}C NMR (151 MHz, CD_2Cl_2, r.t.) δ = 140.8, 132.3, 132.0, 128.8, 128.0, 126.5, 125.8, 124.5, 106.6, 104.9, 103.1, 101.6, 100.4, 100.0, 99.8, 31.5, 22.6, 18.9, 18.9, 18.8, 14.1, 11.5, 11.4 ppm. IR: $\tilde{\nu}$ = 2939, 2866, 1451, 1280, 1261, 1015, 882, 755, 670, 585 cm^{-1}. HR-MS(ESI+): *m/z* $[M]^+$ calcd for $C_{70}H_{96}N_4Si_4$ 1104.6707; found 1104.6709. R_f = 0.54 (SiO_2, PE / Et_2O 15:1, v/v).

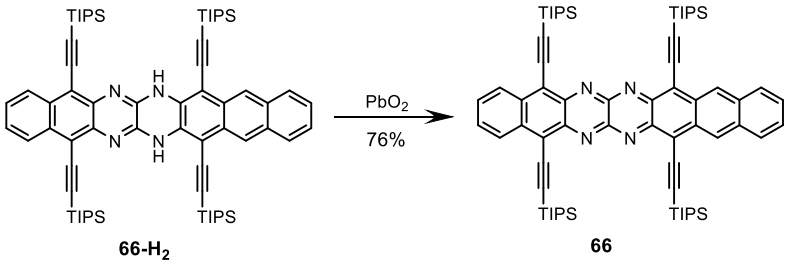

5,8,15,18-tetrakis((triisopropylsilyl)ethynyl)benzo[6,7]quinoxalino[2,3-b]naphtho[2,3-g] quinoxaline (66): **GP8** was applied to dihydro **66-H$_2$** (5.00 mg, 4.52 µmol) and PbO_2 (108 mg, 452 µmol) yielding **66** (3.80 mg, 3.4 µmol, 76%) as a brown crystalline solid. m.p. >200 °C (decomp.). ^{1}H NMR (600 MHz, CD_2Cl_2, r.t.) δ = 8.77 (dd, *J* = 4.6, 2.1 Hz), 7.65 (dd, *J* = 4.6, 2.1 Hz), 7.52 (m, 2H), 7.46 (dd, *J* = 3.7, 2.1 Hz), 6.79 (s, 2H), 1.38-1.21 (m, 84H) ppm. ^{13}C NMR (151 MHz, CD_2Cl_2, r.t.) δ = 147.9, 144.5, 144.1, 137.9, 136.5, 129.8, 129.5, 128.4, 124.8, 122.0, 119.3, 110.9, 107.2, 102.9, 99.3, 75.8, 68.5, 19.3, 11.9, 11.9 ppm. IR: $\tilde{\nu}$ = 2941, 2863, 2175, 1460, 1437, 1390, 1364, 1049, 993, 880, 759, 656 cm^{-1}. HR-MS(ESI+): *m/z* $[M]^+$ calcd for $C_{70}H_{94}N_4Si_4$ 1102.6552; found 1102.6550. R_f = 0.49 (SiO_2, PE / DCM 2:1, v/v).

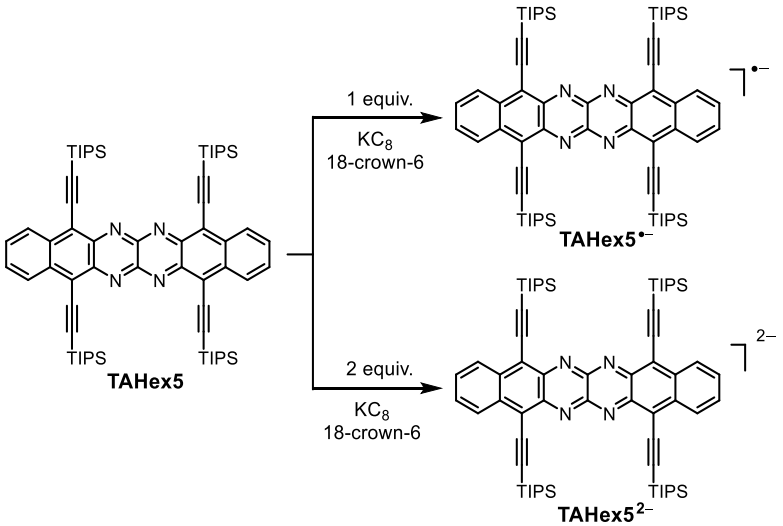

TAHex5$^{\bullet-}$: TAHex5 (3.50 mg, 3.32 µmol) and KC_8-(18-crown-6) (1.40 mg, 3.48 µmol) were dissolved in dry THF (2.5 mL) in a 5 mL vial and stirred for 10 min in a nitrogen filled glove box to generate a dark red solution. After filtration, violet crystals formed on slow diffusion of dry pentane into the filtrate at 4 °C.

TAHex5^{2-}: TAHex5 (3.50 mg, 3.32 µmol) and KC_8-(18-crown-6) (2.8 mg, 6.97 µmol) were dissolved in dry THF (2.5 mL) in a 5 mL vial and stirred for 10 min in a nitrogen filled glove box to generate a dark yellow solution.

7. Appendix

7.1 NMR Spectra

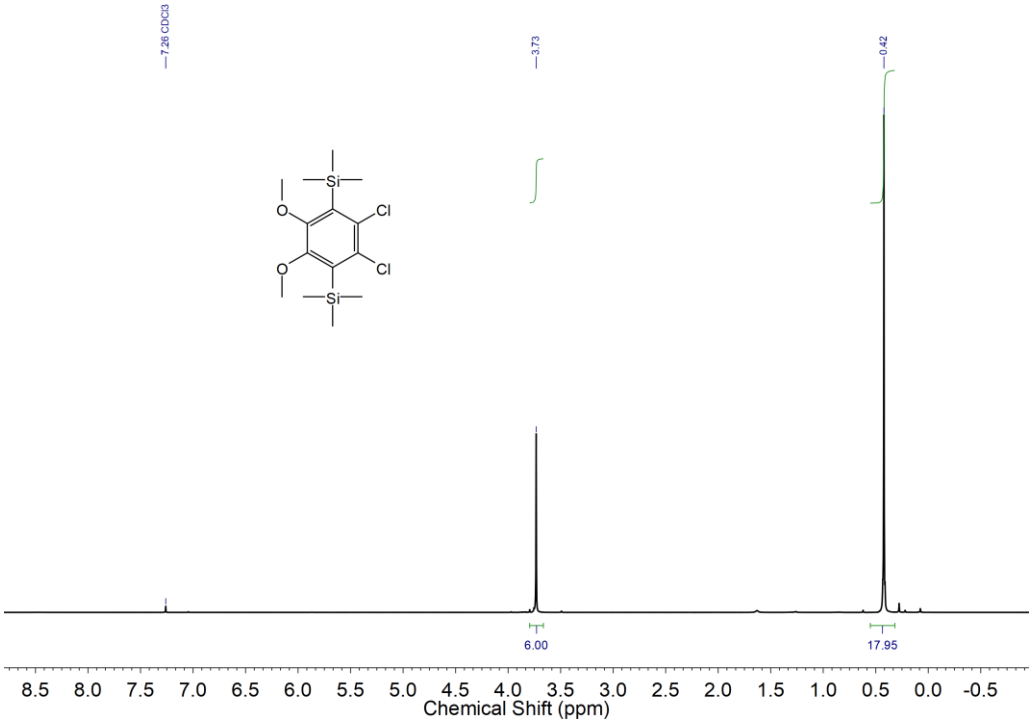

Figure 61. ^{1}H NMR spectrum (300 MHz, 295 K) of **46-Cl$_2$** in $CDCl_3$.

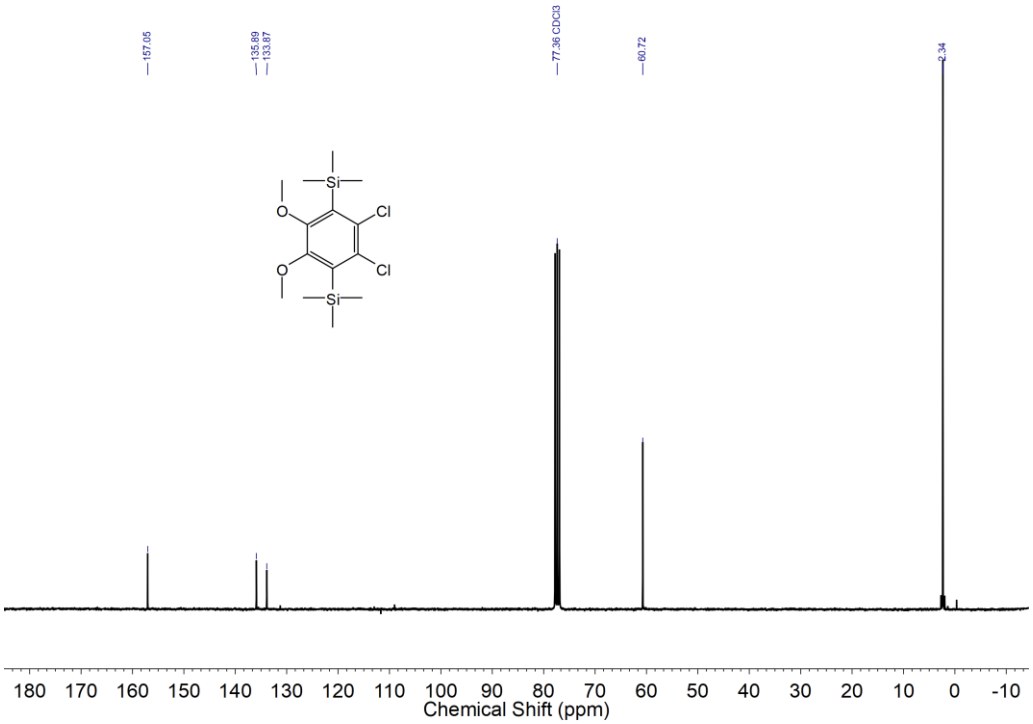

Figure 62. ^{13}C NMR spectrum (75 MHz, 295 K) of **46-Cl$_2$** in $CDCl_3$.

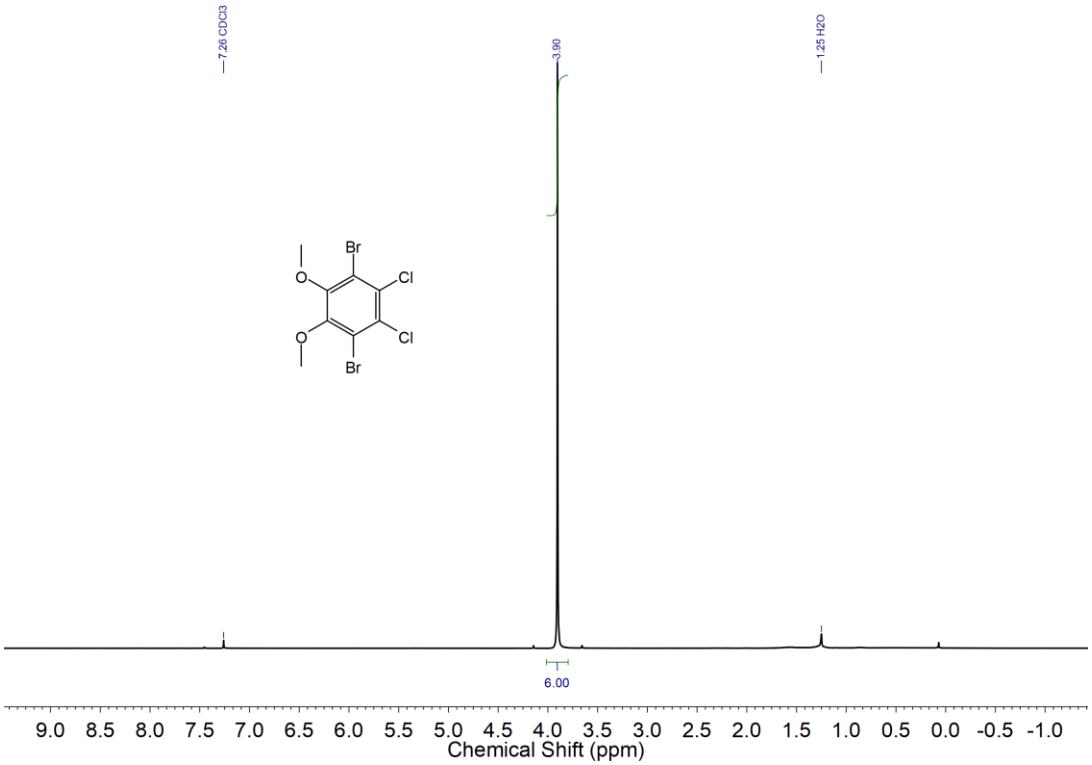

Figure 63. ^{1}H NMR spectrum (300 MHz, 295 K) of **47-Cl_2Br_2** in $CDCl_3$.

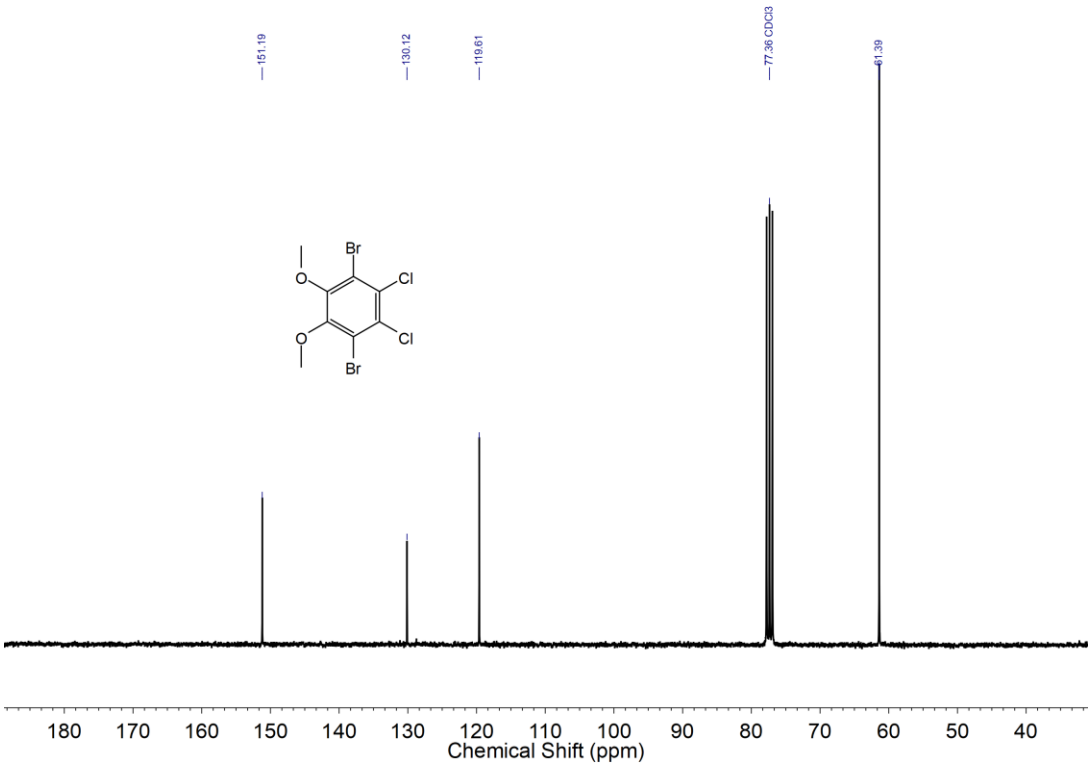

Figure 64. ^{13}C NMR spectrum (75 MHz, 295 K) of **47-Cl_2Br_2** in $CDCl_3$.

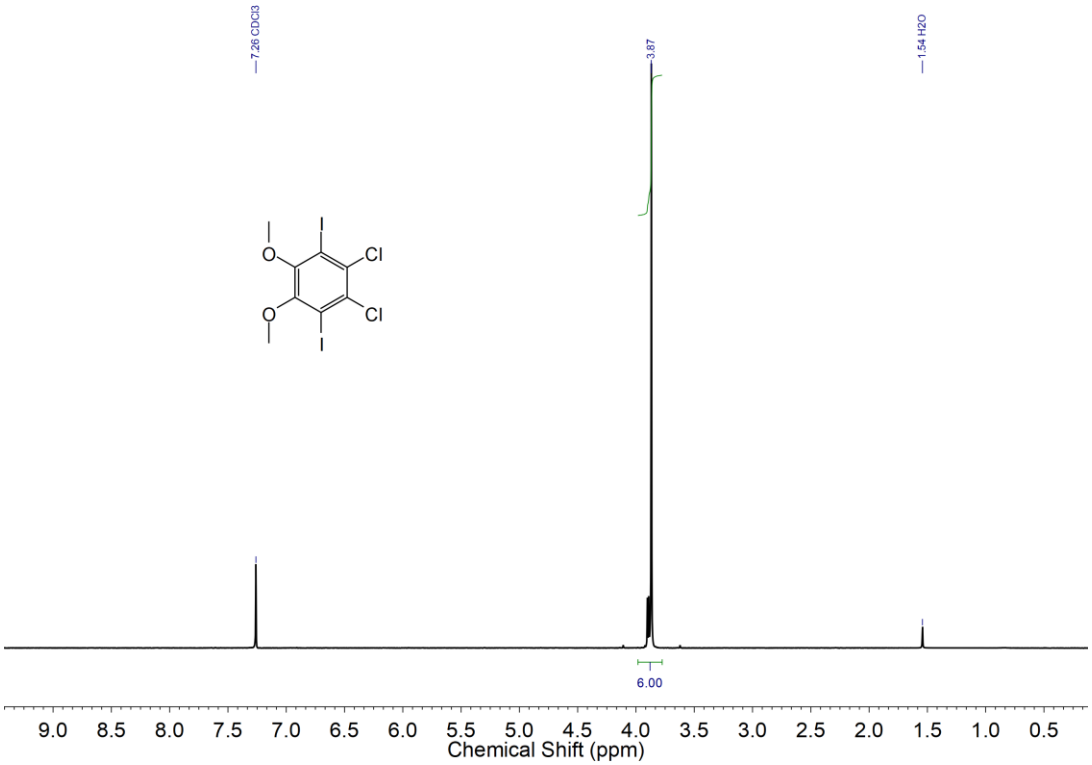

Figure 65. ^{1}H NMR spectrum (300 MHz, 295 K) of **47-Cl_2I_2** in $CDCl_3$.

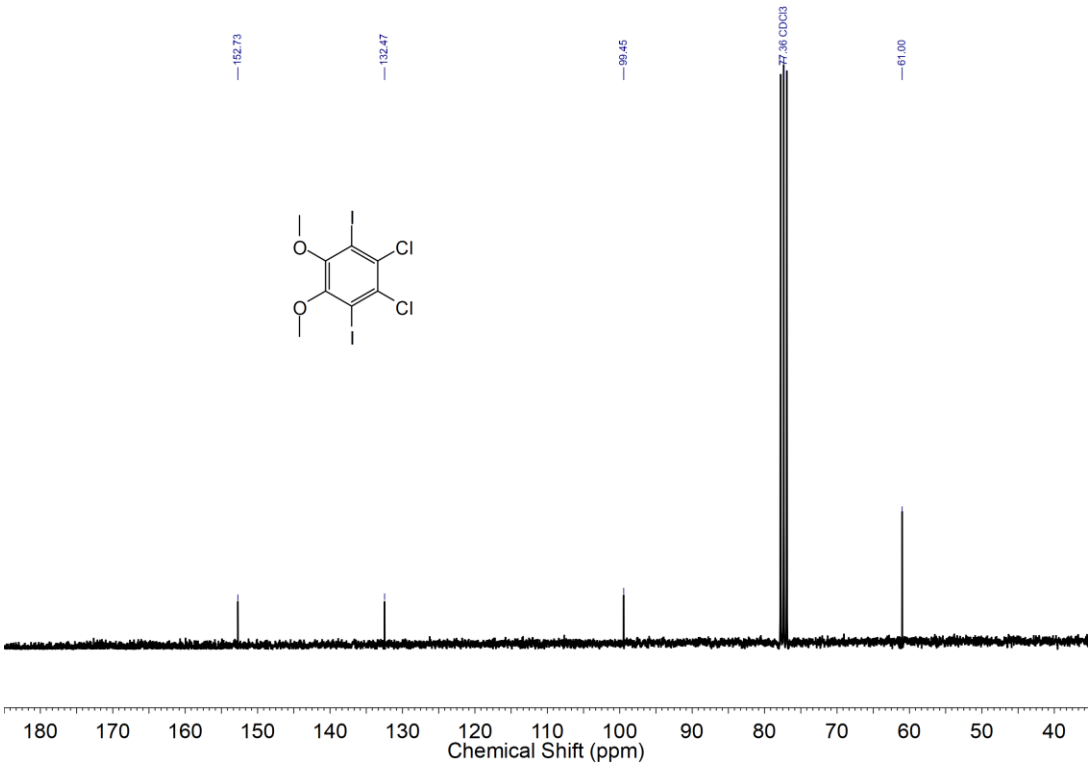

Figure 66. ^{13}C NMR spectrum (75 MHz, 295 K) of **47-Cl_2I_2** in $CDCl_3$.

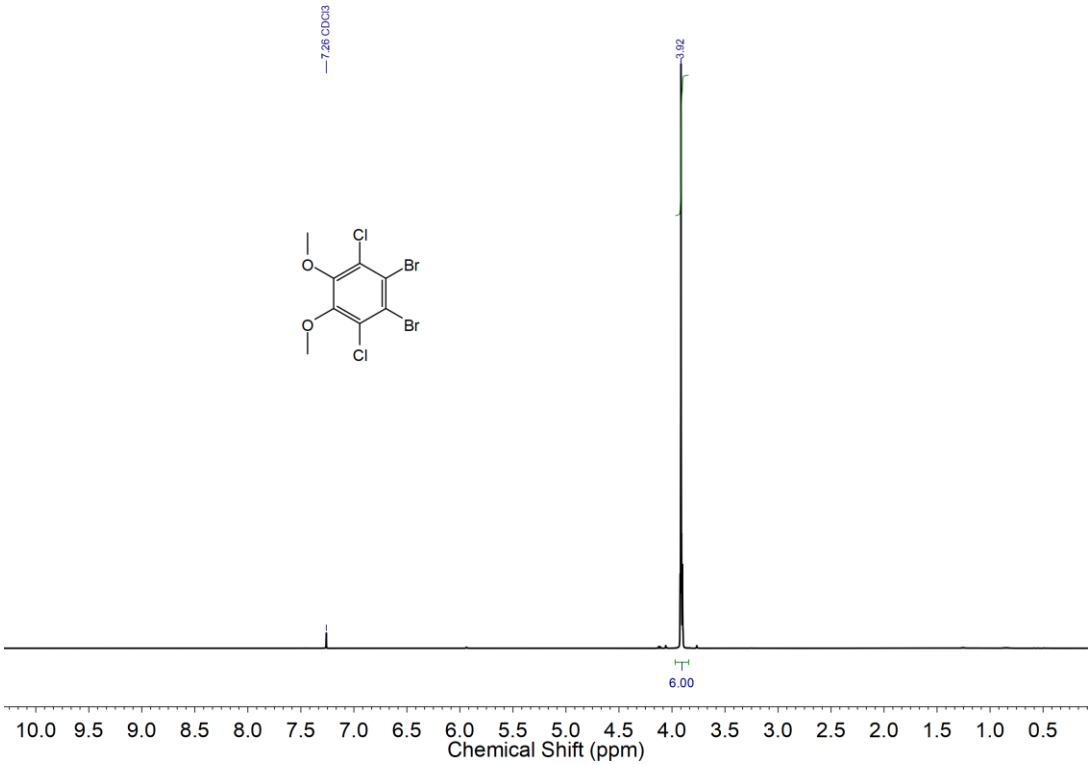

Figure 67. ^{1}H NMR spectrum (500 MHz, 295 K) of **47-Br_2Cl_2** in $CDCl_3$.

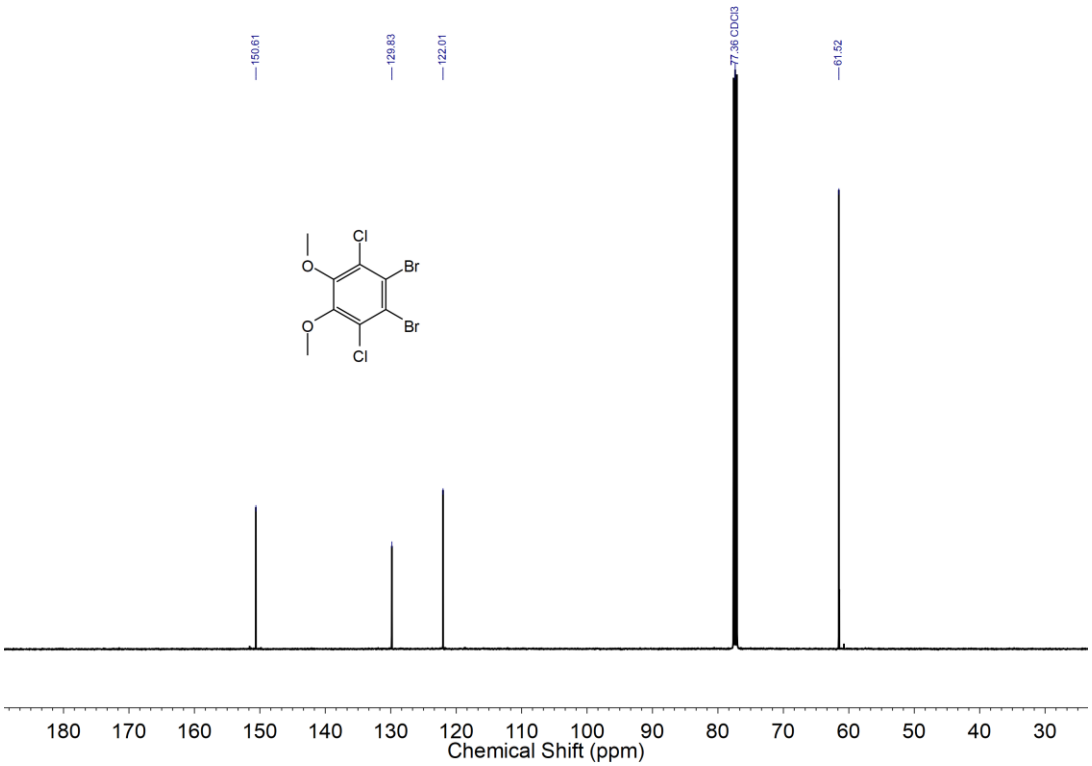

Figure 68. ^{13}C NMR spectrum (126 MHz, 295 K) of **47-Br_2Cl_2** in $CDCl_3$.

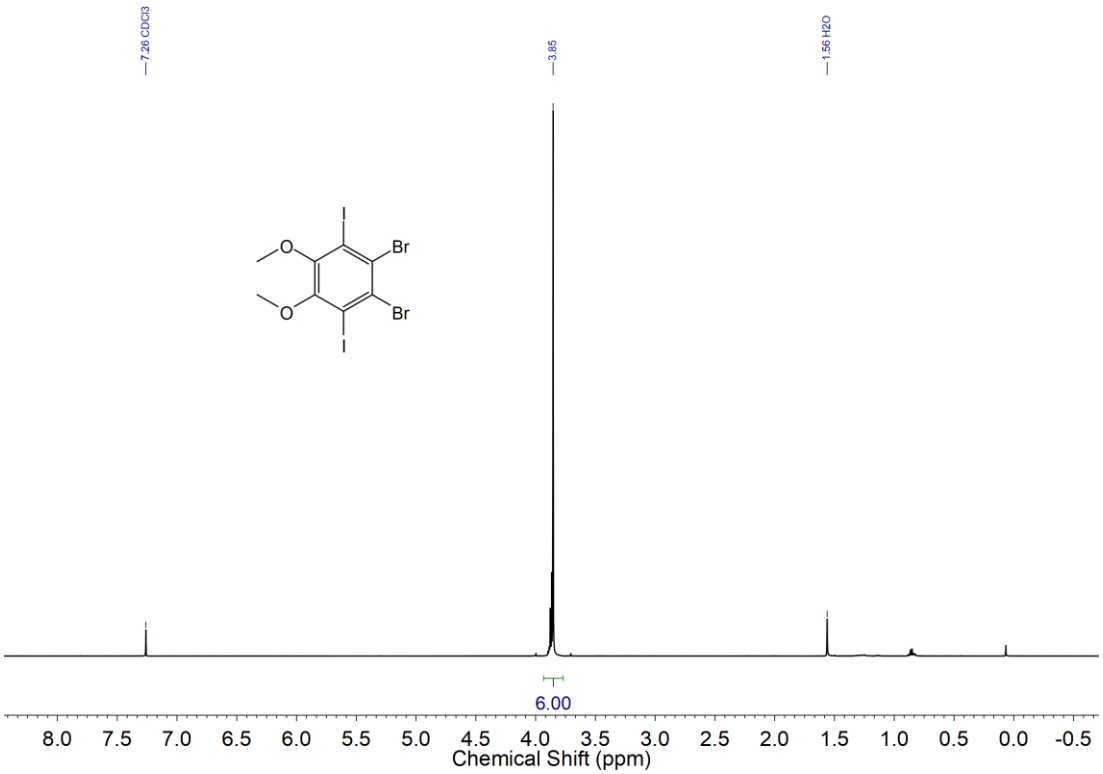

Figure 69. ^{1}H NMR spectrum (500 MHz, 295 K) of **47-Br_2I_2** in $CDCl_3$.

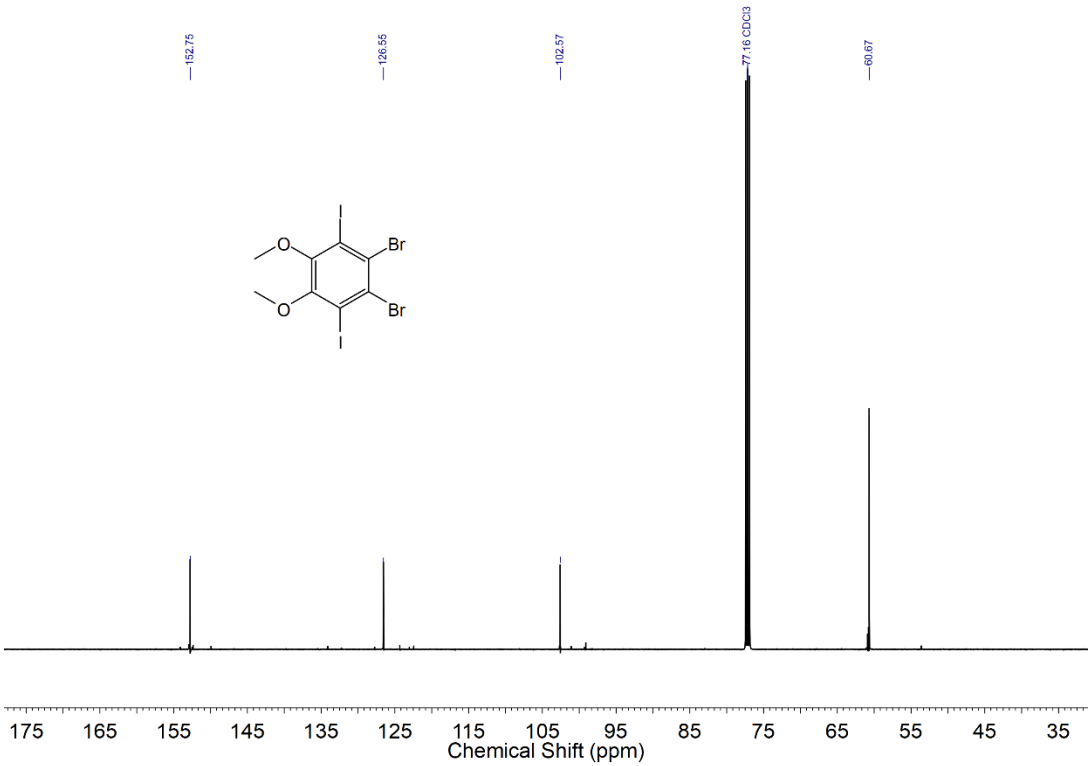

Figure 70. ^{13}C NMR spectrum (126 MHz, 295 K) of **47-Br_2I_2** in $CDCl_3$.

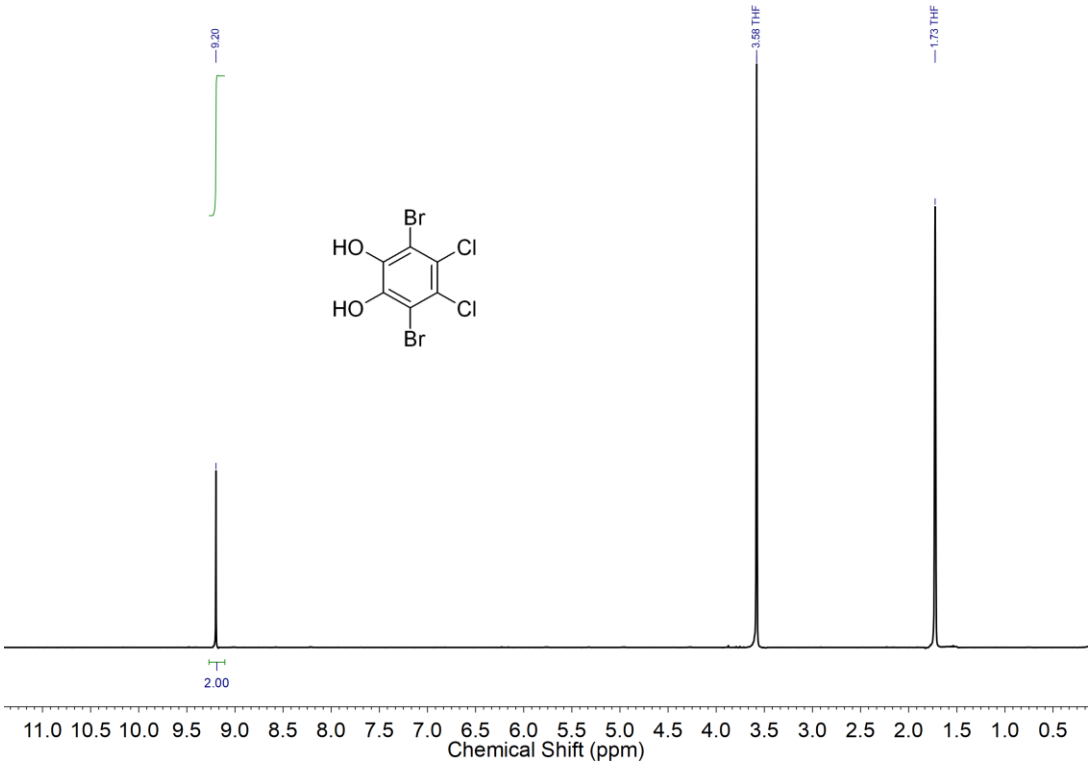

Figure 71. ^{1}H NMR spectrum (500 MHz, 295 K) of **48-Cl$_2$Br$_2$** in THF-d$_8$.

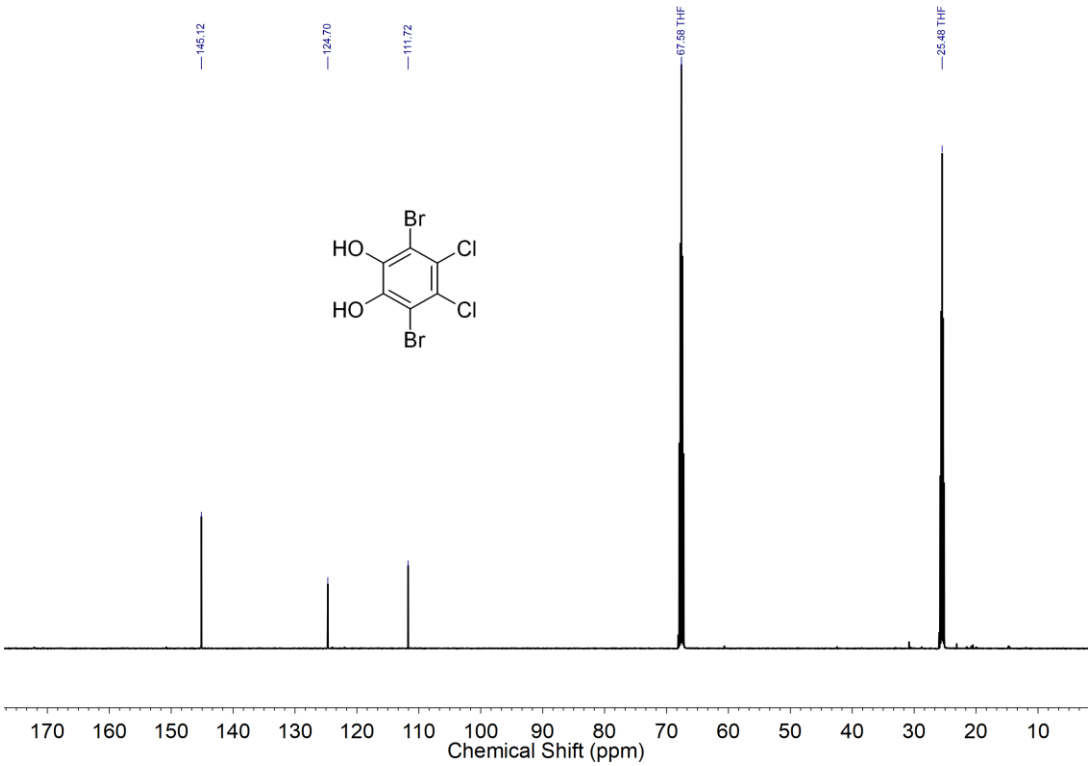

Figure 72. ^{13}C NMR spectrum (126 MHz, 295 K) of **48-Cl$_2$Br$_2$** in THF-d$_8$.

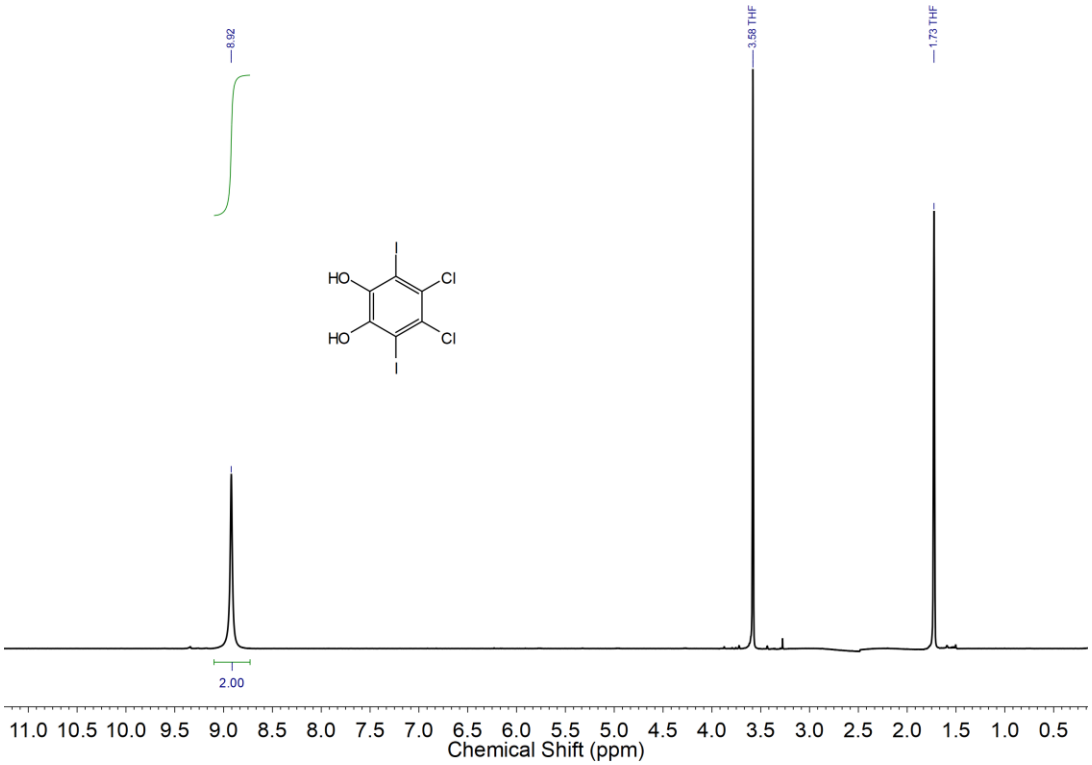

Figure 73. ^{1}H NMR spectrum (400 MHz, 295 K) of **48-Cl_2I_2** in THF-d_8.

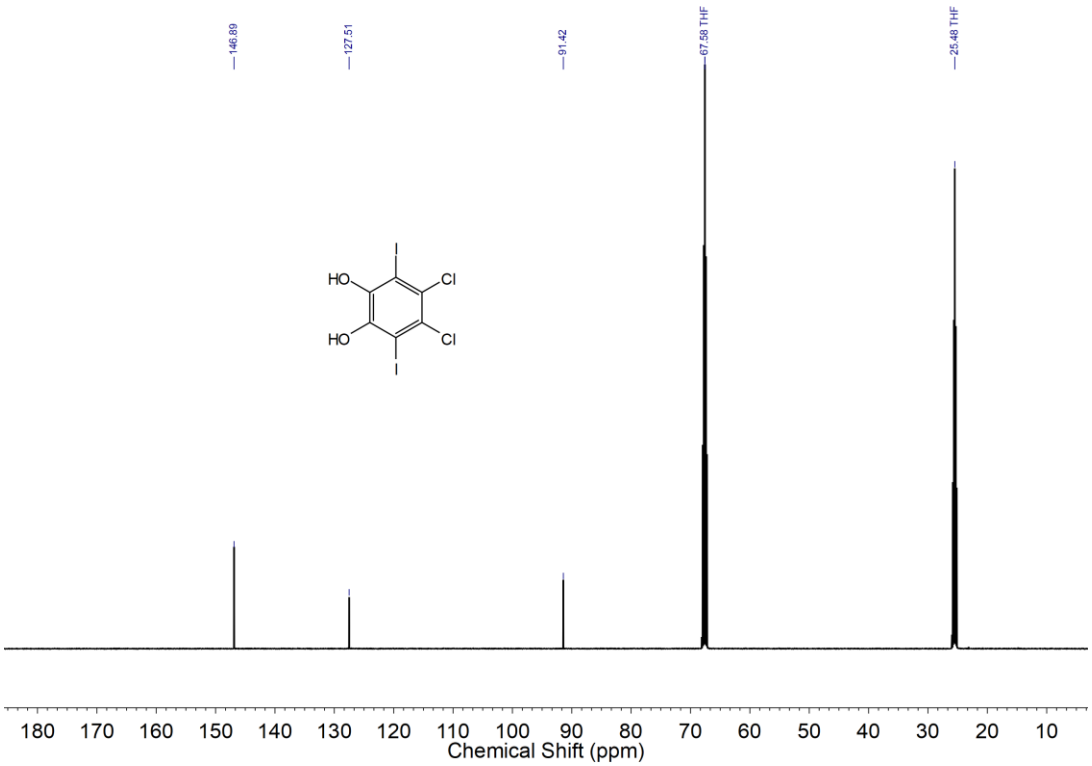

Figure 74. ^{13}C NMR spectrum (101 MHz, 295 K) of **48-Cl_2I_2** in THF-d_8.

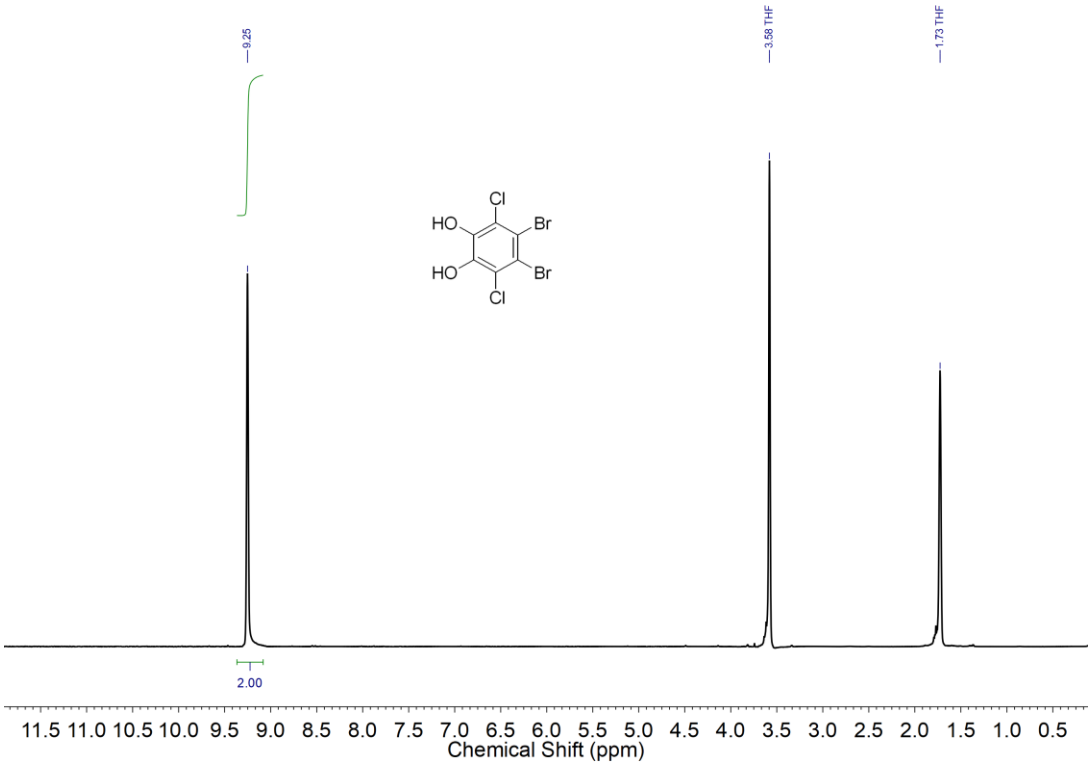

Figure 75. ^{1}H NMR spectrum (400 MHz, 295 K) of **48-Br_2Cl_2** in THF-d_8.

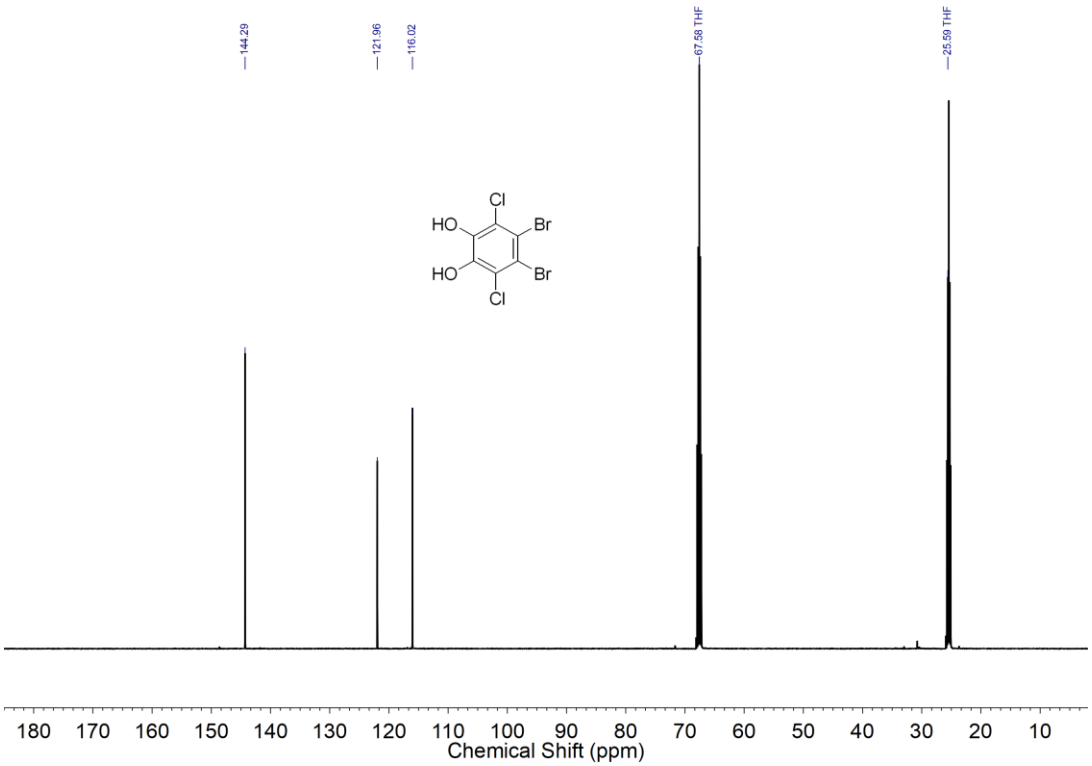

Figure 76. ^{13}C NMR spectrum (101MHz, 295 K) of **48-Br_2Cl_2** in THF-d_8.

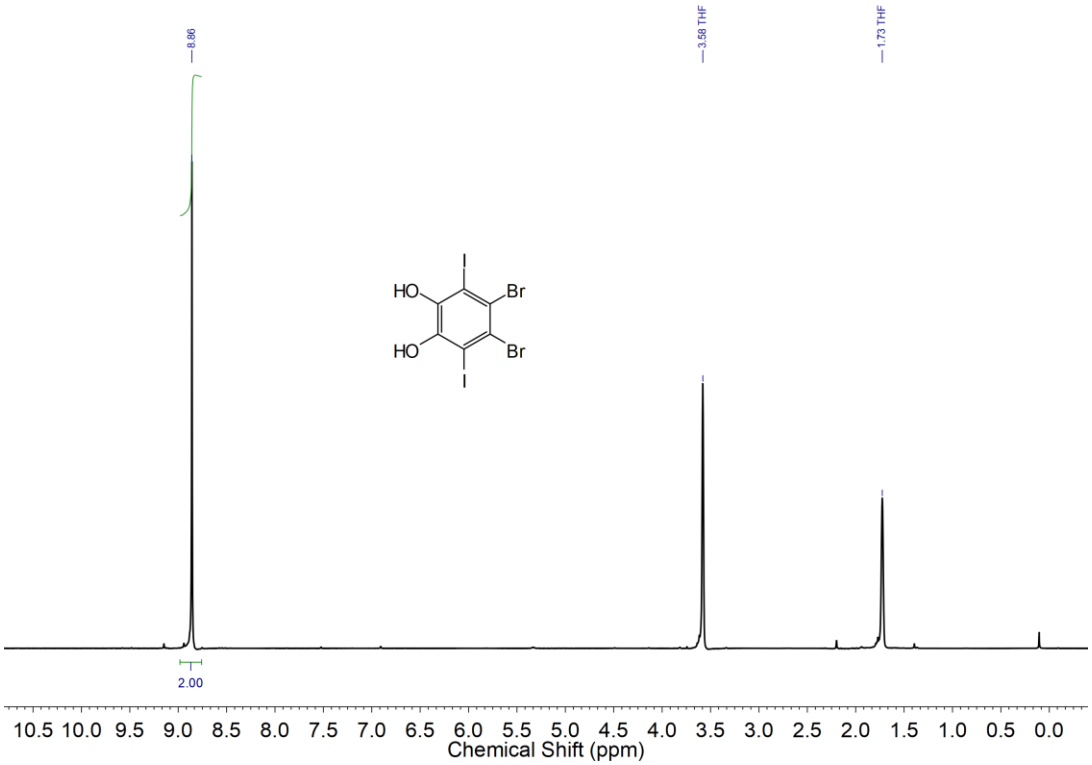

Figure 77. ^{1}H NMR spectrum (300 MHz, 295 K) of **48-Br$_2$I$_2$** in THF-d$_8$.

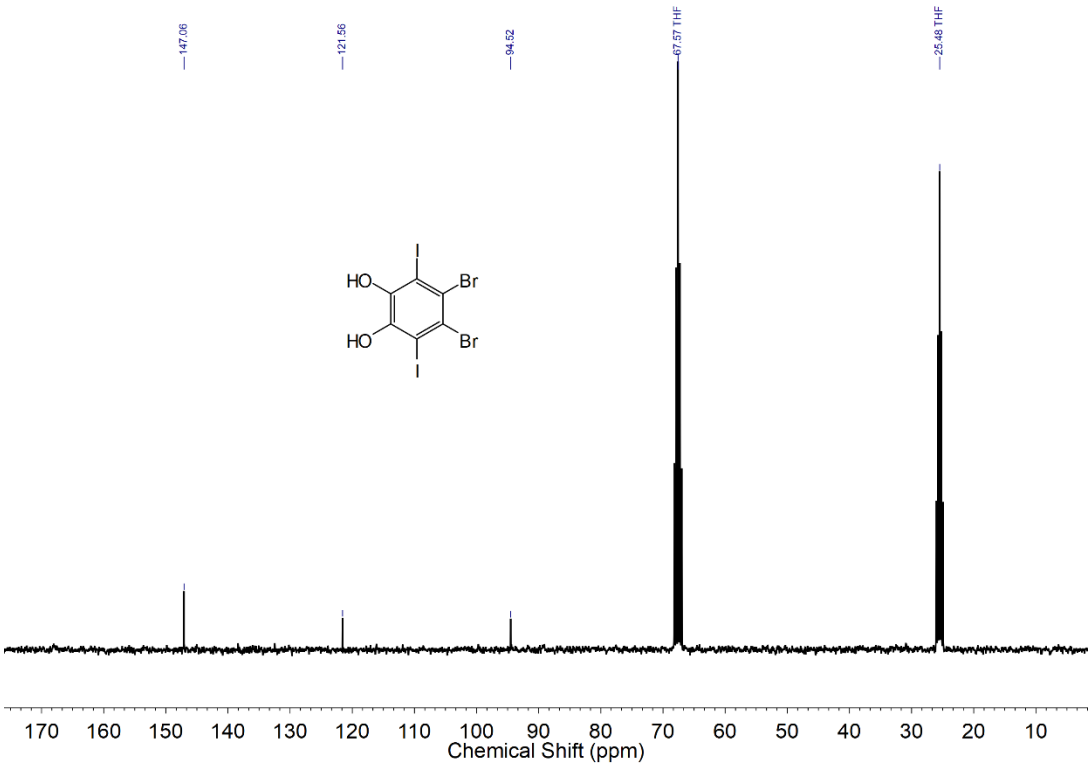

Figure 78. ^{13}C NMR spectrum (76 MHz, 295 K) of **48-Br$_2$I$_2$** in THF-d$_8$.

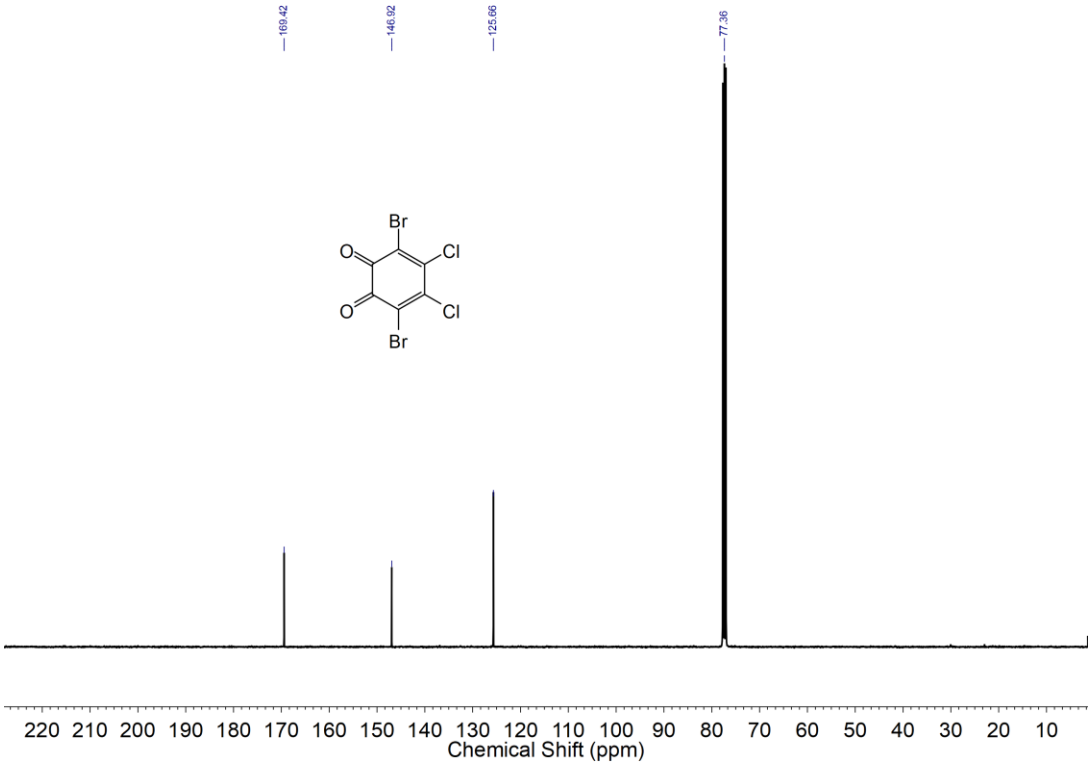

Figure 79. ^{13}C NMR spectrum (101 MHz, 295 K) of **49-Cl_2Br_2** in $CDCl_3$.

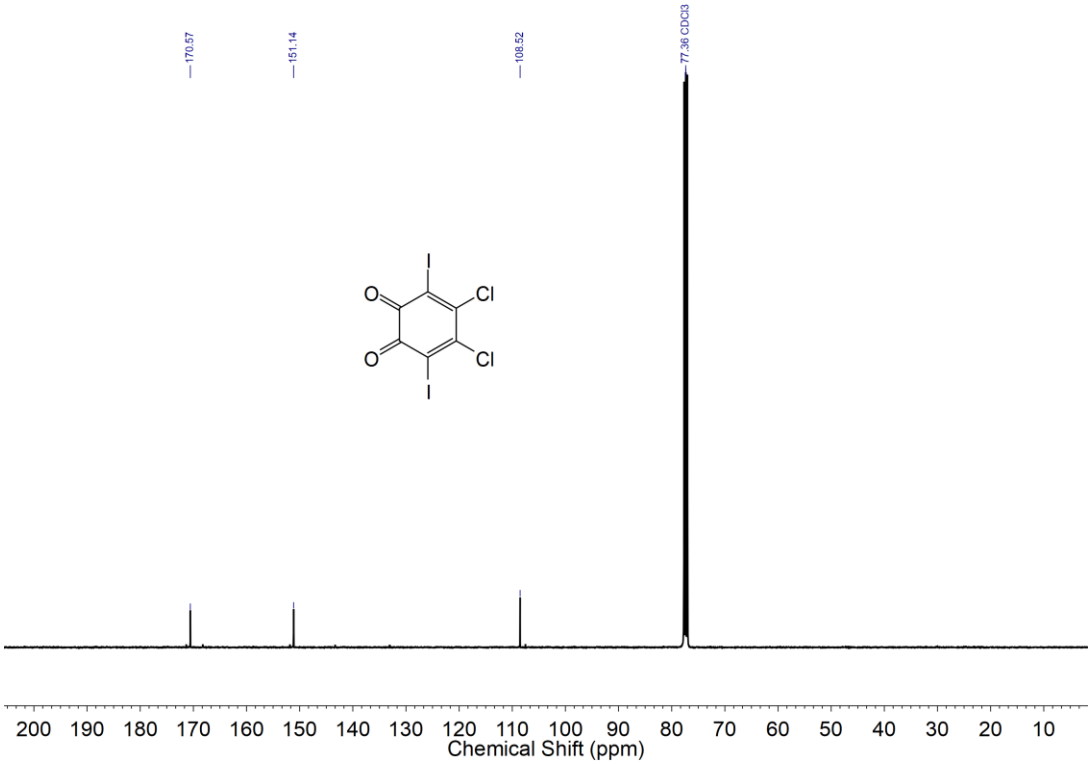

Figure 80. ^{13}C NMR spectrum (101 MHz, 295 K) of **49-Cl_2I_2** in $CDCl_3$.

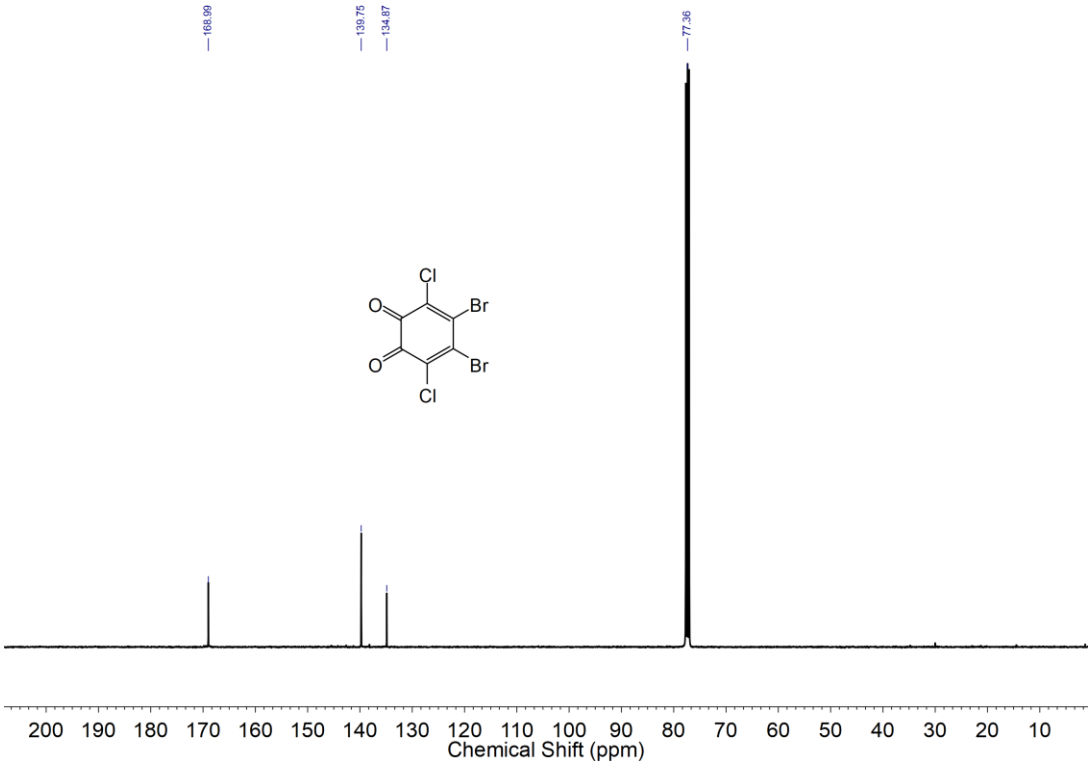

Figure 81. ^{13}C NMR spectrum (101 MHz, 295 K) of **49-Br_2Cl_2** in $CDCl_3$.

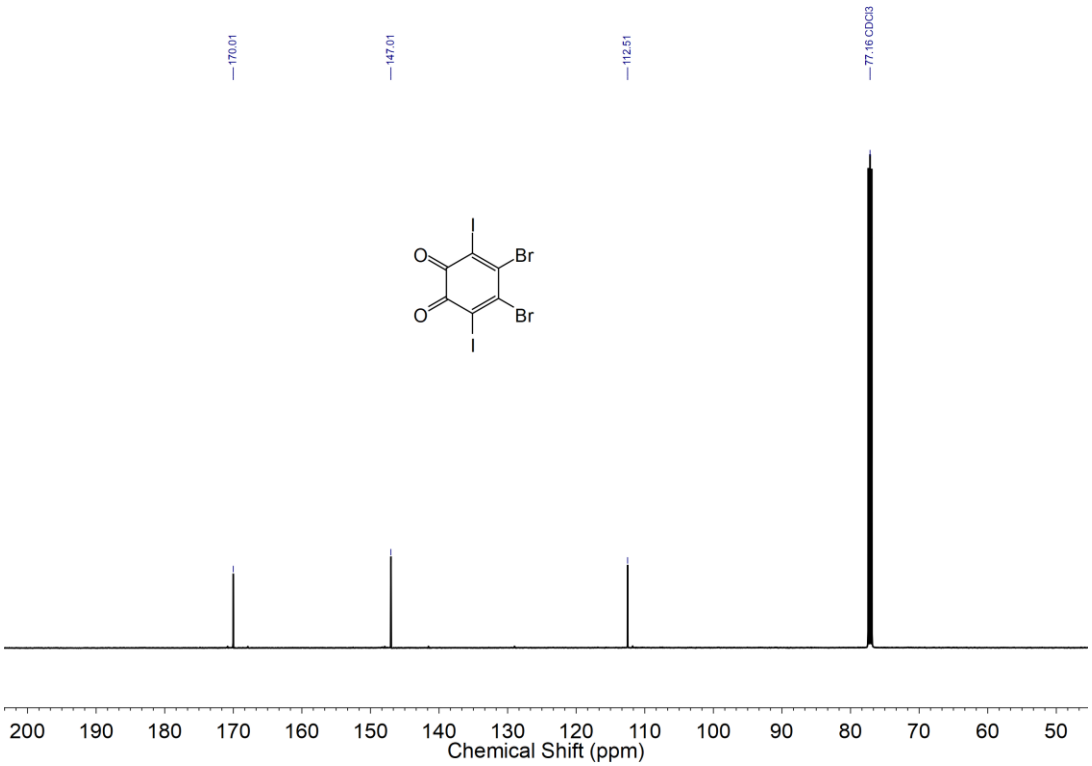

Figure 82. ^{13}C NMR spectrum (126 MHz, 295 K) of **49-Br_2I_2** in $CDCl_3$.

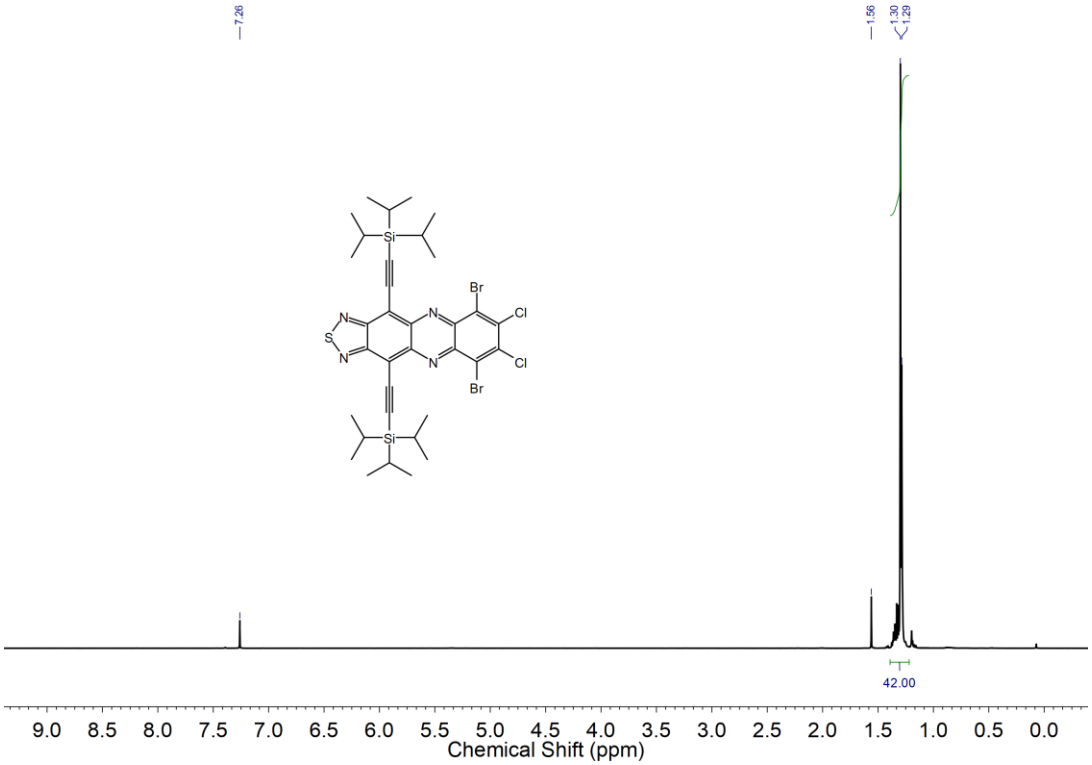

Figure 83. ^{1}H NMR spectrum (500 MHz, 295 K) of **39-Cl$_2$Br$_2$** in $CDCl_3$.

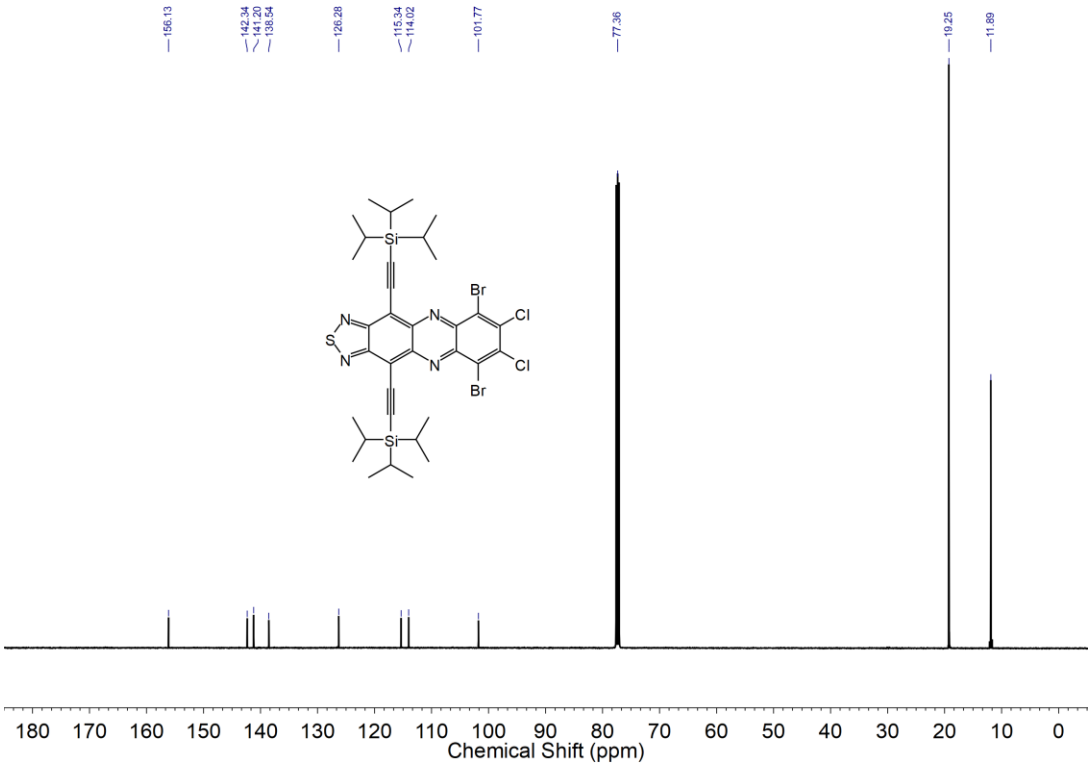

Figure 84. ^{13}C NMR spectrum (126 MHz, 295 K) of **39-Cl$_2$Br$_2$** in $CDCl_3$.

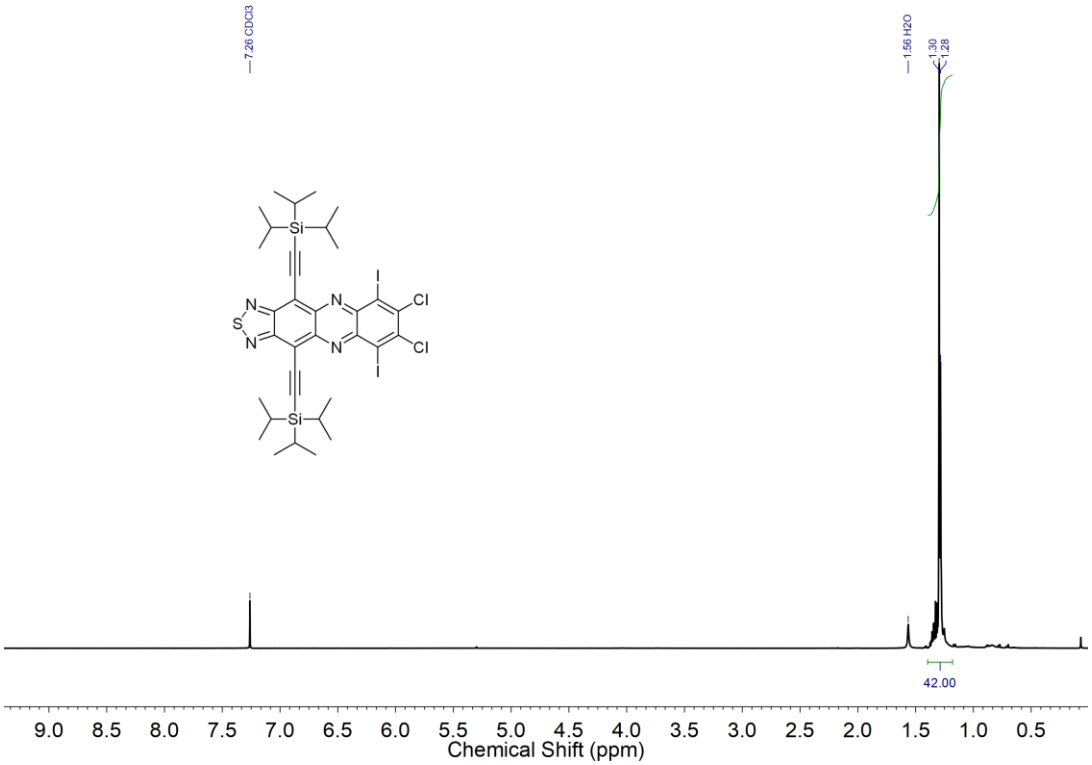

Figure 85. ^{1}H NMR spectrum (500 MHz, 295 K) of **39-Cl$_2$I$_2$** in $CDCl_3$.

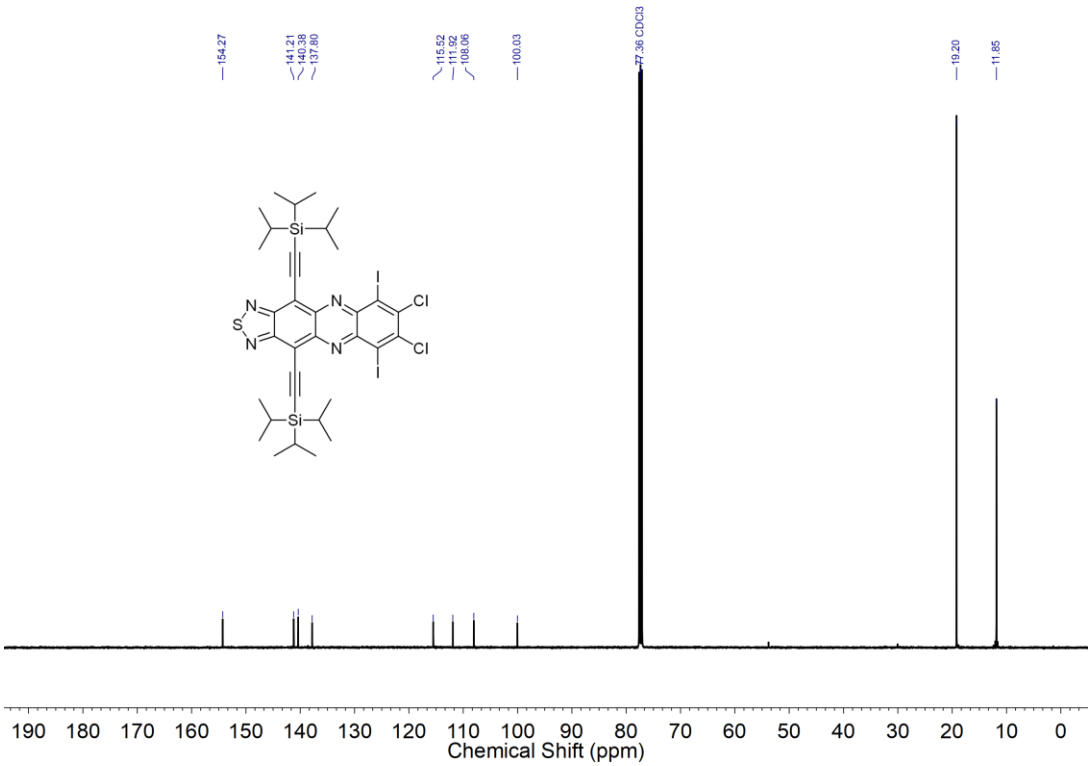

Figure 86. ^{13}C NMR spectrum (126 MHz, 295 K) of **39-Cl$_2$I$_2$** in $CDCl_3$.

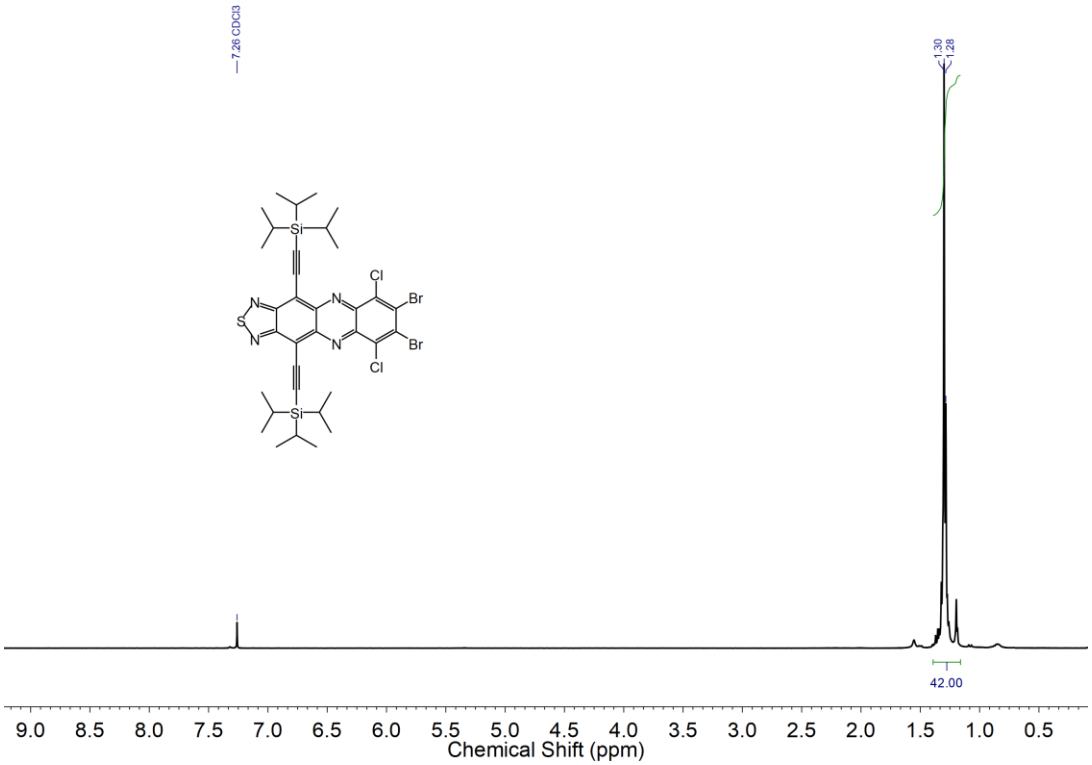

Figure 87. ^{1}H NMR spectrum (300 MHz, 295 K) of **39-Br_2Cl_2** in $CDCl_3$.

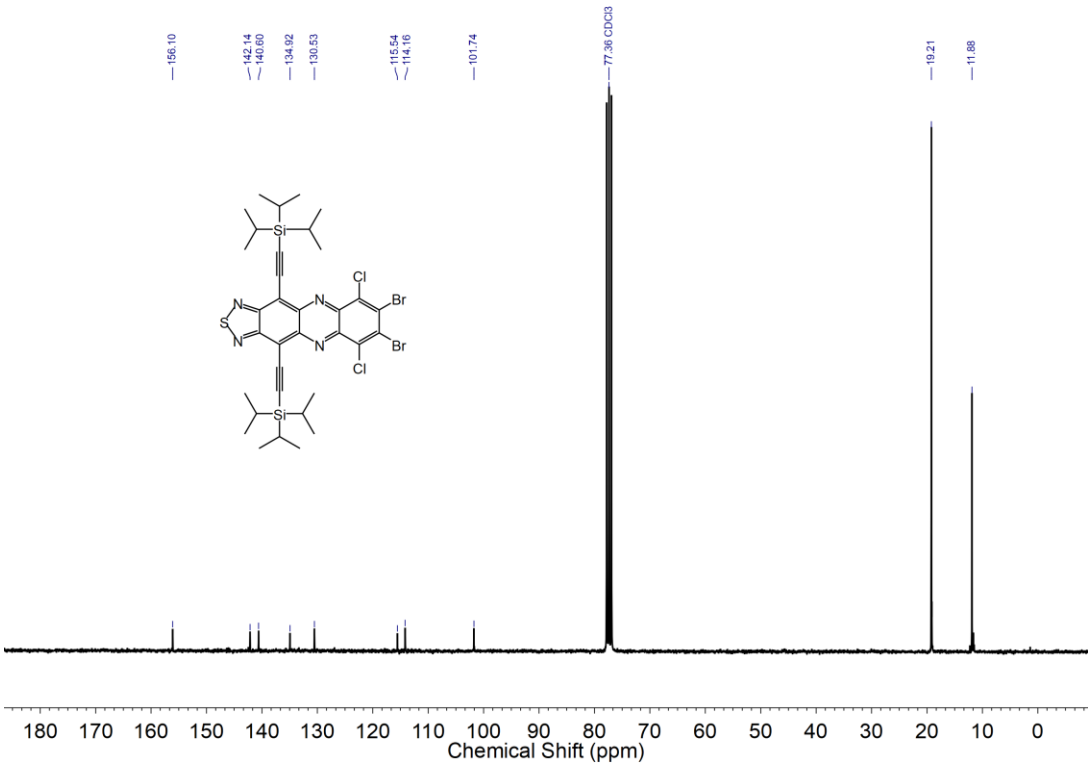

Figure 88. ^{13}C NMR spectrum (75 MHz, 295 K) of **39-Br_2Cl_2** in $CDCl_3$.

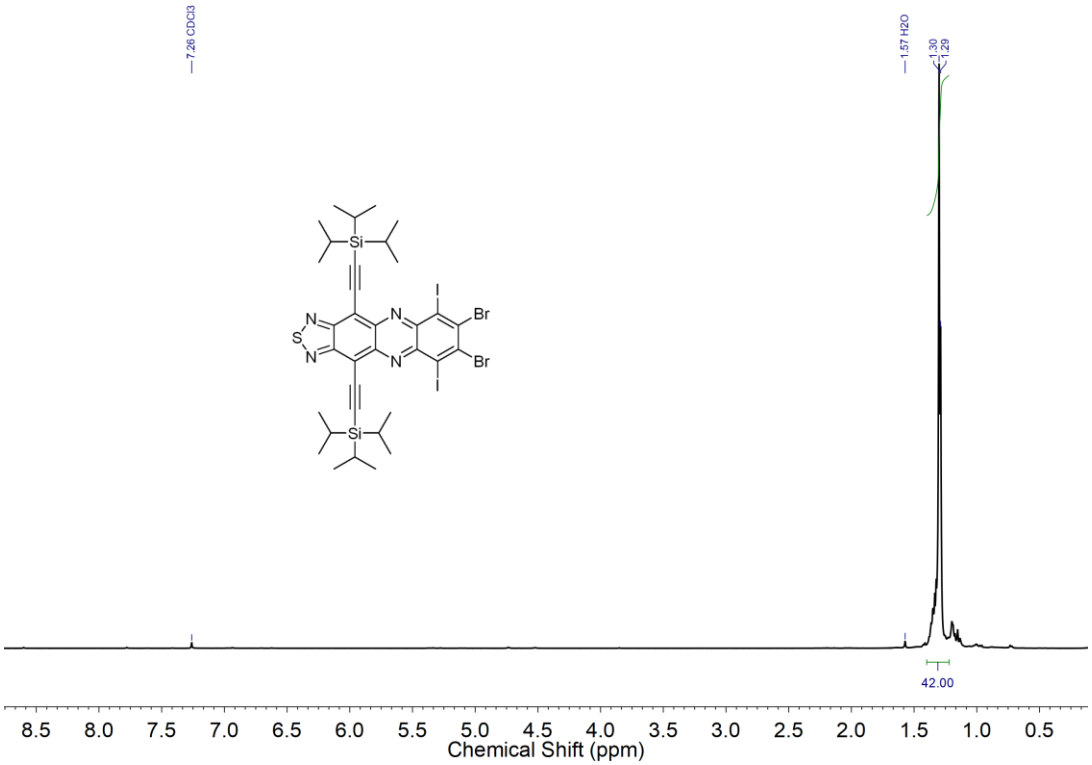

Figure 89. ^{1}H NMR spectrum (500 MHz, 295 K) of **39-Br$_2$I$_2$** in $CDCl_3$.

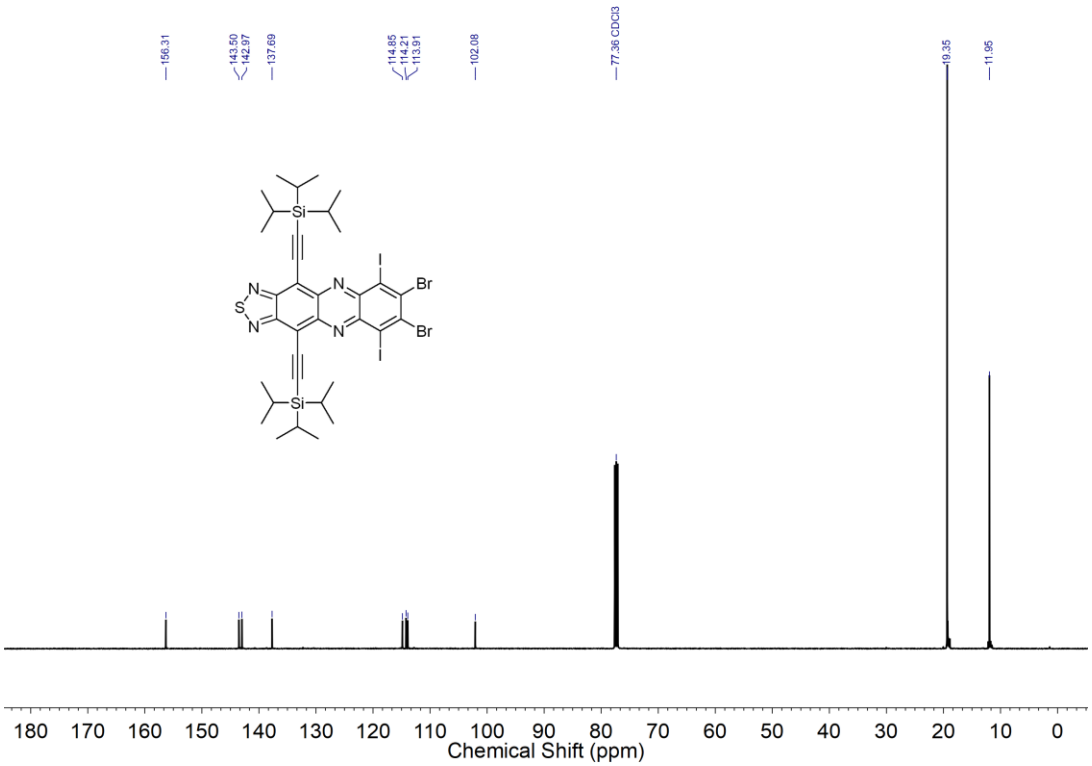

Figure 90. ^{13}C NMR spectrum (126 MHz, 295 K) of **39-Br$_2$I$_2$** in $CDCl_3$.

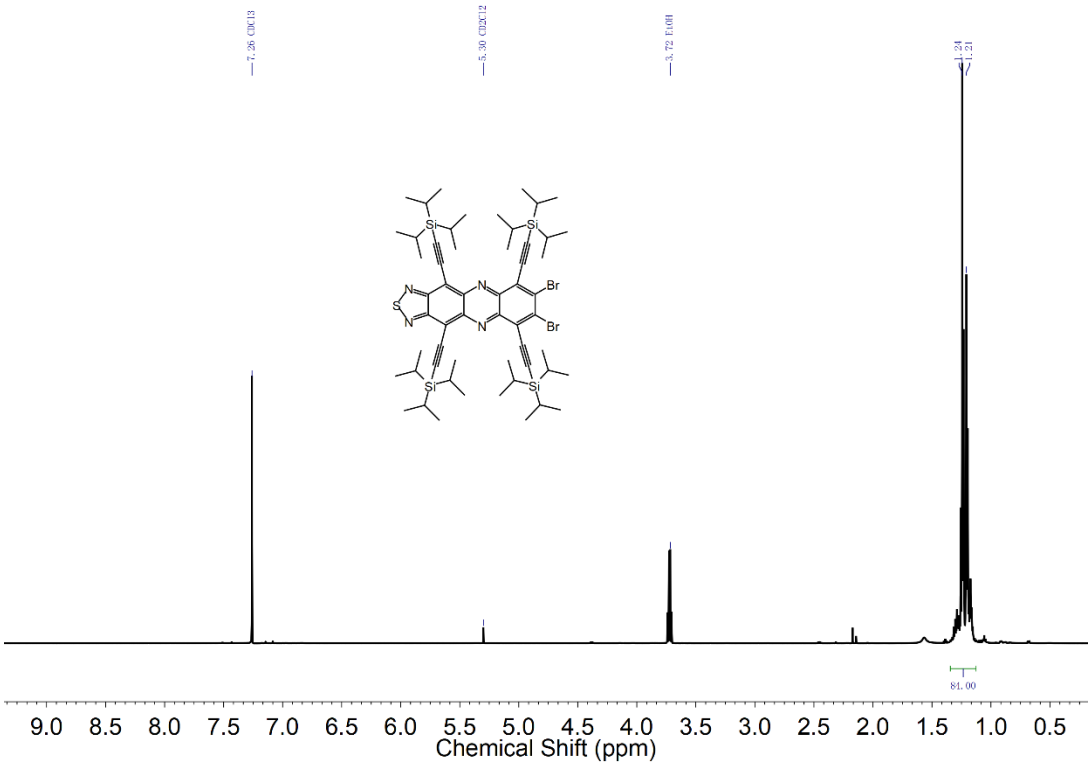

Figure 91. ^{1}H NMR spectrum (600 MHz, 295 K) of **50** in $CDCl_3$.

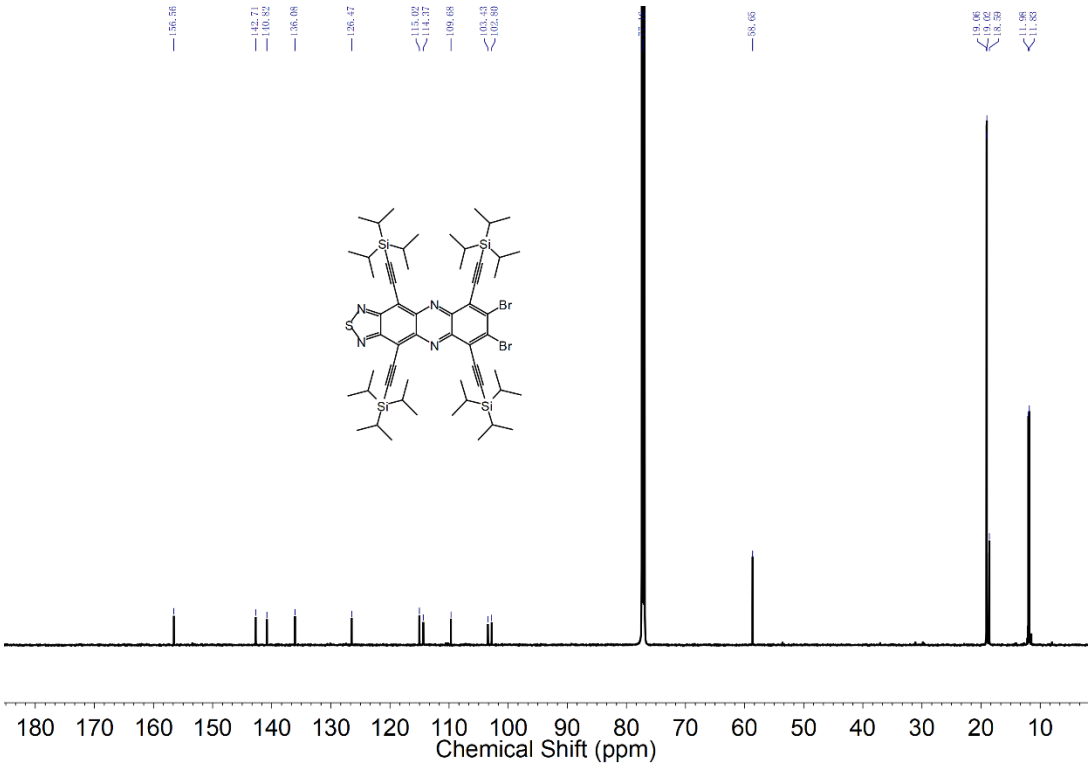

Figure 92. ^{13}C NMR spectrum (151 MHz, 295 K) of **50** in $CDCl_3$.

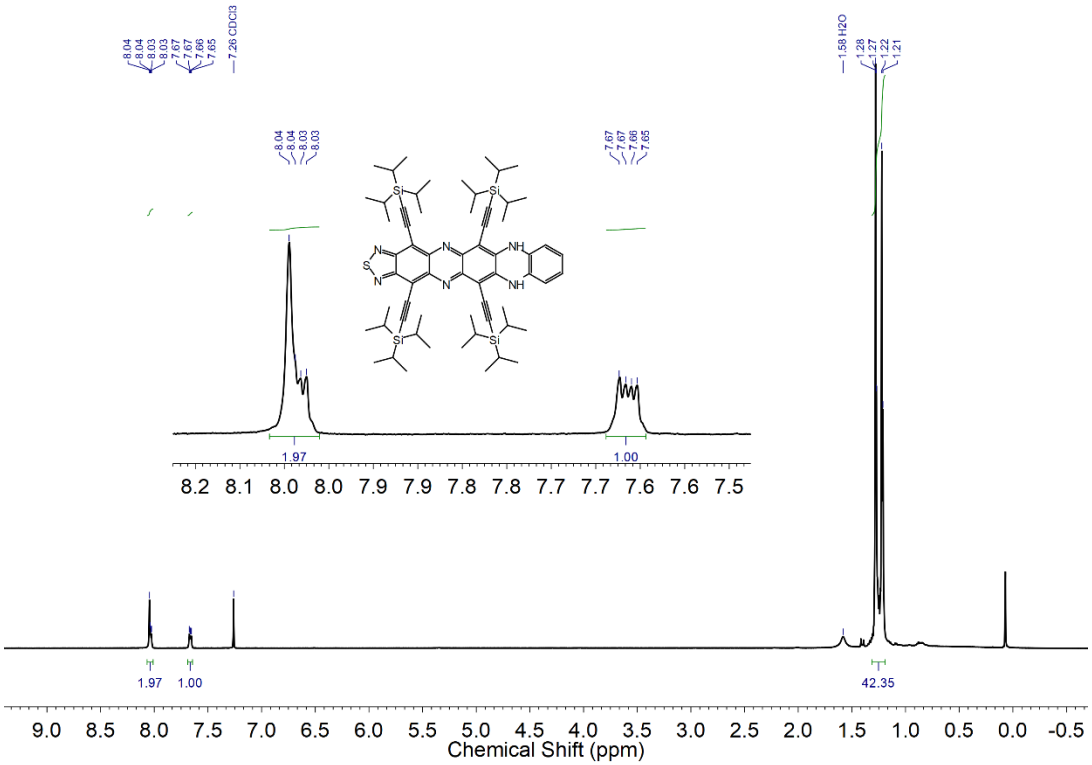

Figure 93. ^{1}H NMR spectrum (500 MHz, 295 K) of **51-H$_2$** in $CDCl_3$.

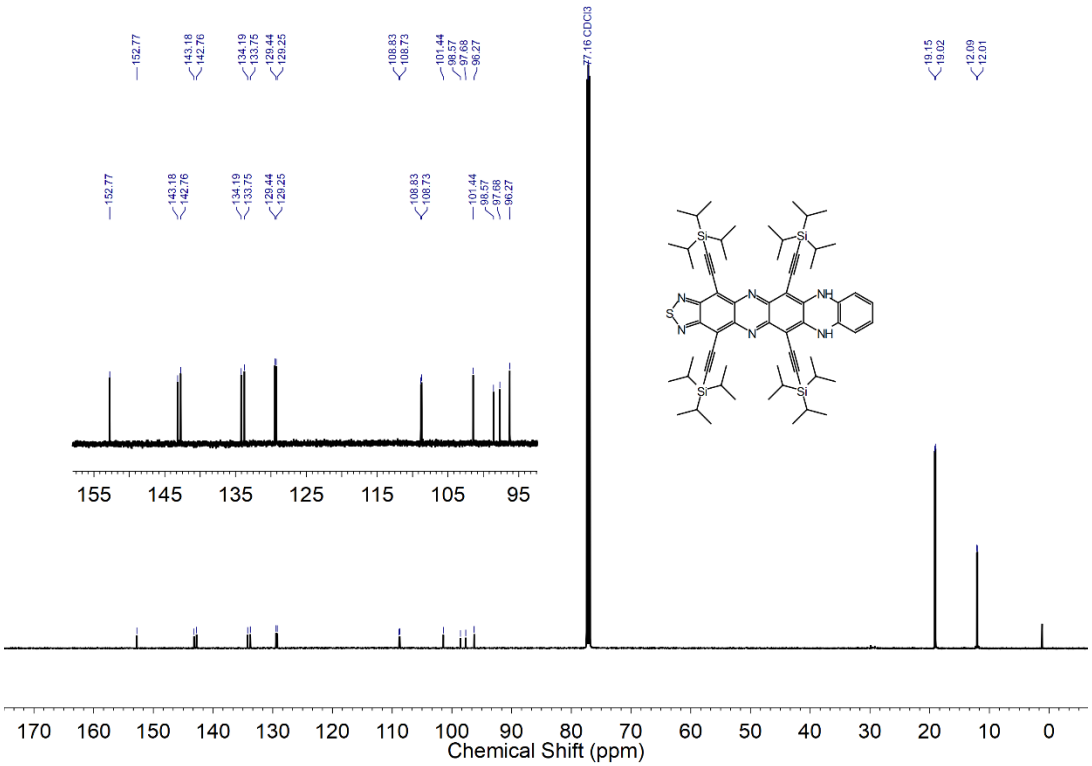

Figure 94. ^{13}C NMR spectrum (126 MHz, 295 K) of **51-H$_2$** in $CDCl_3$.

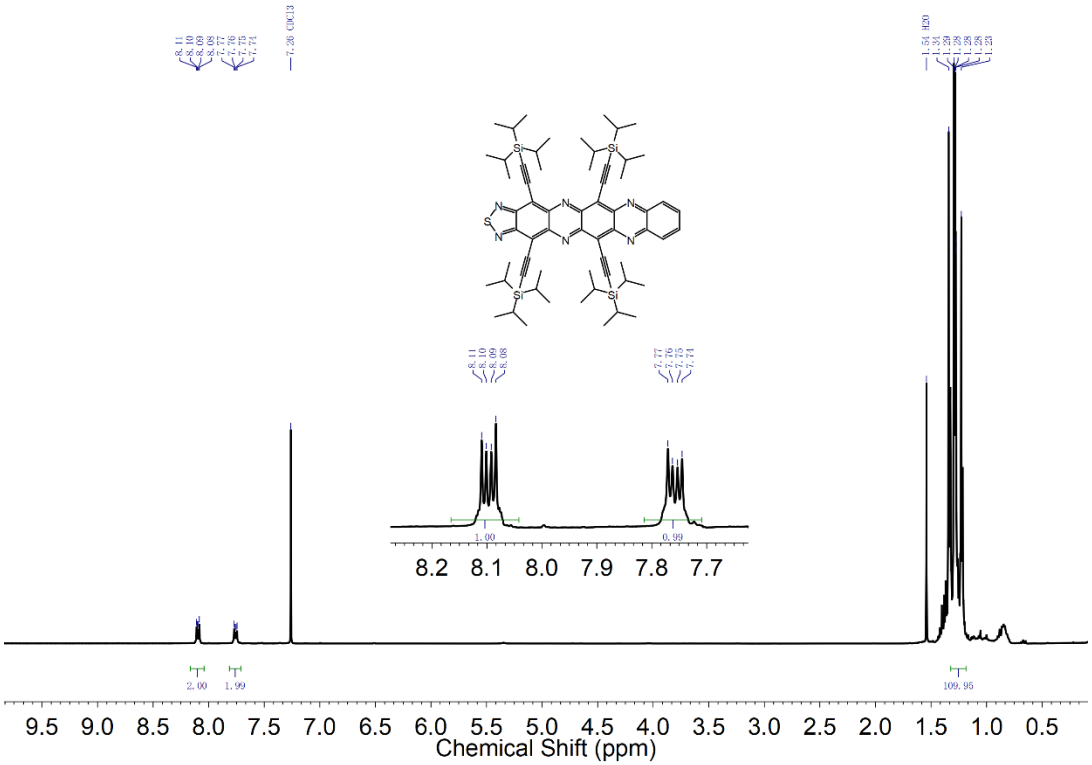

Figure 95. ^{1}H NMR spectrum (500 MHz, 295 K) of **51** in $CDCl_3$.

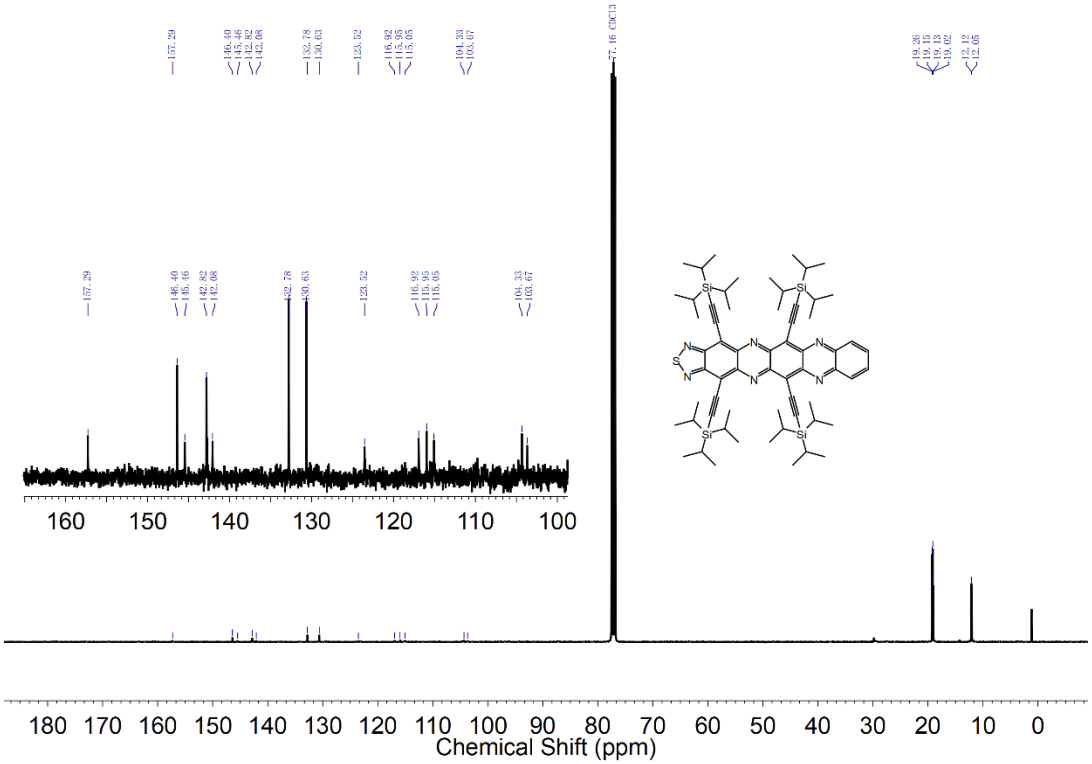

Figure 96. ^{13}C NMR spectrum (126 MHz, 295 K) of **51** in $CDCl_3$.

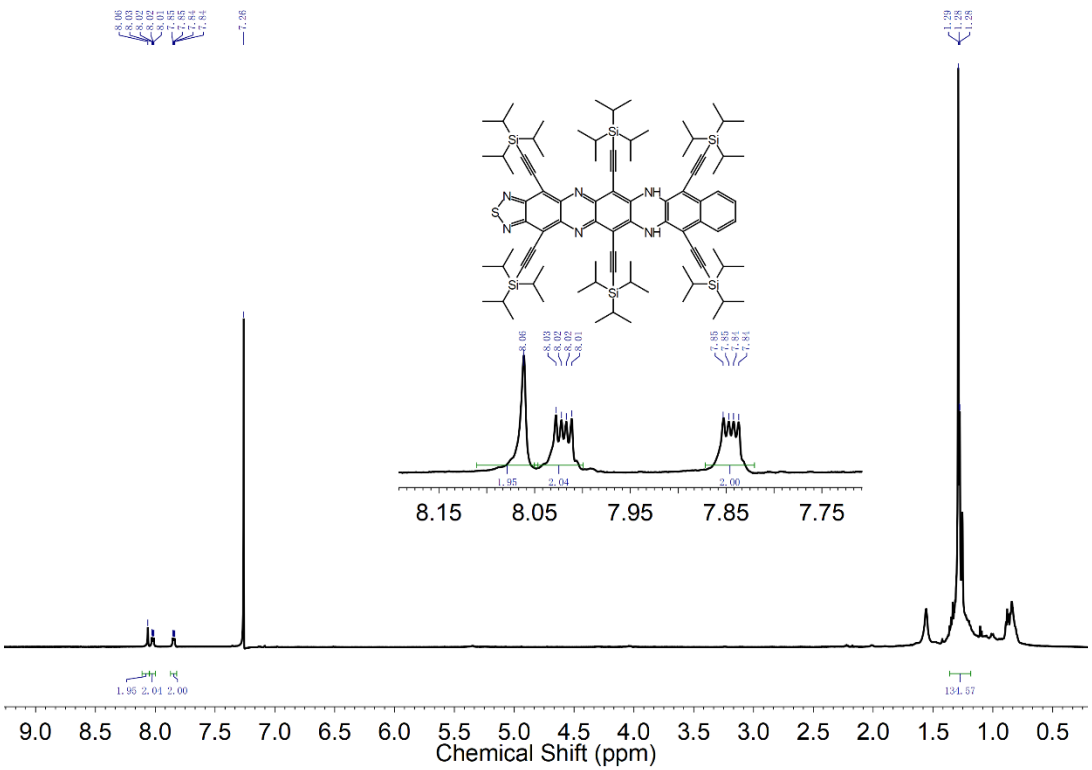

Figure 97. ^{1}H NMR spectrum (500 MHz, 295 K) of **52** in $CDCl_3$.

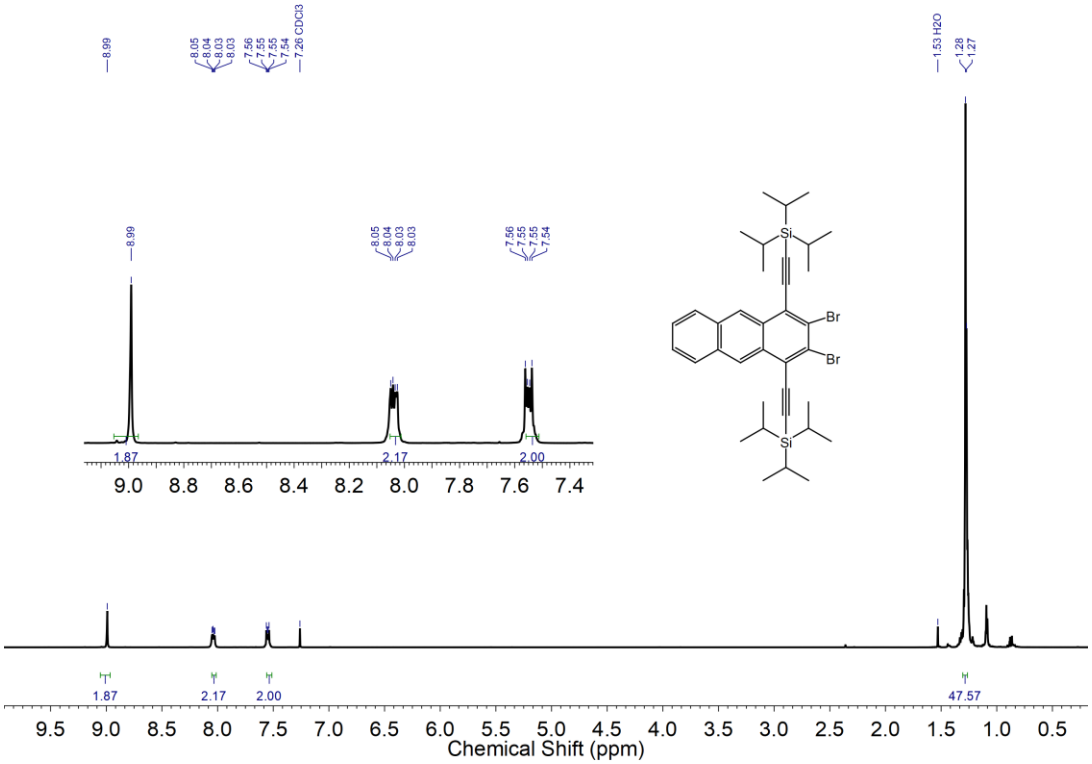

Figure 98. ^{1}H NMR spectrum (500 MHz, 295 K) of **56** in $CDCl_3$.

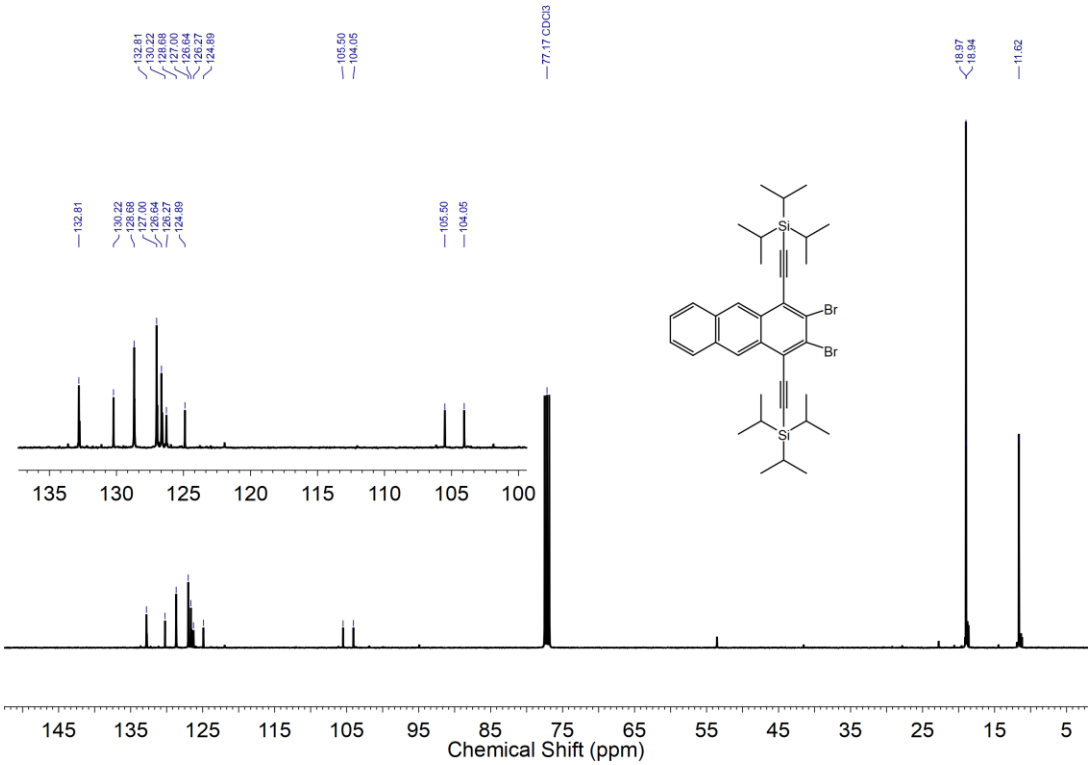

Figure 99. ^{13}C NMR spectrum (126 MHz, 295 K) of **56** in $CDCl_3$.

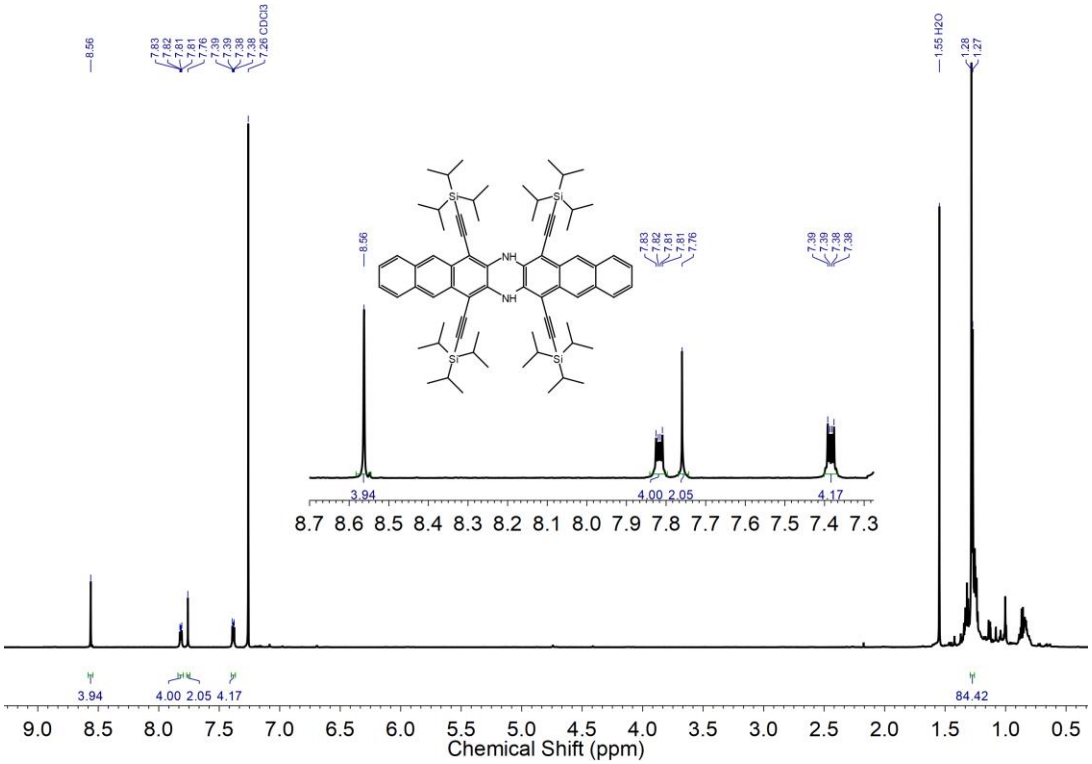

Figure 100. ^{1}H NMR spectrum (600 MHz, 295 K) of **DAH1-H_2** in $CDCl_3$.

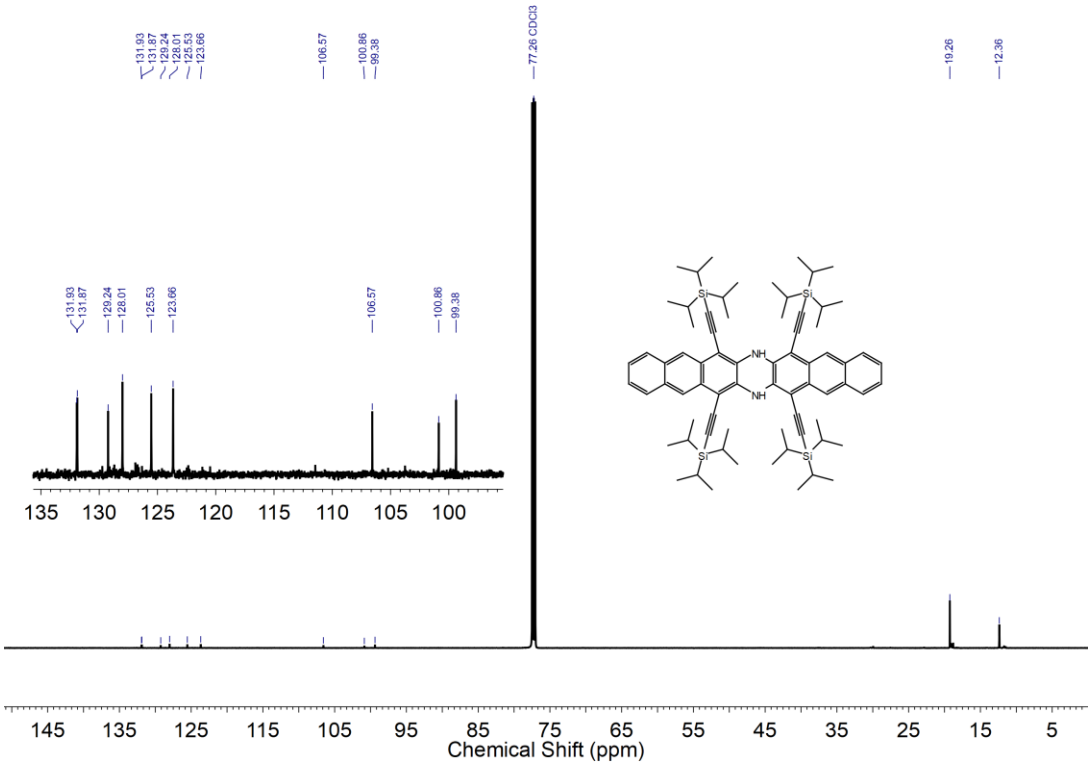

Figure 101. ^{13}C NMR spectrum (151 MHz, 295 K) of **DAH1-H$_2$** in $CDCl_3$.

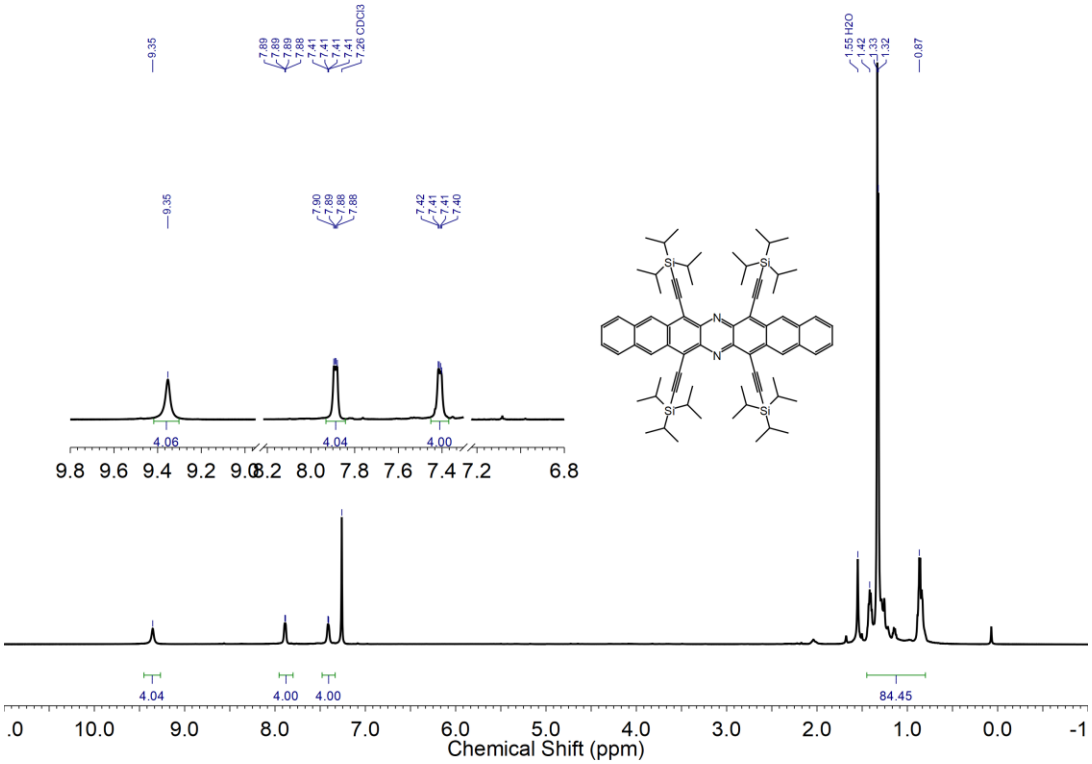

Figure 102. ^{1}H NMR spectrum (600 MHz, 295 K) of **DAH1** in $CDCl_3$.

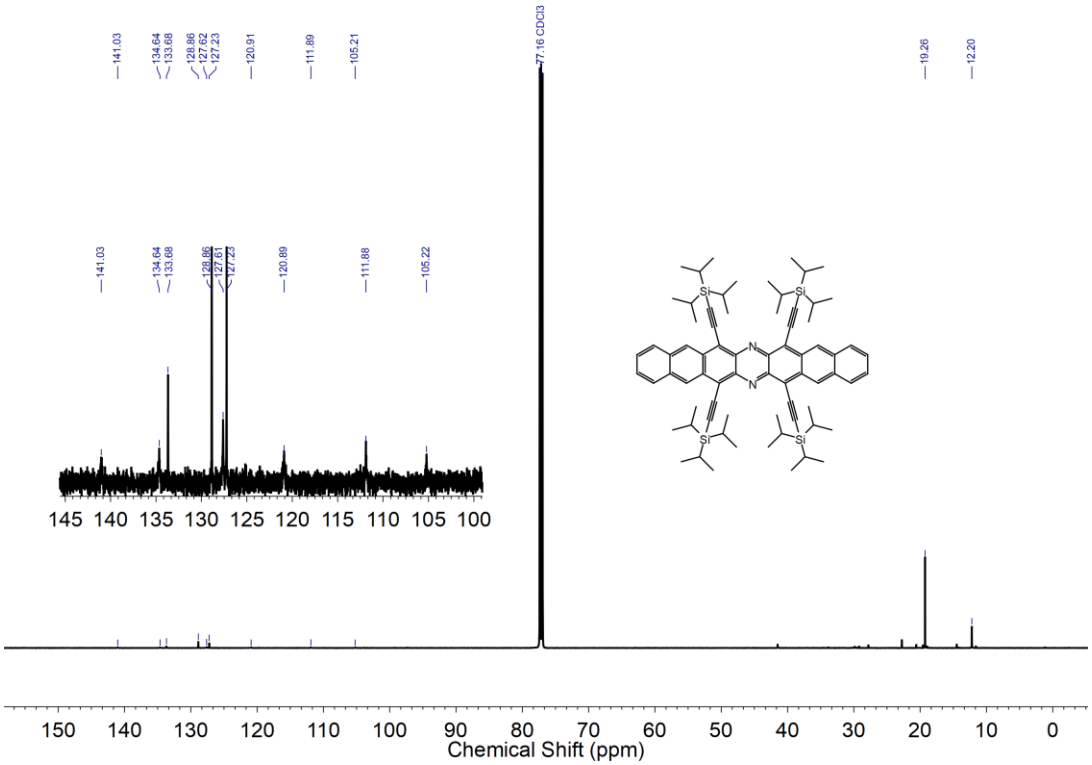

Figure 103. ^{13}C NMR spectrum (151 MHz, 295 K) of **DAH1** in $CDCl_3$.

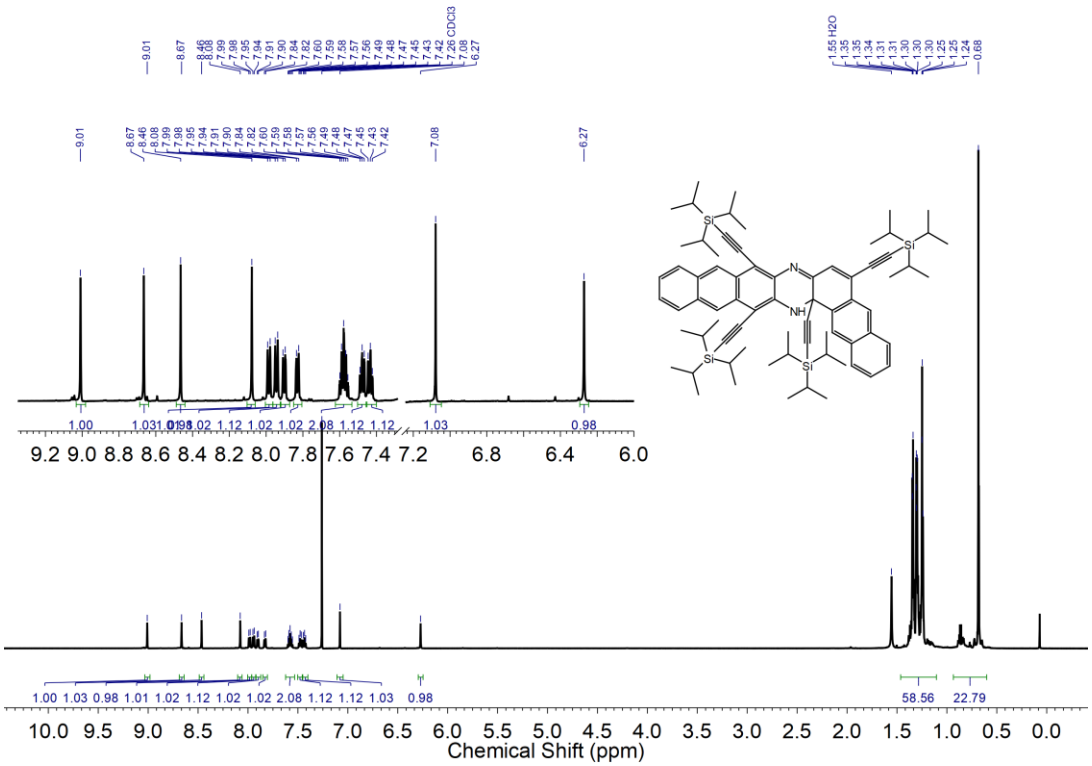

Figure 104. ^{1}H NMR spectrum (600 MHz, 295 K) of **57** in $CDCl_3$.

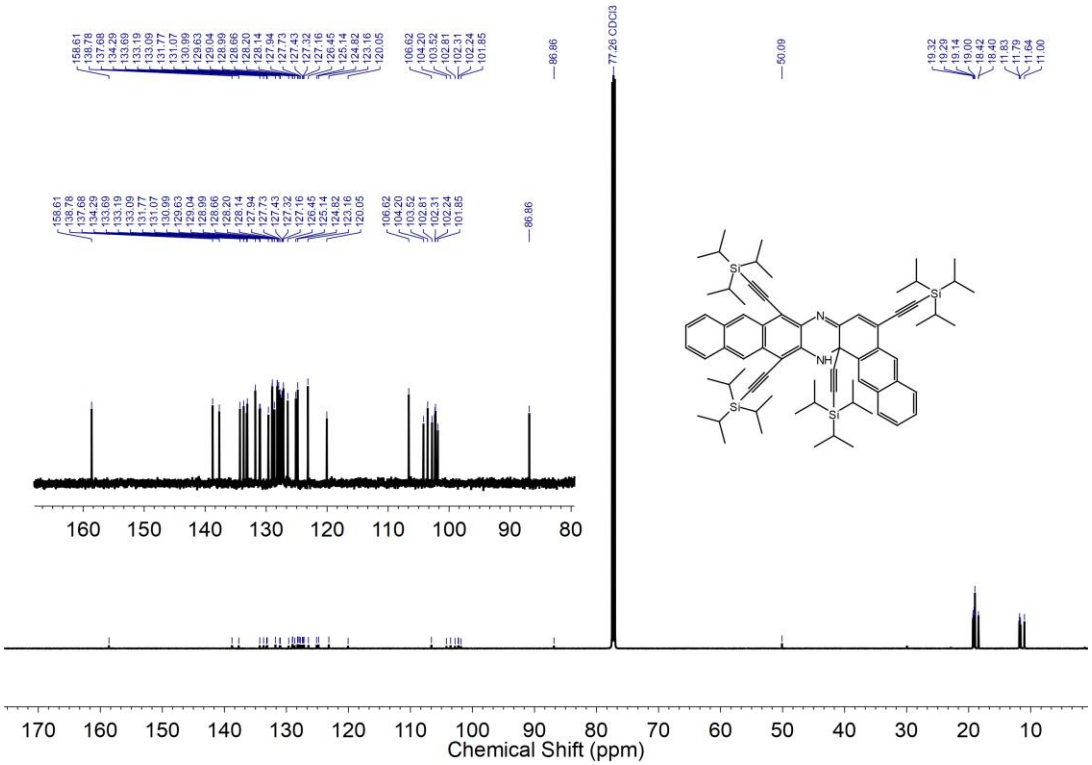

Figure 105. ^{13}C NMR spectrum (151 MHz, 295 K) of **57** in $CDCl_3$.

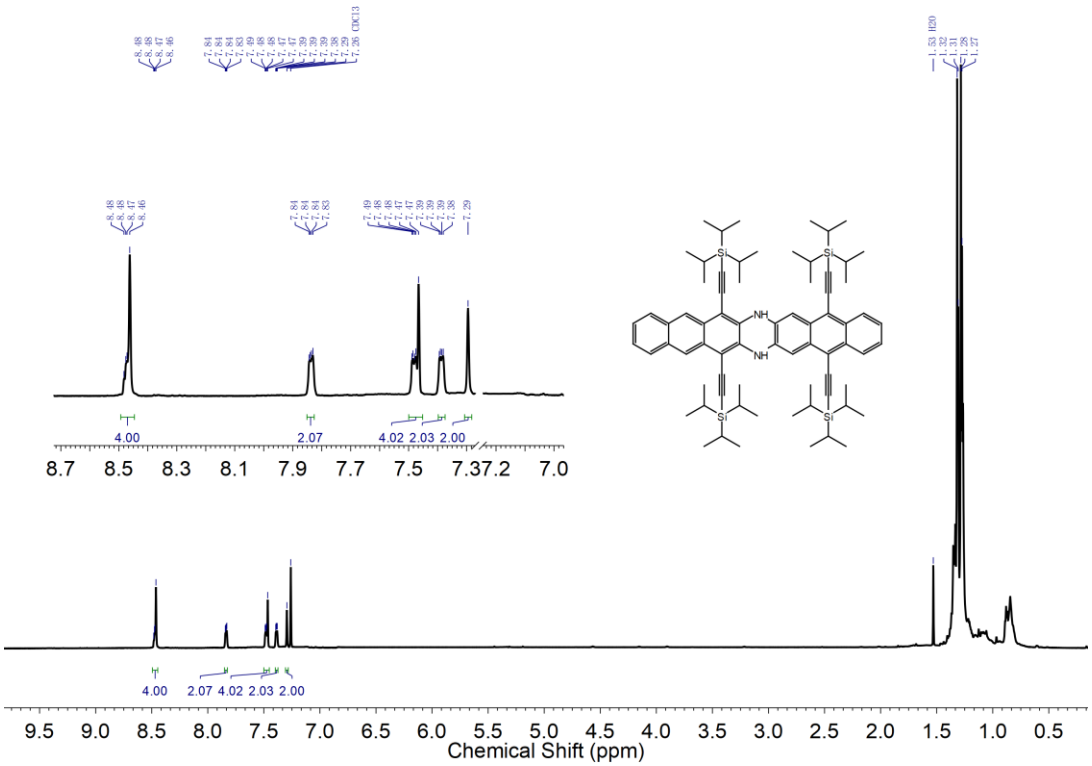

Figure 106. ^{1}H NMR spectrum (600 MHz, 295 K) of **DAH2-H$_2$** in $CDCl_3$.

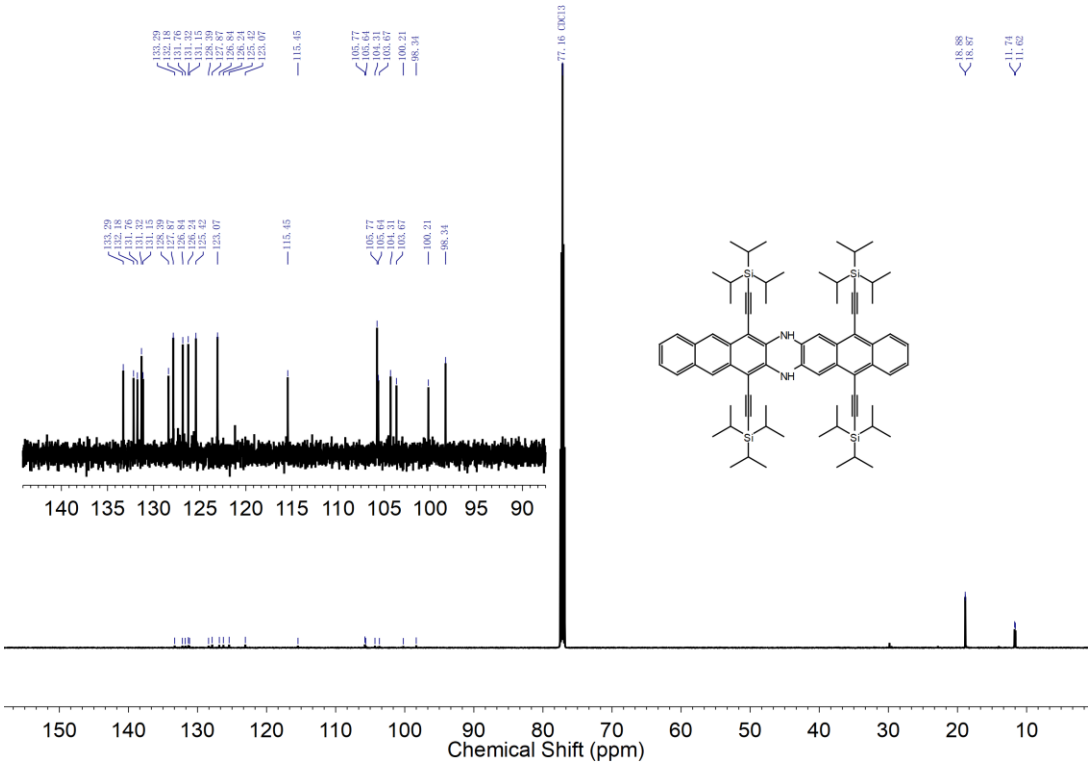

Figure 107. ^{13}C NMR spectrum (151 MHz, 295 K) of **DAH2-H$_2$** in $CDCl_3$.

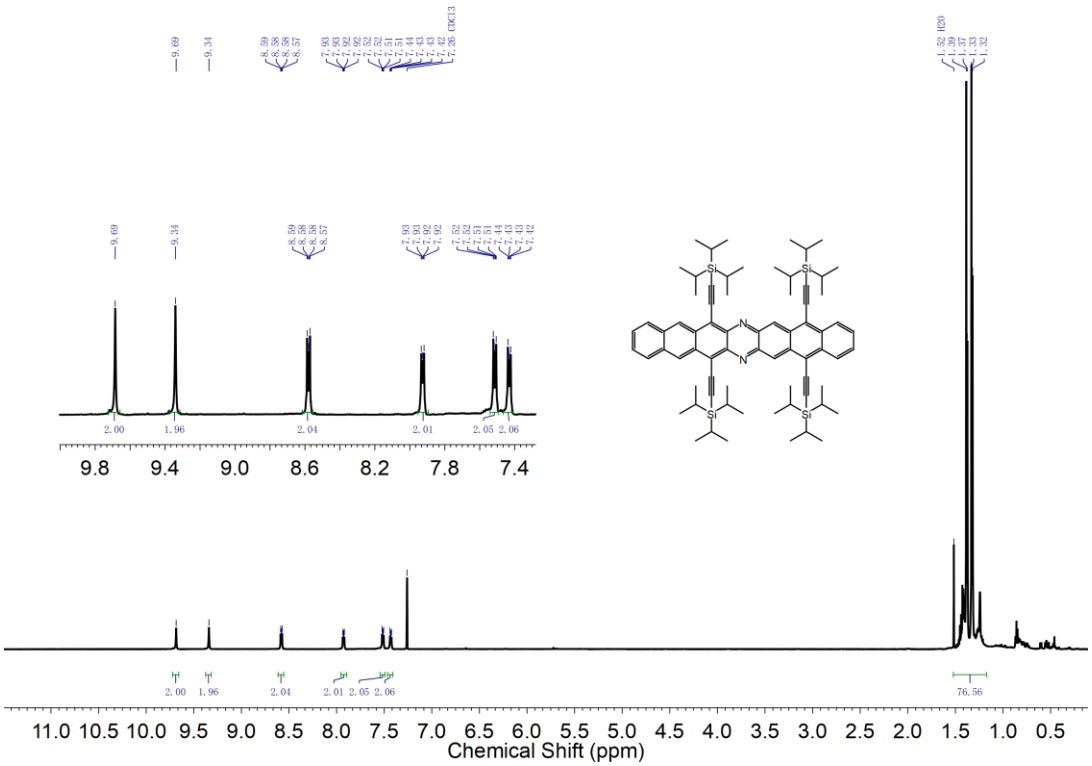

Figure 108. ^{1}H NMR spectrum (600 MHz, 295 K) of **DAH2** in $CDCl_3$.

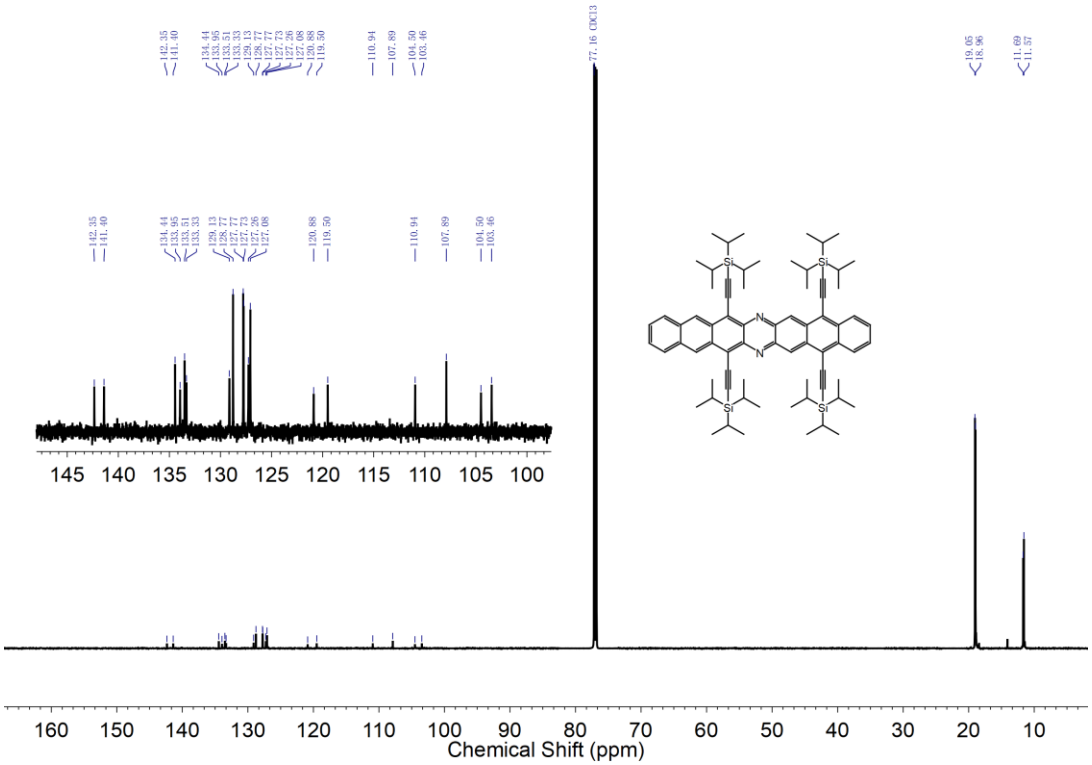

Figure 109. ^{13}C NMR spectrum (151 MHz, 295 K) of **DAH2** in $CDCl_3$.

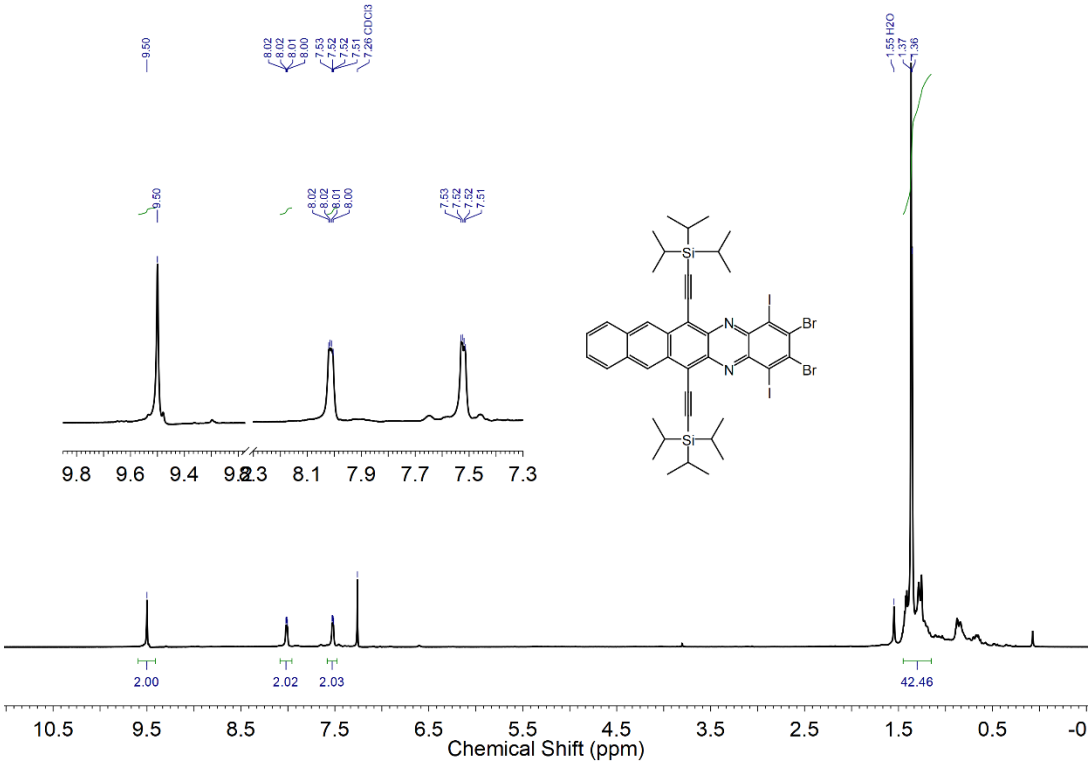

Figure 110. ^{1}H NMR spectrum (600 MHz, 295 K) of **58a** in $CDCl_3$.

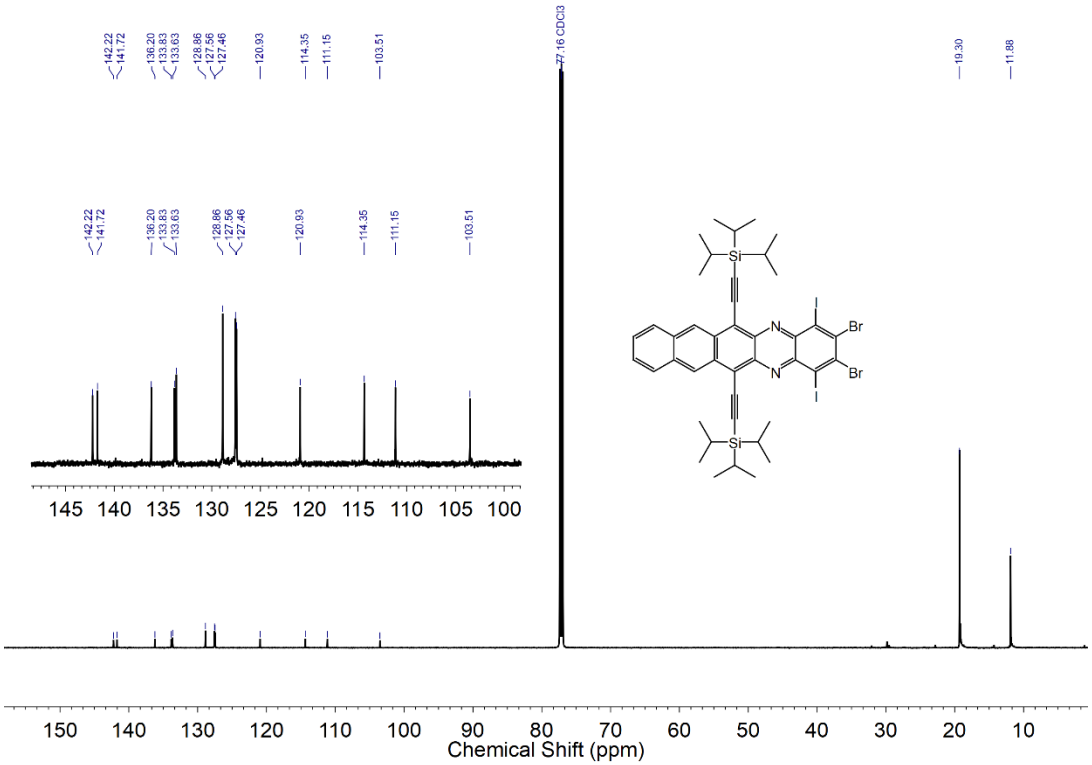

Figure 111. ^{13}C NMR spectrum (151 MHz, 295 K) of **58a** in $CDCl_3$.

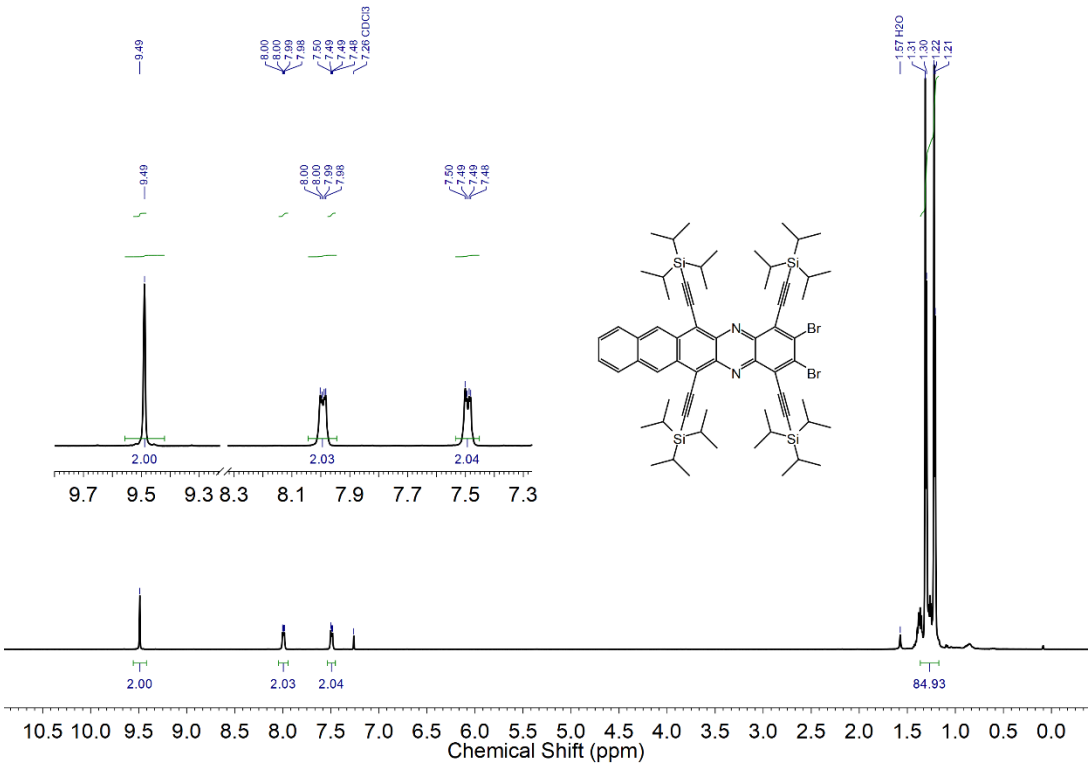

Figure 112. ^{1}H NMR spectrum (500 MHz, 295 K) of **59a** in $CDCl_3$.

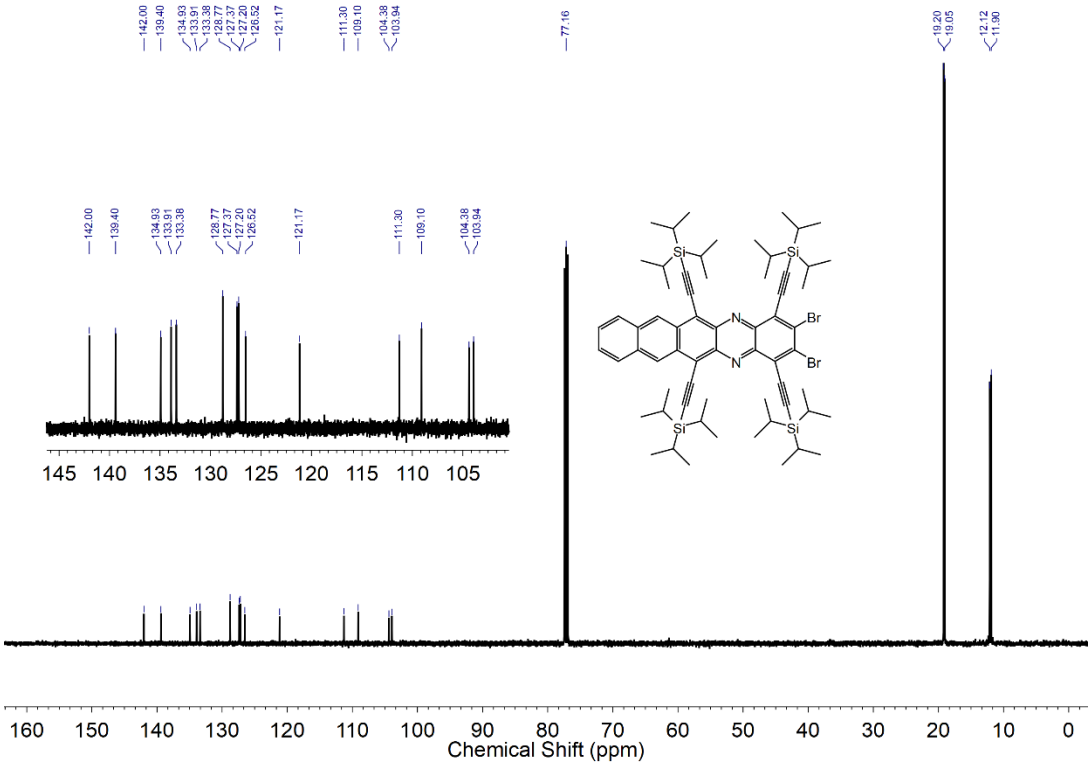

Figure 113. ^{13}C NMR spectrum (126 MHz, 295 K) of **59a** in $CDCl_3$.

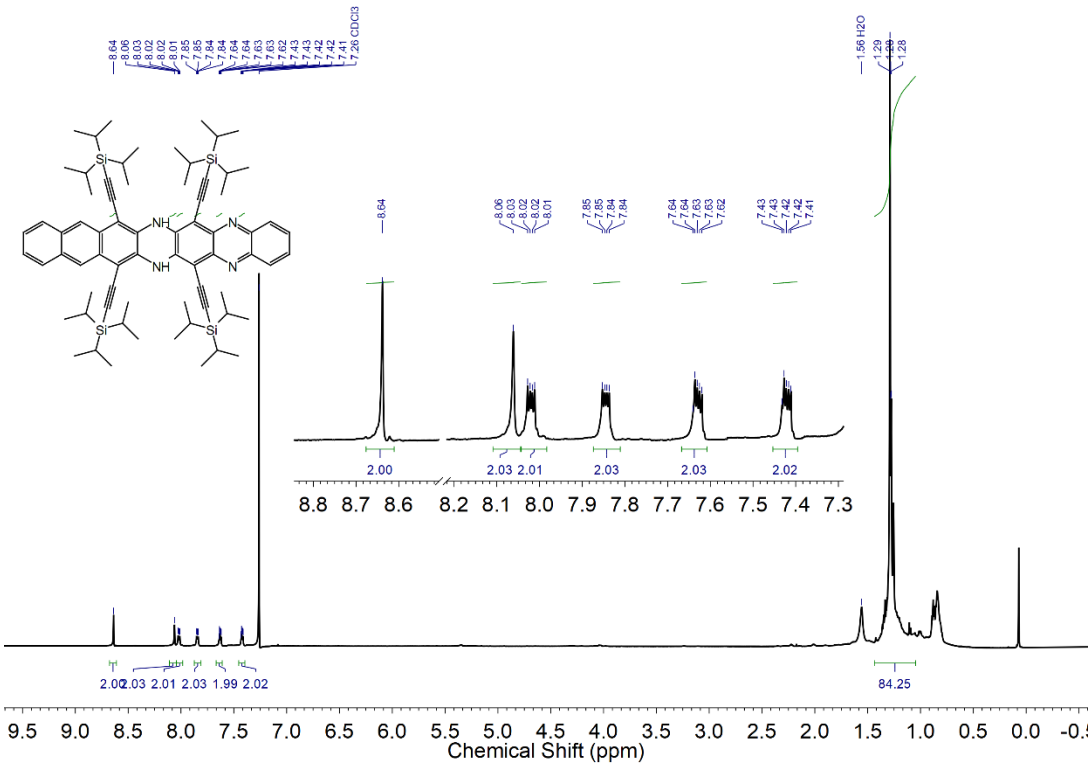

Figure 114. ^{1}H NMR spectrum (600 MHz, 295 K) of **TAH-H₂** in $CDCl_3$.

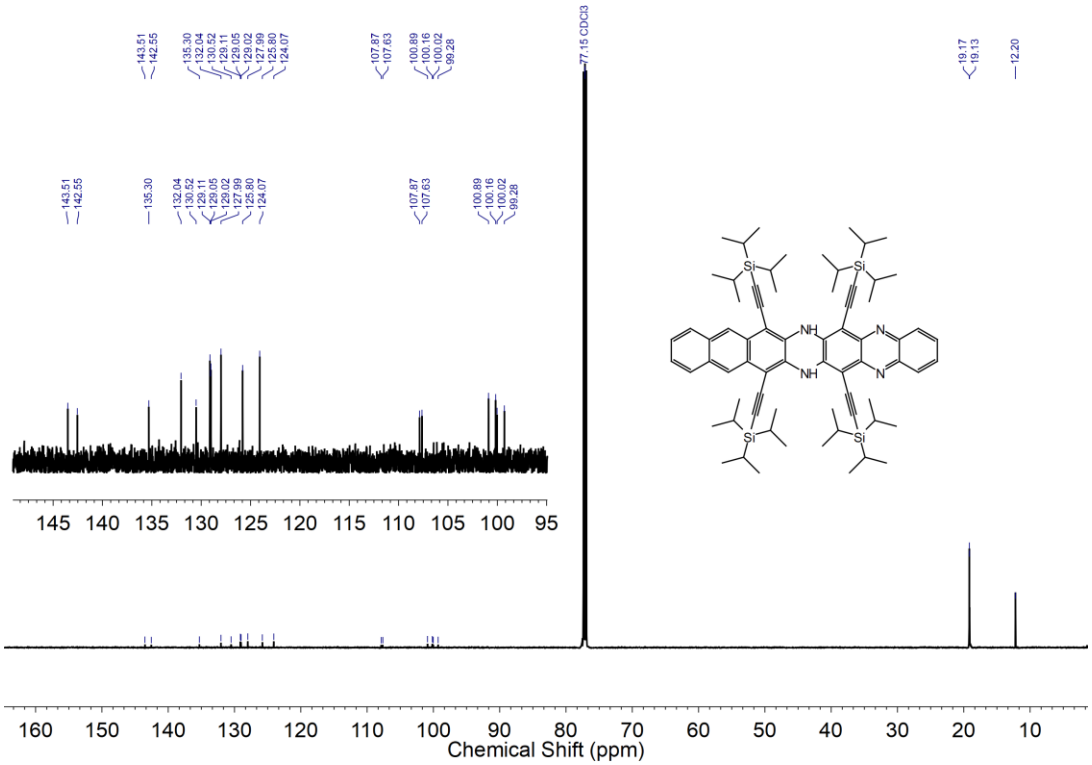

Figure 115. ^{13}C NMR spectrum (151 MHz, 295 K) of **TAH-H$_2$** in $CDCl_3$.

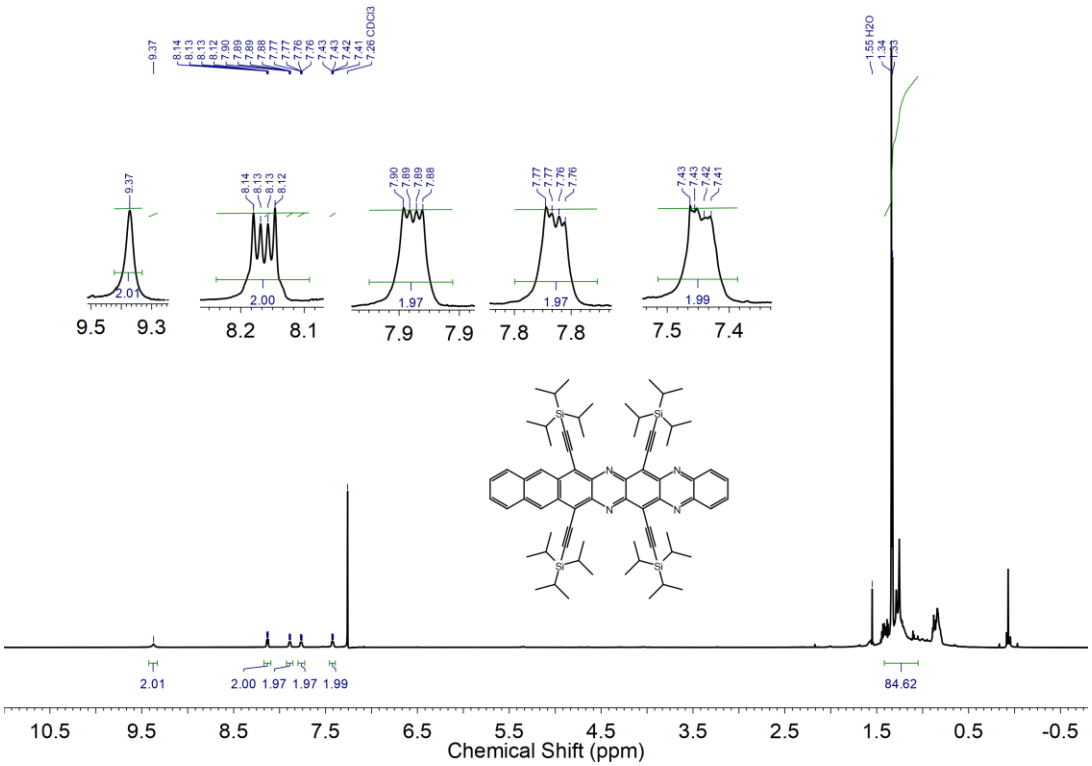

Figure 116. ^{1}H NMR spectrum (600 MHz, 295 K) of **TAH** in $CDCl_3$.

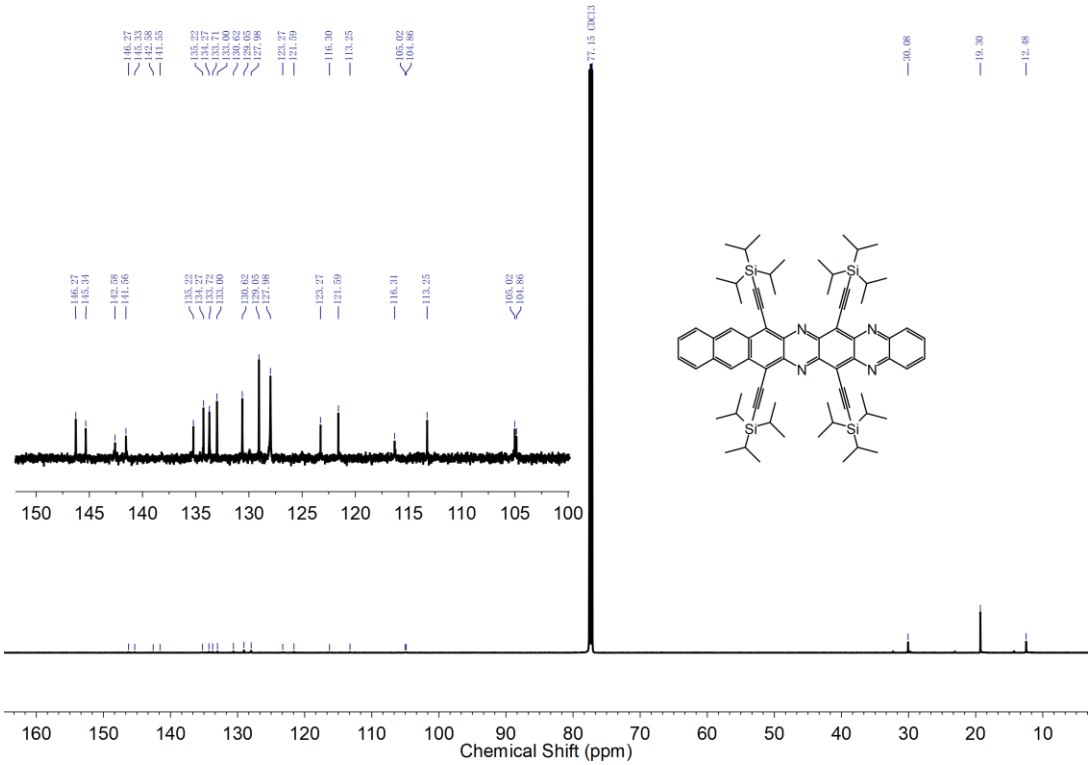

Figure 117. ^{13}C NMR spectrum (151 MHz, 295 K) of **TAH** in $CDCl_3$.

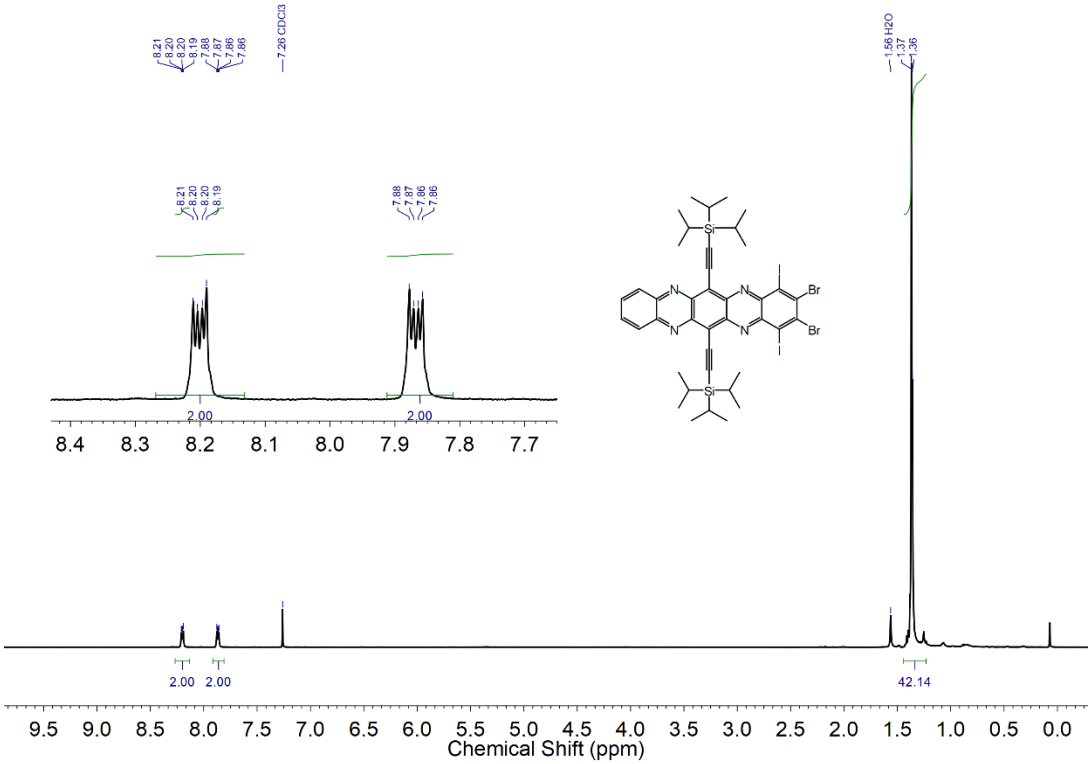

Figure 118. ^{1}H NMR spectrum (500 MHz, 295 K) of **58b** in $CDCl_3$.

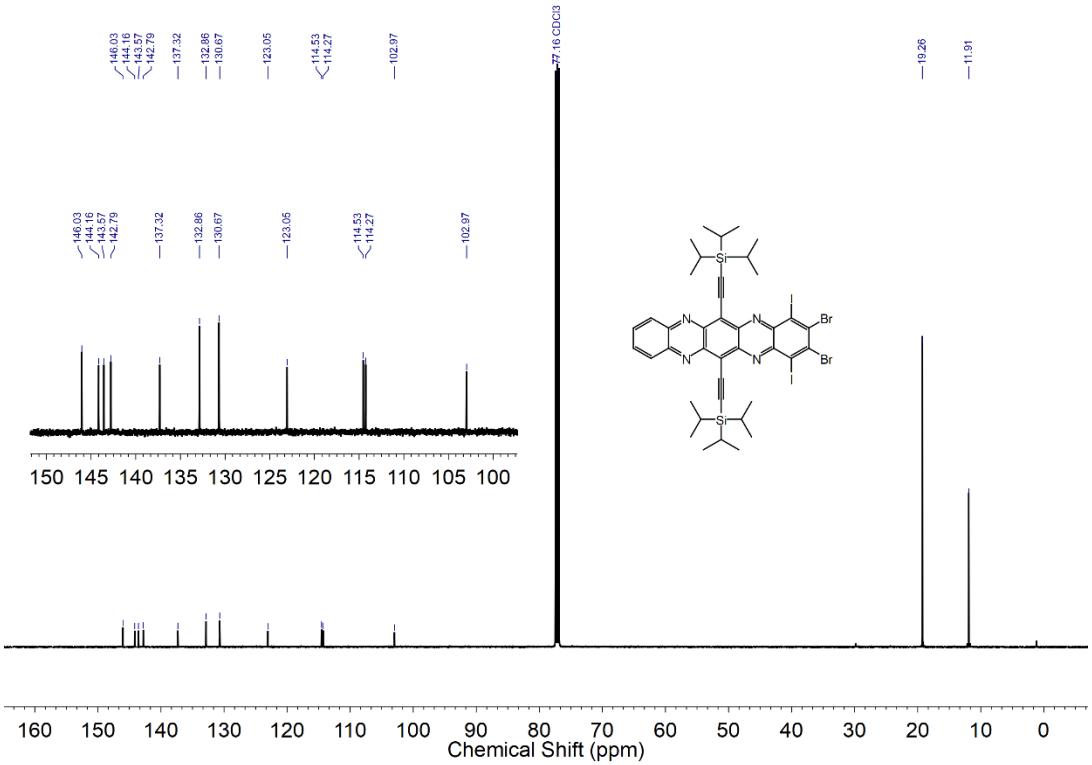

Figure 119. ^{13}C NMR spectrum (126 MHz, 295 K) of **58b** in $CDCl_3$.

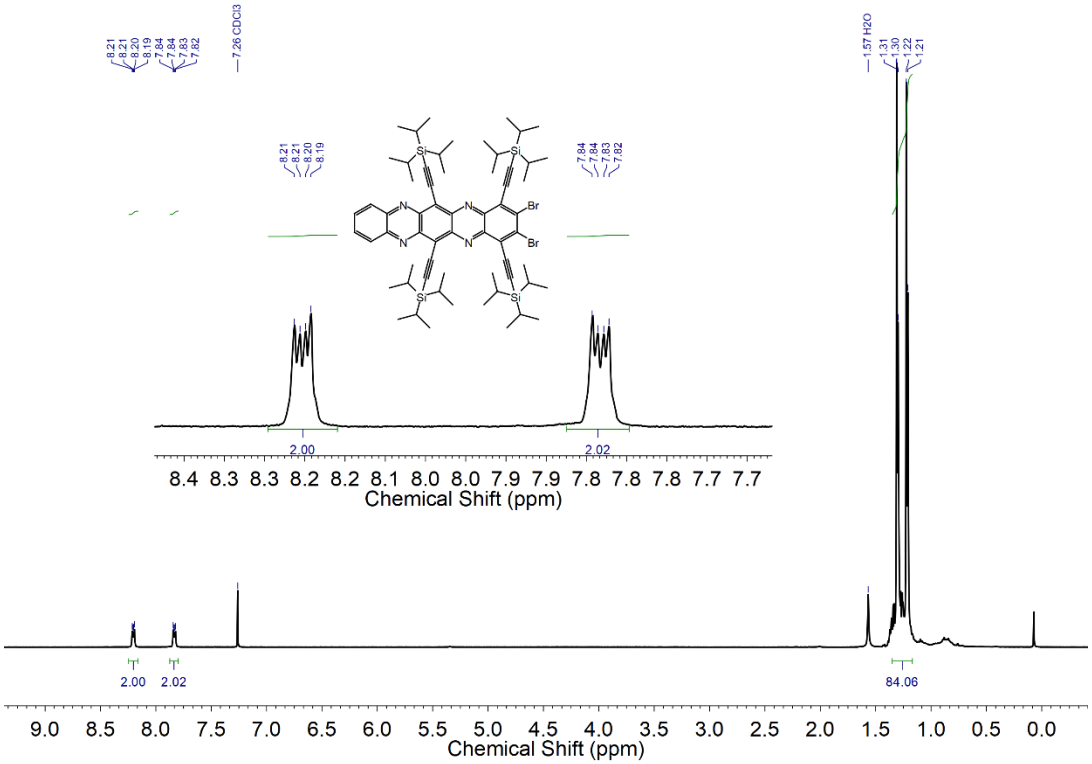

Figure 120. ^{1}H NMR spectrum (500 MHz, 295 K) of **59b** in $CDCl_3$.

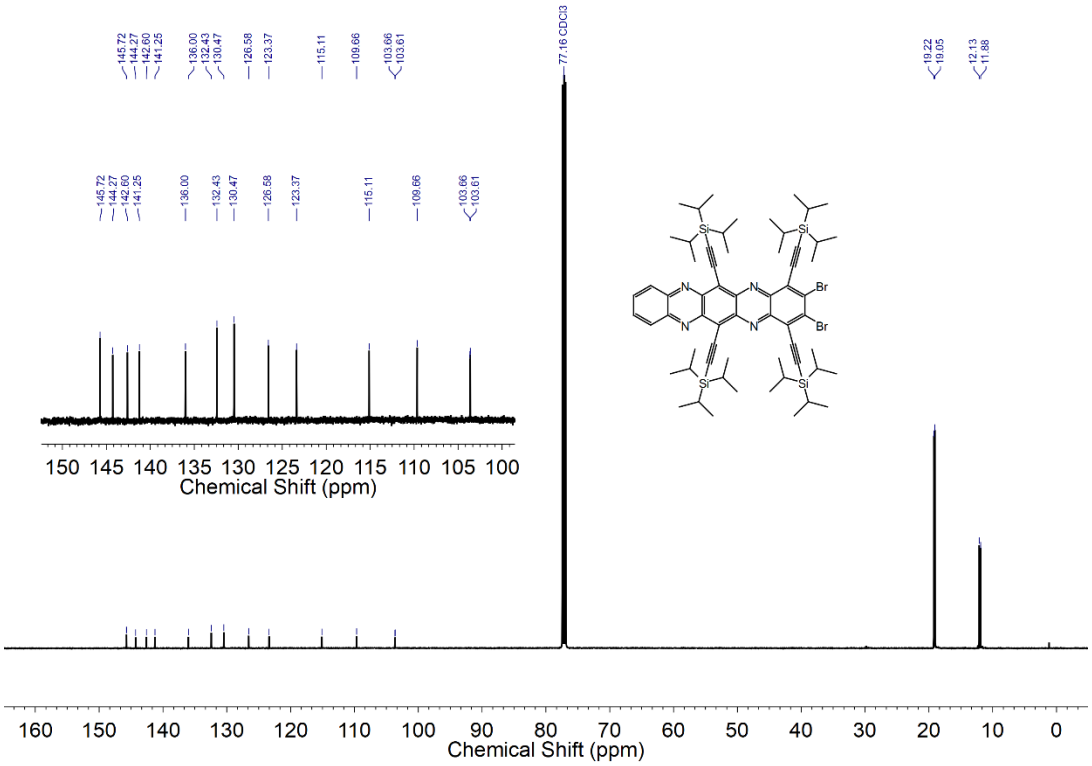

Figure 121. ^{13}C NMR spectrum (126 MHz, 295 K) of **59b** in $CDCl_3$.

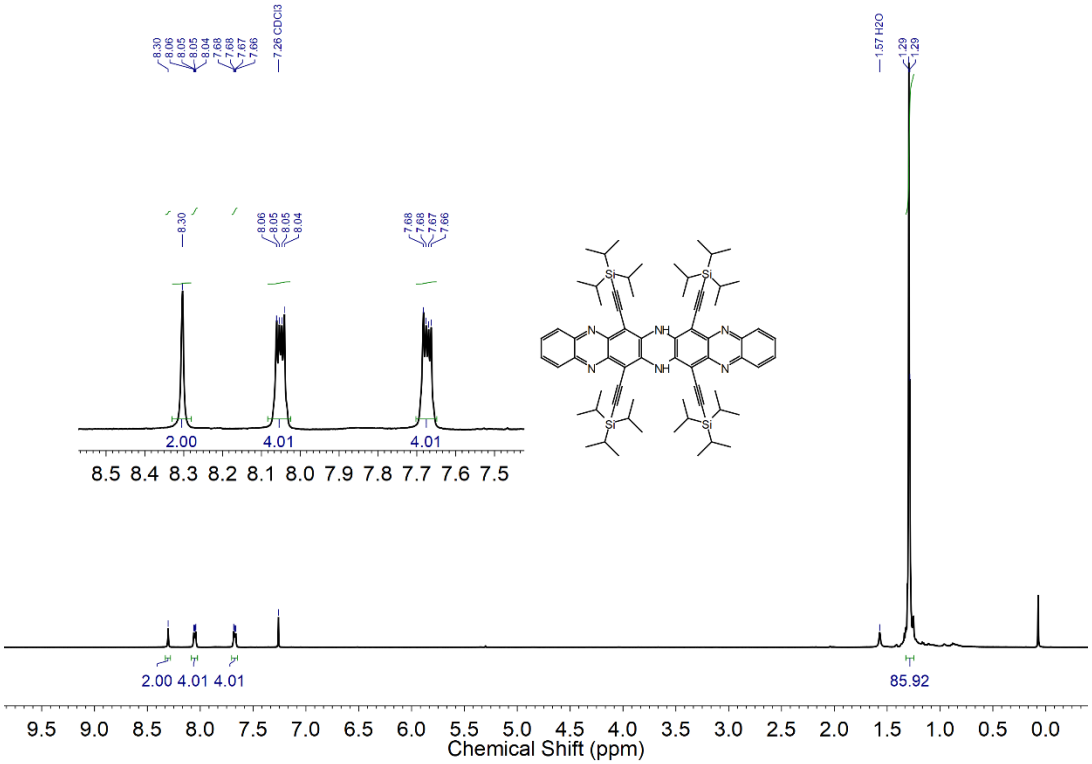

Figure 122. ^{1}H NMR spectrum (500 MHz, 295 K) of **HAH-H$_2$** in $CDCl_3$.

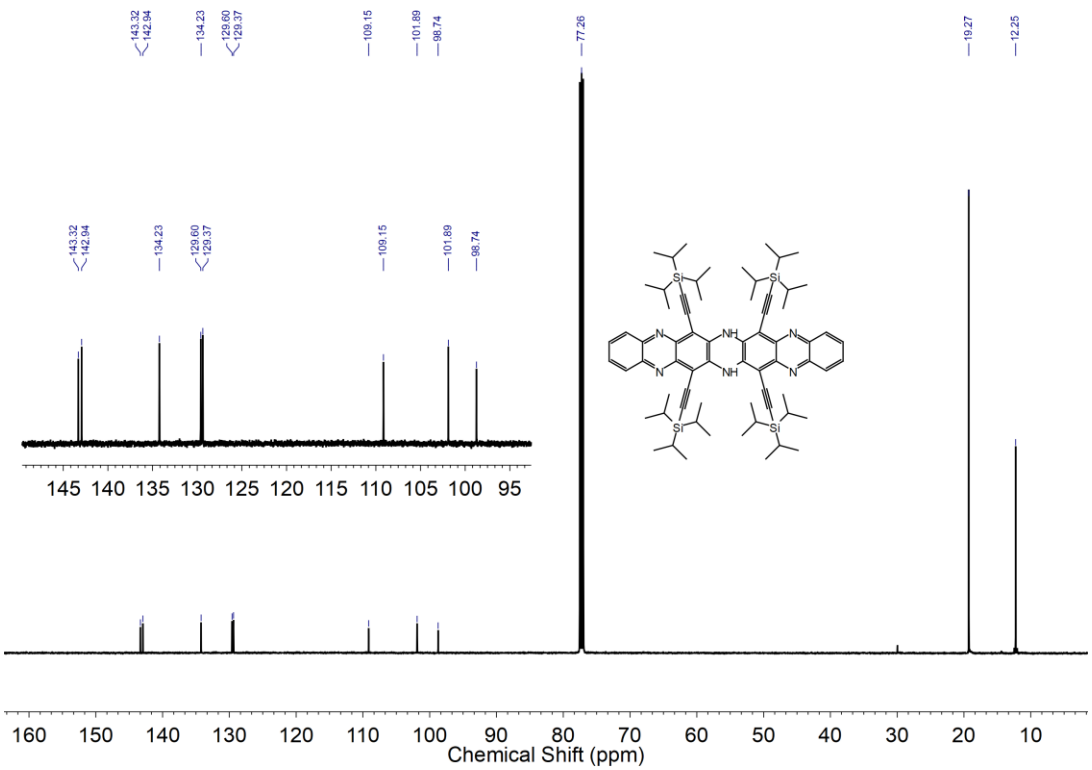

Figure 123. ^{13}C NMR spectrum (126 MHz, 295 K) of **HAH-H$_2$** in $CDCl_3$.

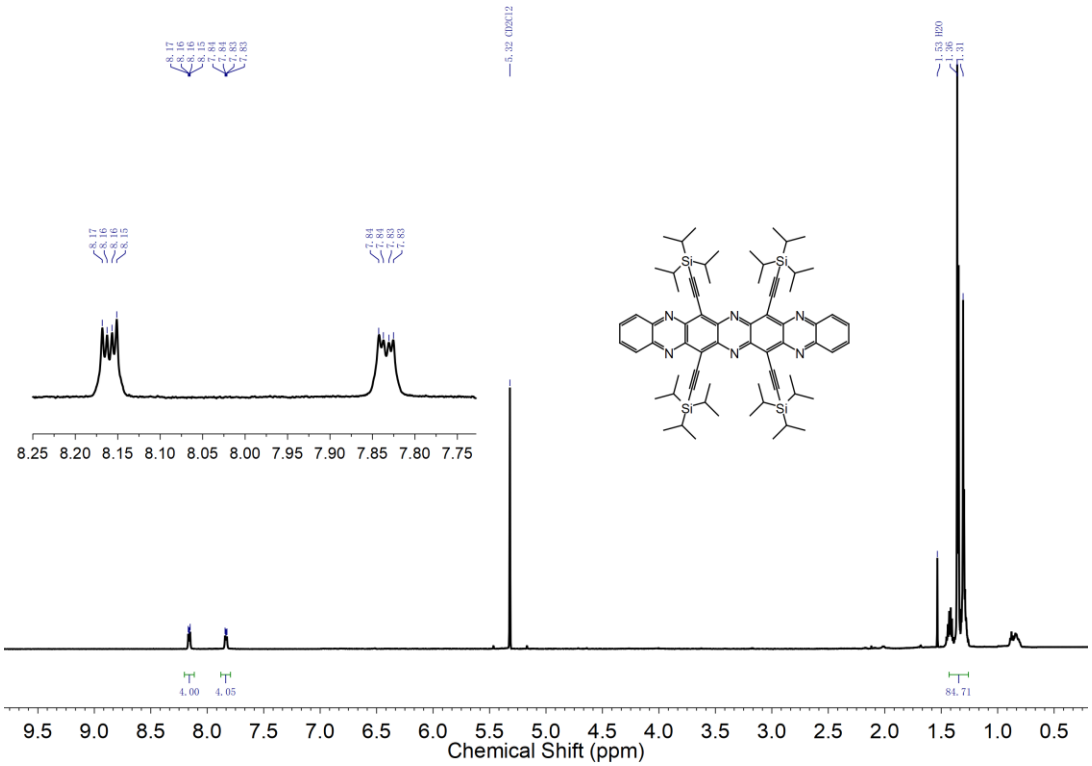

Figure 124. ^{1}H NMR spectrum (600 MHz, 295 K) of **HAH** in CD_2Cl_2 with PbO_2 under an inert atmosphere.

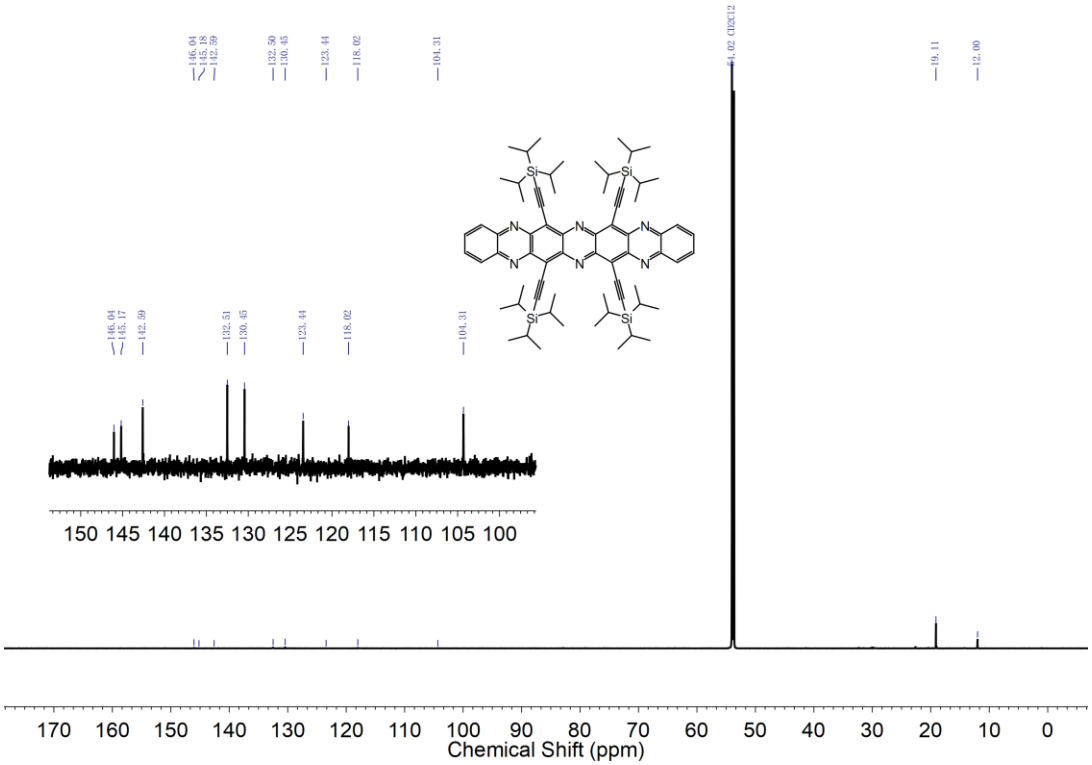

Figure 125. ^{13}C NMR spectrum (151 MHz, 295 K) of **HAH** in CD_2Cl_2 with PbO_2 under an inert atmosphere.

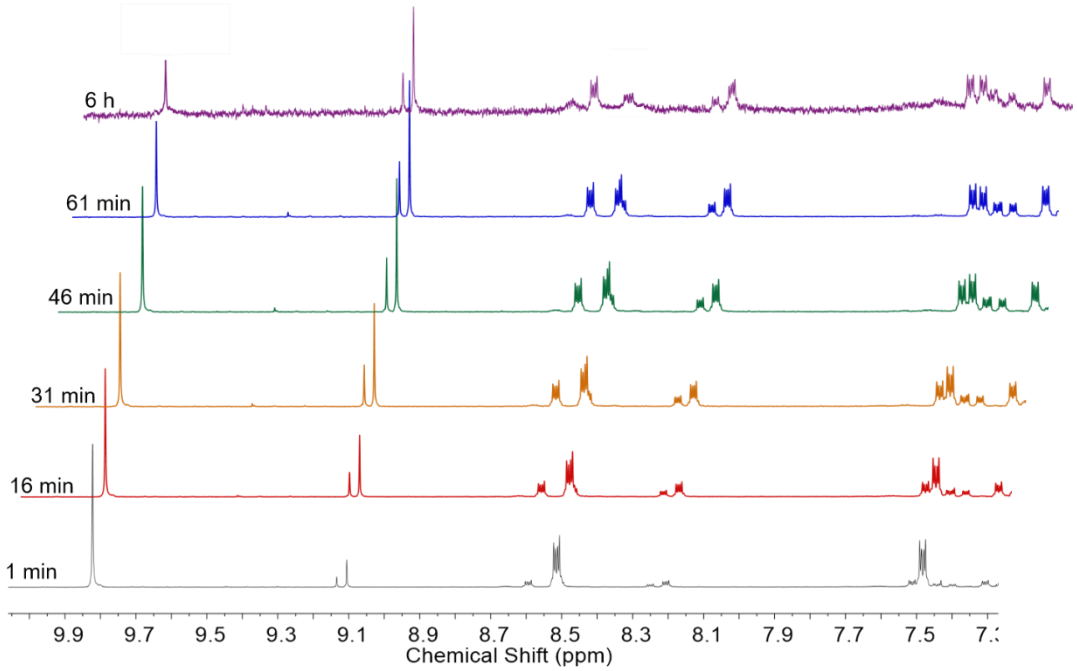

Figure 126. Time-dependent ^{1}H NMR spectra of **DAH3** in $CDCl_3$ under ambient conditions magnifying all signals in the aromatic region.

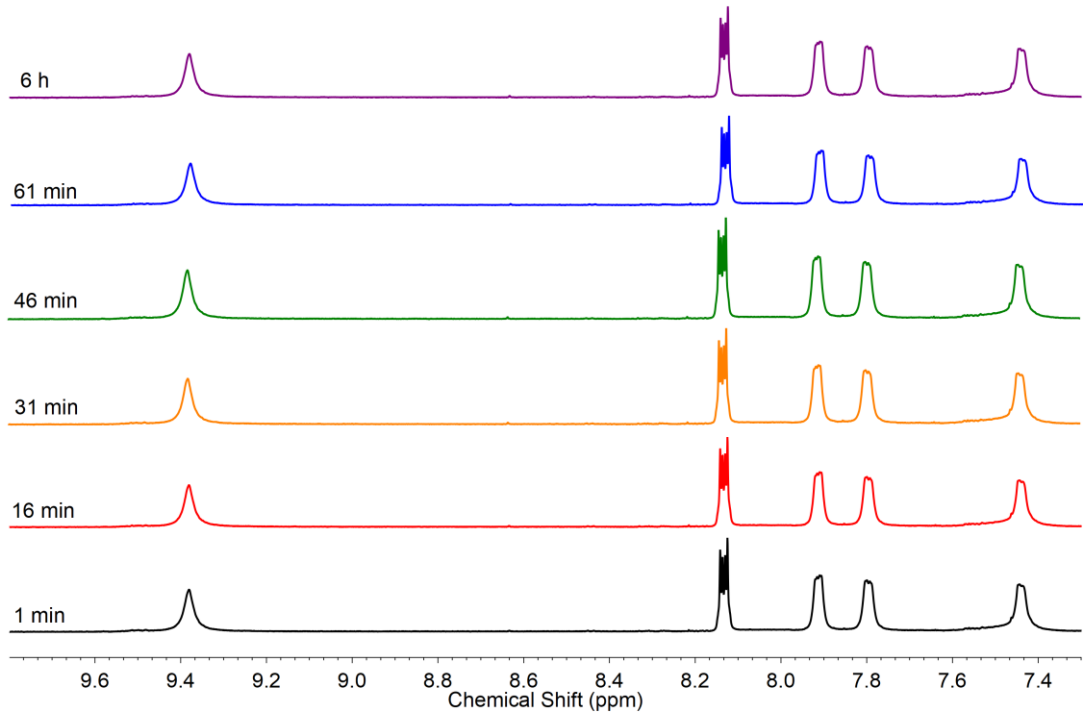

Figure 127. Time-dependent ^{1}H NMR spectra of **TAH** in $CDCl_3$ under ambient conditions magnifying all signals in the aromatic region.

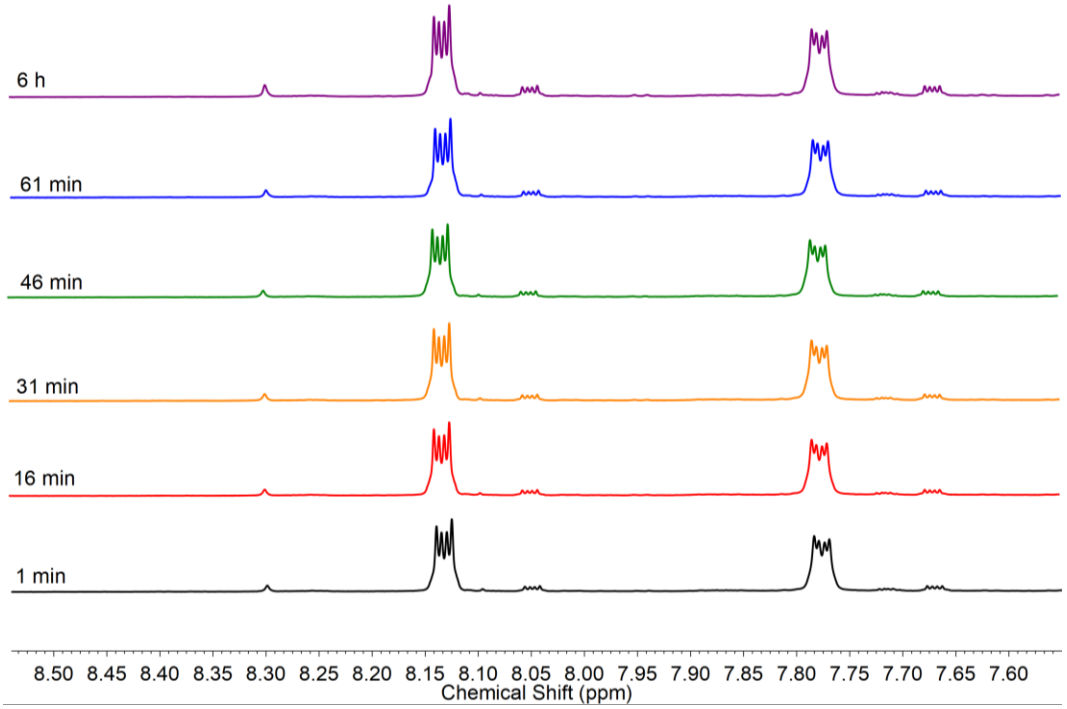

Figure 128. Time-dependent ^{1}H NMR spectra of **HAH** in $CDCl_3$ under ambient conditions magnifying all signals in the aromatic region. Weak signals originating from degradation specie (**HAH-H$_2$**) was observed because of the spontaneous back reduction process of **HAH**, and this part occupied about 7% (estimated from the integration).

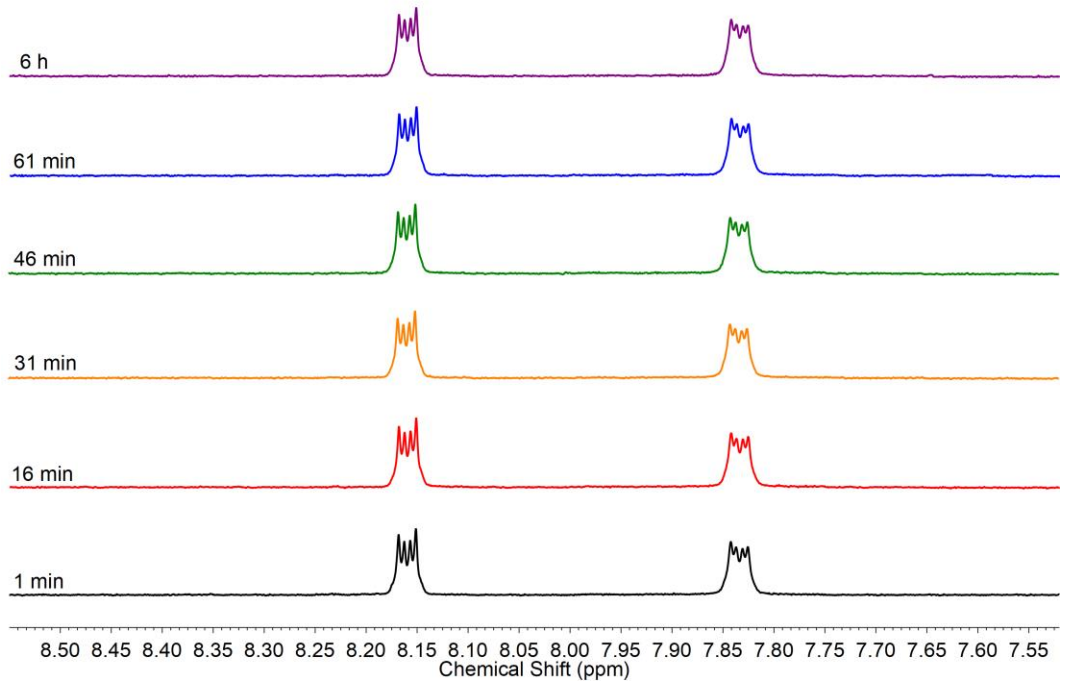

Figure 129. Time-dependent ^{1}H NMR spectra of **HAH** in CD_2Cl_2 with PbO_2 under an inert atmosphere magnifying all signals in the aromatic region.

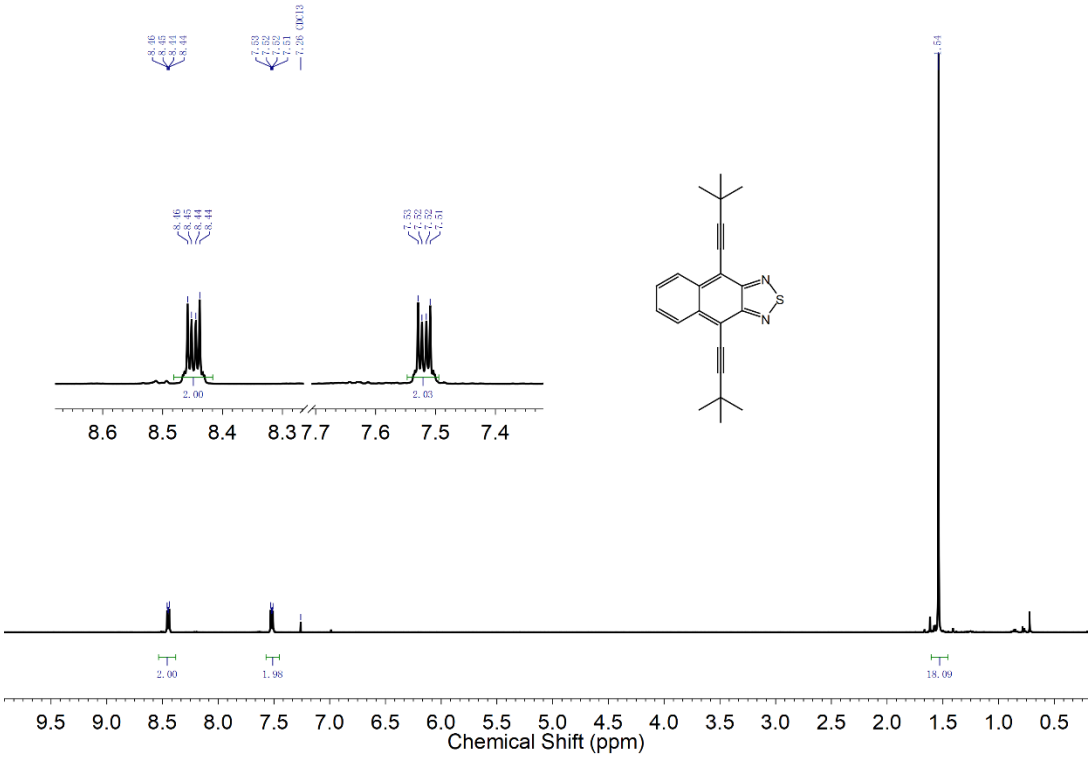

Figure 130. ^{1}H NMR spectrum (500 MHz, 295 K) of **62a** in $CDCl_3$.

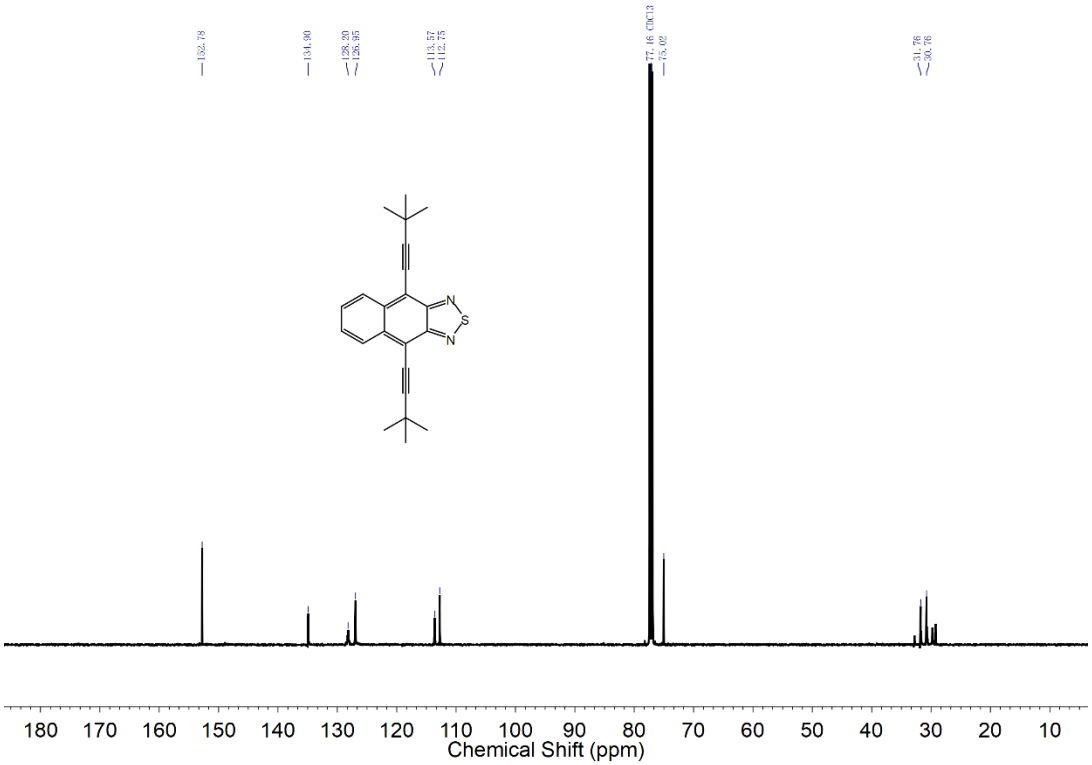

Figure 131. ^{13}C NMR spectrum (126 MHz, 295 K) of **62a** in $CDCl_3$.

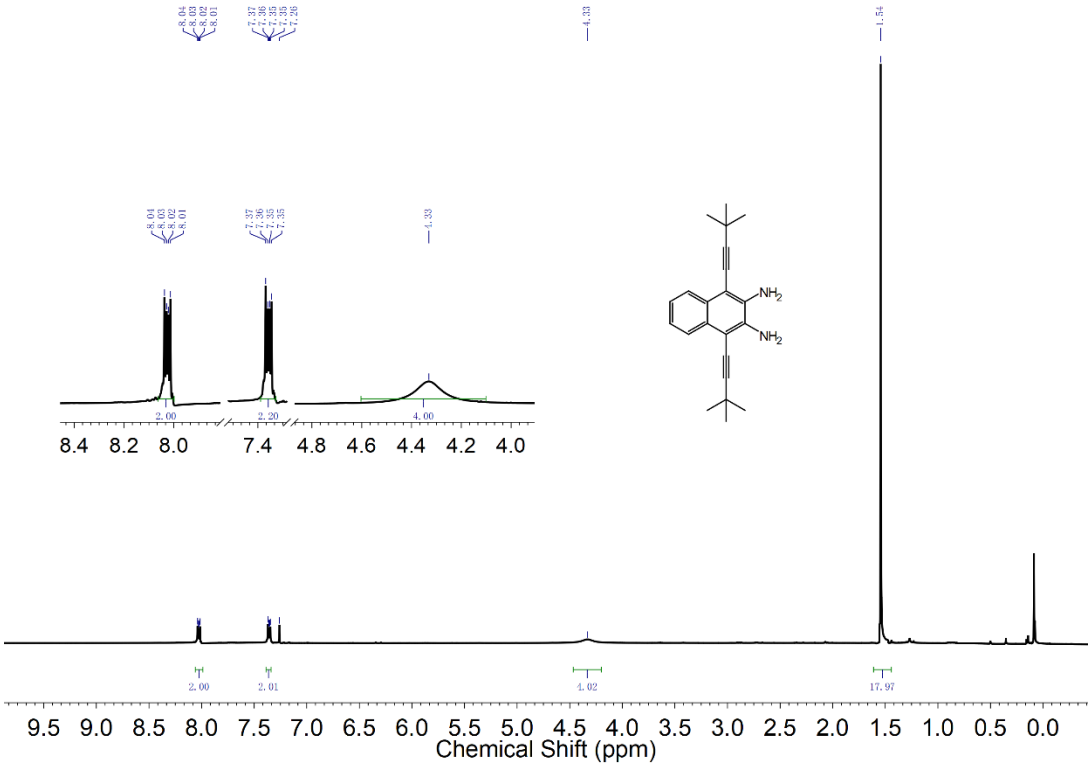

Figure 132. ^{1}H NMR spectrum (400 MHz, 295 K) of **34a** in $CDCl_3$.

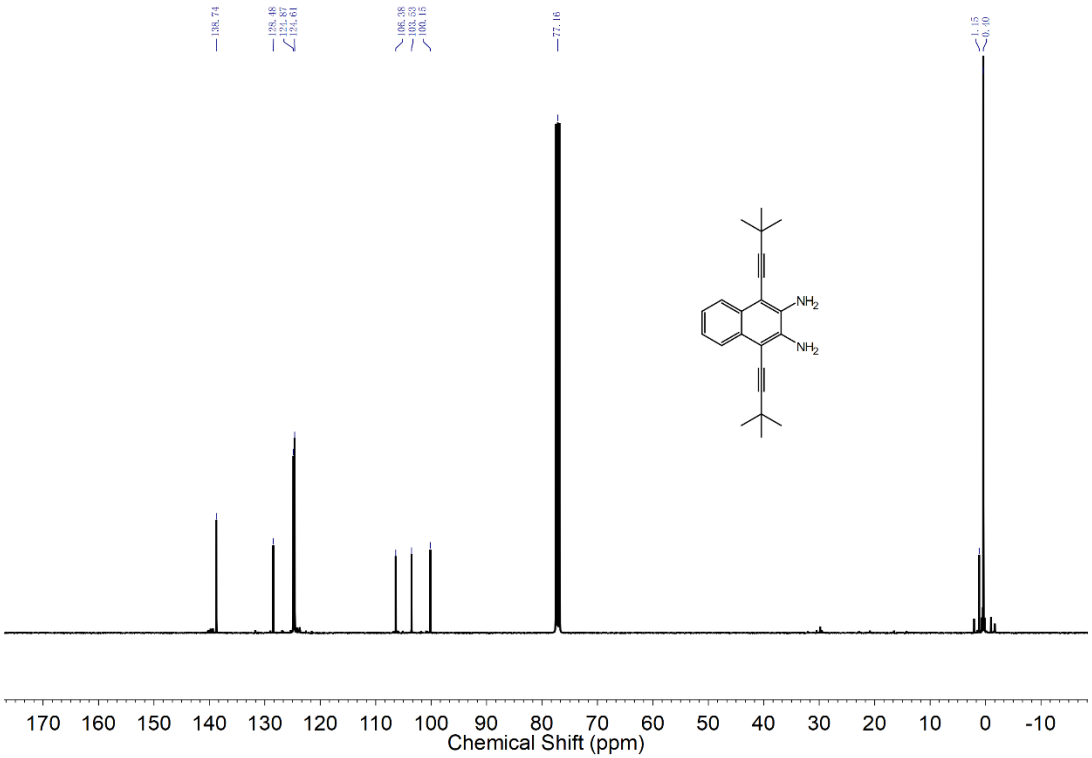

Figure 133. ^{13}C NMR spectrum (101 MHz, 295 K) of **34a** in $CDCl_3$.

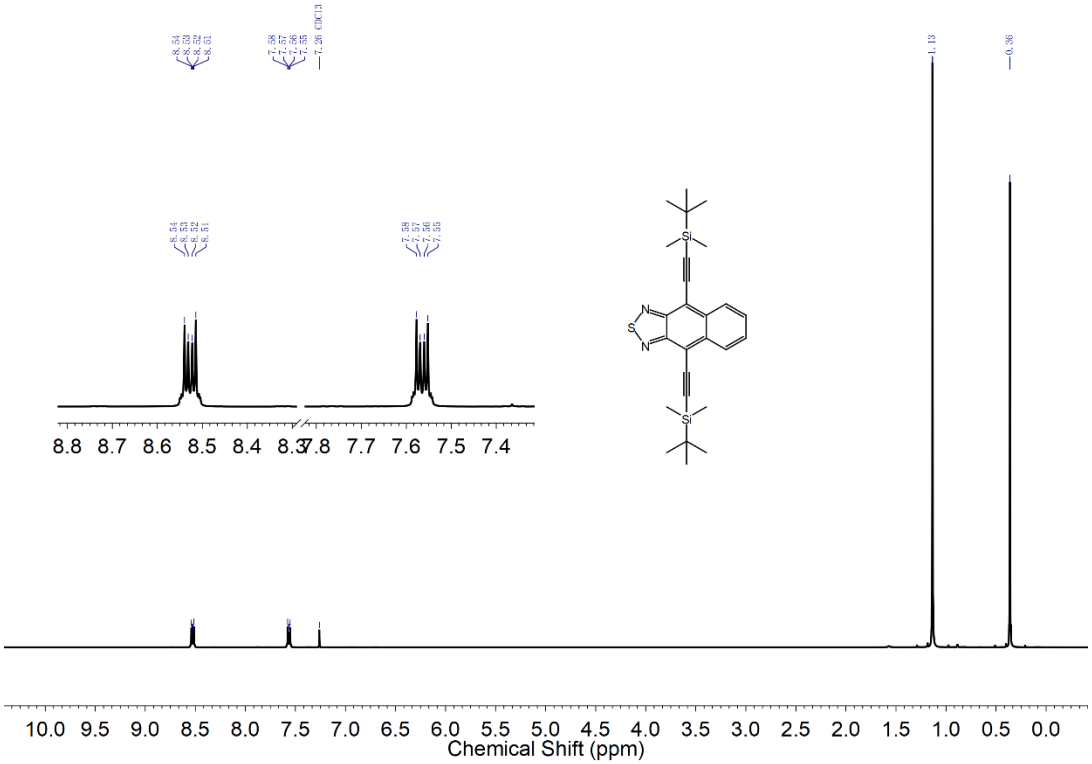

Figure 134. ^{1}H NMR spectrum (400 MHz, 295 K) of **62b** in $CDCl_3$.

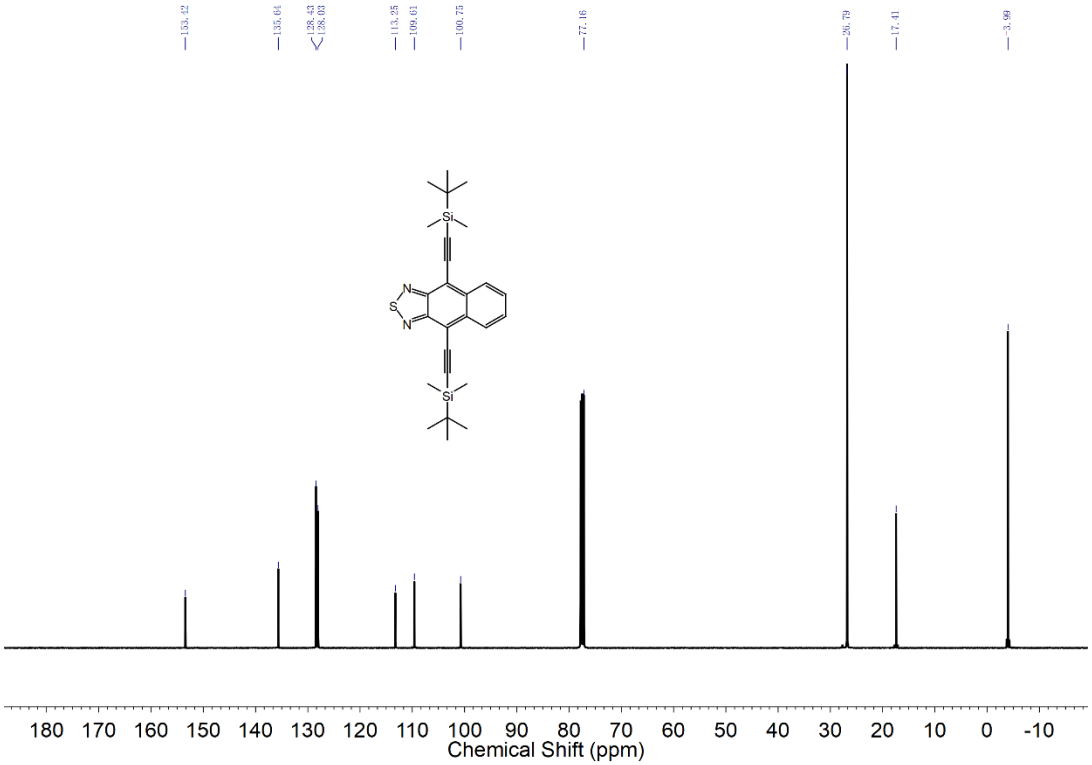

Figure 135. ^{13}C NMR spectrum (101 MHz, 295 K) of **62b** in $CDCl_3$.

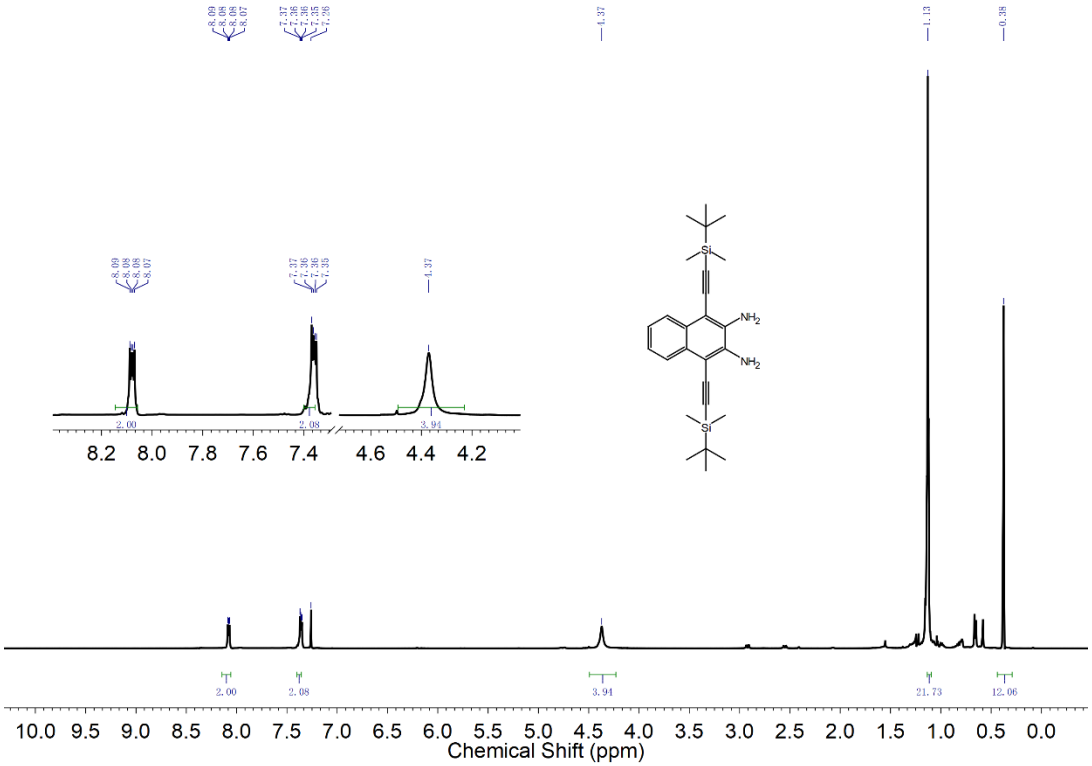

Figure 136. ^{1}H NMR spectrum (400 MHz, 295 K) of **34b** in $CDCl_3$.

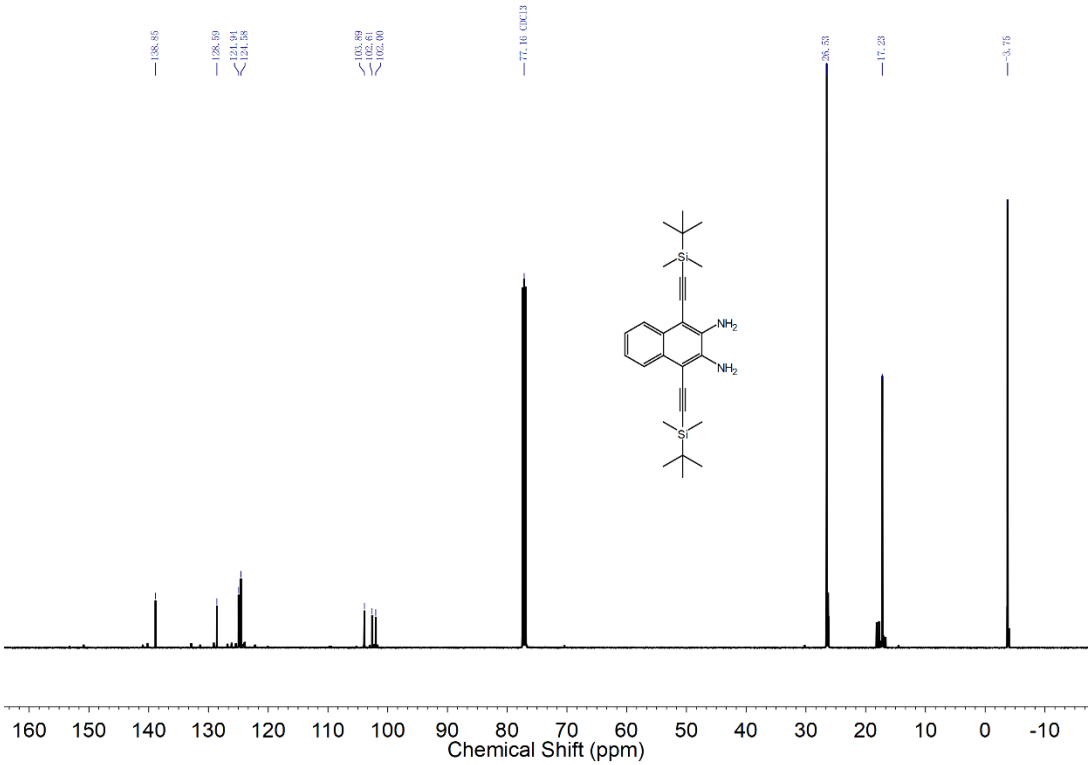

Figure 137. ^{13}C NMR spectrum (101 MHz, 295 K) of **34b** in $CDCl_3$.

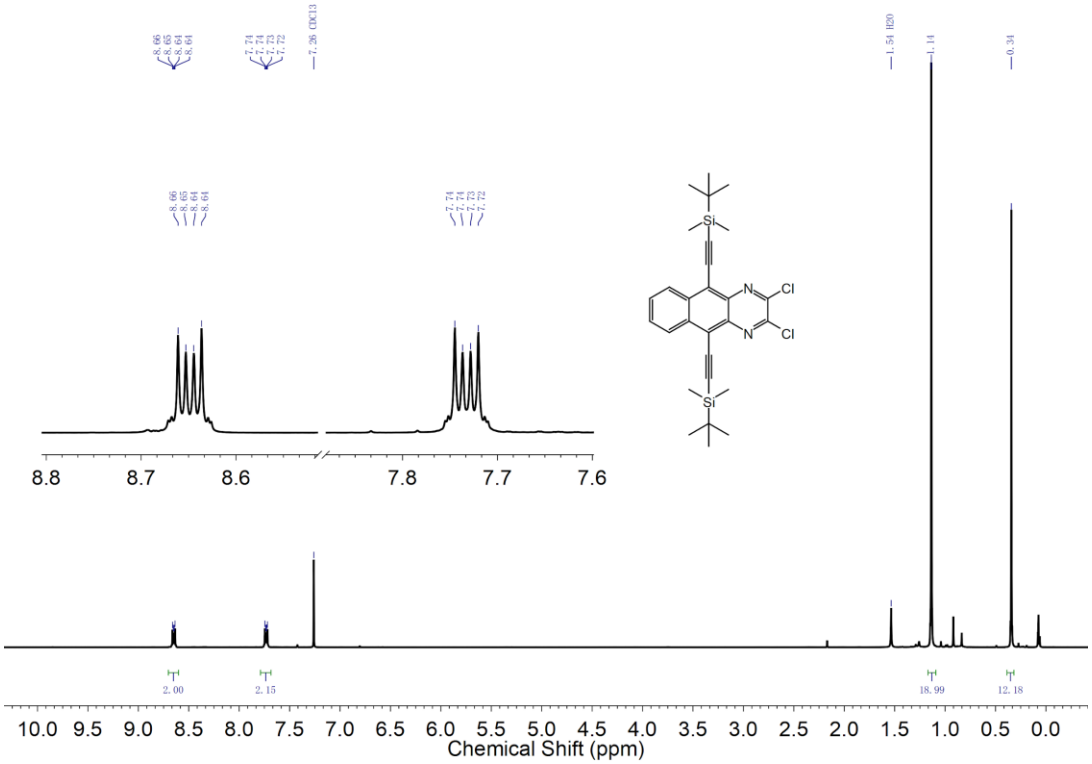

Figure 138. ^{1}H NMR spectrum (400 MHz, 295 K) of **63b** in $CDCl_3$.

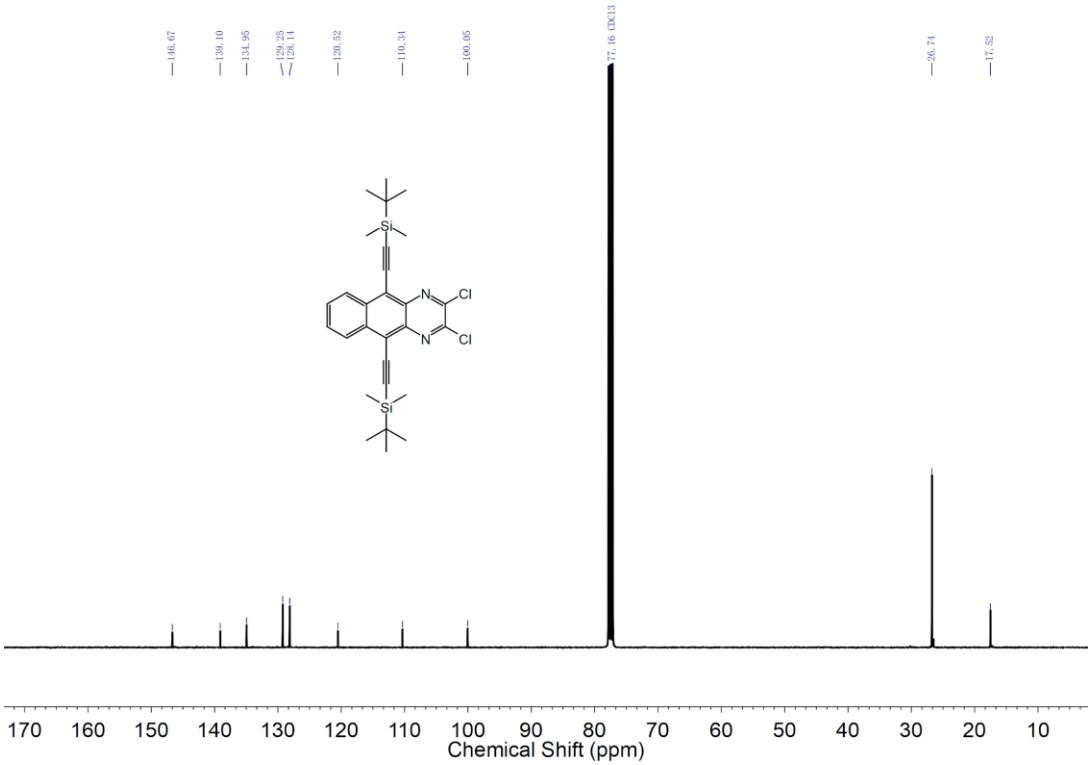

Figure 139. ^{13}C NMR spectrum (101 MHz, 295 K) of **63b** in $CDCl_3$.

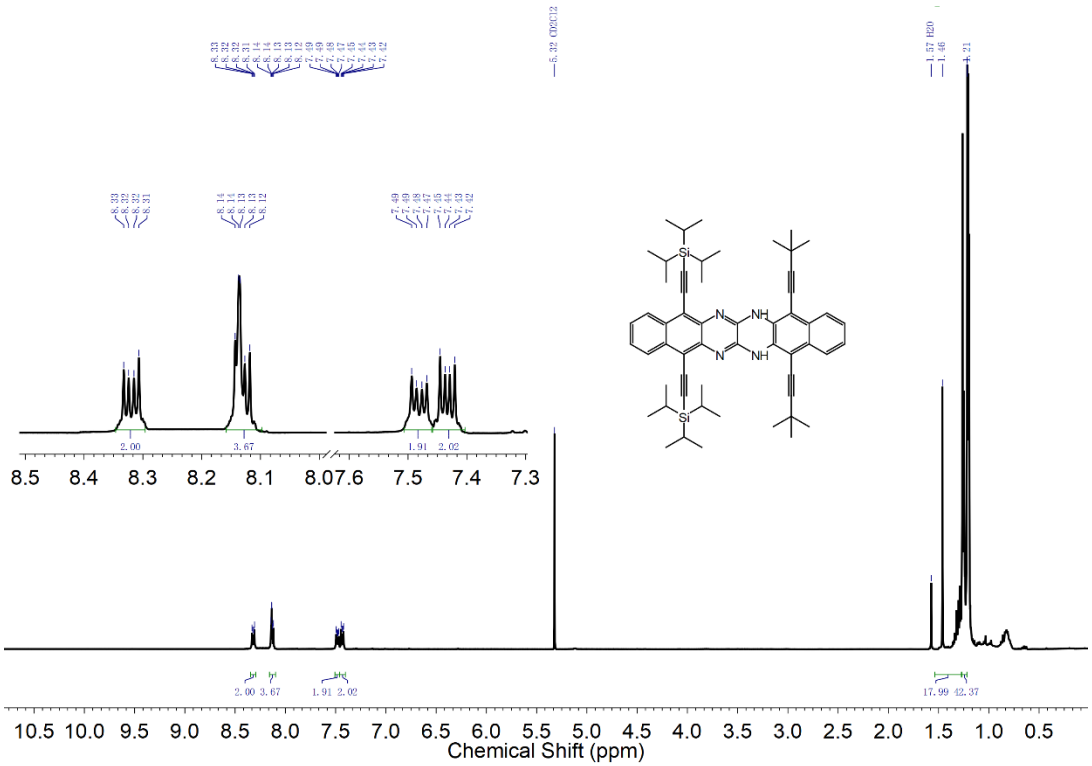

Figure 140. ^{1}H NMR spectrum (600 MHz, 295 K) of **TAHex1-H$_2$** in CD_2Cl_2.

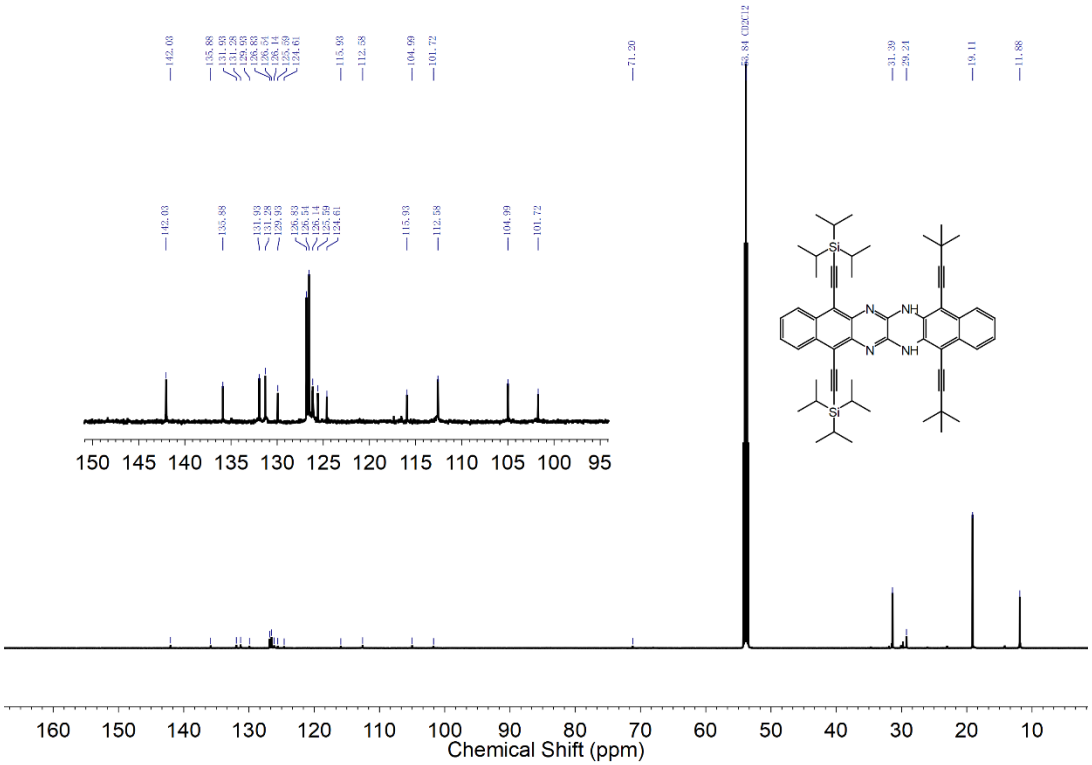

Figure 141. ^{13}C NMR spectrum (151 MHz, 295 K) of **TAHex1-H$_2$** in CD_2Cl_2.

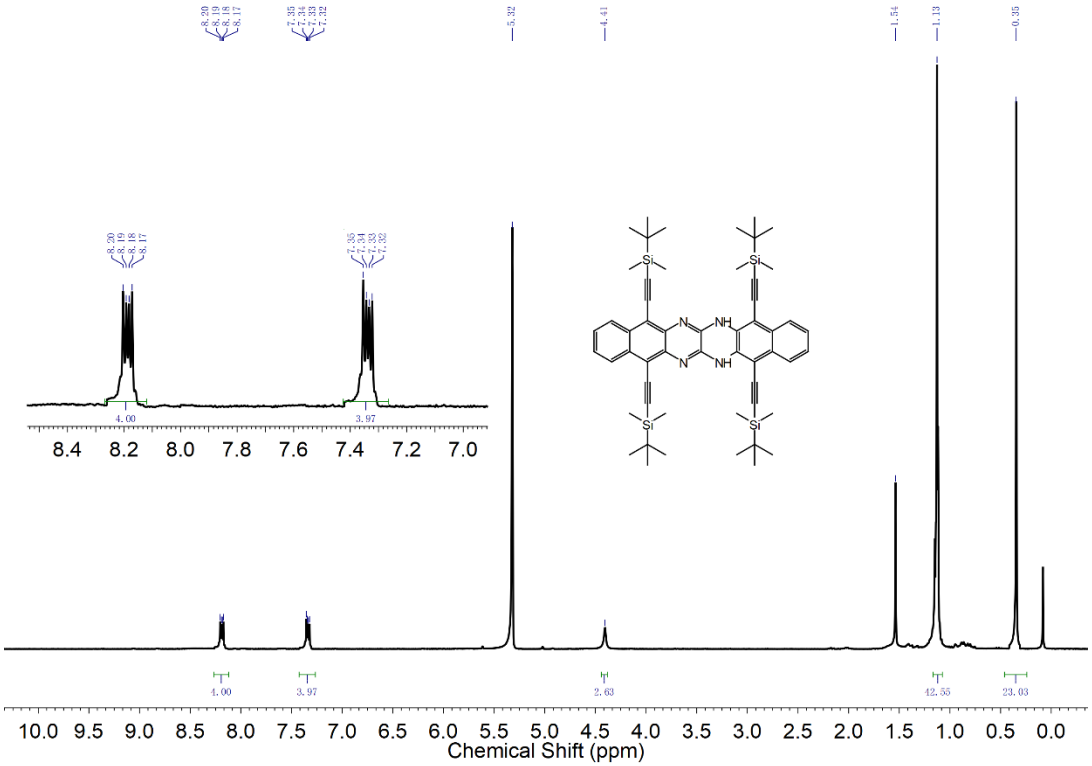

Figure 142. ^{1}H NMR spectrum (400 MHz, 295 K) of **TAHex2-H$_2$** in CD_2Cl_2.

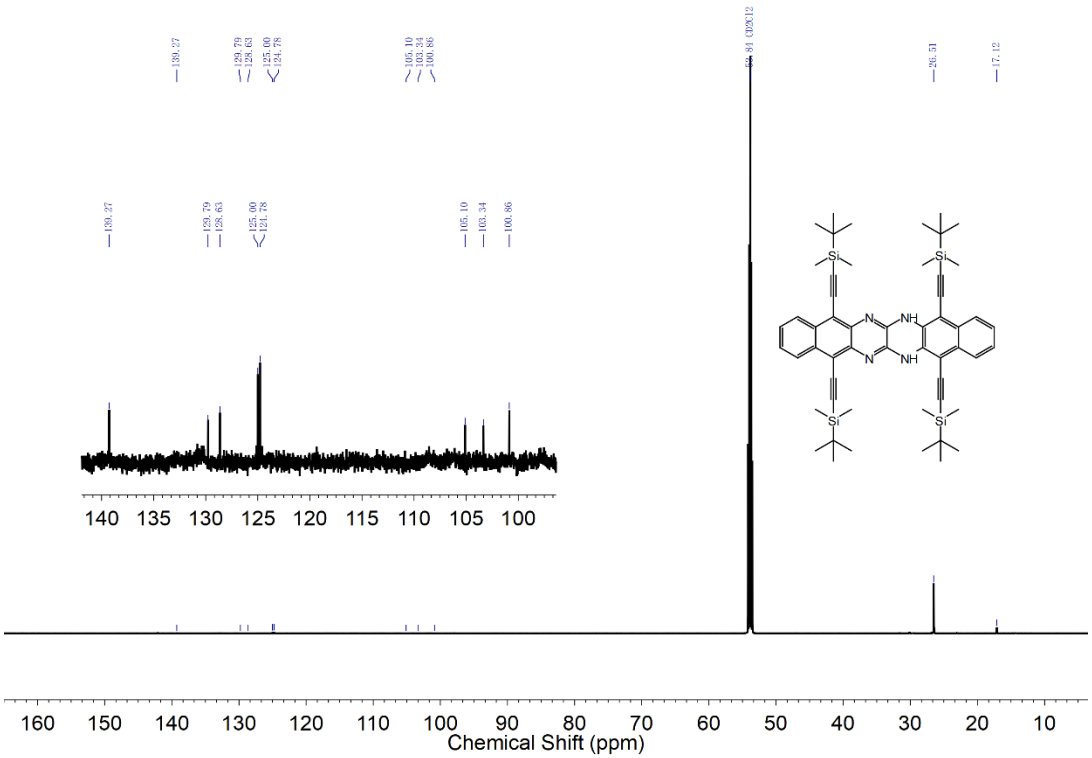

Figure 143. ^{13}C NMR spectrum (101 MHz, 295 K) of **TAHex2-H₂** in CD_2Cl_2.

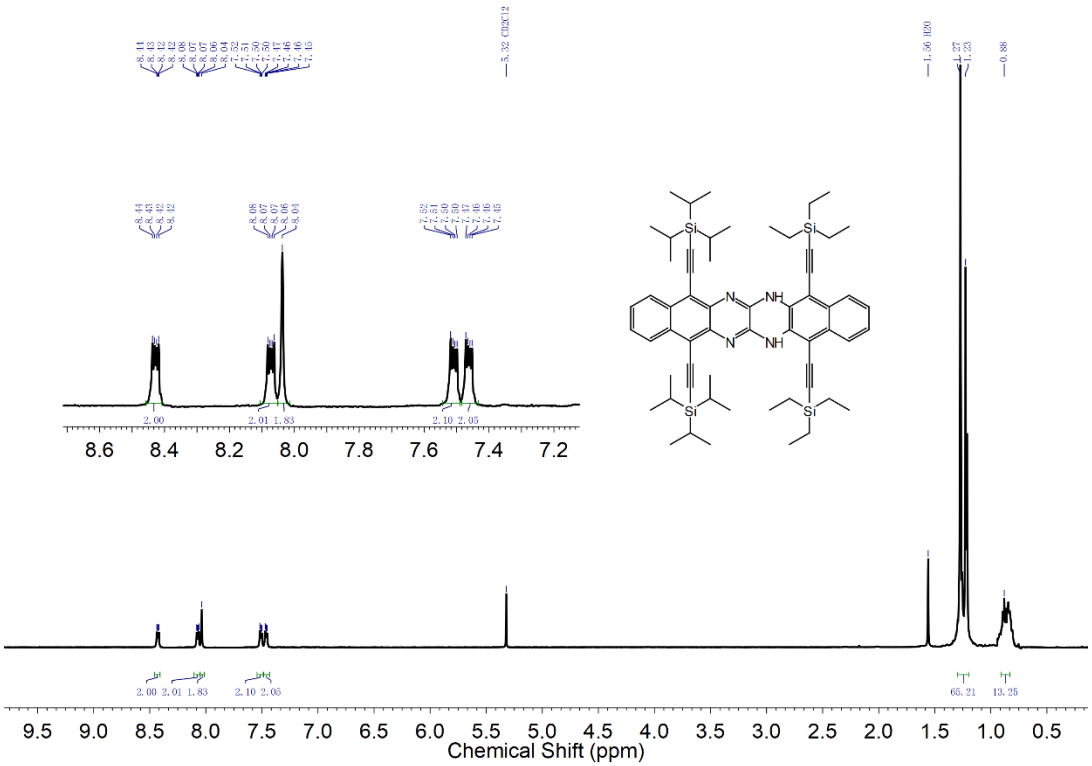

Figure 144. ^{1}H NMR spectrum (400 MHz, 295 K) of **TAHex3-H₂** in CD_2Cl_2.

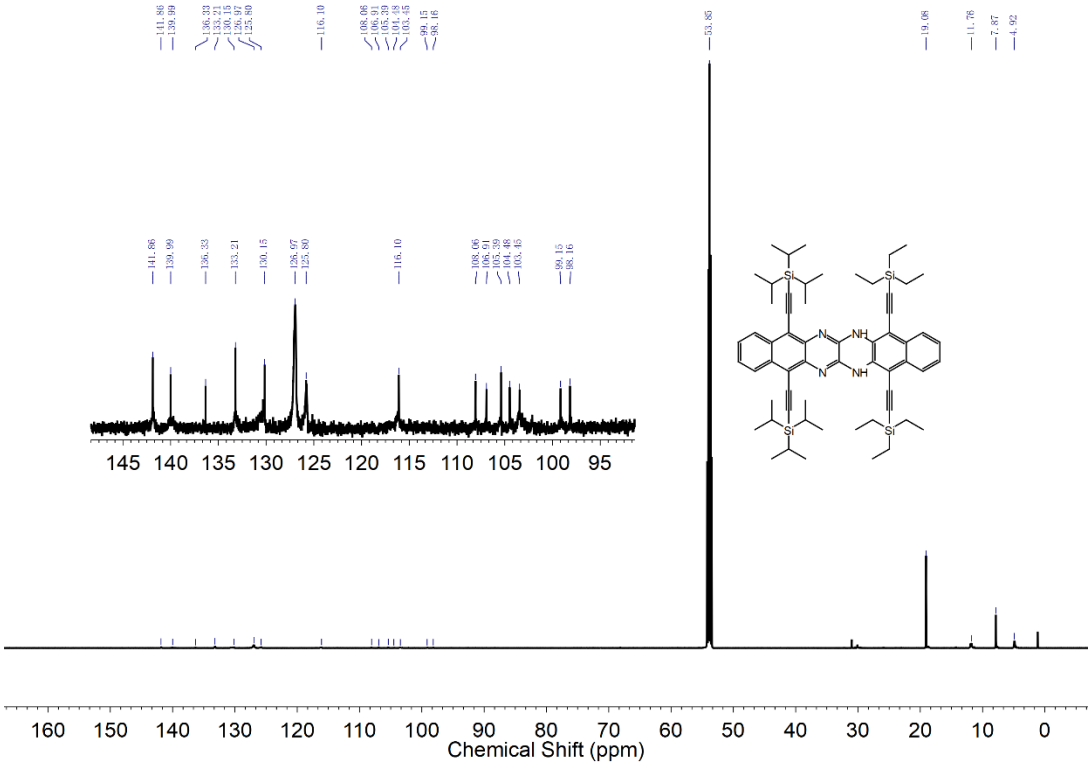

Figure 145. ^{13}C NMR spectrum (101 MHz, 295 K) of **TAHex3-H₂** in CD_2Cl_2.

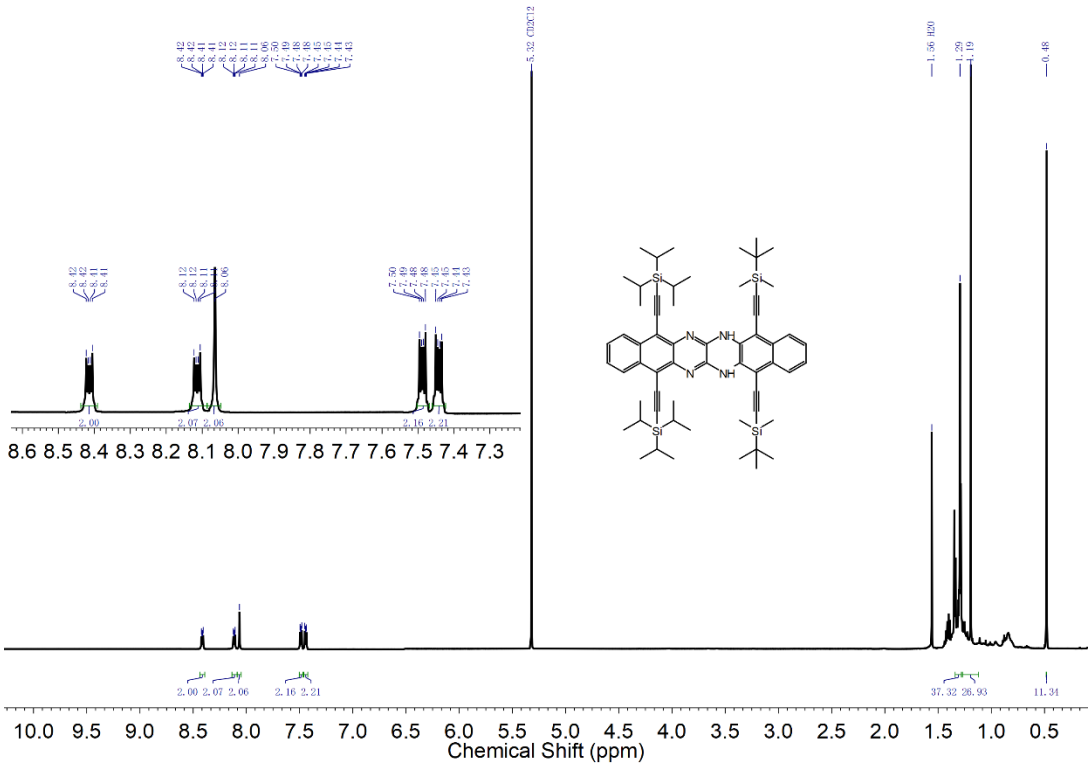

Figure 146. ^{1}H NMR spectrum (400 MHz, 295 K) of **TAHex4-H₂** in CD_2Cl_2.

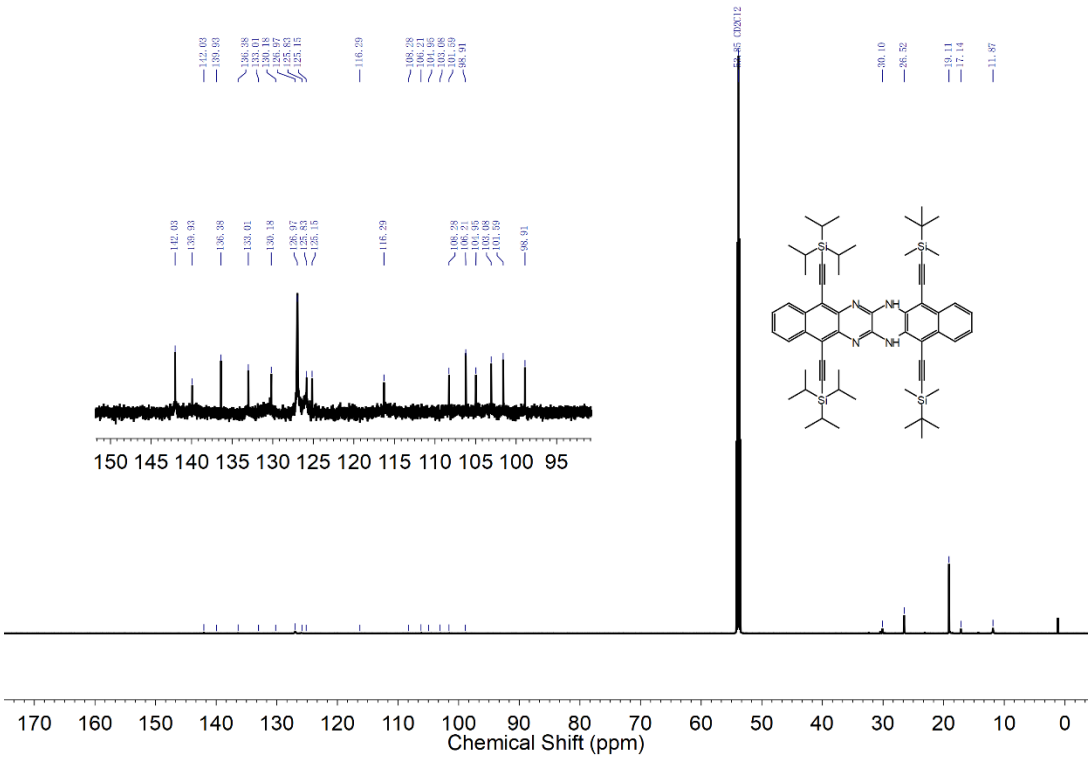

Figure 147. ^{13}C NMR spectrum (101 MHz, 295 K) of **TAHex4-H₂** in CD_2Cl_2.

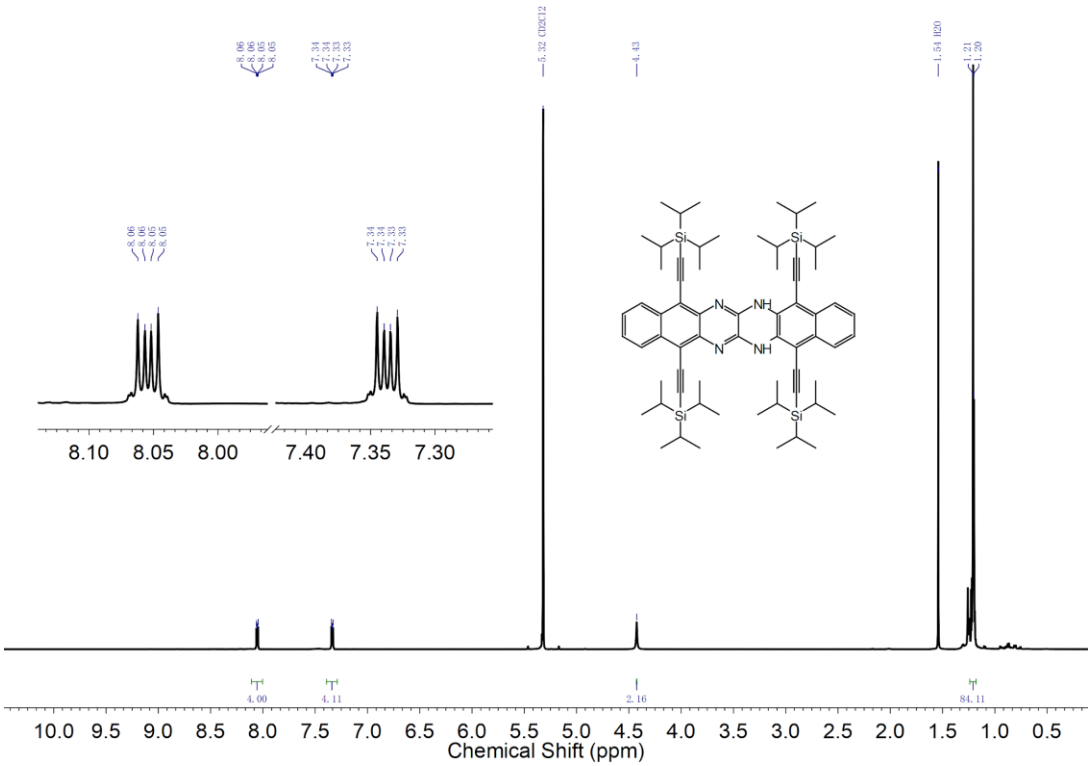

Figure 148. ^{1}H NMR spectrum (600 MHz, 295 K) of **TAHex5-H₂** in CD_2Cl_2.

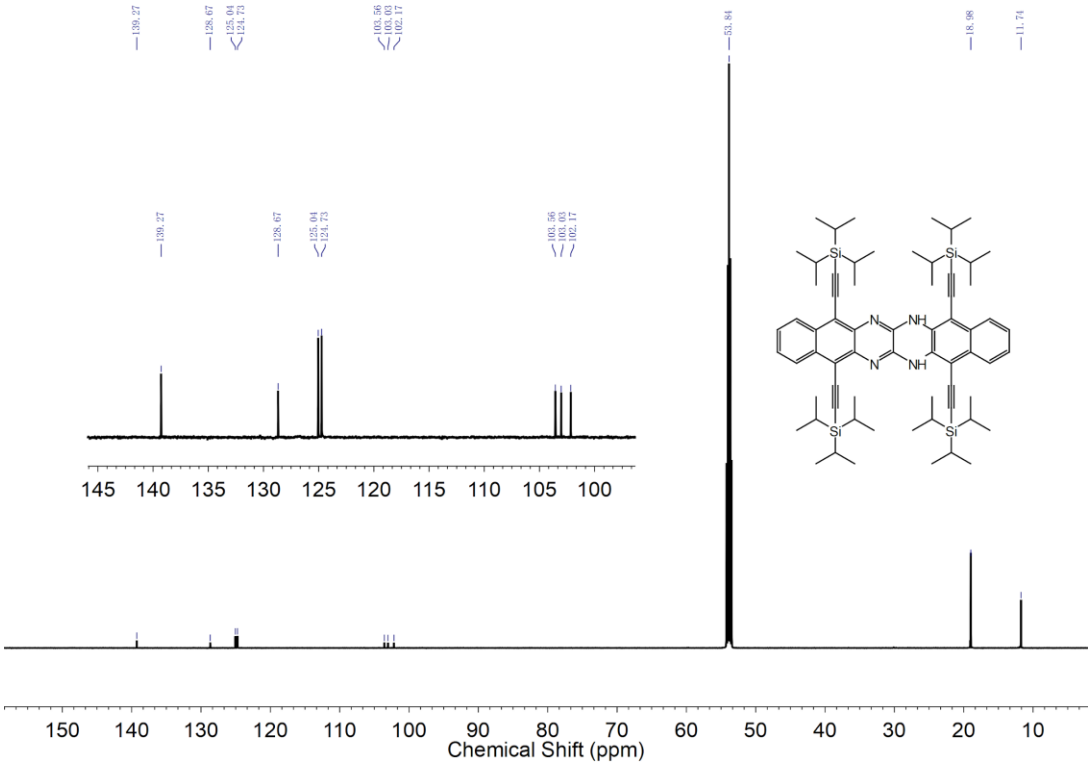

Figure 149. ^{13}C NMR spectrum (151 MHz, 295 K) of **TAHex5-H₂** in CD_2Cl_2.

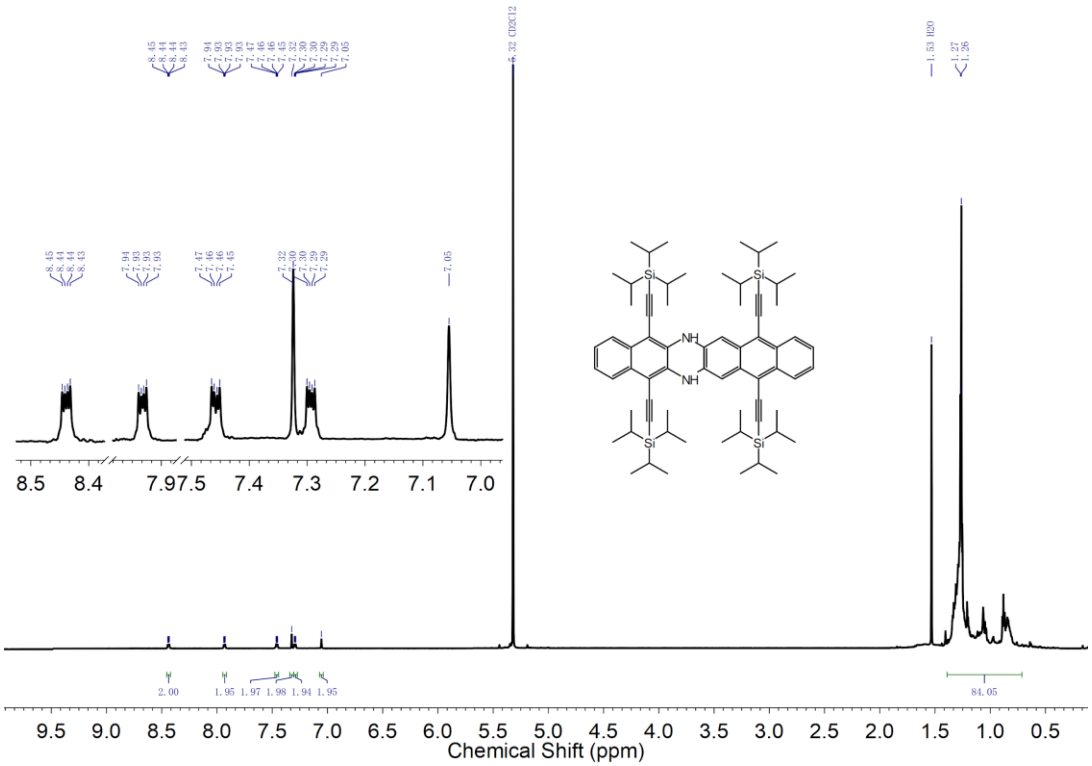

Figure 150. ^{1}H NMR spectrum (500 MHz, 295 K) of **DAHex-H₂** in CD_2Cl_2.

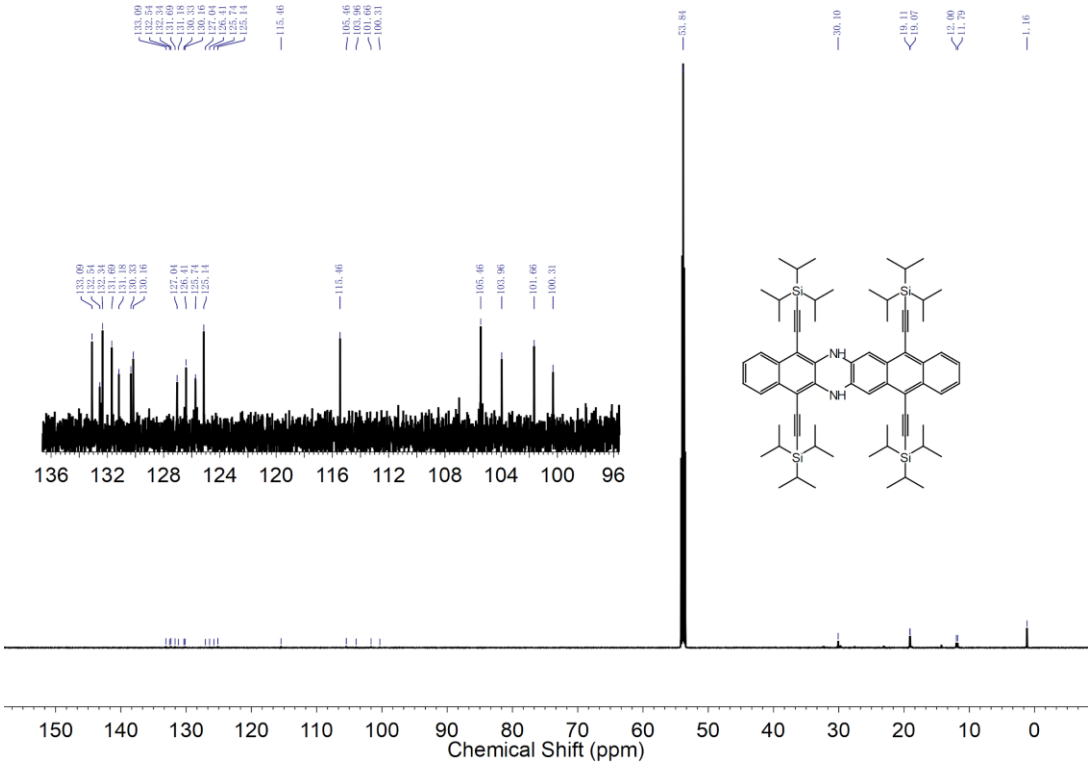

Figure 151. ^{13}C NMR spectrum (126 MHz, 295 K) of **DAHex-H₂** in CD_2Cl_2.

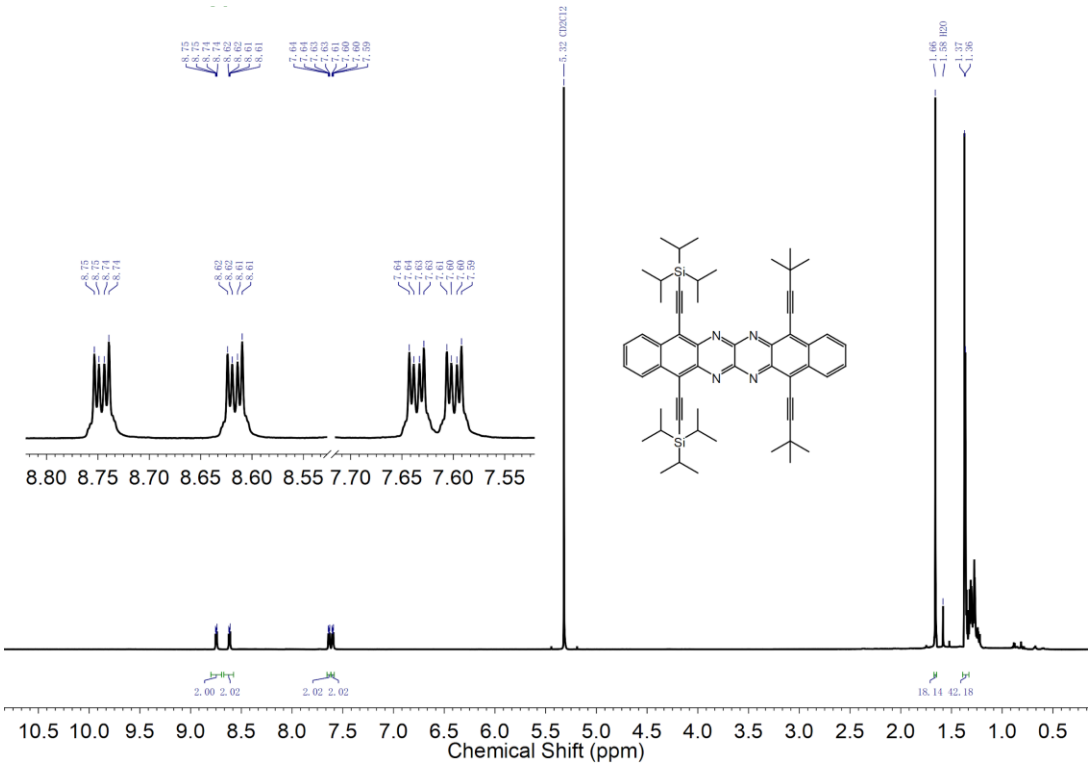

Figure 152. ^{1}H NMR spectrum (600 MHz, 295 K) of **TAHex1** in CD_2Cl_2.

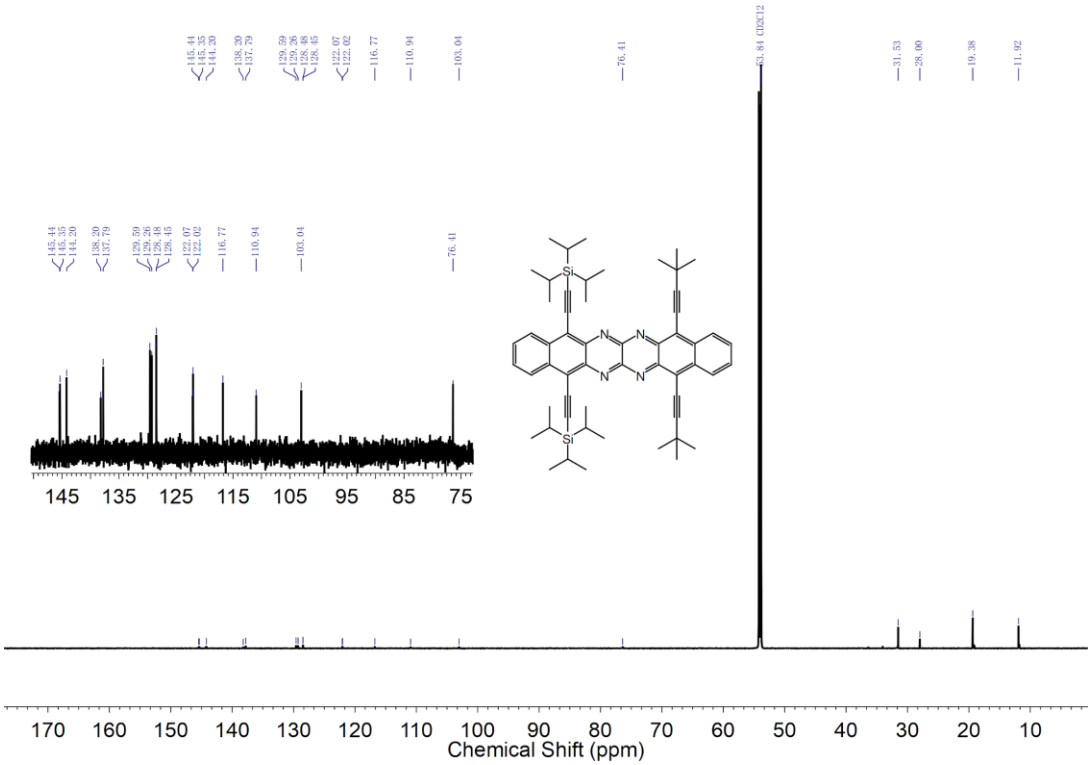

Figure 153. ^{13}C NMR spectrum (151 MHz, 295 K) of **TAHex1** in CD_2Cl_2.

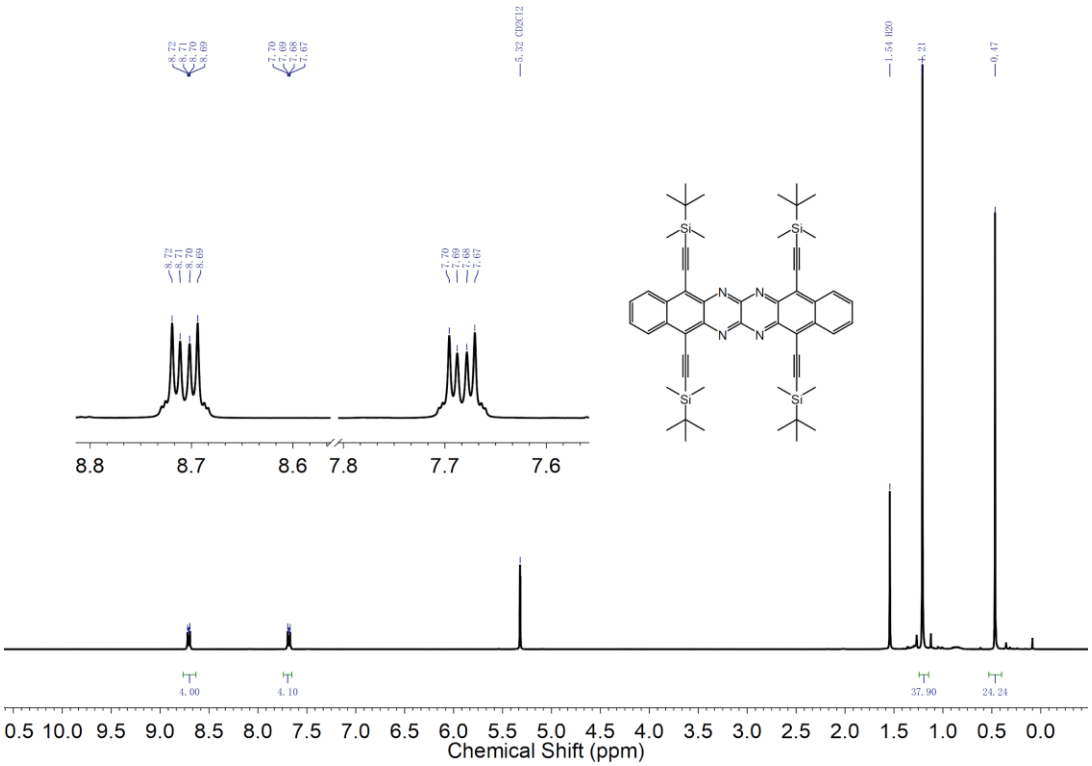

Figure 154. ^{1}H NMR spectrum (400 MHz, 295 K) of **TAHex2** in CD_2Cl_2.

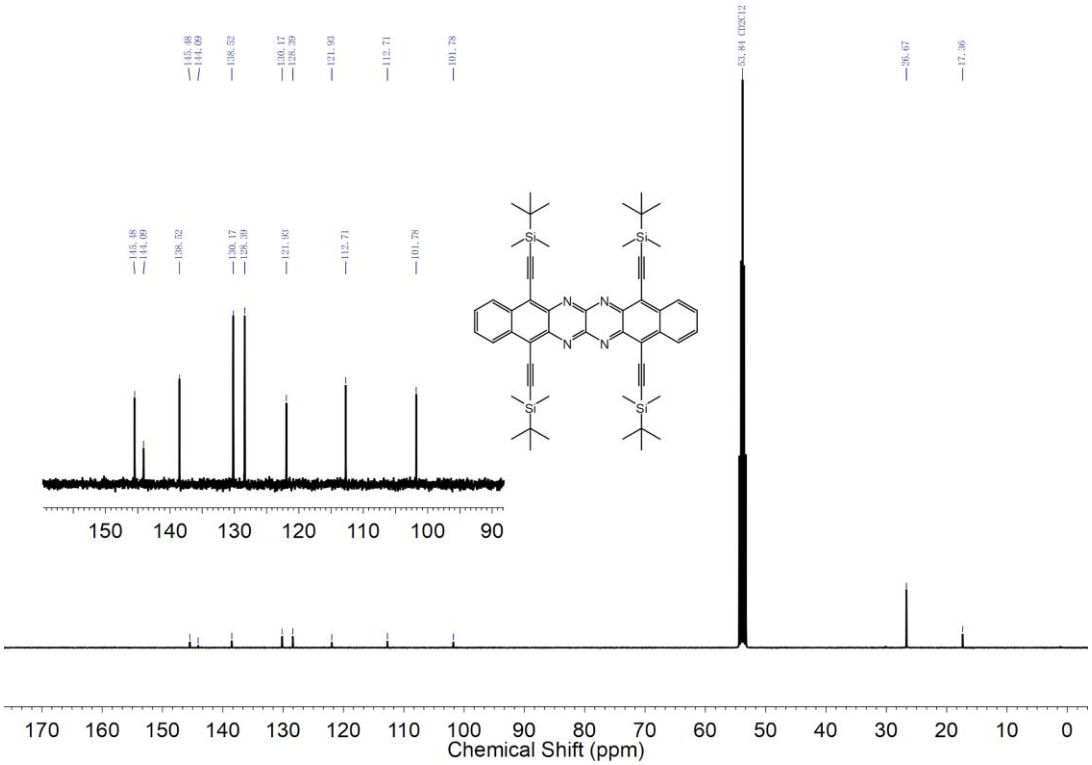

Figure 155. ^{13}C NMR spectrum (101 MHz, 295 K) of **TAHex2** in CD_2Cl_2.

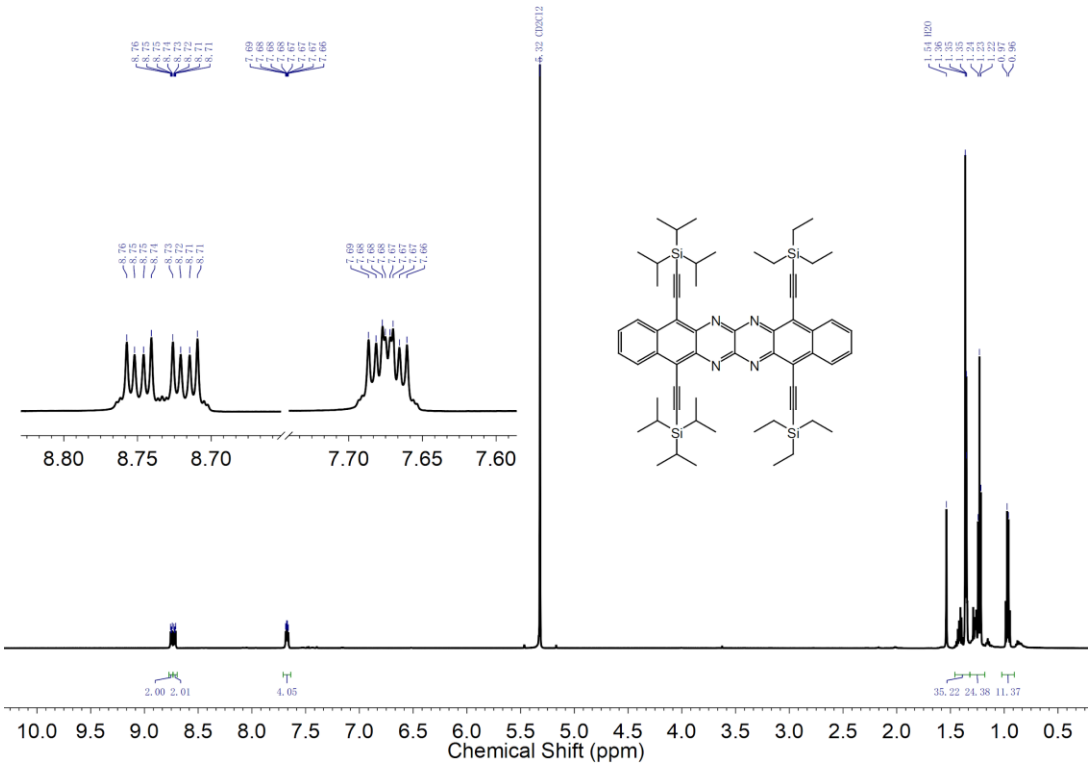

Figure 156. ^{1}H NMR spectrum (600 MHz, 295 K) of **TAHex3** in CD_2Cl_2.

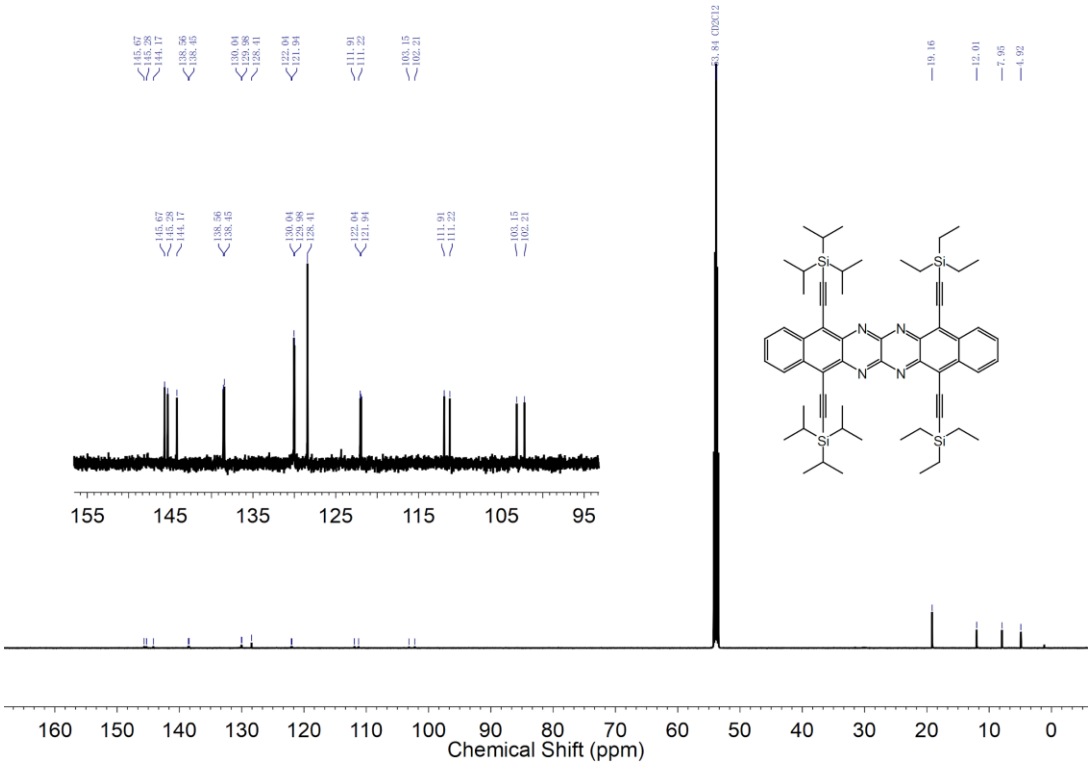

Figure 157. ^{13}C NMR spectrum (151 MHz, 295 K) of **TAHex3** in CD_2Cl_2.

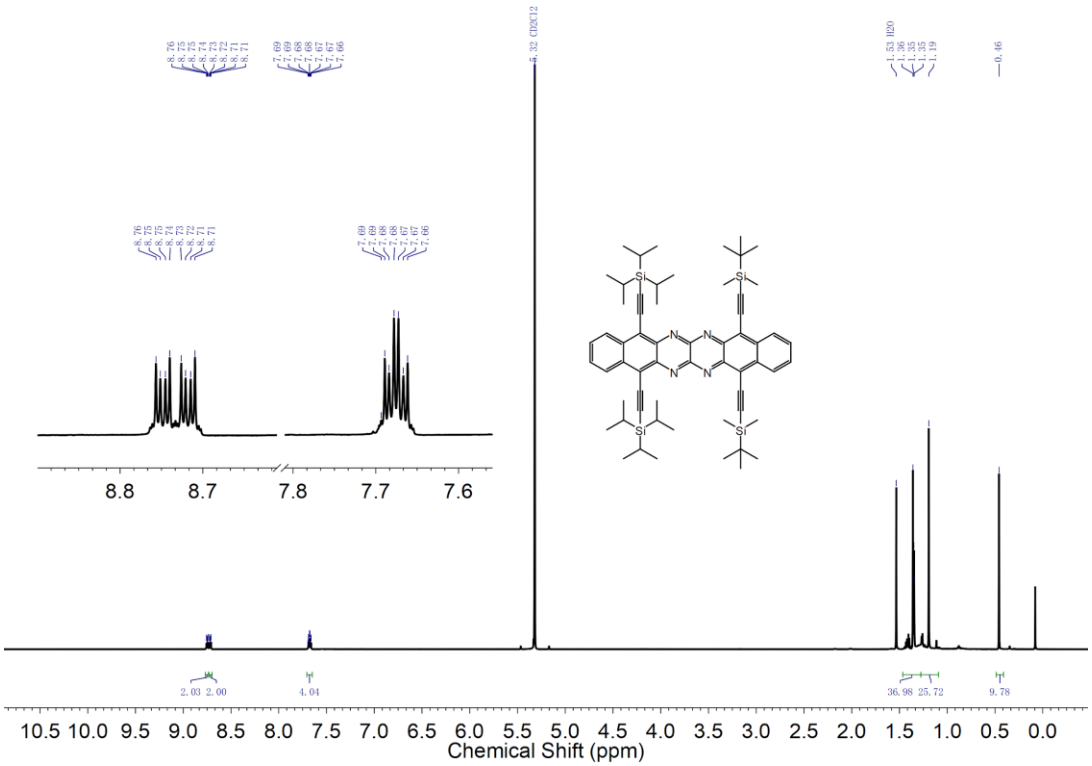

Figure 158. ^{1}H NMR spectrum (600 MHz, 295 K) of **TAHex4** in CD_2Cl_2.

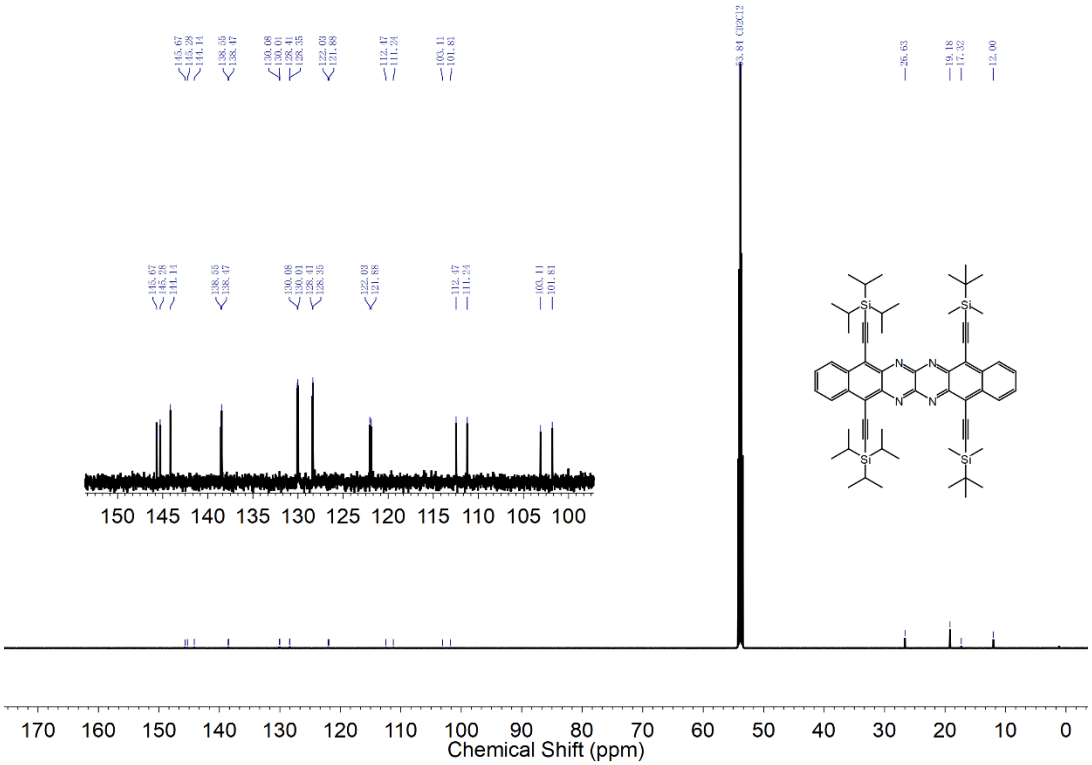

Figure 159. ^{13}C NMR spectrum (151 MHz, 295 K) of **TAHex4** in CD_2Cl_2.

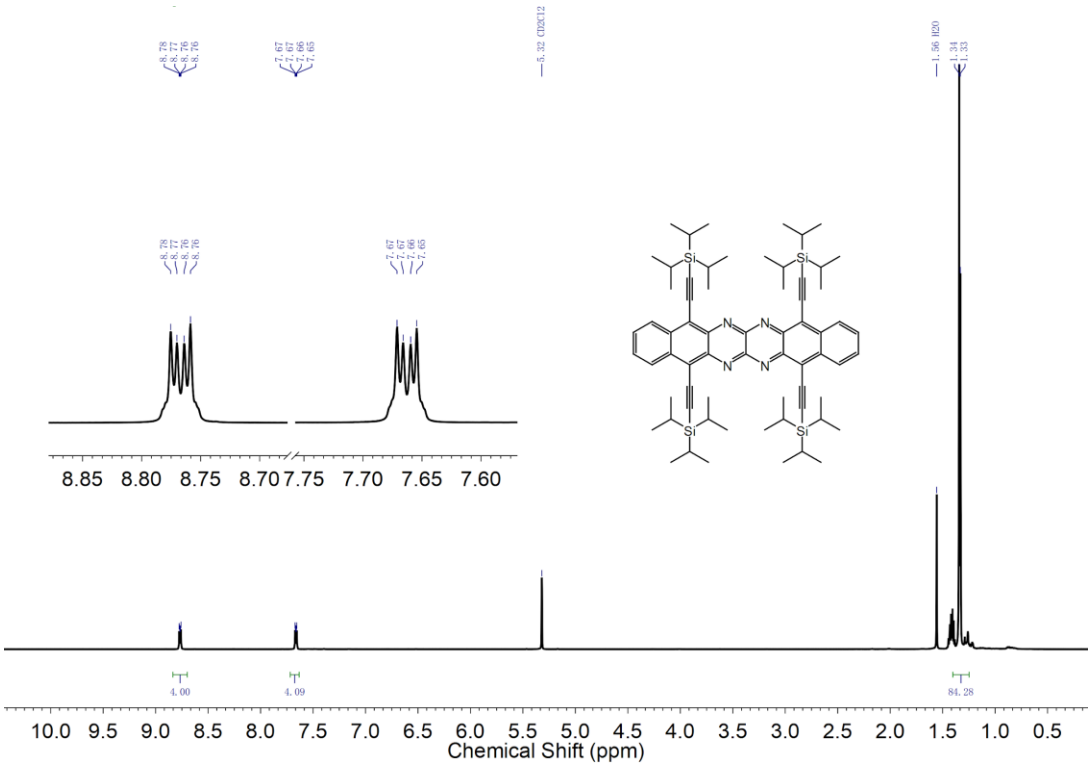

Figure 160. ^{1}H NMR spectrum (600 MHz, 295 K) of **TAHex5** in CD_2Cl_2.

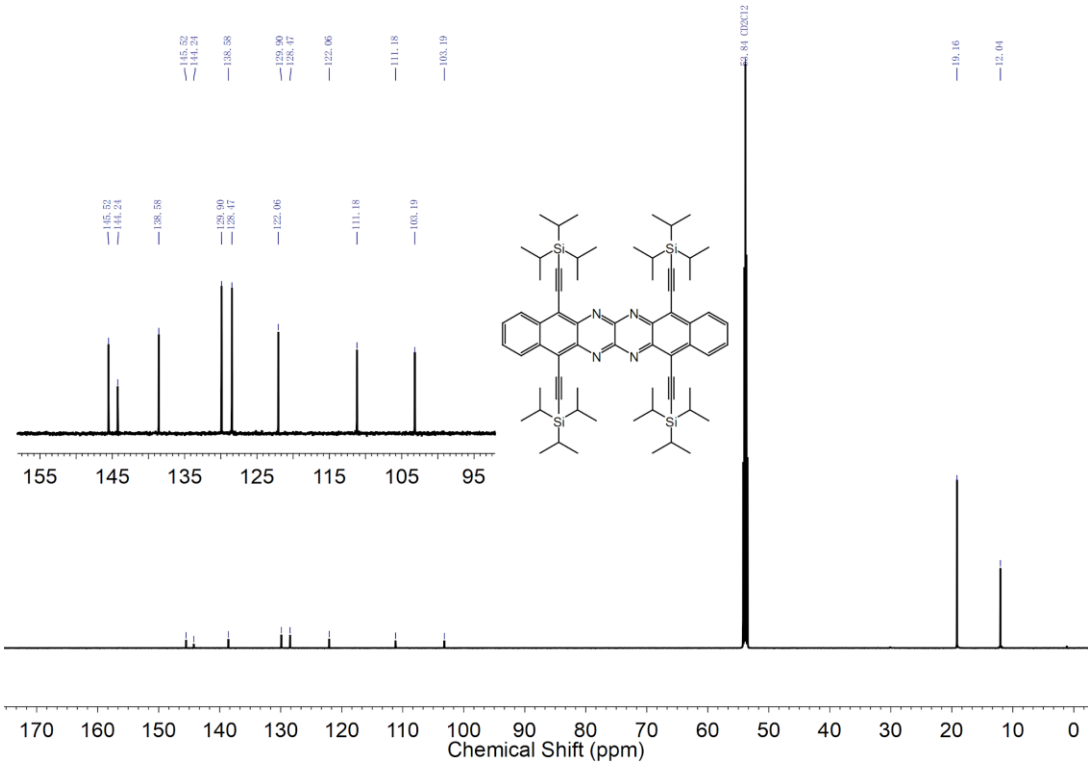

Figure 161. ^{13}C NMR spectrum (151 MHz, 295 K) of **TAHex5** in CD_2Cl_2.

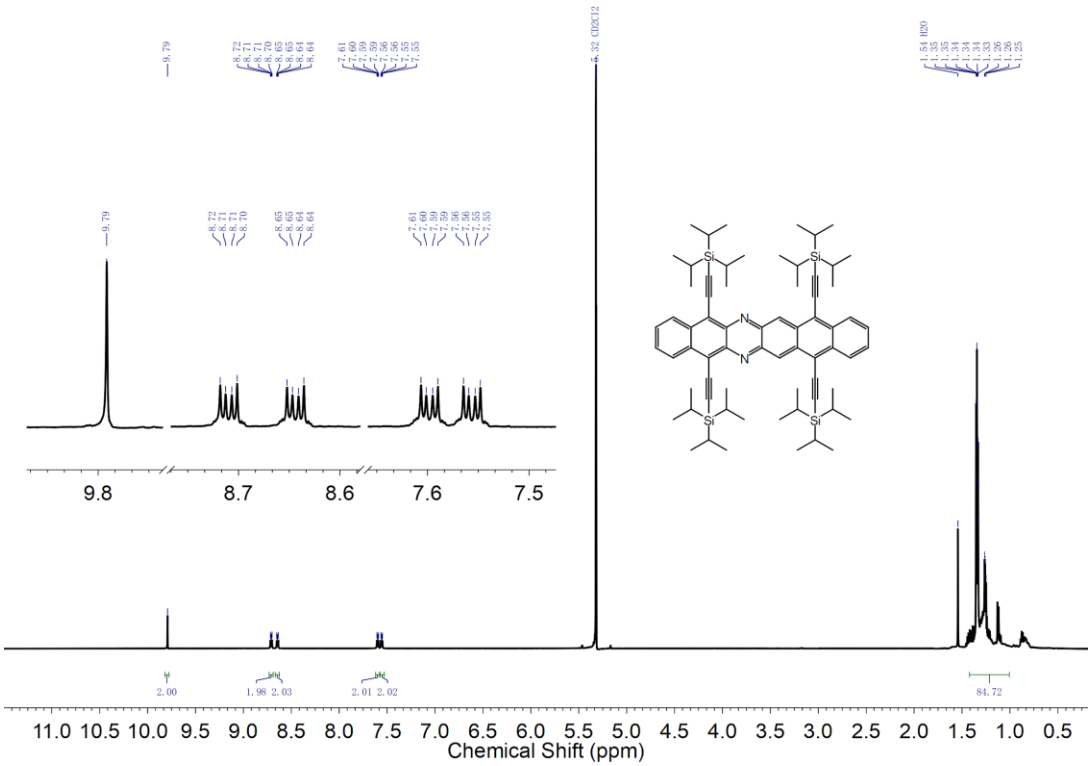

Figure 162. ^{1}H NMR spectrum (600 MHz, 295 K) of **DAHex** in CD_2Cl_2.

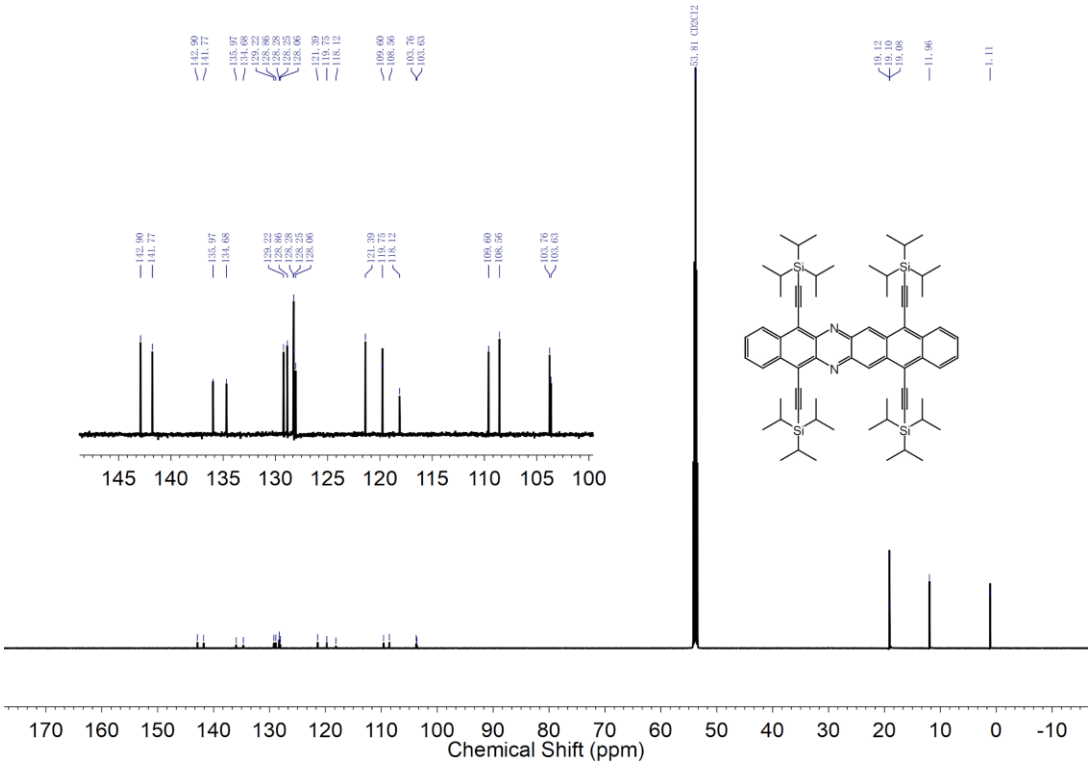

Figure 163. ^{13}C NMR spectrum (151 MHz, 295 K) of **DAHex** in CD_2Cl_2.

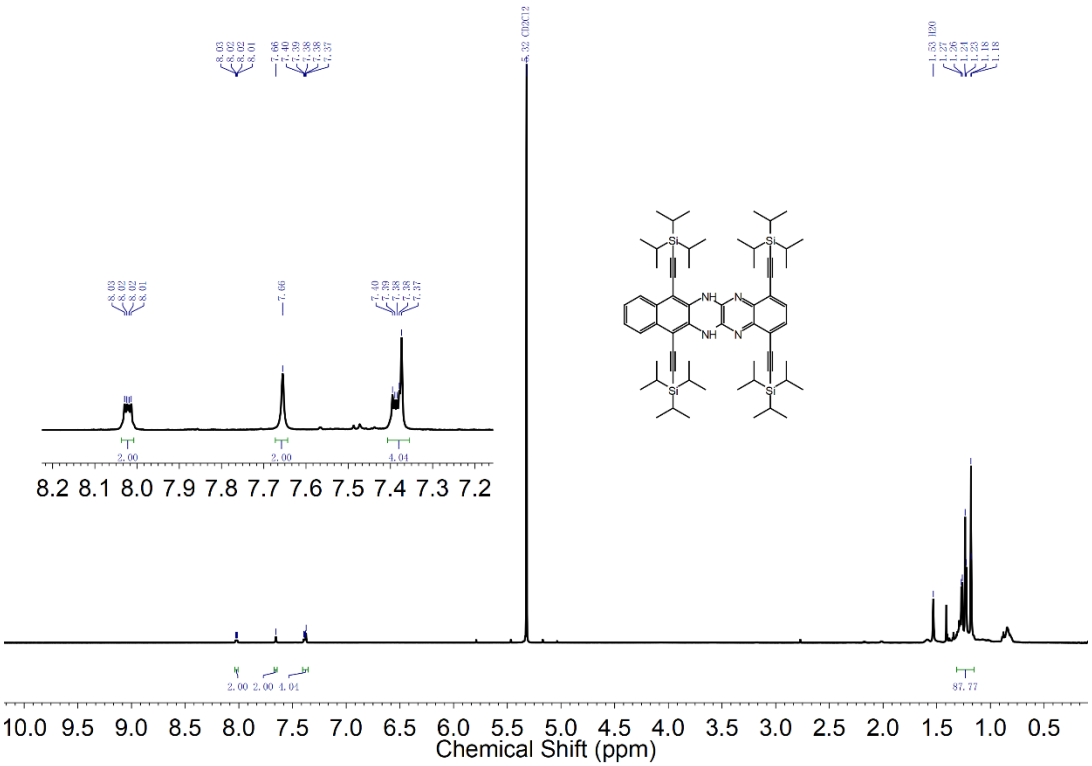

Figure 164. ^{1}H NMR spectrum (600 MHz, 295 K) of **65-H₂** in CD_2Cl_2.

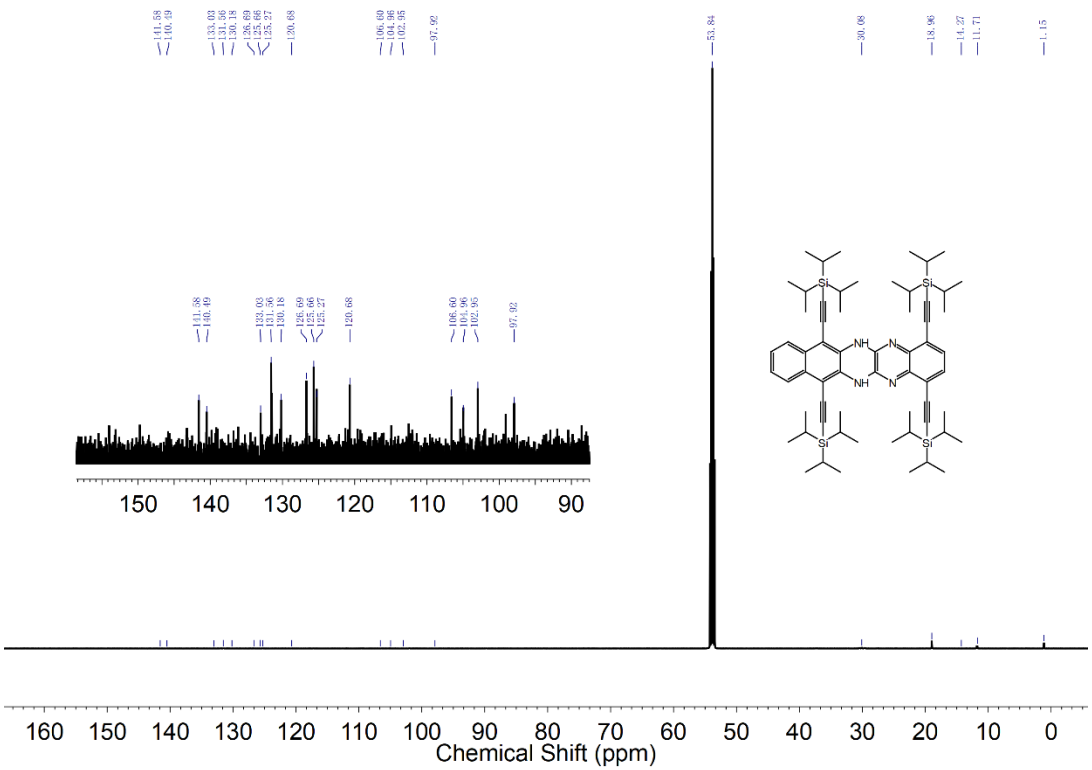

Figure 165. ^{13}C NMR spectrum (151 MHz, 295 K) of **65-H₂** in CD_2Cl_2.

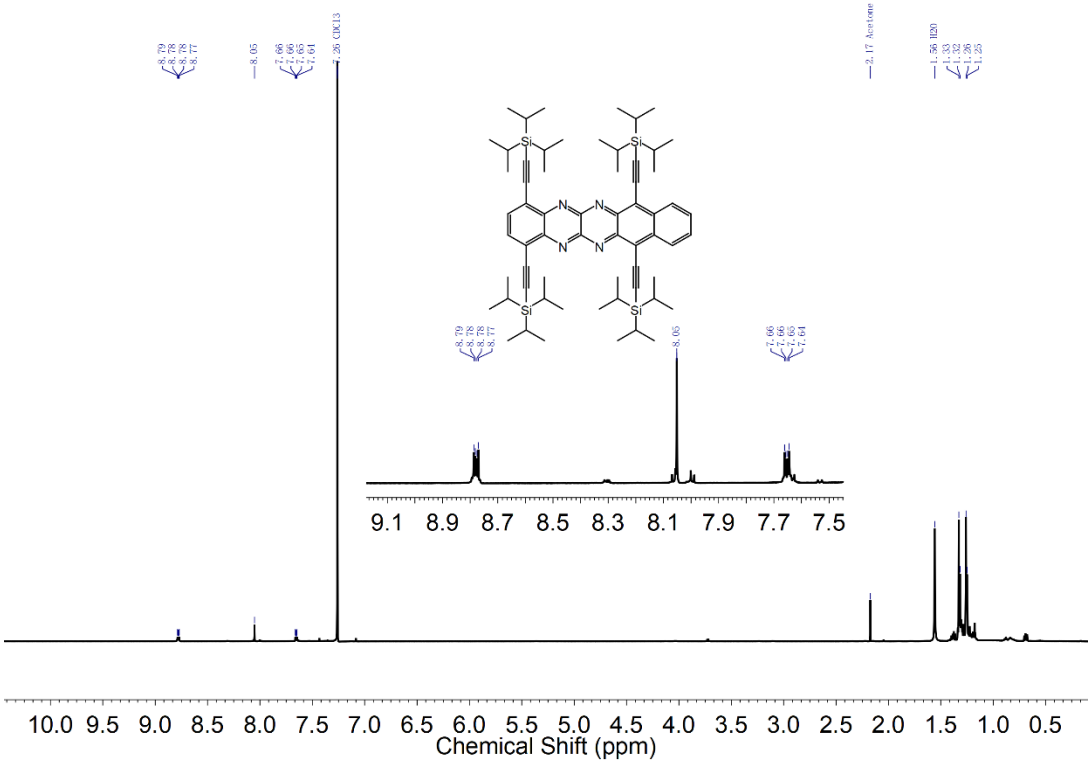

Figure 166. ^{1}H NMR spectrum (600 MHz, 295 K) of **65** in $CDCl_3$.

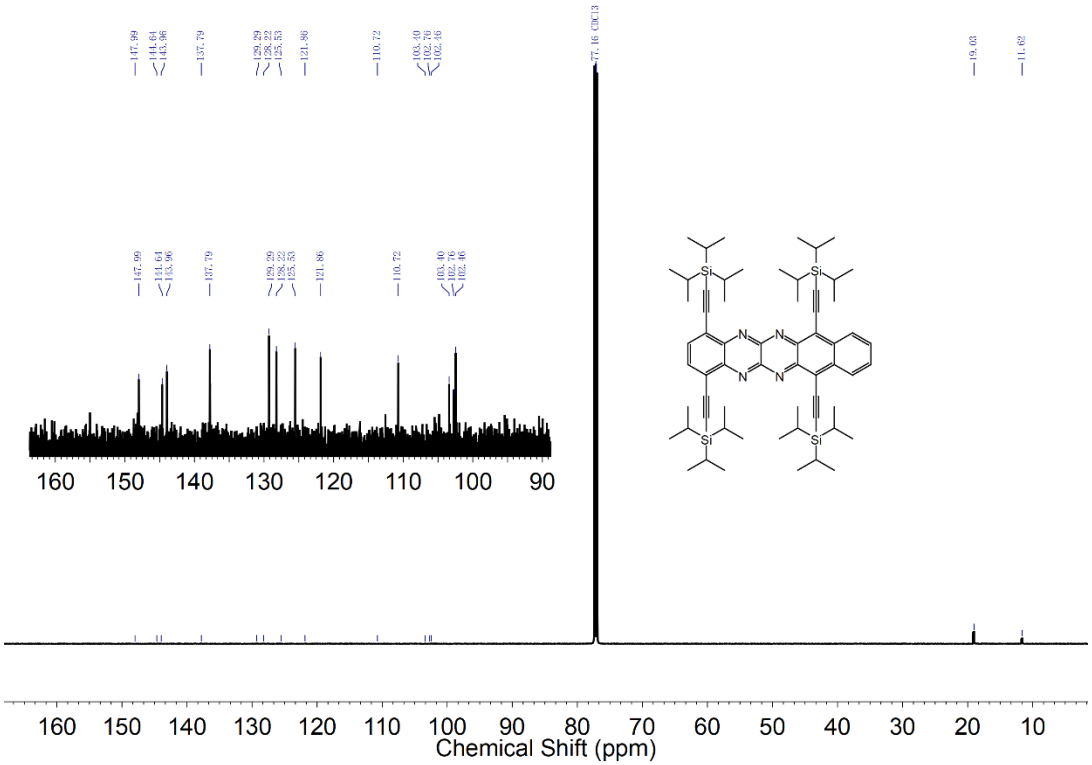

Figure 167. ^{13}C NMR spectrum (151 MHz, 295 K) of **65** in $CDCl_3$.

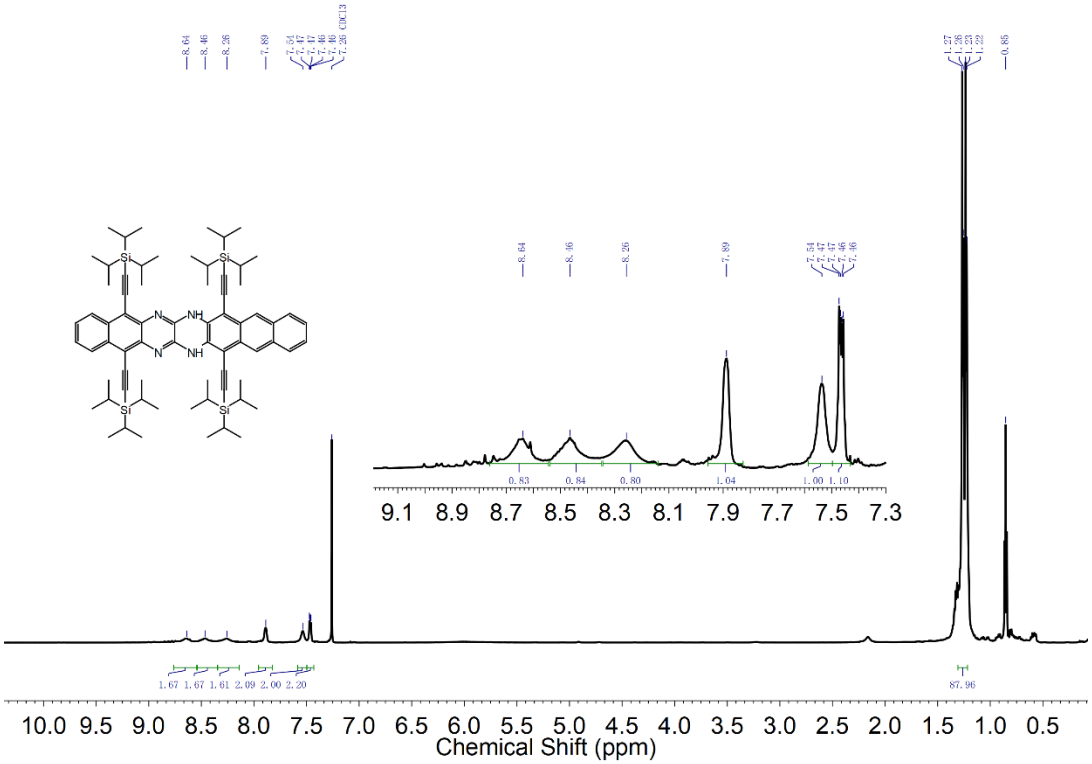

Figure 168. ^{1}H NMR spectrum (600 MHz, 253 K) of **66-H$_2$** in $CDCl_3$.

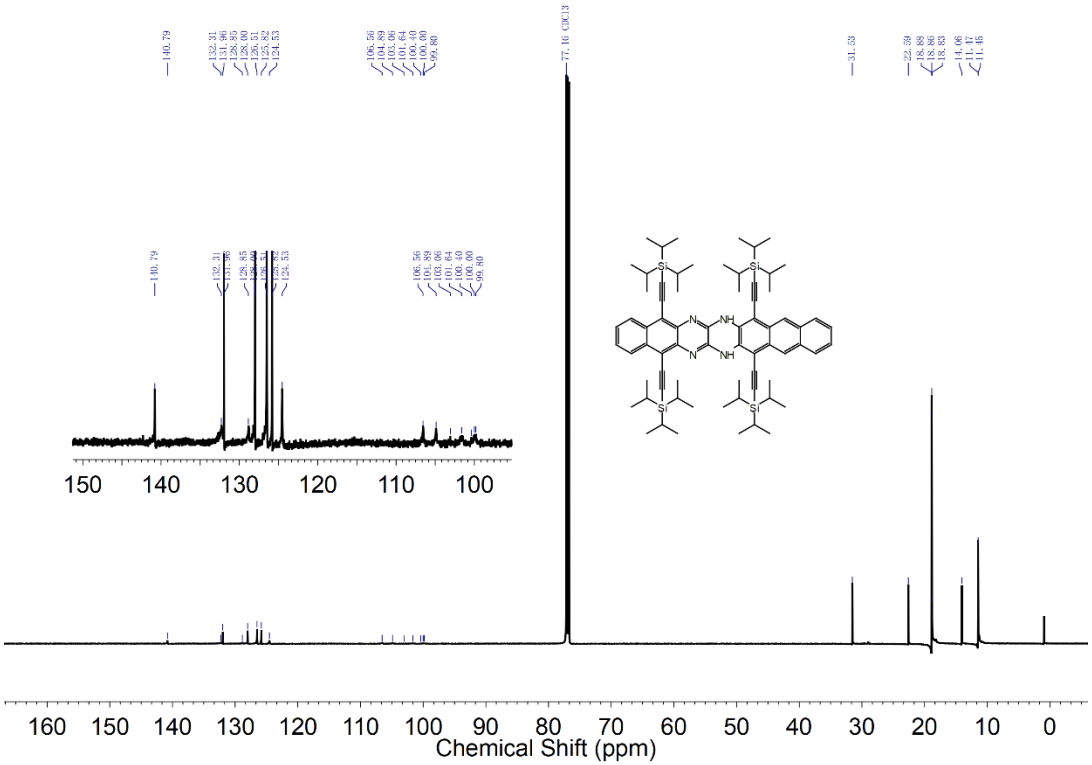

Figure 169. ^{13}C NMR spectrum (151 MHz, 295 K) of **66-H₂** in $CDCl_3$.

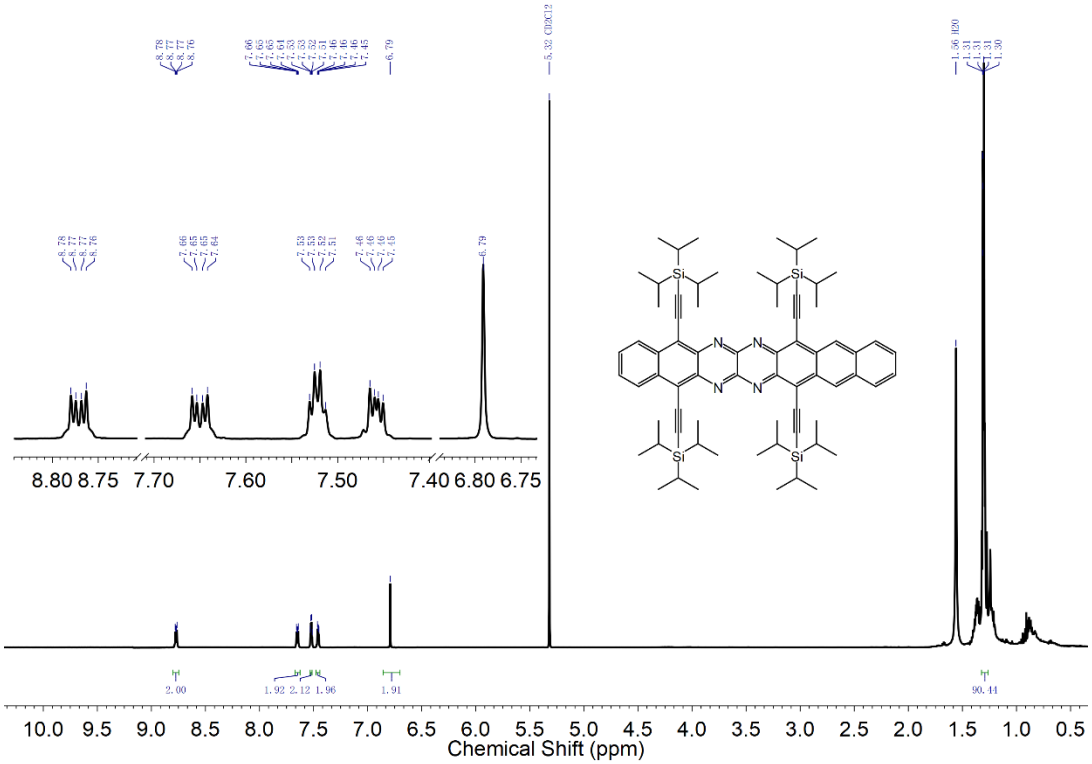

Figure 170. ^{1}H NMR spectrum (600 MHz, 253 K) of **66** in CD_2Cl_2.

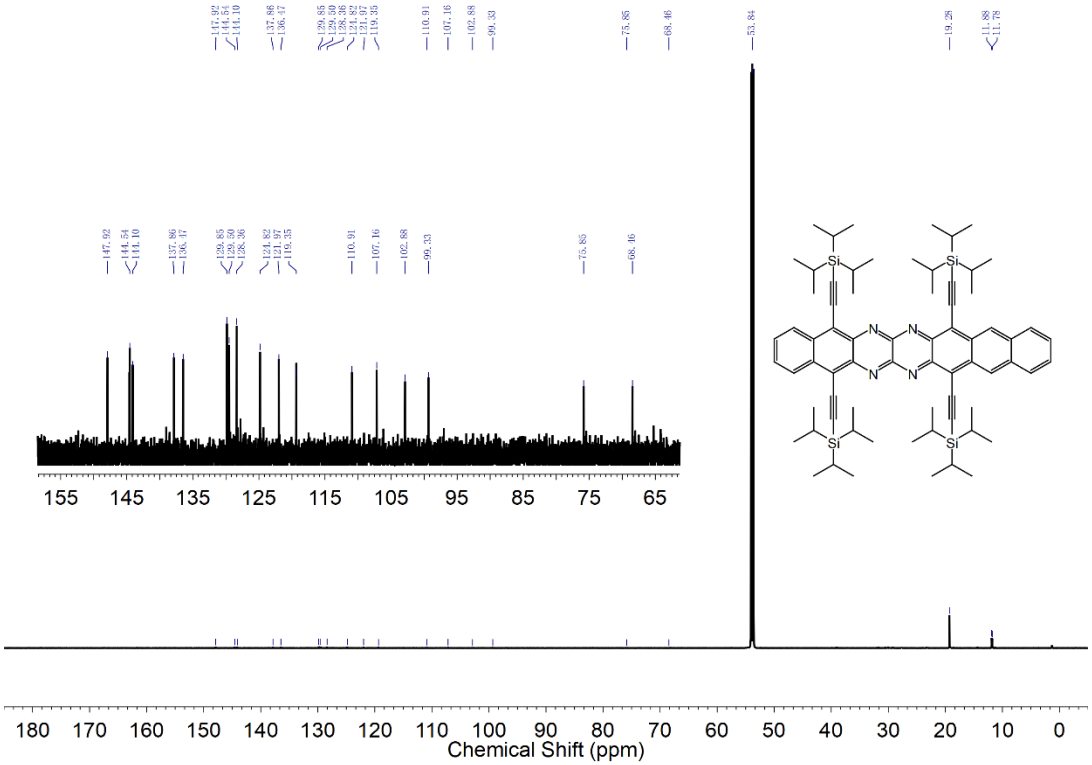

Figure 171. ^{13}C NMR spectrum (151 MHz, 295 K) of **66** in CD_2Cl_2.

7.2 Cyclic Voltammograms Spectra

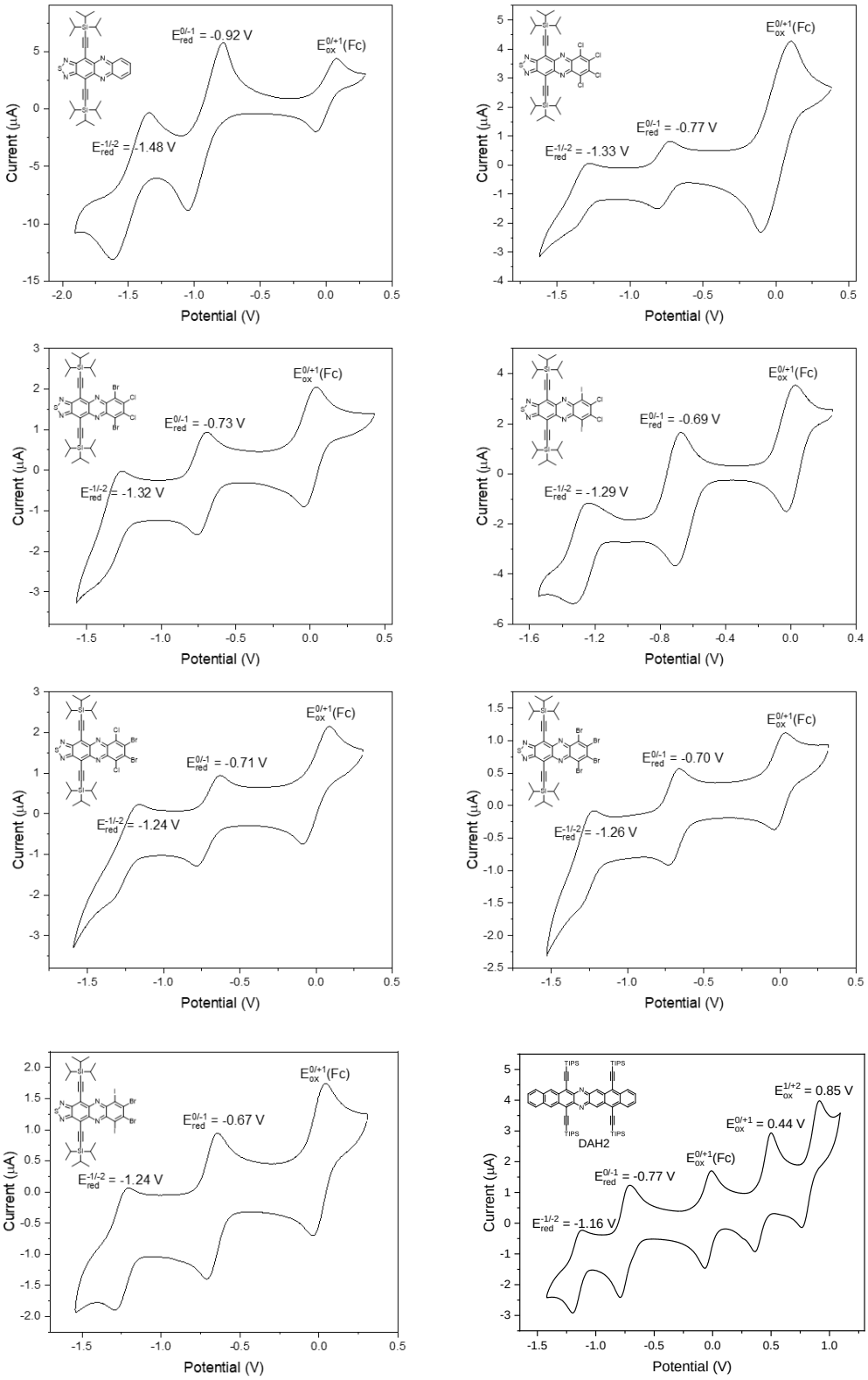

Figure 172. Cyclic voltammograms of **39** and **DAH2** in DCM (internally referenced against Fc/Fc^+ using a Pt working electrode and Bu_4NPF_6 as electrolyte).

7.3 Electron Paramagnetic Resonance Spectra

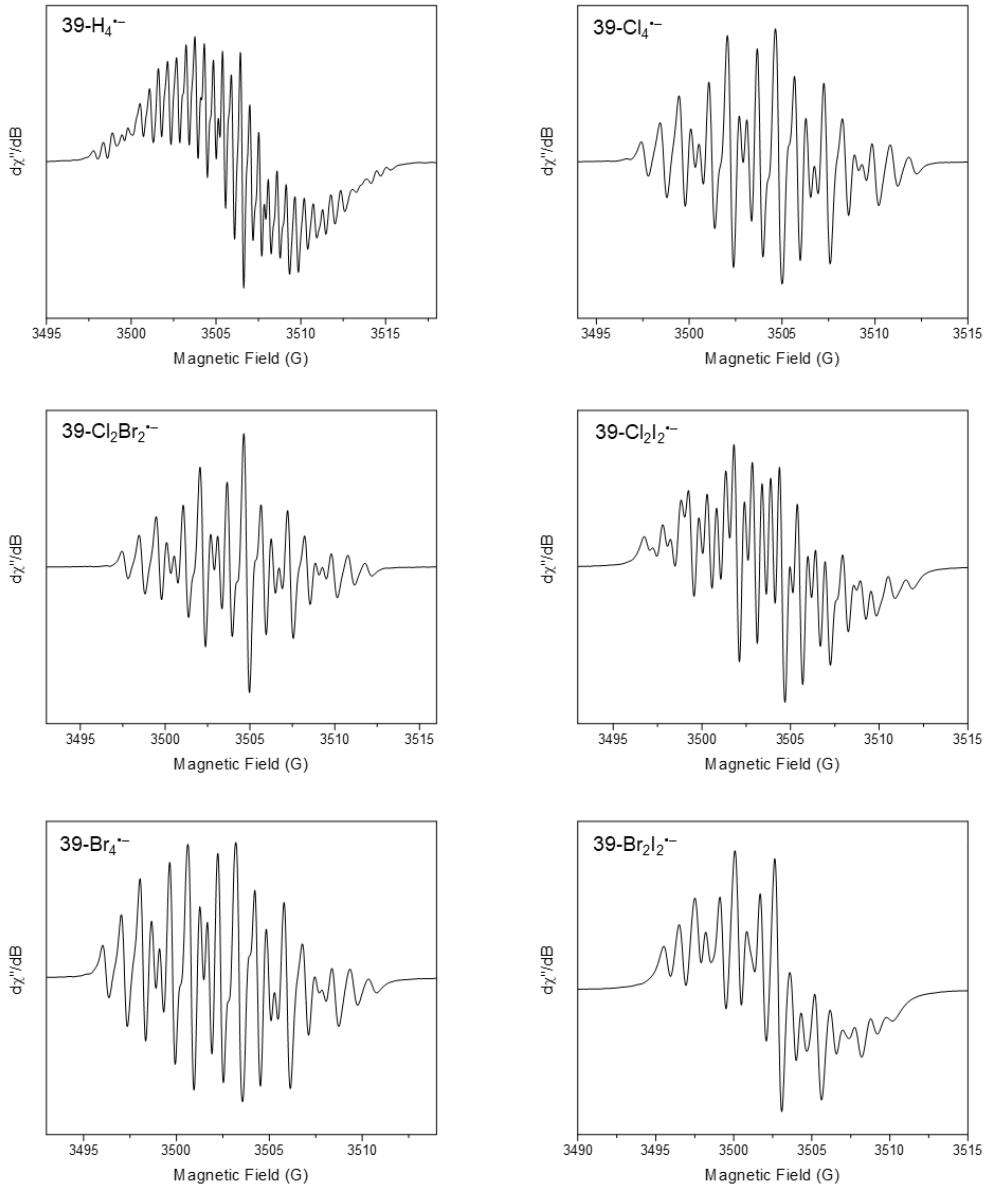

Figure 173. Electron paramagnetic resonance (EPR) spectra for **39**$^{\bullet-}$ in a toluene/THF mixture at room temperature.

7.4 Crystallographic Data

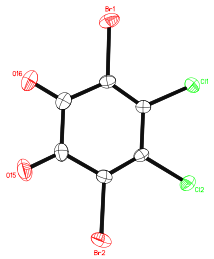

Table 11. Crystal data and structure refinement for **49-Cl_2Br_2**.

CCDC nmuber	2246967	
Empirical formula	$C_6Br_2Cl_2O_2$	
Formula weight	334.78	
Temperature	200(2) K	
Wavelength	0.71073 Å	
Crystal system	orthorhombic	
Space group	Pbca	
Z	8	
Unit cell dimensions	a = 16.9430(10) Å	α = 90 deg.
	b = 5.8819(3) Å	β = 90 deg.
	c = 17.2752(10) Å	γ = 90 deg.
Volume	1721.60(17) $Å^3$	
Density (calculated)	2.58 g/cm^3	
Absorption coefficient	9.99 mm^{-1}	
Crystal shape	plank	
Crystal size	0.291 x 0.038 x 0.018 mm^3	
Crystal colour	red	
Theta range for data collection	2.4 to 28.4 deg.	
Index ranges	-21≤h≤22, -7≤k≤7, -22≤l≤21	
Reflections collected	17274	
Independent reflections	2056 (R(int) = 0.0796)	
Observed reflections	1440 (I > 2σ(I))	
Absorption correction	Semi-empirical from equivalents	
Max. and min. transmission	0.86 and 0.57	
Refinement method	Full-matrix least-squares on F^2	
Data/restraints/parameters	2056 / 0 / 109	
Goodness-of-fit on F^2	1.00	
Final R indices (I>2sigma(I))	R1 = 0.036, wR2 = 0.065	
Largest diff. peak and hole	0.52 and -0.63 $eÅ^{-3}$	

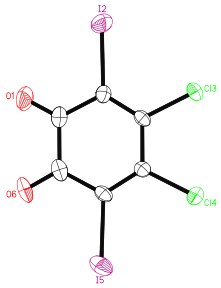

Table 12. Crystal data and structure refinement for **49-Cl_2I_2**.

CCDC nmuber	2246968	
Empirical formula	$C_6Cl_2I_2O_2$	
Formula weight	428.76	
Temperature	200(2) K	
Wavelength	0.71073 Å	
Crystal system	orthorhombic	
Space group	Pbca	
Z	8	
Unit cell dimensions	a = 17.0303(12) Å	α = 90 deg.
	b = 6.1587(4) Å	β = 90 deg.
	c = 17.8988(13) Å	γ = 90 deg.
Volume	1877.3(2) $Å^3$	
Density (calculated)	3.03 g/cm^3	
Absorption coefficient	7.22 mm^{-1}	
Crystal shape	plank	
Crystal size	0.180 x 0.045 x 0.018 mm^3	
Crystal colour	red	
Theta range for data collection	2.3 to 29.3 deg.	
Index ranges	$-22 \le h \le 22$, $-8 \le k \le 8$, $-24 \le l \le 23$	
Reflections collected	12826	
Independent reflections	2319 (R(int) = 0.0466)	
Observed reflections	1741 ($I > 2\sigma(I)$)	
Absorption correction	Semi-empirical from equivalents	
Max. and min. transmission	0.90 and 0.68	
Refinement method	Full-matrix least-squares on F^2	
Data/restraints/parameters	2319 / 0 / 109	
Goodness-of-fit on F^2	1.06	
Final R indices (I>2sigma(I))	R1 = 0.039, wR2 = 0.087	
Largest diff. peak and hole	1.67 and -1.35 $eÅ^{-3}$	

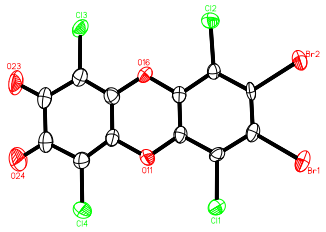

Table 13. Crystal data and structure refinement for the dimer of **49-Br_2Cl_2**.

CCDC nmuber	2246969
Empirical formula	$C_{12}Br_{1.90}Cl_{4.10}O_4$
Formula weight	505.26
Temperature	200(2) K
Wavelength	0.71073 Å
Crystal system	triclinic
Space group	P $\bar{1}$
Z	2
Unit cell dimensions	a = 7.3123(12) Å α = 94.779(4) deg. b = 9.0994(14) Å β = 105.064(4) deg. c = 12.391(2) Å γ = 113.440(4) deg.
Volume	714.0(2) $Å^3$
Density (calculated)	2.35 g/cm^3
Absorption coefficient	6.17 mm^{-1}
Crystal shape	plate
Crystal size	0.053 x 0.036 x 0.018 mm^3
Crystal colour	red
Theta range for data collection	1.7 to 25.4 deg.
Index ranges	$-8 \le h \le 8$, $-10 \le k \le 10$, $-14 \le l \le 14$
Reflections collected	15781
Independent reflections	2612 (R(int) = 0.1150)
Observed reflections	1510 ($I > 2\sigma(I)$)
Absorption correction	Semi-empirical from equivalents
Max. and min. transmission	0.84 and 0.70
Refinement method	Full-matrix least-squares on F^2
Data/restraints/parameters	2612 / 204 / 202
Goodness-of-fit on F^2	1.08
Final R indices (I>2sigma(I))	R1 = 0.078, wR2 = 0.168
Largest diff. peak and hole	0.93 and -0.83 $eÅ^{-3}$

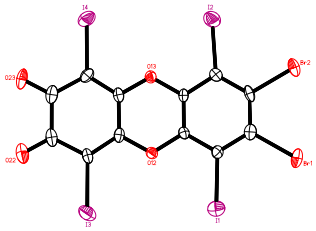

Table 14. Crystal data and structure refinement for the dimer of **49-Br_2I_2**.

CCDC nmuber	2081159	
Empirical formula	$C_{12}Br_2I_4O_4$	
Formula weight	875.54	
Temperature	200(2) K	
Wavelength	0.71073 Å	
Crystal system	monoclinic	
Space group	C2/c	
Z	8	
Unit cell dimensions	a = 22.596(2) Å	α = 90 deg.
	b = 9.6550(9) Å	β =122.1389(17) deg.
	c = 18.2228(17) Å	γ = 90 deg.
Volume	3366.4(5) $Å^3$	
Density (calculated)	3.45 g/cm^3	
Absorption coefficient	12.16 mm^{-1}	
Crystal shape	plank	
Crystal size	0.075 x 0.059 x 0.026 mm^3	
Crystal colour	brown	
Theta range for data collection	2.1 to 26.1 deg.	
Index ranges	$-27\leq h\leq 27$, $-11\leq k\leq 11$, $-22\leq l\leq 22$	
Reflections collected	16749	
Independent reflections	3338 (R(int) = 0.0397)	
Observed reflections	2657 ($I > 2\sigma(I)$)	
Absorption correction	Semi-empirical from equivalents	
Max. and min. transmission	0.77 and 0.62	
Refinement method	Full-matrix least-squares on F^2	
Data/restraints/parameters	3338 / 0 / 199	
Goodness-of-fit on F^2	1.08	
Final R indices (I>2sigma(I))	R1 = 0.036, wR2 = 0.102	
Largest diff. peak and hole	1.65 and -1.98 $eÅ^{-3}$	

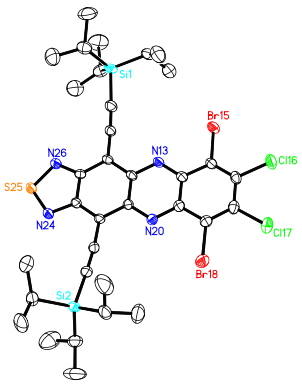

Table 15. Crystal data and structure refinement of **39-Cl_2Br_2**.

CCDC nmuber	2246970	
Empirical formula	$C_{34}H_{42}Br_2Cl_2N_4SSi_2$	
Formula weight	825.67	
Temperature	200(2) K	
Wavelength	0.71073 Å	
Crystal system	triclinic	
Space group	P $\bar{1}$	
Z	2	
Unit cell dimensions	a = 7.9447(8) Å	α = 83.4027(18) deg.
	b = 14.2637(13) Å	β = 80.5117(19) deg.
	c = 17.2022(16) Å	γ = 80.9314(18) deg.
Volume	1890.7(3) $Å^3$	
Density (calculated)	1.45 g/cm^3	
Absorption coefficient	2.43 mm^{-1}	
Crystal shape	plate	
Crystal size	0.148 x 0.134 x 0.010 mm^3	
Crystal colour	blue	
Theta range for data collection	1.5 to 29.9 deg.	
Index ranges	-10≤h≤11, -20≤k≤19, -23≤l≤24	
Reflections collected	38639	
Independent reflections	10065 (R(int) = 0.0574)	
Observed reflections	6526 (I > 2σ(I))	
Absorption correction	Semi-empirical from equivalents	
Max. and min. transmission	0.96 and 0.81	
Refinement method	Full-matrix least-squares on F^2	
Data/restraints/parameters	10065 / 207 / 418	
Goodness-of-fit on F^2	1.01	
Final R indices (I>2sigma(I))	R1 = 0.043, wR2 = 0.095	
Largest diff. peak and hole	0.86 and -0.80 $eÅ^{-3}$	

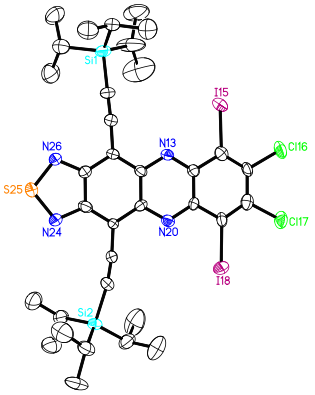

Table 16. Crystal data and structure refinement of **39-Cl_2I_2**.

CCDC nmuber	2246971	
Empirical formula	$C_{35}H_{44}Cl_2I_2N_4SSi_2$	
Formula weight	1004.58	
Temperature	200(2) K	
Wavelength	0.71073 Å	
Crystal system	triclinic	
Space group	P $\bar{1}$	
Z	2	
Unit cell dimensions	a = 9.1982(5) Å	α = 70.9845(14) deg.
	b = 14.1419(7) Å	β = 81.3416(15) deg.
	c = 17.9805(9) Å	γ = 72.9618(15) deg.
Volume	2110.29(19) $Å^3$	
Density (calculated)	1.58 g/cm^3	
Absorption coefficient	1.88 mm^{-1}	
Crystal shape	brick	
Crystal size	0.083 x 0.066 x 0.028 mm^3	
Crystal colour	green	
Theta range for data collection	1.6 to 24.3 deg.	
Index ranges	-10≤h≤10, -16≤k≤16, -20≤l≤20	
Reflections collected	25696	
Independent reflections	6793 (R(int) = 0.0696)	
Observed reflections	4503 (I > 2σ(I))	
Absorption correction	Semi-empirical from equivalents	
Max. and min. transmission	0.96 and 0.91	
Refinement method	Full-matrix least-squares on F^2	
Data/restraints/parameters	6793 / 228 / 445	
Goodness-of-fit on F^2	1.04	
Final R indices (I>2sigma(I))	R1 = 0.057, wR2 = 0.137	
Largest diff. peak and hole	1.25 and -1.08 $eÅ^{-3}$	

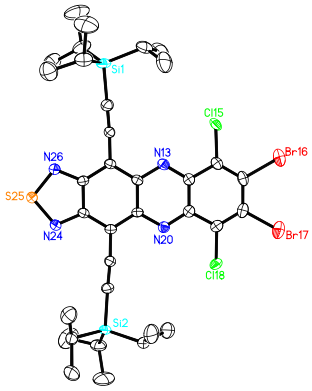

Table 17. Crystal data and structure refinement of **39-Br_2Cl_2**.

CCDC nmuber	2246972	
Empirical formula	$C_{34}H_{42}Br_2Cl_2N_4SSi_2$	
Formula weight	825.67	
Temperature	200(2) K	
Wavelength	0.71073 Å	
Crystal system	triclinic	
Space group	P $\bar{1}$	
Z	2	
Unit cell dimensions	a = 7.8547(8) Å	α = 83.3900(17) deg.
	b = 14.3322(15) Å	β = 80.2118(18) deg.
	c = 17.2740(17) Å	γ = 81.8601(18) deg.
Volume	1888.7(3) $Å^3$	
Density (calculated)	1.45 g/cm^3	
Absorption coefficient	2.44 mm^{-1}	
Crystal shape	plank	
Crystal size	0.343 x 0.065 x 0.038 mm^3	
Crystal colour	blue	
Theta range for data collection	1.4 to 26.1 deg.	
Index ranges	-9≤h≤9, -17≤k≤17, -21≤l≤21	
Reflections collected	31286	
Independent reflections	7438 (R(int) = 0.0297)	
Observed reflections	6117 (I > 2σ(I))	
Absorption correction	Semi-empirical from equivalents	
Max. and min. transmission	0.93 and 0.83	
Refinement method	Full-matrix least-squares on F^2	
Data/restraints/parameters	7438 / 0 / 418	
Goodness-of-fit on F^2	1.05	
Final R indices (I>2sigma(I))	R1 = 0.039, wR2 = 0.105	
Largest diff. peak and hole	0.94 and -0.68 $eÅ^{-3}$	

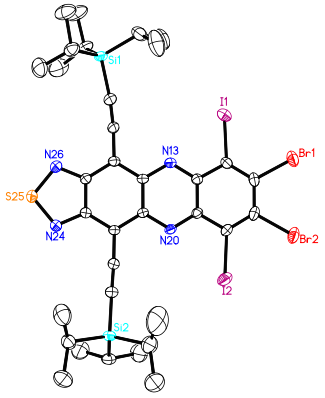

Table 18. Crystal data and structure refinement of **39-Br_2I_2**.

CCDC nmuber	2246973	
Empirical formula	$C_{34}H_{42}Br_2I_2N_4SSi_2$	
Formula weight	1008.57	
Temperature	200(2) K	
Wavelength	0.71073 Å	
Crystal system	triclinic	
Space group	P $\bar{1}$	
Z	2	
Unit cell dimensions	a = 9.2214(7) Å	α = 71.3553(11) deg.
	b = 14.1596(10) Å	β = 83.5353(12) deg.
	c = 18.1458(13) Å	γ = 73.1604(12) deg.
Volume	2148.2(3) $Å^3$	
Density (calculated)	1.56 g/cm^3	
Absorption coefficient	3.45 mm^{-1}	
Crystal shape	plate	
Crystal size	0.400 x 0.180 x 0.011 mm^3	
Crystal colour	brown	
Theta range for data collection	1.2 to 30.2 deg.	
Index ranges	-13≤h≤12, -20≤k≤20, -25≤l≤25	
Reflections collected	44748	
Independent reflections	11819 (R(int) = 0.0410)	
Observed reflections	9073 (I > 2σ(I))	
Absorption correction	Semi-empirical from equivalents	
Max. and min. transmission	0.96 and 0.81	
Refinement method	Full-matrix least-squares on F^2	
Data/restraints/parameters	11819 / 0 / 419	
Goodness-of-fit on F^2	1.03	
Final R indices (I>2sigma(I))	R1 = 0.036, wR2 = 0.094	
Largest diff. peak and hole	0.98 and -1.04 $eÅ^{-3}$	

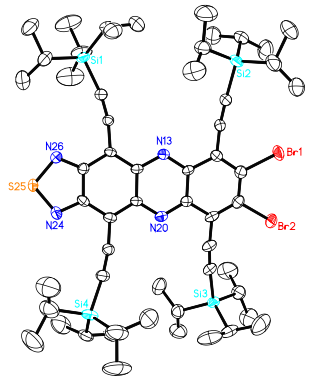

Table 19. Crystal data and structure refinement for **50**.

Identification code	wzo2	
Empirical formula	$C_{56}H_{84}Br_2N_4SSi_4$	
Formula weight	1117.51	
Temperature	200(2) K	
Wavelength	0.71073 Å	
Crystal system	monoclinic	
Space group	$P2_1/c$	
Z	4	
Unit cell dimensions	a = 26.9839(9) Å	α = 90 deg.
	b = 14.8421(5) Å	β = 94.2912(10) deg.
	c = 15.1680(5) Å	γ = 90 deg.
Volume	6057.7(3) $Å^3$	
Density (calculated)	1.23 g/cm^3	
Absorption coefficient	1.49 mm^{-1}	
Crystal shape	plank	
Crystal size	0.121 x 0.062 x 0.022 mm^3	
Crystal colour	blue	
Theta range for data collection	0.8 to 24.2 deg.	
Index ranges	-31≤h≤31, -17≤k≤17, -17≤l≤17	
Reflections collected	88841	
Independent reflections	9768 (R(int) = 0.1004)	
Observed reflections	6682 (I > 2σ(I))	
Absorption correction	Semi-empirical from equivalents	
Max. and min. transmission	0.97 and 0.85	
Refinement method	Full-matrix least-squares on F^2	
Data/restraints/parameters	9768 / 912 / 659	
Goodness-of-fit on F^2	1.04	
Final R indices (I>2sigma(I))	R1 = 0.050, wR2 = 0.115	
Largest diff. peak and hole	0.84 and -0.55 $eÅ^{-3}$	

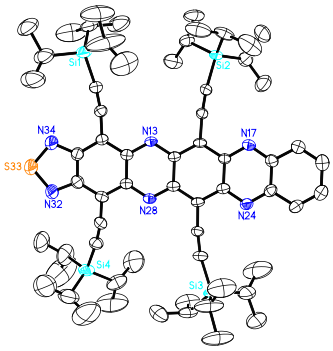

Table 20. Crystal data and structure refinement for **51**.

Identification code	wzo12	
Empirical formula	$C_{62}H_{88}N_6SSi_4$	
Formula weight	1061.80	
Temperature	200(2) K	
Wavelength	0.71073 Å	
Crystal system	monoclinic	
Space group	$P2_1/c$	
Z	4	
Unit cell dimensions	a = 28.3112(16) Å	α = 90 deg.
	b = 15.0007(8) Å	β =100.0457(15) deg.
	c = 15.2437(8) Å	γ = 90 deg.
Volume	6374.6(6) $Å^3$	
Density (calculated)	1.11 g/cm^3	
Absorption coefficient	0.17 mm^{-1}	
Crystal shape	square	
Crystal size	0.170 x 0.169 x 0.023 mm^3	
Crystal colour	green	
Theta range for data collection	0.7 to 23.9 deg.	
Index ranges	-32≤h≤32, -17≤k≤17, -17≤l≤17	
Reflections collected	54048	
Independent reflections	9867 (R(int) = 0.1039)	
Observed reflections	5546 (I > 2σ(I))	
Absorption correction	Semi-empirical from equivalents	
Max. and min. transmission	0.96 and 0.91	
Refinement method	Full-matrix least-squares on F^2	
Data/restraints/parameters	9867 / 1098 / 712	
Goodness-of-fit on F^2	1.03	
Final R indices (I>2sigma(I))	R1 = 0.072, wR2 = 0.167	
Largest diff. peak and hole	0.61 and -0.40 $eÅ^{-3}$	

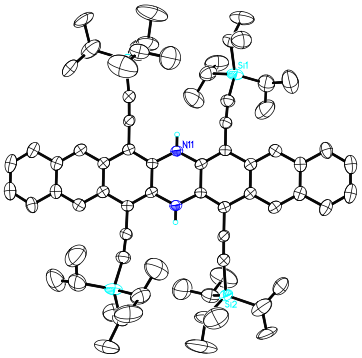

Table 21. Crystal data and structure refinement for **DAH1-H$_2$**.

CCDC number	2168603	
Empirical formula	$C_{72}H_{98}N_2Si_4$	
Formula weight	1103.88	
Temperature	200(2) K	
Wavelength	0.71073 Å	
Crystal system	monoclinic	
Space group	$P2_1/n$	
Z	2	
Unit cell dimensions	a = 9.3027(7) Å	α = 90 deg.
	b = 17.6983(13) Å	β = 95.7216(19) deg.
	c = 20.5902(16) Å	γ = 90 deg.
Volume	3373.1(4) Å^3	
Density (calculated)	1.09 g/cm^3	
Absorption coefficient	0.13 mm^{-1}	
Crystal shape	column	
Crystal size	0.278 x 0.055 x 0.033 mm^3	
Crystal colour	orange	
Theta range for data collection	1.5 to 23.9 deg.	
Index ranges	-10≤h≤10, -20≤k≤19, -23≤l≤23	
Reflections collected	28485	
Independent reflections	5208 (R(int) = 0.0728)	
Observed reflections	3298 (I > 2σ(I))	
Absorption correction	Semi-empirical from equivalents	
Max. and min. transmission	0.96 and 0.92	
Refinement method	Full-matrix least-squares on F^2	
Data/restraints/parameters	5208 / 731 / 419	
Goodness-of-fit on F^2	1.02	
Final R indices (I>2sigma(I))	R1 = 0.062, wR2 = 0.149	
Largest diff. peak and hole	0.38 and -0.26 eÅ^{-3}	

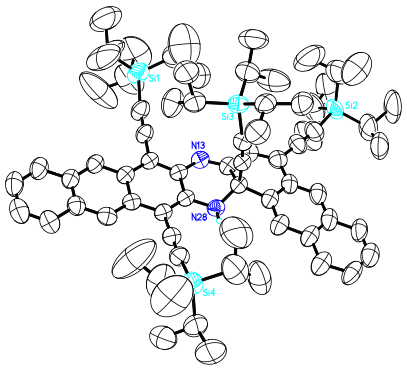

Table 22. Crystal data and structure refinement for **57**.

CCDC number	2168604	
Empirical formula	$C_{72}H_{98}N_2Si_4$	
Formula weight	1103.88	
Temperature	200(2) K	
Wavelength	1.54178 Å	
Crystal system	triclinic	
Space group	P $\bar{1}$	
Z	2	
Unit cell dimensions	a = 13.797(2) Å	α =104.09(1) deg.
	b = 14.614(2) Å	β =105.877(11) deg.
	c = 18.584(2) Å	γ = 94.914(11) deg.
Volume	3448.9(9) $Å^3$	
Density (calculated)	1.06 g/cm^3	
Absorption coefficient	1.09 mm^{-1}	
Crystal shape	brick	
Crystal size	0.105 x 0.042 x 0.030 mm^3	
Crystal colour	dark orange	
Theta range for data collection	3.4 to 59.3 deg.	
Index ranges	-14≤h≤15, -13≤k≤15, -18≤l≤20	
Reflections collected	23298	
Independent reflections	9374 (R(int) = 0.0412)	
Observed reflections	5145 (I > 2σ(I))	
Absorption correction	Semi-empirical from equivalents	
Max. and min. transmission	0.97 and 0.57	
Refinement method	Full-matrix least-squares on F^2	
Data/restraints/parameters	9374 / 2118 / 747	
Goodness-of-fit on F^2	1.03	
Final R indices (I>2sigma(I))	R1 = 0.089, wR2 = 0.235	
Largest diff. peak and hole	0.37 and -0.28 $eÅ^{-3}$	

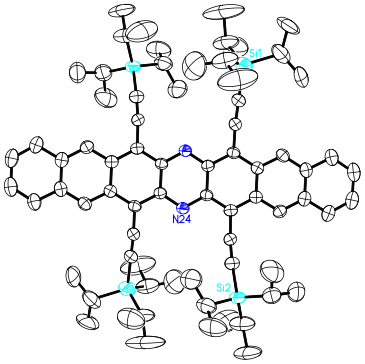

Table 23. Crystal data and structure refinement for **DAH1**.

CCDC number	2168605	
Empirical formula	$C_{72}H_{96}N_2Si_4$	
Formula weight	1101.86	
Temperature	200(2) K	
Wavelength	1.54178 Å	
Crystal system	monoclinic	
Space group	$P2_1/n$	
Z	2	
Unit cell dimensions	a = 9.1368(2) Å	α = 90 deg.
	b = 17.9587(5) Å	β = 95.607(2) deg.
	c = 20.6347(4) Å	γ = 90 deg.
Volume	3369.65(14) $Å^3$	
Density (calculated)	1.09 g/cm^3	
Absorption coefficient	1.11 mm^{-1}	
Crystal shape	column	
Crystal size	0.430 x 0.032 x 0.030 mm^3	
Crystal colour	dark green	
Theta range for data collection	3.3 to 71.6 deg.	
Index ranges	-11≤h≤7, -20≤k≤21, -23≤l≤25	
Reflections collected	23373	
Independent reflections	6348 (R(int) = 0.0438)	
Observed reflections	3881 (I > 2σ(I))	
Absorption correction	Semi-empirical from equivalents	
Max. and min. transmission	0.96 and 0.87	
Refinement method	Full-matrix least-squares on F^2	
Data/restraints/parameters	6348 / 729 / 403	
Goodness-of-fit on F^2	1.03	
Final R indices (I>2sigma(I))	R1 = 0.062, wR2 = 0.160	
Largest diff. peak and hole	0.49 and -0.35 $eÅ^{-3}$	

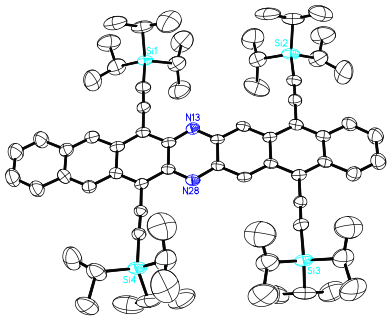

Table 24. Crystal data and structure refinement for **DAH2**.

CCDC number	2254467	
Empirical formula	$C_{72.50}H_{97}ClN_2Si_4$	
Formula weight	1144.33	
Temperature	200(2) K	
Wavelength	0.71073 Å	
Crystal system	triclinic	
Space group	$P\bar{1}$	
Z	4	
Unit cell dimensions	a = 15.0283(15) Å	α = 79.290(3) deg.
	b = 15.0685(15) Å	β = 79.201(3) deg.
	c = 32.471(3) Å	γ = 89.738(3) deg.
Volume	7093.7(12) $Å^3$	
Density (calculated)	1.07 g/cm^3	
Absorption coefficient	0.16 mm^{-1}	
Crystal shape	plate	
Crystal size	0.195 x 0.168 x 0.022 mm^3	
Crystal colour	green	
Theta range for data collection	0.6 to 22.0 deg.	
Index ranges	-15≤h≤15, -15≤k≤15, -34≤l≤34	
Reflections collected	52446	
Independent reflections	17341 (R(int) = 0.0945)	
Observed reflections	8726 (I > 2σ(I))	
Absorption correction	Semi-empirical from equivalents	
Max. and min. transmission	0.96 and 0.89	
Refinement method	Full-matrix least-squares on F^2	
Data/restraints/parameters	17341 / 8997 / 1705	
Goodness-of-fit on F^2	1.03	
Final R indices (I>2sigma(I))	R1 = 0.088, wR2 = 0.199	
Largest diff. peak and hole	0.43 and -0.61 $eÅ^{-3}$	

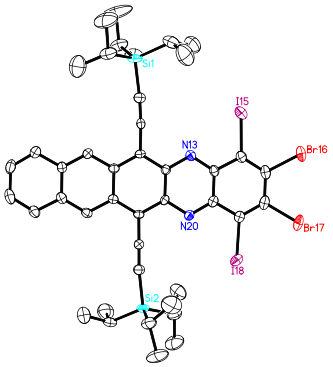

Table 25. Crystal data and structure refinement for **58a**.

CCDC number	2081160	
Empirical formula	$C_{42}H_{48}Br_2I_2N_2Si_2$	
Formula weight	1050.62	
Temperature	200(2) K	
Wavelength	0.71073 Å	
Crystal system	monoclinic	
Space group	$P2_1/c$	
Z	4	
Unit cell dimensions	a = 8.6096(4) Å	α = 90 deg.
	b = 35.6295(17) Å	β = 101.6028(12) deg.
	c = 14.4632(8) Å	γ = 90 deg.
Volume	4346.0(4) $Å^3$	
Density (calculated)	1.61 g/cm^3	
Absorption coefficient	3.37 mm^{-1}	
Crystal shape	plate	
Crystal size	0.232 x 0.093 x 0.016 mm^3	
Crystal colour	green	
Theta range for data collection	1.5 to 28.4 deg.	
Index ranges	-11≤h≤11, -45≤k≤47, -18≤l≤18	
Reflections collected	47770	
Independent reflections	10074 (R(int) = 0.0610)	
Observed reflections	6476 (I > 2σ(I))	
Absorption correction	Semi-empirical from equivalents	
Max. and min. transmission	0.96 and 0.85	
Refinement method	Full-matrix least-squares on F^2	
Data/restraints/parameters	10074 / 0 / 480	
Goodness-of-fit on F^2	1.02	
Final R indices (I>2sigma(I))	R1 = 0.044, wR2 = 0.087	
Largest diff. peak and hole	0.78 and -0.72 $eÅ^{-3}$	

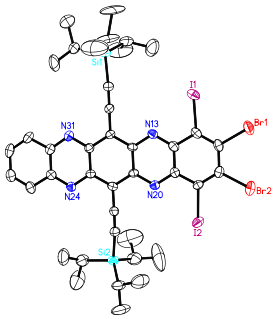

Table 26. Crystal data and structure refinement for **58b**.

CCDC number	2081161	
Empirical formula	$C_{40}H_{46}Br_2I_2N_4Si_2$	
Formula weight	1052.61	
Temperature	200(2) K	
Wavelength	0.71073 Å	
Crystal system	monoclinic	
Space group	$P2_1/c$	
Z	4	
Unit cell dimensions	a = 19.1981(13) Å	α = 90 deg.
	b = 13.9124(10) Å	β = 111.1688(15) deg.
	c = 17.1871(12) Å	γ = 90 deg.
Volume	4280.8(5) $Å^3$	
Density (calculated)	1.63 g/cm^3	
Absorption coefficient	3.42 mm^{-1}	
Crystal shape	plate	
Crystal size	0.242 x 0.050 x 0.016 mm^3	
Crystal colour	green	
Theta range for data collection	1.9 to 28.6 deg.	
Index ranges	$-25 \le h \le 25$, $-18 \le k \le 18$, $-22 \le l \le 22$	
Reflections collected	49039	
Independent reflections	10609 (R(int) = 0.0690)	
Observed reflections	6249 ($I > 2\sigma(I)$)	
Absorption correction	Semi-empirical from equivalents	
Max. and min. transmission	0.96 and 0.83	
Refinement method	Full-matrix least-squares on F^2	
Data/restraints/parameters	10609 / 627 / 523	
Goodness-of-fit on F^2	1.00	
Final R indices (I>2sigma(I))	R1 = 0.044, wR2 = 0.077	
Largest diff. peak and hole	0.71 and -0.96 $eÅ^{-3}$	

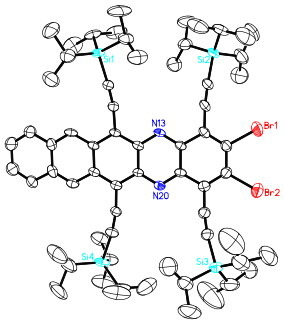

Table 27. Crystal data and structure refinement for **59a**.

CCDC number	2081162	
Empirical formula	$C_{64}H_{90}Br_2N_2Si_4$	
Formula weight	1159.55	
Temperature	200(2) K	
Wavelength	0.71073 Å	
Crystal system	monoclinic	
Space group	$P2_1/c$	
Z	4	
Unit cell dimensions	a = 28.443(2) Å	α = 90 deg.
	b = 15.1439(11) Å	β = 102.959(2) deg.
	c = 15.3047(12) Å	γ = 90 deg.
Volume	6424.4(8) $Å^3$	
Density (calculated)	1.20 g/cm^3	
Absorption coefficient	1.37 mm^{-1}	
Crystal shape	plate	
Crystal size	0.113 x 0.106 x 0.012 mm^3	
Crystal colour	green	
Theta range for data collection	0.7 to 21.5 deg.	
Index ranges	-29≤h≤29, -15≤k≤15, -15≤l≤15	
Reflections collected	44850	
Independent reflections	7326 (R(int) = 0.1067)	
Observed reflections	4387 (I > 2σ(I))	
Absorption correction	Semi-empirical from equivalents	
Max. and min. transmission	0.97 and 0.88	
Refinement method	Full-matrix least-squares on F^2	
Data/restraints/parameters	7326 / 1887 / 722	
Goodness-of-fit on F^2	1.03	
Final R indices (I>2sigma(I))	R1 = 0.060, wR2 = 0.137	
Largest diff. peak and hole	0.83 and -0.83 $eÅ^{-3}$	

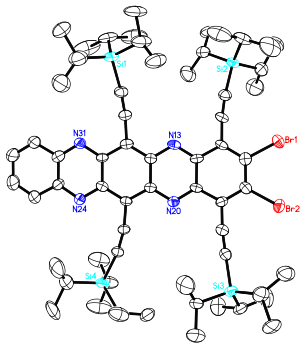

Table 28. Crystal data and structure refinement for **59b**.

CCDC number	2081163	
Empirical formula	$C_{62}H_{88}Br_2N_4Si_4$	
Formula weight	1161.54	
Temperature	200(2) K	
Wavelength	1.54178 Å	
Crystal system	monoclinic	
Space group	$P2_1/c$	
Z	4	
Unit cell dimensions	a = 29.2059(8) Å	α = 90 deg.
	b = 14.9414(4) Å	β =104.853(2) deg.
	c = 15.1021(4) Å	γ = 90 deg.
Volume	6370.0(3) $Å^3$	
Density (calculated)	1.21 g/cm^3	
Absorption coefficient	2.62 mm^{-1}	
Crystal shape	plate	
Crystal size	0.085 x 0.053 x 0.015 mm^3	
Crystal colour	green	
Theta range for data collection	4.2 to 60.0 deg.	
Index ranges	$-32 \le h \le 31$, $-16 \le k \le 11$, $-16 \le l \le 12$	
Reflections collected	36257	
Independent reflections	9187 (R(int) = 0.1250)	
Observed reflections	5570 ($I > 2\sigma(I)$)	
Absorption correction	Semi-empirical from equivalents	
Max. and min. transmission	0.96 and 0.59	
Refinement method	Full-matrix least-squares on F^2	
Data/restraints/parameters	9187 / 0 / 682	
Goodness-of-fit on F^2	1.11	
Final R indices (I>2sigma(I))	R1 = 0.077, wR2 = 0.121	
Largest diff. peak and hole	0.42 and -0.37 $eÅ^{-3}$	

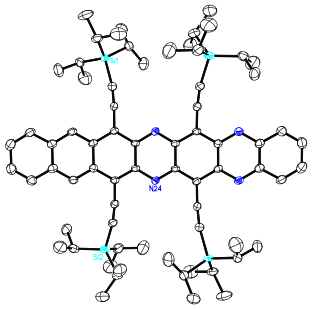

Table 29. Crystal data and structure refinement for **TAH**.

CCDC number	2081164	
Empirical formula	$C_{70}H_{94}N_4Si_4$	
Formula weight	1103.85	
Temperature	200(2) K	
Wavelength	0.71073 Å	
Crystal system	monoclinic	
Space group	$P2_1/c$	
Z	2	
Unit cell dimensions	a = 9.4940(10) Å	α = 90 deg.
	b = 20.153(2) Å	β = 91.266(3) deg.
	c = 17.1397(19) Å	γ = 90 deg.
Volume	3278.7(6) $Å^3$	
Density (calculated)	1.12 g/cm^3	
Absorption coefficient	0.13 mm^{-1}	
Crystal shape	column	
Crystal size	0.163 x 0.031 x 0.021 mm^3	
Crystal colour	green	
Theta range for data collection	1.6 to 25.1 deg.	
Index ranges	$-11 \le h \le 11$, $-24 \le k \le 24$, $-20 \le l \le 20$	
Reflections collected	30908	
Independent reflections	5837 (R(int) = 0.1134)	
Observed reflections	3399 ($I > 2\sigma(I)$)	
Absorption correction	Semi-empirical from equivalents	
Max. and min. transmission	0.96 and 0.75	
Refinement method	Full-matrix least-squares on F^2	
Data/restraints/parameters	5837 / 608 / 394	
Goodness-of-fit on F^2	1.00	
Final R indices (I>2sigma(I))	R1 = 0.060, wR2 = 0.115	
Largest diff. peak and hole	0.28 and -0.26 $eÅ^{-3}$	

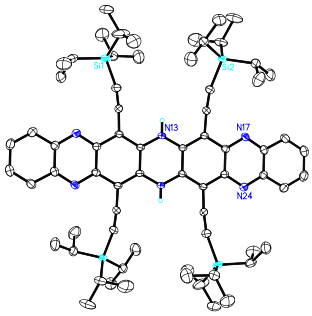

Table 30. Crystal data and structure refinement for **HAH**.

CCDC number	2081165	
Empirical formula	$C_{68}H_{93.12}N_6Si_4$	
Formula weight	1106.96	
Temperature	200(2) K	
Wavelength	0.71073 Å	
Crystal system	monoclinic	
Space group	$P2_1/c$	
Z	2	
Unit cell dimensions	a = 9.4977(3) Å	α = 90 deg.
	b = 20.0687(7) Å	β = 90.9157(8) deg.
	c = 17.0470(6) Å	γ = 90 deg.
Volume	3248.85(19) $Å^3$	
Density (calculated)	1.13 g/cm^3	
Absorption coefficient	0.14 mm^{-1}	
Crystal shape	column	
Crystal size	0.188 x 0.058 x 0.044 mm^3	
Crystal colour	red	
Theta range for data collection	1.6 to 29.9 deg.	
Index ranges	-13≤h≤13, -26≤k≤26, -23≤l≤23	
Reflections collected	39075	
Independent reflections	8611 (R(int) = 0.0484)	
Observed reflections	5943 (I > 2σ(I))	
Absorption correction	Semi-empirical from equivalents	
Max. and min. transmission	0.96 and 0.92	
Refinement method	Full-matrix least-squares on F^2	
Data/restraints/parameters	8611 / 261 / 362	
Goodness-of-fit on F^2	1.03	
Final R indices (I>2sigma(I))	R1 = 0.053, wR2 = 0.122	
Largest diff. peak and hole	0.69 and -0.67 $eÅ^{-3}$	

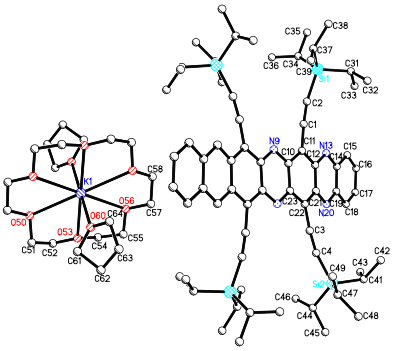

Table 31. Crystal data and structure refinement for **TAH**$^{\bullet-}$.

CCDC number	2107146	
Empirical formula	$C_{90}H_{134}KN_4O_8Si_4$	
Formula weight	1551.46	
Temperature	200(2) K	
Wavelength	1.54178 Å	
Crystal system	monoclinic	
Space group	$P2_1/c$	
Z	2	
Unit cell dimensions	a = 18.2223(12) Å	α = 90 deg.
	b = 20.2118(10) Å	β = 109.371(5) deg.
	c = 14.5386(9) Å	γ = 90 deg.
Volume	5051.5(5) Å^3	
Density (calculated)	1.02 g/cm^3	
Absorption coefficient	1.29 mm^{-1}	
Crystal shape	hexagonal plate	
Crystal size	0.285 x 0.210 x 0.012 mm^3	
Crystal colour	violet	
Theta range for data collection	2.6 to 57.9 deg.	
Index ranges	$-20 \le h \le 18$, $-21 \le k \le 22$, $-10 \le l \le 15$	
Reflections collected	24566	
Independent reflections	6958 (R(int) = 0.0630)	
Observed reflections	4316 ($I > 2\sigma(I)$)	
Absorption correction	Semi-empirical from equivalents	
Max. and min. transmission	0.95 and 0.22	
Refinement method	Full-matrix least-squares on F^2	
Data/restraints/parameters	6958 / 1017 / 484	
Goodness-of-fit on F^2	1.05	
Final R indices (I>2sigma(I))	R1 = 0.102, wR2 = 0.252	
Largest diff. peak and hole	0.46 and -0.27 eÅ^{-3}	

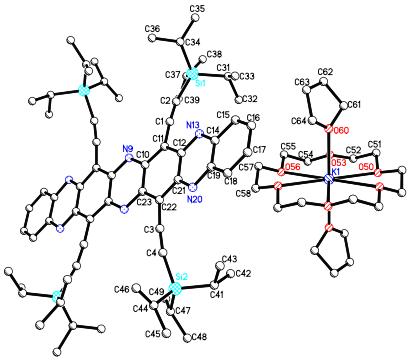

Table 32. Crystal data and structure refinement for **HAH**$^{\bullet-}$.

CCDC number	2107147	
Empirical formula	$C_{88}H_{132}KN_6O_8Si_4$	
Formula weight	1553.45	
Temperature	200(2) K	
Wavelength	0.71073 Å	
Crystal system	monoclinic	
Space group	$P2_1/c$	
Z	2	
Unit cell dimensions	a = 18.2861(7) Å	α = 90 deg.
	b = 20.0794(8) Å	β =108.9009(10) deg.
	c = 14.4496(6) Å	γ = 90 deg.
Volume	5019.4(3) Å^3	
Density (calculated)	1.03 g/cm^3	
Absorption coefficient	0.15 mm^{-1}	
Crystal shape	plate	
Crystal size	0.302 x 0.230 x 0.034 mm^3	
Crystal colour	violet	
Theta range for data collection	1.2 to 25.0 deg.	
Index ranges	-21≤h≤21, -23≤k≤23, -17≤l≤16	
Reflections collected	47388	
Independent reflections	8856 (R(int) = 0.0510)	
Observed reflections	5232 (I > 2σ(I))	
Absorption correction	Semi-empirical from equivalents	
Max. and min. transmission	0.96 and 0.91	
Refinement method	Full-matrix least-squares on F^2	
Data/restraints/parameters	8856 / 621 / 484	
Goodness-of-fit on F^2	1.04	
Final R indices (I>2sigma(I))	R1 = 0.089, wR2 = 0.240	
Largest diff. peak and hole	0.71 and -0.29 eÅ^{-3}	

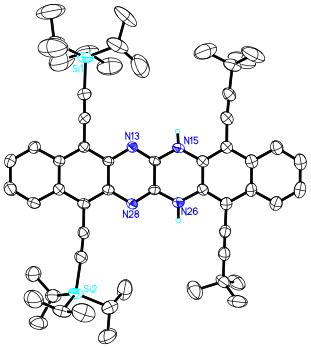

Table 33. Crystal data and structure refinement for **TAHex1-H$_2$**.

Identification code	wzo52	
Empirical formula	$C_{56}H_{70}N_4O_{0.10}Si_2$	
Formula weight	856.91	
Temperature	200(2) K	
Wavelength	0.71073 Å	
Crystal system	monoclinic	
Space group	$P2_1/n$	
Z	4	
Unit cell dimensions	a = 14.1837(16) Å	α = 90 deg.
	b = 22.308(2) Å	β = 99.323(3) deg.
	c = 16.3412(18) Å	γ = 90 deg.
Volume	5102.2(10) Å^3	
Density (calculated)	1.12 g/cm^3	
Absorption coefficient	0.11 mm^{-1}	
Crystal shape	column	
Crystal size	0.317 x 0.059 x 0.045 mm^3	
Crystal colour	orange	
Theta range for data collection	1.6 to 22.5 deg.	
Index ranges	-15≤h≤15, -23≤k≤23, -17≤l≤17	
Reflections collected	38295	
Independent reflections	6624 (R(int) = 0.1249)	
Observed reflections	3503 (I > 2σ(I))	
Absorption correction	Semi-empirical from equivalents	
Max. and min. transmission	0.96 and 0.83	
Refinement method	Full-matrix least-squares on F^2	
Data/restraints/parameters	6624 / 1681 / 756	
Goodness-of-fit on F^2	1.02	
Final R indices (I>2sigma(I))	R1 = 0.066, wR2 = 0.140	
Largest diff. peak and hole	0.35 and -0.21 eÅ^{-3}	

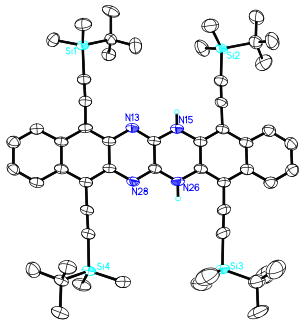

Table 34. Crystal data and structure refinement for **TAHex2-H$_2$**.

Identification code	wzo48	
Empirical formula	$C_{55}H_{73}N_4OSi_4$	
Formula weight	918.53	
Temperature	200(2) K	
Wavelength	1.54178 Å	
Crystal system	monoclinic	
Space group	$P2_1/n$	
Z	4	
Unit cell dimensions	a = 18.4456(5) Å	α = 90 deg.
	b = 10.0824(2) Å	β = 95.280(2) deg.
	c = 29.7417(7) Å	γ = 90 deg.
Volume	5507.8(2) Å^3	
Density (calculated)	1.11 g/cm^3	
Absorption coefficient	1.30 mm^{-1}	
Crystal shape	plank	
Crystal size	0.250 x 0.035 x 0.020 mm^3	
Crystal colour	yellow	
Theta range for data collection	2.7 to 68.2 deg.	
Index ranges	-21≤h≤21, -10≤k≤11, -20≤l≤35	
Reflections collected	31620	
Independent reflections	9714 (R(int) = 0.0500)	
Observed reflections	5684 (I > 2σ(I))	
Absorption correction	Semi-empirical from equivalents	
Max. and min. transmission	0.98 and 0.78	
Refinement method	Full-matrix least-squares on F^2	
Data/restraints/parameters	9714 / 0 / 608	
Goodness-of-fit on F^2	1.04	
Final R indices (I>2sigma(I))	R1 = 0.072, wR2 = 0.171	
Largest diff. peak and hole	0.72 and -0.22 eÅ^{-3}	

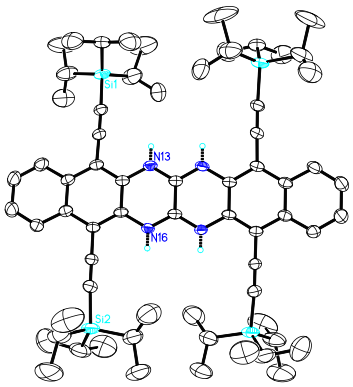

Table 35. Crystal data and structure refinement for **TAHex5-H$_2$**.

Identification code	wzo19	
Empirical formula	$C_{66}H_{94}N_4Si_4$	
Formula weight	1055.81	
Temperature	200(2) K	
Wavelength	0.71073 Å	
Crystal system	monoclinic	
Space group	C2/c	
Z	8	
Unit cell dimensions	a = 21.2866(7) Å	α = 90 deg.
	b = 21.2370(7) Å	β =104.1590(8) deg.
	c = 29.9027(10) Å	γ = 90 deg.
Volume	13107.3(8) Å^3	
Density (calculated)	1.07 g/cm^3	
Absorption coefficient	0.13 mm^{-1}	
Crystal shape	plate	
Crystal size	0.095 x 0.090 x 0.028 mm^3	
Crystal colour	yellow	
Theta range for data collection	1.4 to 26.0 deg.	
Index ranges	-26≤h≤26, -26≤k≤25, -36≤l≤36	
Reflections collected	66554	
Independent reflections	12933 (R(int) = 0.0630)	
Observed reflections	7863 (I > 2σ(I))	
Absorption correction	Semi-empirical from equivalents	
Max. and min. transmission	0.96 and 0.92	
Refinement method	Full-matrix least-squares on F^2	
Data/restraints/parameters	12933 / 3358 / 899	
Goodness-of-fit on F^2	1.02	
Final R indices (I>2sigma(I))	R1 = 0.069, wR2 = 0.172	
Largest diff. peak and hole	1.01 and -0.44 eÅ^{-3}	

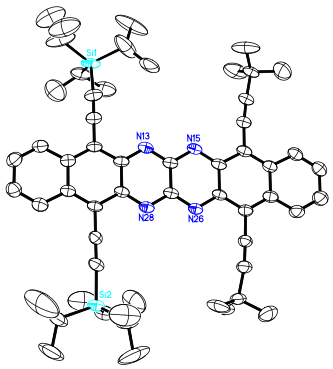

Table 36. Crystal data and structure refinement for **TAHex1**.

Identification code	wzo33	
Empirical formula	$C_{57}H_{70}Cl_2N_4Si_2$	
Formula weight	938.25	
Temperature	200(2) K	
Wavelength	0.71073 Å	
Crystal system	triclinic	
Space group	P $\bar{1}$	
Z	2	
Unit cell dimensions	a = 12.0423(9) Å	α = 74.7219(19) deg.
	b = 12.9358(10) Å	β = 84.4813(19) deg.
	c = 18.4940(13) Å	γ = 78.703(2) deg.
Volume	2722.3(4) Å^3	
Density (calculated)	1.14 g/cm^3	
Absorption coefficient	0.20 mm^{-1}	
Crystal shape	plate	
Crystal size	0.190 x 0.101 x 0.016 mm^3	
Crystal colour	green	
Theta range for data collection	1.1 to 21.5 deg.	
Index ranges	-12≤h≤12, -13≤k≤13, -19≤l≤19	
Reflections collected	26110	
Independent reflections	6247 (R(int) = 0.1021)	
Observed reflections	3451 (I > 2σ(I))	
Absorption correction	Semi-empirical from equivalents	
Max. and min. transmission	0.96 and 0.90	
Refinement method	Full-matrix least-squares on F^2	
Data/restraints/parameters	6247 / 1303 / 691	
Goodness-of-fit on F^2	1.02	
Final R indices (I>2sigma(I))	R1 = 0.060, wR2 = 0.151	
Largest diff. peak and hole	0.65 and -0.26 eÅ^{-3}	

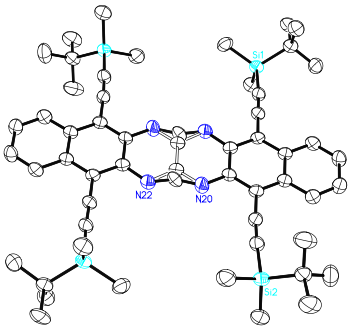

Table 37. Crystal data and structure refinement for **TAHex2** (solvate free). Specimen was grown by slow diffusion of methanol into a chloroform solution.

Identification code	wzo64	
Empirical formula	$C_{54}H_{68}N_4Si_4$	
Formula weight	885.48	
Temperature	200(2) K	
Wavelength	1.54178 Å	
Crystal system	monoclinic	
Space group	C2/c	
Z	4	
Unit cell dimensions	a = 33.800(2) Å	α = 90 deg.
	b = 6.2467(3) Å	β =114.560(4) deg.
	c = 27.331(3) Å	γ = 90 deg.
Volume	5248.5(7) $Å^3$	
Density (calculated)	1.12 g/cm^3	
Absorption coefficient	1.33 mm^{-1}	
Crystal shape	plank	
Crystal size	0.070 x 0.022 x 0.019 mm^3	
Crystal colour	green/brown	
Theta range for data collection	2.9 to 54.3 deg.	
Index ranges	-33≤h≤35, -3≤k≤6, -28≤l≤26	
Reflections collected	13999	
Independent reflections	3147 (R(int) = 0.0625)	
Observed reflections	1820 (I > 2σ(I))	
Absorption correction	Semi-empirical from equivalents	
Max. and min. transmission	0.99 and 0.87	
Refinement method	Full-matrix least-squares on F^2	
Data/restraints/parameters	3147 / 242 / 295	
Goodness-of-fit on F^2	0.95	
Final R indices (I>2sigma(I))	R1 = 0.046, wR2 = 0.082	
Largest diff. peak and hole	0.16 and -0.21 $eÅ^{-3}$	

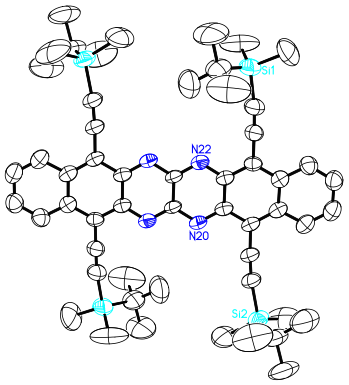

Table 38. Crystal data and structure refinement for **TAHex2** (with DCM as solvate). Specimen was grown by slow diffusion of methanol into a DCM solution.

Identification code	wzo66	
Empirical formula	$C_{56}H_{72}Cl_4N_4Si_4$	
Formula weight	1055.33	
Temperature	200(2) K	
Wavelength	0.71073 Å	
Crystal system	triclinic	
Space group	$P\bar{1}$	
Z	1	
Unit cell dimensions	a = 7.7616(6) Å	α = 71.1920(17) deg.
	b = 12.2775(9) Å	β = 80.1199(19) deg.
	c = 17.0214(13) Å	γ = 87.7513(19) deg.
Volume	1512.4(2) $Å^3$	
Density (calculated)	1.16 g/cm^3	
Absorption coefficient	0.31 mm^{-1}	
Crystal shape	prism	
Crystal size	0.196 x 0.110 x 0.105 mm^3	
Crystal colour	green	
Theta range for data collection	1.3 to 27.9 deg.	
Index ranges	$-10 \le h \le 10$, $-16 \le k \le 16$, $-21 \le l \le 22$	
Reflections collected	21356	
Independent reflections	6402 (R(int) = 0.0406)	
Observed reflections	4490 ($I > 2\sigma(I)$)	
Absorption correction	Semi-empirical from equivalents	
Max. and min. transmission	0.96 and 0.91	
Refinement method	Full-matrix least-squares on F^2	
Data/restraints/parameters	6402 / 331 / 317	
Goodness-of-fit on F^2	1.05	
Final R indices (I>2sigma(I))	R1 = 0.051, wR2 = 0.130	
Largest diff. peak and hole	0.33 and -0.44 $eÅ^{-3}$	

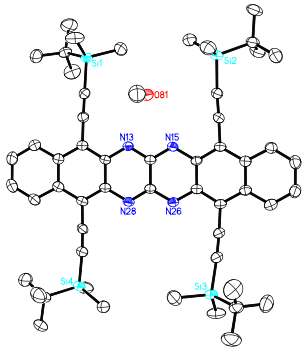

Table 39. Crystal data and structure refinement for **TAHex2** (with methanol as solvate). Specimen was grown by slow diffusion of methanol into a DCM solution.

Identification code	wzo54	
Empirical formula	$C_{55}H_{72}N_4OSi_4$	
Formula weight	917.52	
Temperature	200(2) K	
Wavelength	1.54178 Å	
Crystal system	monoclinic	
Space group	$P2_1/c$	
Z	4	
Unit cell dimensions	a = 16.1545(4) Å	α = 90 deg.
	b = 16.1491(3) Å	β =103.400(2) deg.
	c = 21.6825(5) Å	γ = 90 deg.
Volume	5502.5(2) $Å^3$	
Density (calculated)	1.11 g/cm^3	
Absorption coefficient	1.30 mm^{-1}	
Crystal shape	cuboid	
Crystal size	0.134 x 0.048 x 0.047 mm^3	
Crystal colour	orange	
Theta range for data collection	2.8 to 68.6 deg.	
Index ranges	-8≤h≤19, -19≤k≤18, -25≤l≤25	
Reflections collected	34306	
Independent reflections	9730 (R(int) = 0.0365)	
Observed reflections	6770 (I > 2σ(I))	
Absorption correction	Semi-empirical from equivalents	
Max. and min. transmission	0.91 and 0.82	
Refinement method	Full-matrix least-squares on F^2	
Data/restraints/parameters	9730 / 0 / 599	
Goodness-of-fit on F^2	1.01	
Final R indices (I>2sigma(I))	R1 = 0.050, wR2 = 0.122	
Largest diff. peak and hole	0.89 and -0.32 $eÅ^{-3}$	

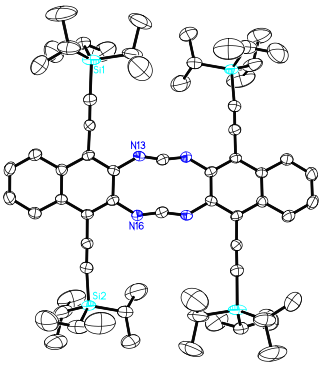

Table 40. Crystal data and structure refinement for **TAHex5**.

Identification code	wzo18	
Empirical formula	$C_{66}H_{92}N_4Si_4$	
Formula weight	1053.79	
Temperature	200(2) K	
Wavelength	1.54178 Å	
Crystal system	monoclinic	
Space group	C2/c	
Z	8	
Unit cell dimensions	a = 21.2209(9) Å	α = 90 deg.
	b = 21.2068(7) Å	β =103.739(3) deg.
	c = 29.9023(13) Å	γ = 90 deg.
Volume	13071.8(9) $Å^3$	
Density (calculated)	1.07 g/cm^3	
Absorption coefficient	1.14 mm^{-1}	
Crystal shape	plate	
Crystal size	0.157 x 0.116 x 0.012 mm^3	
Crystal colour	green	
Theta range for data collection	3.0 to 63.7 deg.	
Index ranges	-24≤h≤23, -12≤k≤24, -31≤l≤34	
Reflections collected	42421	
Independent reflections	10682 (R(int) = 0.1381)	
Observed reflections	5835 (I > 2σ(I))	
Absorption correction	Semi-empirical from equivalents	
Max. and min. transmission	0.98 and 0.55	
Refinement method	Full-matrix least-squares on F^2	
Data/restraints/parameters	10682 / 2956 / 868	
Goodness-of-fit on F^2	1.12	
Final R indices (I>2sigma(I))	R1 = 0.091, wR2 = 0.164	
Largest diff. peak and hole	0.35 and -0.38 $eÅ^{-3}$	

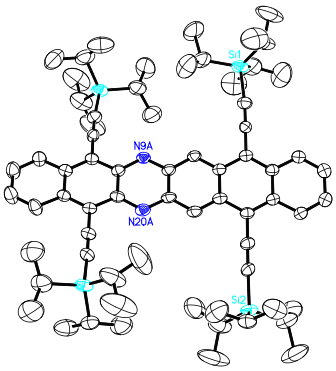

Table 41. Crystal data and structure refinement for **DAHex**.

Identification code	wzo55	
Empirical formula	$C_{68}H_{94}N_2Si_4$	
Formula weight	1051.81	
Temperature	200(2) K	
Wavelength	1.54178 Å	
Crystal system	monoclinic	
Space group	C2/c	
Z	8	
Unit cell dimensions	a = 21.2963(8) Å	α = 90 deg.
	b = 21.2794(8) Å	β =103.852(3) deg.
	c = 29.8646(12) Å	γ = 90 deg.
Volume	13140.2(9) $Å^3$	
Density (calculated)	1.06 g/cm^3	
Absorption coefficient	1.12 mm^{-1}	
Crystal shape	plate	
Crystal size	0.096 x 0.027 x 0.020 mm^3	
Crystal colour	green	
Theta range for data collection	3.0 to 63.7 deg.	
Index ranges	-22≤h≤24, -24≤k≤19, -29≤l≤34	
Reflections collected	38608	
Independent reflections	10705 (R(int) = 0.1147)	
Observed reflections	4959 (I > 2σ(I))	
Absorption correction	Semi-empirical from equivalents	
Max. and min. transmission	0.98 and 0.90	
Refinement method	Full-matrix least-squares on F^2	
Data/restraints/parameters	10705 / 3076 / 832	
Goodness-of-fit on F^2	1.02	
Final R indices (I>2sigma(I))	R1 = 0.084, wR2 = 0.161	
Largest diff. peak and hole	0.36 and -0.29 $eÅ^{-3}$	

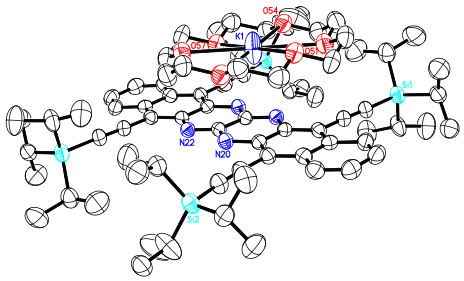

Table 42. Crystal data and structure refinement for **TAHex5**$^{\bullet-}$.

Identification code	wzo50	
Empirical formula	$C_{78}H_{116}KN_4O_{6.29}Si_4$	
Formula weight	1361.84	
Temperature	200(2) K	
Wavelength	1.54178 Å	
Crystal system	monoclinic	
Space group	$P2_1/c$	
Z	2	
Unit cell dimensions	a = 18.0349(8) Å	α = 90 deg.
	b = 8.7364(3) Å	β = 91.334(4) deg.
	c = 24.9991(11) Å	γ = 90 deg.
Volume	3937.8(3) Å^3	
Density (calculated)	1.15 g/cm^3	
Absorption coefficient	1.57 mm^{-1}	
Crystal shape	plate	
Crystal size	0.075 x 0.034 x 0.010 mm^3	
Crystal colour	metallic bronze	
Theta range for data collection	3.5 to 61.2 deg.	
Index ranges	$-14 \le h \le 20$, $-9 \le k \le 9$, $-22 \le l \le 28$	
Reflections collected	19420	
Independent reflections	5816 (R(int) = 0.0869)	
Observed reflections	2960 ($I > 2\sigma(I)$)	
Absorption correction	Semi-empirical from equivalents	
Max. and min. transmission	0.98 and 0.90	
Refinement method	Full-matrix least-squares on F^2	
Data/restraints/parameters	5816 / 615 / 473	
Goodness-of-fit on F^2	1.02	
Final R indices (I>2sigma(I))	R1 = 0.067, wR2 = 0.112	
Largest diff. peak and hole	0.25 and -0.25 eÅ^{-3}	

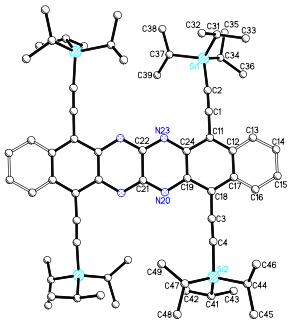

Table 43. Crystal data and structure refinement for **65**.

Identification code	wzo61	
Empirical formula	$C_{62}H_{90}N_4Si_4$	
Formula weight	1003.73	
Temperature	180(2) K	
Wavelength	1.54178 Å	
Crystal system	monoclinic	
Space group	C2/c	
Z	8	
Unit cell dimensions	a = 21.2320(12) Å	α = 90 deg.
	b = 21.1897(10) Å	β = 105.053(5) deg.
	c = 28.831(2) Å	γ = 90 deg.
Volume	12525.8(13) $Å^3$	
Density (calculated)	1.07 g/cm^3	
Absorption coefficient	1.16 mm^{-1}	
Crystal shape	plate	
Crystal size	0.116 x 0.064 x 0.030 mm^3	
Crystal colour	blue	
Theta range for data collection	3.0 to 52.6 deg.	
Index ranges	-13≤h≤21, -18≤k≤21, -29≤l≤29	
Reflections collected	33121	
Independent reflections	7155 (R(int) = 0.1347)	
Observed reflections	3724 (I > 2σ(I))	
Absorption correction	Semi-empirical from equivalents	
Max. and min. transmission	0.97 and 0.85	
Refinement method	Full-matrix least-squares on F^2	
Data/restraints/parameters	7155 / 1565 / 713	
Goodness-of-fit on F^2	1.09	
Final R indices (I>2sigma(I))	R1 = 0.095, wR2 = 0.167	
Largest diff. peak and hole	0.25 and -0.24 $eÅ^{-3}$	

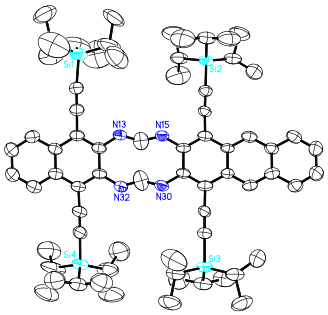

Table 44. Crystal data and structure refinement for **66**.

Identification code	wzo24	
Empirical formula	$C_{70}H_{94}N_4Si_4$	
Formula weight	1103.85	
Temperature	200(2) K	
Wavelength	1.54178 Å	
Crystal system	monoclinic	
Space group	P2/c	
Z	4	
Unit cell dimensions	a = 30.3138(17) Å	α = 90 deg.
	b = 15.0661(6) Å	β = 94.749(4) deg.
	c = 15.0276(7) Å	γ = 90 deg.
Volume	6839.7(6) $Å^3$	
Density (calculated)	1.07 g/cm^3	
Absorption coefficient	1.11 mm^{-1}	
Crystal shape	plate	
Crystal size	0.150 x 0.110 x 0.012 mm^3	
Crystal colour	orange	
Theta range for data collection	2.9 to 62.1 deg.	
Index ranges	-32≤h≤34, -16≤k≤7, -16≤l≤16	
Reflections collected	34153	
Independent reflections	10306 (R(int) = 0.1121)	
Observed reflections	6056 (I > 2σ(I))	
Absorption correction	Semi-empirical from equivalents	
Max. and min. transmission	0.98 and 0.33	
Refinement method	Full-matrix least-squares on F^2	
Data/restraints/parameters	10306 / 1509 / 722	
Goodness-of-fit on F^2	1.11	
Final R indices (I>2sigma(I))	R1 = 0.129, wR2 = 0.297	
Largest diff. peak and hole	0.69 and -0.34 $eÅ^{-3}$	

8. References

[1] H. Shirakawa, E. J. Louis, A. G. MacDiarmid, C. K. Chiang and A. J. Heeger, *J. Chem. Soc., Chem. Commun.* **1977**, 578-580.

[2] T. W. Kelley, P. F. Baude, C. Gerlach, D. E. Ender, D. Muyres, M. A. Haase, D. E. Vogel and S. D. Theiss, *Chem. Mater.* **2004**, *16*, 4413-4422.

[3] B. Kang, W. H. Lee and K. Cho, *ACS Appl. Mater. Interfaces* **2013**, *5*, 2302-2315.

[4] M. Muccini, *Nat. Mater.* **2006**, *5*, 605-613.

[5] D. Braga and G. Horowitz, *Adv. Mater.* **2009**, *21*, 1473-1486.

[6] B. Kippelen and J.-L. Brédas, *Energy Environ. Sci.* **2009**, *2*, 251-261.

[7] K. A. Mazzio and C. K. Luscombe, *Chem. Soc. Rev.* **2015**, *44*, 78-90.

[8] T. Sekitani and T. Someya, *Adv. Mater.* **2010**, *22*, 2228-2246.

[9] S. Logothetidis, *Mater. Sci. Eng. B* **2008**, *152*, 96-104.

[10] C. Liao, M. Zhang, M. Y. Yao, T. Hua, L. Li and F. Yan, *Adv. Mater.* **2015**, *27*, 7493-7527.

[11] M. Magliulo, M. Mulla, M. Singh, E. Macchia, A. Tiwari, L. Torsi and K. Manoli, *J. Mater. Chem. C* **2015**, *3*, 12347-12363.

[12] S. R. Forrest, *Nature* **2004**, *428*, 911-918.

[13] https://streetcommunication.com/de/innovative-flexible-oled-screen-displays. Copyright *14. 05. 2023*.

[14] https://www.eletimes.com/tag/semi-transparent-organic-solar-cells. Copyright *14. 05. 2023*.

[15] https://www.iptechllc.com/flexible-circuits. Copyright *14. 05. 2023*.

[16] J. Takeya, M. Yamagishi, Y. Tominari, R. Hirahara, Y. Nakazawa, T. Nishikawa, T. Kawase, T. Shimoda and S. Ogawa, *Appl. Phys. Lett.* **2007**, *90*, 102120.

[17] R. R. Tykwinski, *Acc. Chem. Res.* **2019**, *52*, 2056-2069.

[18] M. Kitamura and Y. Arakawa, *J. Phys. Condens.* **2008**, *20*, 184011.

[19] R. Ruiz, D. Choudhary, B. Nickel, T. Toccoli, K.-C. Chang, A. C. Mayer, P. Clancy, J. M. Blakely, R. L. Headrick and S. Iannotta, *Chem. Mater.* **2004**, *16*, 4497-4508.

[20] A. Mishra, C.-Q. Ma and P. Bauerle, *Chem. Rev.* **2009**, *109*, 1141-1276.

[21] H. E. Katz, A. J. Lovinger, J. Johnson, C. Kloc, T. Siegrist, W. Li, Y. Y. Lin and A. Dodabalapur,

Nature **2000**, *404*, 478-481.

[22] H. E. Katz, J. Johnson, A. J. Lovinger and W. Li, *J. Am. Chem. Soc.* **2000**, *122*, 7787-7792.

[23] D. Shukla, S. F. Nelson, D. C. Freeman, M. Rajeswaran, W. G. Ahearn, D. M. Meyer and J. T. Carey, *Chem. Mater.* **2008**, *20*, 7486-7491.

[24] P. Gawrys, D. Boudinet, M. Zagorska, D. Djurado, J.-M. Verilhac, G. Horowitz, J. Pécaud, S. Pouget and A. Pron, *Synth. Met.* **2009**, *159*, 1478-1485.

[25] A. Tsumura, H. Koezuka and T. Ando, *Appl. Phys. Lett.* **1986**, *49*, 1210-1212.

[26] H. Koezuka, A. Tsumura and T. Ando, *Synth. Met.* **1987**, *18*, 699-704.

[27] A. Tsumura, H. Koezuka and T. Ando, *Synth. Met.* **1988**, *25*, 11-23.

[28] B. Schmaltz, T. Weil and K. Müllen, *Adv. Mater.* **2009**, *21*, 1067-1078.

[29] L. A. Majewski, R. Schroeder and M. Grell, *Adv. Funct. Mater.* **2005**, *15*, 1017-1022.

[30] C. Wang, H. Dong, W. Hu, Y. Liu and D. Zhu, *Chem. Rev.* **2012**, *112*, 2208-2267.

[31] J. T. Quinn, J. Zhu, X. Li, J. Wang and Y. Li, *J. Mater. Chem. C* **2017**, *5*, 8654-8681.

[32] X. Gao and Y. Hu, *J. Mater. Chem. C* **2014**, *2*, 3099-3117.

[33] X. Zhao and X. Zhan, *Chem. Soc. Rev.* **2011**, *40*, 3728-3743.

[34] J. E. Anthony, A. Facchetti, M. Heeney, S. R. Marder and X. Zhan, *Adv. Mater.* **2010**, *22*, 3876-3892.

[35] J. Zaumseil and H. Sirringhaus, *Chem. Rev.* **2007**, *107*, 1296-1323.

[36] J. Bourgoin, M. Vandevyver, A. Barraud, G. Tremblay and P. Hesto, *Mol. Eng.* **1993**, *2*, 309-314.

[37] M. Halik, H. Klauk, U. Zschieschang, G. Schmid, S. Ponomarenko, S. Kirchmeyer and W. Weber, *Adv. Mater.* **2003**, *15*, 917-922.

[38] T. Izawa, E. Miyazaki and K. Takimiya, *Adv. Mater.* **2008**, *20*, 3388-3392.

[39] J. E. Anthony, D. L. Eaton and S. R. Parkin, *Org. Lett.* **2002**, *4*, 15-18.

[40] A. Assadi, C. Svensson, M. Willander and O. Inganäs, *Appl. Phys. Lett.* **1988**, *53*, 195-197.

[41] P. W. Blom, M. De Jong and J. Vleggaar, *Appl. Phys. Lett.* **1996**, *68*, 3308-3310.

[42] A. Brown, D. De Leeuw, E. Lous and E. Havinga, *Synth. Met.* **1994**, *66*, 257-261.

[43] B. Yoo, T. Jung, D. Basu, A. Dodabalapur, B. A. Jones, A. Facchetti, M. R. Wasielewski and T. J. Marks, *Appl. Phys. Lett.* **2006**, *88*, 082104.

[44] R. T. Weitz, K. Amsharov, U. Zschieschang, E. B. Villas, D. K. Goswami, M. Burghard, H. Dosch,

M. Jansen, K. Kern and H. Klauk, *J. Am. Chem. Soc.* **2008**, *130*, 4637-4645.

[45] J. Rivnay, L. H. Jimison, J. E. Northrup, M. F. Toney, R. Noriega, S. Lu, T. J. Marks, A. Facchetti and A. Salleo, *Nat. Mater.* **2009**, *8*, 952-958.

[46] C. Waldauf, P. Schilinsky, M. Perisutti, J. Hauch and C. J. Brabec, *Adv. Mater.* **2003**, *15*, 2084-2088.

[47] T. D. Anthopoulos, C. Tanase, S. Setayesh, E. J. Meijer, J. C. Hummelen, P. W. Blom and D. M. de Leeuw, *Adv. Mater.* **2004**, *16*, 2174-2179.

[48] T. B. Singh, N. Marjanović, P. Stadler, M. Auinger, G. Matt, S. Günes, N. Sariciftci, R. Schwödiauer and S. Bauer, *J. Appl.Phys.* **2005**, *97*, 083714.

[49] S. Miao, A. L. Appleton, N. Berger, S. Barlow, S. R. Marder, K. I. Hardcastle and U. H. F. Bunz, *Chem. Eur. J.* **2009**, *15*, 4990-4993.

[50] Z. Chen, Y. Zheng, H. Yan and A. Facchetti, *J. Am. Chem. Soc.* **2009**, *131*, 8-9.

[51] J. L. Bredas, Z. Bao, J. Locklin, H. Yang, T. Someya, G. Horowitz, V. Podzorov, Y. L. Loo, T. J. Shin, G. Malliaras, A. C. Arias, C D. Frisbie, L. Torsi, M. G Kane, H. E Katz, D. M DeLongchamp, A. Maliakal, H. Sirringhaus and L. Wang, *Organic Field-Effect Transistors*, Taylor & Francis, **2007**.

[52] I. Hill, *Appl. Phys. Lett.* **2005**, *87*, 163505.

[53] D. Gupta, M. Katiyar and D. Gupta, *Org. Electron.* **2009**, *10*, 775-784.

[54] C.-H. Shim, F. Maruoka and R. Hattori, *IEEE Trans. Electron Devices* **2009**, *57*, 195-200.

[55] G. Schweicher, G. Garbay, R. Jouclas, F. Vibert, F. Devaux and Y. H. Geerts, *Adv. Mater.* **2020**, *32*, e1905909.

[56] Q. Miao, *Adv. Mater.* **2014**, *26*, 5541-5549.

[57] D. Sparfel, F. Gobert and J. Rigaudy, *Tetrahedron* **1980**, *36*, 2225-2235.

[58] E. Clar, *Berichte der deutschen chemischen Gesellschaft (A and B Series)* **1939**, *72*, 2137-2139.

[59] Y. Ruiz-Morales, *J. Phys. Chem. A* **2002**, *106*, 11283-11308.

[60] O. Berg, E. L. Chronister, T. Yamashita, G. W. Scott, R. M. Sweet and J. Calabrese, *J. Phys. Chem. A* **1999**, *103*, 2451-2459.

[61] A. R. Reddy and M. Bendikov, *Chem. Commun.* **2006**, 1179-1181.

[62] J. Han, X. Liu, Y. Li, Z. Lou, M. Yi, H. Kong and J. Luo, *Org. Chem. Front.* **2019**, *6*, 2839-2843.

[63] J. E. Anthony, J. S. Brooks, D. L. Eaton and S. R. Parkin, *J. Am. Chem. Soc.* **2001**, *123*, 9482-9483.

[64] M. M. Payne, S. R. Parkin and J. E. Anthony, *J. Am. Chem. Soc.* **2005**, *127*, 8028-8029.

[65] S. K. Park, T. N. Jackson, J. E. Anthony and D. A. Mourey, *Appl. Phys. Lett.* **2007**, *91*, 063514.

[66] M. M. Payne, S. R. Parkin, J. E. Anthony, C. C. Kuo and T. N. Jackson, *J. Am. Chem. Soc.* **2005**, *127*, 4986-4987.

[67] T. Sakanoue and H. Sirringhaus, *Nat. Mater.* **2010**, *9*, 736-740.

[68] Y. Sakamoto, T. Suzuki, M. Kobayashi, Y. Gao, Y. Fukai, Y. Inoue, F. Sato and S. Tokito, *J. Am. Chem. Soc.* **2004**, *126*, 8138-8140.

[69] Z. Zhang, W. A. Ogden, V. G. Young and C. J. Douglas, *Chem. Commun.* **2016**, *52*, 8127-8130.

[70] C. R. Swartz, S. R. Parkin, J. E. Bullock, J. E. Anthony, A. C. Mayer and G. G. Malliaras, *Org. Lett.* **2005**, *7*, 3163-3166.

[71] M. L. Tang, J. H. Oh, A. D. Reichardt and Z. Bao, *J. Am. Chem. Soc.* **2009**, *131*, 3733-3740.

[72] O. Fischer and E. Hepp, *Berichte der deutschen chemischen Gesellschaft* **1890**, *23*, 2789-2793.

[73] O. Hinsberg, *Justus Liebigs Annalen der Chemie* **1901**, *319*, 257-286.

[74] G. Badger and R. Pettit, *J. Chem. Soc. (Resumed)* **1951**, 3211-3215.

[75] F. Kummer and H. Zimmermann, *Berichte der Bunsengesellschaft für physikalische Chemie* **1967**, *71*, 1119-1126.

[76] E. Leete, O. Ekechukwu and P. Delvigs, *J. Org. Chem.* **1966**, *31*, 3734-3739.

[77] Q. Miao, T. Q. Nguyen, T. Someya, G. B. Blanchet and C. Nuckolls, *J. Am. Chem. Soc.* **2003**, *125*, 10284-10287.

[78] Q. Tang, D. Zhang, S. Wang, N. Ke, J. Xu, J. C. Yu and Q. Miao, *Chem. Mater.* **2009**, *21*, 1400-1405.

[79] Q. Tang, Z. Liang, J. Liu, J. Xu and Q. Miao, *Chem. Commun.* **2010**, *46*, 2977-2979.

[80] Z. Liang, Q. Tang, J. Xu and Q. Miao, *Adv. Mater.* **2011**, *23*, 1535-1539.

[81] D. Liu, X. Xu, Y. Su, Z. He, J. Xu and Q. Miao, *Angew. Chem. Int. Ed.* **2013**, *52*, 6222-6227.

[82] C. Wang, Z. Liang, Y. Liu, X. Wang, N. Zhao, Q. Miao, W. Hu and J. Xu, *J. Mater. Chem.* **2011**, *21*, 15201-15204.

[83] N. D. Lang and W. Kohn, *Phys. Rev. B* **1971**, *3*, 1215-1223.

[84] H. B. Michaelson, *J. Appl. Phys.* **1977**, *48*, 4729-4733.

[85] Z. Liang, Q. Tang, R. Mao, D. Liu, J. Xu and Q. Miao, *Adv. Mater.* **2011**, *23*, 5514-5518.

[86] Z. He, R. Mao, D. Liu and Q. Miao, *Org. lett.* **2012**, *14*, 4190-4193.

[87] D. Miklík, S. F. Mousavi, Z. Burešová, A. Middleton, Y. Matsushita, J. Labuta, A. Ahsan, L. Buimaga-Iarinca, P. A. Karr, F. Bureš, G. J. Richards, P. Švec, T. Mori, K. Ariga, Y. Wakayama, C. Morari,

F. D'Souza, T. A. Jung and J. P. Hill, *Commun. Chem.* **2021**, *4*, 29.

[88] M. Chu, J. X. Fan, S. Yang, D. Liu, C. F. Ng, H. Dong, A. M. Ren and Q. Miao, *Adv. Mater.* **2018**, *30*, e1803467.

[89] H. Reiss, L. Ji, J. Han, S. Koser, O. Tverskoy, J. Freudenberg, F. Hinkel, M. Moos, A. Friedrich, I. Krummenacher, C. Lambert, H. Braunschweig, A. Dreuw, T. B. Marder and U. H. F. Bunz, *Angew. Chem. Int. Ed.* **2018**, *57*, 9543-9547.

[90] T. Wiesner, Z. Wu, J. Han, L. Ji, A. Friedrich, I. Krummenacher, M. Moos, C. Lambert, H. Braunschweig, B. Rudin, H. Reiss, O. Tverskoy, F. Rominger, A. Dreuw, T. Marder, J. Freudenberg and U. H. F. Bunz, *Chem. Eur. J.* **2022**, *28*, e202201919.

[91] M. Watanabe, Y. J. Chang, S. W. Liu, T. H. Chao, K. Goto, M. M. Islam, C. H. Yuan, Y. T. Tao, T. Shinmyozu and T. J. Chow, *Nat. Chem.* **2012**, *4*, 574-578.

[92] F. Wurthner and R. Schmidt, *Chemphyschem* **2006**, *7*, 793-797.

[93] J. E. Anthony, *Angew. Chem. Int. Ed.* **2008**, *47*, 452-483.

[94] B. Purushothaman, S. R. Parkin and J. E. Anthony, *Org. Lett.* **2010**, *12*, 2060-2063.

[95] B. D. Lindner, J. U. Engelhart, O. Tverskoy, A. L. Appleton, F. Rominger, A. Peters, H. J. Himmel and U. H. F. Bunz, *Angew. Chem. Int. Ed.* **2011**, *50*, 8588-8591.

[96] J. U. Engelhart, B. D. Lindner, M. Schaffroth, D. Schrempp, O. Tverskoy and U. H. F. Bunz, *Chem. Eur. J.* **2015**, *21*, 8121-8129.

[97] J. U. Engelhart, B. D. Lindner, O. Tverskoy, F. Rominger and U. H. F. Bunz, *Chem. Eur. J.* **2013**, *19*, 15089-15092.

[98] D. Chun, Y. Cheng and F. Wudl, *Angew. Chem. Int. Ed.* **2008**, *47*, 8380-8385.

[99] N. Zeitter, N. Hippchen, S. Maier, F. Rominger, A. Dreuw, J. Freudenberg and U. H. F. Bunz, *Angew. Chem. Int. Ed.* **2022**, *61*, e202200918.

[100] J. U. Engelhart, O. Tverskoy and U. H. F. Bunz, *J. Am. Chem. Soc.* **2014**, *136*, 15166-15169.

[101] M. Müller, H. Reiss, O. Tverskoy, F. Rominger, J. Freudenberg and U. H. F. Bunz, *Chem. Eur. J.* **2018**, *24*, 12801-12805.

[102] B. Gao, M. Wang, Y. Cheng, L. Wang, X. Jing and F. Wang, *J. Am. Chem. Soc.* **2008**, *130*, 8297-8306.

[103] A. H. Endres, M. Schaffroth, F. Paulus, H. Reiss, H. Wadepohl, F. Rominger, R. Kramer and U. H. F. Bunz, *J. Am. Chem. Soc.* **2016**, *138*, 1792-1795.

[104] A. L. Appleton, S. Barlow, S. R. Marder, K. I. Hardcastle and U. H. F. Bunz, *Synlett* **2011**, *22*, 1983-1986.

[105] J. Wang, M. Chu, J. X. Fan, T. K. Lau, A. M. Ren, X. Lu and Q. Miao, *J. Am. Chem. Soc.* **2019**, *141*, 3589-3596.

[106] F. Paulus, J. U. Engelhart, P. E. Hopkinson, C. Schimpf, A. Leineweber, H. Sirringhaus, Y. Vaynzof and U. H. F. Bunz, *J. Mater. Chem. C* **2016**, *4*, 1194-1200.

[107] D. Leibold, V. Lami, Y. J. Hofstetter, D. Becker-Koch, A. Weu, P. Biegger, F. Paulus, U. H. F. Bunz, P. E. Hopkinson and A. A. Bakulin, *Org. Electron.* **2018**, *57*, 285-291.

[108] T. C. Parker, D. G. D. Patel, K. Moudgil, S. Barlow, C. Risko, J.-L. Brédas, J. R. Reynolds and S. R. Marder, *Mater. Horiz.* **2015**, *2*, 22-36.

[109] A. L. Appleton, S. Miao, S. M. Brombosz, N. J. Berger, S. Barlow, S. R. Marder, B. M. Lawrence, K. I. Hardcastle and U. H. F. Bunz, *Org. Lett.* **2009**, *11*, 5222-5225.

[110] B. D. Lindner, F. Paulus, A. L. Appleton, M. Schaffroth, J. U. Engelhart, K. M. Schelkle, O. Tverskoy, F. Rominger, M. Hamburger and U. H. F. Bunz, *J. Mater. Chem. C* **2014**, *2*, 9609-9612.

[111] P. Biegger, M. Schaffroth, K. Brödner, O. Tverskoy, F. Rominger and U. H. F. Bunz, *Chem. Commun.* **2015**, *51*, 14844-14847.

[112] D. B. Xia, X. Guo, L. Chen, M. Baumgarten, A. Keerthi and K. Müllen, *Angew. Chem. Int. Ed.* **2016**, *55*, 941-944.

[113] M. Müller, S. Koser, O. Tverskoy, F. Rominger, J. Freudenberg and U. H. F. Bunz, *Chem. Eur. J.* **2019**, *25*, 6082-6086.

[114] M. Fahlman, A. Crispin, X. Crispin, S. Henze, M. P. de Jong, W. Osikowicz, C. Tengstedt and W. R. Salaneck, *Journal of Physics: Condensed Matter* **2007**, *19*, 183202.

[115] L. Ji, M. Haehnel, I. Krummenacher, P. Biegger, F. L. Geyer, O. Tverskoy, M. Schaffroth, J. Han, A. Dreuw, T. B. Marder and U. H. F. Bunz, *Angew. Chem. Int. Ed.* **2016**, *55*, 10498-10501.

[116] L. Ji, A. Friedrich, I. Krummenacher, A. Eichhorn, H. Braunschweig, M. Moos, S. Hahn, F. L. Geyer, O. Tverskoy, J. Han, C. Lambert, A. Dreuw, T. B. Marder and U. H. F. Bunz, *J. Am. Chem. Soc.* **2017**, *139*, 15968-15976.

[117] T. Lei, Y. Zhou, C. Y. Cheng, Y. Cao, Y. Peng, J. Bian and J. Pei, *Org. Lett.* **2011**, *13*, 2642-2645.

[118] D. Cortizo-Lacalle, C. Gozalvez, M. Olano, X. N. Sun, M. Melle-Franco, L. E. Hueso and A. Mateo-Alonso, *Org. Lett.* **2015**, *17*, 5902-5905.

[119] M. R. Ams, N. Trapp, A. Schwab, J. V. Milic and F. Diederich, *Chem. Eur. J.* **2019**, *25*, 323-333.

[120] A. L. Appleton, S. Miao, S. M. Brombosz, N. J. Berger, S. Barlow, S. R. Marder, B. M. Lawrence, K. I. Hardcastle and U. H. F. Bunz, *Org. Lett.* **2009**, *11*, 5222-5225.

[121] F. Schlütter, T. Nishiuchi, V. Enkelmann and K. Müllen, *Angew. Chem. Int. Ed.* **2014**, *53*, 1538-1542.

[122] V. Murugesan, V. Balakrishnan and R. Rasappan, *J. Catal.* **2019**, *377*, 293-298.

[123] Y. Jiang, M. Yang, X. Huang, J. Gao, C. Zhan and S. Xiao, *Polym. Chem.* **2014**, *6*, 1383-1392.

[124] D. S. Surry and S. L. Buchwald, *Angew. Chem. Int. Ed.* **2008**, *47*, 6338-6361.

[125] G. W. T. M. J. Frisch, H. B. Schlegel, G. E. Scuseria, M. A. Robb, J. R. Cheeseman, G. Scalmani, V. Barone, G. A. Petersson, H. Nakatsuji, X. Li, M. Caricato, A. V. Marenich, J. Bloino, B. G. Janesko, R. Gomperts, B. Mennucci, H. P. Hratchian, J. V. Ortiz, A. F. Izmaylov, J. L. Sonnenberg, D. Williams-Young, F. Ding, F. Lipparini, F. Egidi, J. Goings, B. Peng, A. Petrone, T. Henderson, D. Ranasinghe, V. G. Zakrzewski, J. Gao, N. Rega, G. Zheng, W. Liang, M. Hada, M. Ehara, K. Toyota, R. Fukuda, J. Hasegawa, M. Ishida, T. Nakajima, Y. Honda, O. Kitao, H. Nakai, T. Vreven, K. Throssell, J. A. Montgomery, Jr., J. E. Peralta, F. Ogliaro, M. J. Bearpark, J. J. Heyd, E. N. Brothers, K. N. Kudin, V. N. Staroverov, T. A. Keith, R. Kobayashi, J. Normand, K. Raghavachari, A. P. Rendell, J. C. Burant, S. S. Iyengar, J. Tomasi, M. Cossi, J. M. Millam, M. Klene, C. Adamo, R. Cammi, J. W. Ochterski, R. L. Martin, K. Morokuma, O. Farkas, J. B. Foresman and D. J. Fox, Gaussian, Inc., Wallingford CT, **2016**.

[126] C. M. Cardona, W. Li, A. E. Kaifer, D. Stockdale and G. C. Bazan, *Adv. Mater.* **2011**, *23*, 2367-2371.

[127] J. A. Weil and J. R. Bolton, *Electron Paramagnetic Resonance: Elementary Theory and Practical Applications, 2nd Edition*, **2006**.

[128] Y. Diao, L. Shaw, Z. Bao and S. C. B. Mannsfeld, *Energy Environ. Sci.* **2014**, *7*, 2145-2159.

[129] S. Liu, J.-K. Wu, C.-C. Fan, G.-B. Xue, H.-Z. Chen, H. L. Xin and H.-Y. Li, *Sci. Bull.* **2015**, *60*, 1122-1127.

[130] D. Liu, Z. He, Y. Su, Y. Diao, S. C. B. Mannsfeld, Z. Bao, J. Xu and Q. Miao, *Adv. Mater.* **2014**, *26*, 7190-7196.

[131] S. Maier, N. Hippchen, F. Rominger, J. Freudenberg and U. H. F. Bunz, *Chem. Eur. J.* **2021***, 27,* 16320-16324.

[132] G. te Velde, F. M. Bickelhaupt, E. J. Baerends, C. F. Guerra, S. J. A. Van Gisbergen, J. G. Snijders and T. Ziegler, *J. Comput. Chem.* **2001**, *22*, 931-967.

[133] M. M. Payne., S. R. Parkin., J. E. Anthony., C.-C. Kuo. and T. N. Jackson., *J. Am. Chem. Soc.* **2005**, *127*, 4986-4987.

[134] W. Fudickar and T. Linker, *J. Am. Chem. Soc.* **2012**, *134*, 15071-15082.

[135] H. Qu and C. Chi, *Org. Lett.* **2010**, *12*, 3360-3363.

[136] S. Dutt, *J. Chem. Soc. (Resumed)* **1926**, *129*, 1171-1184.

[137] J. B. Li, Y. Q. Shen, J. Q. Wan, X. L. Yu and Q. C. Zhang, *Eur. J. Org. Chem.* **2018**, *2018*, 3375-3390.

[138] Z. Zeng, X. Shi, C. Chi, J. T. L. Navarrete, J. Casado and J. Wu, *Chem. Soc. Rev.* **2015**, *44*, 6578-6596.

[139] X.-D. Tang., Y. Liao., H. G. . and Z.-G. Shuai., *J. Mater. Chem.* **2011**, *22*, 18181-18191.

[140] X. Xu, Y. Yao, B. Shan, X. Gu, D. Liu, J. Liu, J. Xu, N. Zhao, W. Hu and Q. Miao, *Adv. Mater.* **2016**, *28*, 5276-5283.

[141] V. Stehr, J. Pfister, R. Fink, B. Engels and C. Deibel, *Phys. Rev. B* **2011**, *83*, 155208.

[142] J. McCullough, H. Finke, J. Messerly, S. Todd, T. Kincheloe and G. Waddington, *J. Phys. Chem.* **1957**, *61*, 1105-1116.

[143] J. H. Hildebrand, A. D. Duschak, A. Foster and C. Beebe, *J. Am. Chem. Soc.* **1917**, *39*, 2293-2297.

[144] S. Miao, S. M. Brombosz, P. v. R. Schleyer, J. I. Wu, S. Barlow, S. R. Marder, K. I. Hardcastle and U. H. F. Bunz, *J. Am. Chem. Soc.* **2008**, *130*, 7339-7344.

[145] B. D. Lindner, Y. Zhang, S. Höfle, N. Berger, C. Teusch, M. Jesper, K. I. Hardcastle, X. Qian, U. Lemmer and A. Colsmann, *J. Mater. Chem. C* **2013**, *1*, 5718-5724.

[146] B. D. Lindner, J. U. Engelhart, M. Marken, O. Tverskoy, A. L. Appleton, F. Rominger, K. I. Hardcastle, M. Enders and U. H. F. Bunz, *Chem. Eur. J.* **2012**, *18*, 4627-4633.

[147] J. U. Engelhart, B. D. Lindner, O. Tverskoy, M. Schaffroth, F. Rominger and U. H. F. Bunz, *J. Org. Chem.* **2013**, *78*, 1249-1253.

[148] N. Akai, S. Kudoh and M. Nakata, *Chem. Phys. Lett.* **2003**, *375*, 605-611.

[149] G. R. Fulmer, A. J. Miller, N. H. Sherden, H. E. Gottlieb, A. Nudelman, B. M. Stoltz, J. E. Bercaw and K. I. Goldberg, *Organometallics* **2010**, *29*, 2176-2179.

Eidesstattliche Erklärung

GESAMTFAKULTÄT FÜR MATHEMATIK, INGENIEUR-
UND NATURWISSENSCHAFTEN
COMBINED FACULTY OF MATHEMATICS, ENGINEERING
AND NATURAL SCIENCES

Eidesstattliche Versicherung gemäß § 8 der Promotionsordnung für die Gesamtfakultät für Mathematik, Ingenieur- und Naturwissenschaften der Universität Heidelberg /

Sworn Affidavit according to § 8 of the doctoral degree regulations of the Combined Faculty of Mathematics, Engineering and Natural Sciences at Heidelberg University

1. Bei der eingereichten Dissertation zu dem Thema / The thesis I have submitted entitled *„Synthesis and characterization of larger azaacenes and stable azaacene radical anions“* handelt es sich um meine eigenständig erbrachte Leistung / is my own work.

2. Ich habe nur die angegebenen Quellen und Hilfsmittel benutzt und mich keiner unzulässigen Hilfe Dritter bedient. Insbesondere habe ich wörtlich oder sinngemäß aus anderen Werken übernommene Inhalte als solche kenntlich gemacht. / I have only used the sources indicated and have not made unauthorised use of services of a third party. Where the work of others has been quoted or reproduced, the source is always given.

3. Die Arbeit oder Teile davon habe ich wie folgt/bislang nicht an einer Hochschule des In- oder Auslands als Bestandteil einer Prüfungs- oder Qualifikationsleistung vorgelegt. / I have not yet/have already presented this thesis or parts thereof to a university as part of an examination or degree.

4. Die Richtigkeit der vorstehenden Erklärungen bestätige ich. / I confirm that the declarations made above are correct.

5. Die Bedeutung der eidesstattlichen Versicherung und die strafrechtlichen Folgen einer unrichtigen oder unvollständigen eidesstattlichen Versicherung sind mir bekannt. / I am aware of the importance of a sworn affidavit and the criminal prosecution in case of a false or incomplete affidavit.

Ich versichere an Eides statt, dass ich nach bestem Wissen die reine Wahrheit erklärt und nichts verschwiegen habe. / I affirm that the above is the absolute truth to the best of my knowledge and that I have not concealed anything.

Heidelberg, 12.06.2023 .....

Ort und Datum / Place and date Unterschrift / Signature

The German text is legally binding.